Technical Report

MASS TRANSFER FROM ROUGH SURFACES

by

S. B. Verma

and

J. E. Cermak

The work upon which this report is based was
supported by funds provided by the
United States Department of the Interior,
Office of Water Resources Research,
as authorized under the
Water Resources Research Act of 1964
through Contract No. 14-01-0001.

Fluid Dynamics and Diffusion Laboratory
College of Engineering
Colorado State University
Fort Collins, Colorado

May 1971

CER70-71SBV-JEC59

From a dissertation submitted to the Graduate Faculty
of Colorado State University in partial fulfillment of
the requirements for the degree of Doctor of Philosophy

ABSTRACT

MASS TRANSFER FROM ROUGH SURFACES

This report is an experimental investigation of the problem of mass transfer from rough surfaces, as manifested by evaporation. Sinusoidal wavy surfaces of three different sizes were used to represent a controlled and defined shape of roughness. Simultaneous measurements of the mean velocity, humidity and temperature distributions made at various stations over the saturated wavy surfaces are reported. A technique was developed to measure the distribution of the local mass transfer coefficient on the wavy surface. Visualization techniques were used to investigate the airflow pattern inside the wave troughs.

In the region far downstream of the leading wave, where the equilibrium boundary layer conditions were achieved, the average mass transfer coefficient was found to be a simple power function of the surface Reynolds number. Based on this result, the mass transfer data from this study correlated well with the mass transfer data from surfaces of various other geometries, e.g., evaporation data from water waves, evaporation data from flat plate and sublimation data from surfaces roughened with irregular pyramids and spanwise humps. Estimates of the Owen-Thomson parameter B^{-1} (a nondimensional number used to measure the discrepancy between the transport of mass and momentum to, or from, a surface) were obtained and compared with the results from other pertinent mass transfer studies.

TABLE OF CONTENTS

TABLE OF CONTENTS - (Continued)

TABLE OF CONTENTS - (Continued)

LIST OF TABLES

LIST OF FIGURES

LIST OF FIGURES - (Continued)

LIST OF FIGURES - (Continued)

LIST OF FIGURES - (Continued)

LIST OF FIGURES - (Continued)

LIST OF SYMBOLS

Symbol	Definition	Dimension
a	Wave amplitude	L
B^{-1}	Reciprocal of sublayer Stanton number of Owen and Thomson (56)	--
C_f	Effective average skin friction coefficient	--
C_p	Specific heat at constant pressure	$HM^{-1}\Theta^{-1}$
d	Zero plane displacement	L
D	Molecular mass diffusivity	L^2T^{-1}
E	Evaporation rate per unit area	$ML^{-2}T^{-1}$
$f_+(z)$	Resistance to transport of momentum	--
g	Acceleration due to gravity	LT^{-2}
Gu	Gukhman number	--
H	Form factor also Heat flux	$HL^{-2}T^{-1}$
h	Wave height	L
k	Karman constant	--
K_c	Mass transfer coefficient = mass transfer rate per unit area/Δq	$ML^{-2}T^{-1}$
K_x, K_y, K_z	Exchange coefficients of water vapor in x, y, z directions	L^2T^{-1}
K_M	Exchange coefficient of momentum	L^2T^{-1}
K_h	Exchange coefficient of heat	L^2T^{-1}
L	Monin Obukhov length	L
L_e	Latent heat of evaporation	HM^{-1}
ℓ	Characteristic length	L
m, n	Exponents	--
p	Pressure	$ML^{-1}T^{-2}$
Pr	Prandtl number	--

LIST OF SYMBOLS - (Continued)

Symbol	Definition	Dimension
q	Specific humidity ($\frac{\text{gm of water vapor}}{\text{gm of dry air}}$)	--
q_{amb}	Ambient specific humidity	--
q_s	Surface air humidity	--
q_∞	Specific humidity in free stream	--
q'	Fluctuations in q	--
q_*	Friction specific humidity	--
Δq	$q_s - q_\infty$	--
Re	Reynolds number	--
$r_+(z)$	Resistance to transport of mass	--
$(Re_*)_o$	Surface Reynolds number (based on u_* and z_o)	--
Sc	Schmidt number	--
Sh	Sherwood number	--
$(Sh)_h$	Sherwood number based on h	--
$(Sh)_o$	Sherwood number based on z_o	--
T	Temperature	Θ
T_s	Surface air temperature	Θ
T	Ambient air temperature	Θ
T_*	Friction temperature	Θ
t	Time	T
U,V,W	Mean velocity components in x,y,z direction	LT^{-1}
u',v',w'	Velocity fluctuations in x,y,z direction	LT^{-1}
u_*	Friction velocity	LT^{-1}
x	Distance along longitudinal direction	L
y	Distance along lateral direction	L
z	Distance above effective zero plane in vertical direction	L

LIST OF SYMBOLS - (Continued)

Symbol	Definition	Dimension
z_c	Distance above wave crest in vertical direction	L
z_T	Distance above wave bottom in vertical direction	L
z_o	Roughness parameter	L
z_{om}	Hypothetical length parameter associated with humidity profile	L
z_{ot}	Hypothetical length parameter associated with temperature profile	L
α	Molecular thermal diffusivity	L^2T^{-1}
δ	Boundary layer thickness for momentum transfer	L
δ_m	Mass boundary layer thickness	L
δ_t	Temperature boundary layer thickness	L
δ^*	Displacement thickness	L
θ	Momentum thickness	L
μ	Coefficient of kinematic viscosity	$ML^{-1}T^{-1}$
ν	Coefficient of dynamic viscosity	L^2T^{-1}
ρ	Mean mass density	ML^{-3}
τ	Shear Stress	$ML^{-1}T^{-2}$
λ	Wave length	L

Chapter I

Introduction

Mass transfer is a phenomenon of special interest to researchers in many branches of modern science. Chemical engineers were the first to contribute extensively to the basic theory of mass transfer. Later, mechanical and aeronautical engineers became concerned with this branch of science because of the development of aircraft propulsion and missile cooling systems. Meteorologists, combustion and air conditioning technologists, and many others also have become interested in this area because of its numerous applications to technological and environmental control problems.

One of the most familiar forms of mass transfer is the process known as evaporation. Evaporation is of great importance because of its diverse influence. Irrigation engineers need accurate estimates of the amount of evaporation from reservoirs, lakes, canals, and the soil. Meteorologists need to know humidity and temperature distributions near ocean surfaces for obtaining the rates of exchange of energy between the ocean surfaces and the atmosphere which is a fundamental requirement for understanding general circulation. Hydrologists, agronomists, and many others are also interested in the phenomena of evaporation.

This report is a systematic experimental study of the problem of mass transfer from rough surfaces, as manifested by evaporation. Wavy (sinusoidal) surfaces were chosen to represent a controlled and defined shape of roughness. The work reported here is part of a comprehensive research program designed to study the transfer of both

mass and momentum from rough surfaces. The significance of this program is that it presents the means by which man may make intelligent decisions for controlling, at least to a limited extent, the local atmospheric diffusion characteristics over vegetated areas, corrugated fields, and other applicable places.

Seeding arid range land is not always successful because inadequate soil moisture frequently limits seed germination and retards early growth (49). In addition, a successful seeding method must control soil erosion. Accordingly, deep furrow planting has been suggested. Preliminary field and wind-tunnel observations (48) indicate that furrowed surfaces (microridging) effectively reduce wind erosion and improve seed germination. Therefore, it is important to obtain, under controlled conditions, laboratory data on local evaporation loss over the surface of corrugated areas, so that available moisture for plant growth can be maximized. Mass transfer information from wavy surfaces can be also used to give an estimate of evaporated loss from water waves on a lake or ocean surface. Evaporation data obtained in this study could be used to help make an overall energy balance for a saturated surface.

Some investigations have been conducted on mass transfer from smooth surfaces but few results are available that deal with mass transfer from rough surfaces. A few analytical approaches by Calder (7), Sutton (82), Rider et. al. (71) etc. attempted to predict the mass transfer rates by solving the diffusion equation, but these solutions fail to consider the effect of change in aerodynamic roughness on momentum transfer. A number of investigations in the field have tried to understand the mechanism of mass transfer from the earth's

surface, but the resulting measurements are difficult to interpret because of the numerous uncontrolled variables involved. Moreover, sufficiently accurate and simultaneous measurements of mean velocity, humidity and temperature distributions over and downstream of a rough saturated surface have not been available. It is the purpose of this study to provide experimental data that can be used for developing practical methods to predict evaporation rates from various kinds of surfaces. This study also enables a comparison to be made of the transfer coefficients for mass (water vapor) and momentum transport.

Briefly, the main objectives of this study are:

1. to determine the local mass transfer coefficients over saturated wavy surfaces for several wave sizes and flow conditions;
2. to obtain detailed distributions of mean velocity, humidity, and temperature above saturated wavy surfaces;
3. to develop, by using the acquired experimental data, a general model of the mass transfer mechanism in terms of the various pertinent flow parameters, and
4. to correlate the mass transfer data obtained from saturated fixed wavy surfaces with mass transfer data from saturated surfaces of various other geometries (e.g., flat plate, water waves, solid irregular surfaces, etc.).

Also, the mass transfer results are compared with certain other pertinent investigations. Practical applications of this study are discussed.

Chapter II

Theoretical and Experimental Background

This chapter deals with the basic concepts of mass transfer in turbulent flows. A brief review of pertinent literature in connection with mass transfer from both smooth and rough surfaces is given. To start with, the governing diffusion equation is introduced and relevant works are reviewed which are of both theoretical and experimental nature; the latter referred mainly to the investigations of meteorological problems. A more complete way of describing a mass transfer phenomena is to correlate the dimensionless variables involved in the problem concerned, thus, some emphasis is given in this direction. Some aspects of the so-called "Reynolds analogy" is considered as far as the problem of mass transfer from rough surfaces is concerned.

2.1 Concept and Application of K-theory -- Diffusion Equation

The two-dimensional boundary-layer flow of an incompressible fluid is considered. Let $q(x,y,z,t)$ be the concentration of a diffusing substance, e.g., the amount of water vapor associated with unit weight of dry air, let U, V, and W denote the components of mean velocity, and let u', v', and w' be the corresponding fluctuations in the x, y, and z directions, respectively, with q' being the fluctuation in q. Then, the equation of diffusion can be written:

$$\frac{\partial q}{\partial t} + U \frac{\partial q}{\partial x} + V \frac{\partial q}{\partial y} + W \frac{\partial q}{\partial z} = \frac{\partial}{\partial x}\left(K_x \frac{\partial q}{\partial x}\right) + \frac{\partial}{\partial y}\left(K_y \frac{\partial q}{\partial y}\right) + \frac{\partial}{\partial z}\left(K_z \frac{\partial q}{\partial z}\right), \quad (2\text{-}1)$$

in which K_x, K_y, and K_z are the exchange coefficients for mass transfer in the three directions. These exchange coefficients are obtained from the assumption of proportionality between the respective diffusion fluxes and the concentration gradients, e.g.,

$$\overline{u'q'} = - K_x \frac{\partial q}{\partial x}, \quad \overline{v'q'} = - K_y \frac{\partial q}{\partial y} \quad \text{and} \quad \overline{w'q'} = - K_z \frac{\partial q}{\partial z} \quad . \tag{2-2}$$

For a steady, two dimensional problem with $V = W = 0$ when the longitudinal dispersion term is neglected, since it is much smaller than the corresponding term in the z-direction and the convective term, the diffusion equation reduces to

$$U \frac{\partial q}{\partial x} = \frac{\partial}{\partial z} \left(K_z \frac{\partial q}{\partial z}\right) \quad . \tag{2-3}$$

Equation (2-3) can be solved analytically only if the functional form of the exchange coefficient K_z and the velocity profile are known. Many scientists have solved this equation by assuming various forms of K_z and U.

Jeffreys (33) and Roberts (69) obtained a solution for the case of a constant exchange coefficient and wind independent of height. Although their investigations must be recognized historically, their predictions did not correlate well with real field observations. Obviously, the discrepancies are because both the exchange coefficient and the wind velocity show a considerable variation with height under normal conditions in the lower atmosphere.

Later, Roberts [see Calder (7)] assumed a power law profile for velocity. On the assumption of constancy of shear stress in the lower

layers of the atmosphere and using $K_z = K_M$, where K_M is the exchange coefficient for momentum transfer in the z-direction, he found an exact solution for Eq. (2-3).

Aris (2) investigated the integrated forms of the diffusion equation. Instead of trying to solve the diffusion Eq. (2-3) directly, he formed the differential equation for the moments of q, namely $q_n(x,z) = \int_{-\infty}^{\infty} y^n q(x,y,z)dy$. Later, the Aris moment method was used successfully by other investigators, e.g., Smith (73), Saffman (71), Fischer (24), Sayre (72), and Atesman (4).

O. G. Sutton (78) investigated the problem of evaporation from a saturated or free liquid surface, of finite extent downwind, level with the earth's surface, and of such dimensions that no detectable variation of wind structure was produced. To formulate the problem mathematically, he assumed that for an infinite cross wind saturated strip, of length x_o downwind and situated at ground level $(z = 0)$, the appropriate boundary conditions were:

$$\left.\begin{aligned} &\lim_{z\to 0} q(x,z) = q_s \text{ (a constant)} && (0 < x \leq x_o) \\ &\lim_{z\to\infty} q(x,z) = 0 && (0 \leq x \leq 0) \\ &\lim_{x\to 0} q(x,z) = 0 && (0 < z) \end{aligned}\right\} \qquad (2\text{-}4)$$

He hypothesized the following functional form for the correlation coefficient R_ξ,

$$R_\xi = \left(\frac{\nu}{\nu + \overline{w'^2}\xi}\right)^n \qquad (2\text{-}5)$$

with the requirement that ν be small compared to $\overline{w'^2}\xi$. Then, assuming $K_z = K_M$, Sutton used Taylor's theory of diffusion by continuous movements, and Prandtl's mixing length theory to obtain:

$$K_z = \frac{(0.251)^{1-n}}{1-n} \nu^n \left[\left(\frac{\partial U}{\partial z}\right)^3 \left(\frac{\partial^2 U}{\partial z^2}\right)^{-2}\right]^{1-n} . \qquad (2\text{-}6)$$

Substituting this expression into $K_z \frac{\partial u}{\partial z} = \frac{\tau}{\rho}$ = constant, which simply means that the shear stress is invariant with height in the lower atmosphere, the following familiar power law of velocity was recovered

$$\frac{U}{U_1} = \left(\frac{z}{z_1}\right)^{\frac{n}{2-n}} . \qquad (2.7)$$

Hence, Sutton was able to obtain an analytical solution of the diffusion equation with the above functional forms of K_z and U.

Sutton's theory, though applicable to aerodynamically smooth surfaces only, has received considerable experimental and some theoretical attention. Evaporation measurements of many investigators, e.g. Himus (30), Hine (31), Powell and Griffith (63), and Thiesenhausen (82) agreed reasonably with Sutton's theory.

In 1943, Pasquill (56) modified Sutton's theory by replacing ν by D, the molecular diffusivity of water vapor, to obtain better agreement with his wind tunnel results.

Yih (88) presented a solution of Eq. (2-3), using a procedure similar to that first used by Blasius and later by Goldstein (29) and Mangler (46) in their analysis of boundary-layer problems. Kohler (37) had obtained the same solution in an attempt to solve equation (2-3) by Sutton's theory. Cermak (8) adapted Karman's (35) equation for heat transfer,

$$\frac{1}{C_H} = \frac{2}{C_f} + 5\left(\frac{2}{C_f}\right)^{1/2} \left\{\sigma - 1 + \ln\left[1 + \frac{5}{6}(\sigma - 1)\right]\right\}, \qquad (2.8)$$

to vapor transport by writing instead of C_H,

$$C_e = E/\rho g U_\infty \Delta q \quad . \tag{2.9}$$

Assuming a 1/7 power relationship of velocity distribution, he finally obtained the following equation for the range of $10^3 \leq R_x \leq 10^5$:

$$N^{-1} = \frac{6.23\ R_x^{-8/9}}{(\frac{x_1'}{X_1})^{4/45}} - \frac{3.77\ R_x^{-1}}{(\frac{x_1'}{X_1})^{1/10}} \quad , \tag{2.10}$$

in which $\tau = C_f\ \rho\ \frac{U_\infty^2}{2}$, $Q = C_H\ \rho\ C_p\ U_\infty \Delta T$, $R_x = \frac{U_* x}{D}$, $N = \frac{E' x}{D \Delta q}$, x_1 = distance downstream from the beginning of evaporation boundary, x_1' = distance downstream from the leading edge of boundary, and E' = Evaporation weight/time x area.

Before this, Frost (26) had attempted to extend the considerations to hydrodynamically rough surfaces. He developed a form for K_z that included the roughness parameter. In his work, he assumed that the mixing length over a rough surface can be written as

$$\ell_1 = z^{1-m} z_o^{\ m} \quad , \tag{2.11}$$

in which z_o = roughness parameter and m = constant. The shear stress, which is given by

$$\tau = \rho\ \ell_1^2\ (\frac{\partial U}{\partial z})^2 \quad , \tag{2.12}$$

then becomes

$$\frac{\tau}{\rho} = z^{2-2m} z_o^{\ 2m}\ (\frac{\partial U}{\partial z})^2 \quad . \tag{2.13}$$

Again, assuming the constancy of shear stress in the lower 30 meters of the atmosphere, and integrating, the relation

$$U = \frac{1}{m} \sqrt{\tau/\rho} \left(\frac{z}{z_o}\right)^m \tag{2.14}$$

is obtained. Thus, the assumption in (2-11) is compatible with the power law

$$\frac{U}{U_1} = \left(\frac{z}{z_1}\right)^m \tag{2.15}$$

for a wind profile similar to equation (2-7). Next, using

$$K_z = \ell_1^2 \frac{\partial U}{\partial z} , \tag{2.16}$$

and Eqs. (2-11) and (2-15), Frost solved the diffusion equation analytically to obtain the evaporation rates from rough surfaces.

In an effort to include the effect of stability, Deacon (19) proposed a general wind profile

$$U = \frac{u_*}{k(1-\beta_1)} \left[\left(\frac{z}{z_o}\right)^{1-\beta_1} - 1\right] \tag{2.17}$$

for rough flows, in which the boundary requirement is that $\frac{U}{u_*} = 0$ at $\frac{z}{z_o} = 1$. The limiting values in Eq. (2.17) are $0.75 \leq \beta_1 \leq 1.25$, where

$$\left.\begin{array}{ll} & \beta_1 < 1 \quad \text{for stable conditions,} \\ & \beta_1 = 1 \quad \text{for neutral conditions,} \\ \text{and} \quad & \beta_1 > 1 \quad \text{for unstable conditions.} \end{array}\right\} \tag{2.18}$$

Then, the relation $\tau = \rho K_z \frac{\partial U}{\partial z} = \text{constant}$ and Eq. (2-17) can be used to obtain a form for K_z that enables the diffusion Eq. (2-3) to be solved.

Calder (7) also studied the problem of evaporation from smooth and rough surfaces, of a finite extent downwind, in a turbulent flow. In a so-called "aerodynamically smooth flow", the drag exerted on the fluid by the boundary surface is a function of the Reynolds number only, and, except for a region very close to the surface, the distribution of mean velocity is represented by the law

$$\frac{U}{u_*} = \frac{1}{k} \ln \frac{u_* z}{\nu} + 5.5 \quad . \tag{2.19}$$

On the other hand, for "aerodynamically rough flow," the drag is independent of the Reynolds number and is proportional to the square of velocity with the mean velocity distribution

$$\frac{U}{u_*} = \frac{1}{k} \ln \left(\frac{z-d}{z_o}\right) \quad \text{for} \quad z \geq z_o + d \quad , \tag{2.20}$$

in which d is the zero plane displacement, z is measured from the base of the roughness, and z_o is called the roughness parameter. Because of the intractibility of certain mathematical developments, Calder chose to use the relations

$$\frac{U}{u_*} = q'' \left(\frac{u_* z}{\nu}\right)^{\alpha} \quad , \tag{2.21}$$

and

$$\frac{U}{u_*} = q''' \left(\frac{z-d}{z_o}\right)^{\alpha} \tag{2.22}$$

in place of (2-19) and (2-20), respectively. In Eq. (2-21) q'' and α depend on the range of $\frac{u_* z}{\nu}$ such that Eq. (2-21) agrees approximately with Eq. (2-19), and similarly q''' and α also will depend on the range of $(z-d)/z_o$ such that Eq. (2-22) agrees with the more accurate

Eq. (2-20). Also, in the turbulent layer over a smooth or a rough surface, there is a region not too far removed from the surface in which the turbulent shear stress, given by

$$\tau = \rho\, K_M(z)\, \frac{\partial U}{\partial z} \quad , \tag{2.23}$$

can be regarded as effectively independent of the distance from the surface. From Eqs. (2-21) and (2-22), one can easily obtain

$$\tau_o = \rho \left(\frac{U}{q''}\right)^{2/1+\alpha} \left(\frac{\nu}{z}\right)^{2\alpha/1+\alpha} \tag{2.24}$$

for smooth surfaces, and

$$\tau_o = \rho \frac{U^2}{q'''^2} \left(\frac{z_o}{z}\right)^{2\alpha} \tag{2.25}$$

for rough surfaces. Equations (2-24) and (2-25) are special cases of a more general equation

$$\tau_o = \varepsilon\rho\, U^{2\beta} \left(\frac{\delta}{z}\right)^{2\alpha\beta} \quad , \tag{2.26}$$

in which $\beta = \frac{1}{1+\alpha}$, $\delta = \nu$, and $\varepsilon = \left(\frac{1}{q''}\right)^{2/1+\alpha}$ for smooth surfaces,

and

$\beta = 1$, $\delta = z_o$, and $\varepsilon = 1/q'''^2$ for rough surfaces. (2.27)

Thus, Calder was able to adopt a uniform mathematical treatment for both smooth and rough surfaces. In both cases, using

$$\frac{U}{U_1} = \left(\frac{z}{z_1}\right)^{\alpha} \quad , \tag{2.28}$$

in which U_1 is the velocity at a standard height z_1, an expression for $K_M(z)$ was obtained applying Eqs. (2-23), (2-26) and (2-27).

Calder assumed that the concentration of vapor over a rough surface, which is saturated, was constant over a plane at a distance from the datum plane equal to the zero plane displacement d of the velocity profile. At this distance, turbulence can be regarded as first becoming operative. Thus, the boundary conditions (2-4) were assumed valid for a rough surface also, if the plane $z = 0$ is at a distance d from the datum plane of height reference in the velocity profile equation. He treated the infinitely crosswind strip of evaporating surface defined by $z = 0$, $0 < x \leq x_o$, as an aggregate of elemental, continuous, infinite, crosswind, line sources of vapor. And finally, assuming $K_M(z) = K_z(z)$, Calder obtained the expressions for vapor concentration distribution $q(x,z)$ and the evaporation rate. His expression for vapor concentration above a smooth saturated strip is identical with the one first obtained by O. G. Sutton (79).

Phillip (60) and Rider et al.(69) studied the problem of horizontal transport of heat and moisture in the lower atmosphere. They solved the steady state two-dimensional equations of diffusion of heat and moisture using energy balance considerations. Their solution has some formal similarity to the solution obtained for the evaporation problem by Sutton (79) and Calder (7). The analyses by Sutton and Calder, however, neglected energy-balance considerations and required that the surface temperature of the evaporating surface be known. In the study pursued by Rider et al. (69), because the energy balance was taken into account, the surface temperature of the downwind wet area emerged as part of the solution.

Davies (16, 17, 18, and 19) introduced a variable lateral diffusivity and solved the three dimensional diffusion equation:

$$U \frac{\partial q}{\partial x} = \frac{\partial}{\partial y} \left(K_y \frac{\partial q}{\partial y}\right) + \frac{\partial}{\partial z} \left(K_z \frac{\partial q}{\partial z}\right) . \qquad (2.29)$$

The results showed a better agreement, (compared to the two dimensional theory) with experiments on diffusion of water vapor.

In this section, some of the relevant investigations in connection with mass transfer from smooth or rough surfaces have been discussed. It is clear that these theories available at present are adequate to give qualitative information and provide order of magnitude answers to quantitative questions. However, there remain significant discrepancies among these theories and observations; considerable extensions are needed before these theories can take into consideration such complicated factor as changes in aerodynamic roughness.

2.2 Semi-empirical Theories of Turbulent Diffusion

In a fully turbulent flow, that is a flow in which molecular diffusion is largely outweighed by turbulent mixing, the mean upward vertical flux F of an entity S per unit mass of the fluid, is given by

$$F = \rho \overline{w's'} = - \rho K \frac{\partial \overline{S}}{\partial z} , \qquad (2.30)$$

in which w' and s' are the fluctuations in the vertical component of velocity, and concentration, respectively, $\overline{S}$ is the averaged concentration of the entity, ρ is the density of the fluid, and K is the eddy diffusivity. The justification of Eq. (2.30) rests mainly on empirical grounds and is based on the mixing length approach to atmospheric diffusion, which has an analogy with the molecular motion.

The turbulent shear stress, which is given by $\tau = -\rho\overline{u'w'}$, can also be interpreted as a transport of the x-momentum across a plane normal to the vertical z-axis, and so Eq. (2.30) gives

$$\tau = -\rho\overline{u'w'} = \rho K_M \frac{\partial U}{\partial z} \quad , \tag{2.31}$$

in which K_M is defined as the eddy momentum diffusivity. In the constant flux-layer, one can define a friction velocity u_* such that

$$\tau = \rho u_*^2 \quad , \tag{2.32}$$

in which u_* is assumed to be independent of z for a given wind velocity profile. For a nearly neutral case, dimensional analysis of these variables leads to an expression for the vertical gradient of mean wind speed U:

$$\frac{\partial U}{\partial z} = \frac{u_*}{kz} \quad , \tag{2.33}$$

in which k is a dimensionless constant. Integration of the above equation gives the known logarithmic velocity profile

$$\frac{U}{u_*} = \frac{1}{k} \ln \frac{z}{z_o} \qquad (z>z_o) \ , \tag{2.34}$$

where z_o is termed as the roughness length, and k as Karmans constant. For rough surfaces, if z_T is measured from the base of the roughness rather than from the level of the zero mean wind, which may be somewhat higher, it is necessary to introduce a zero plane displacement d so that Eq. (2.34) becomes

$$\frac{U}{u_*} = \frac{1}{k} \ln \frac{z_T - d}{z_o} \ , \tag{2.35}$$

which is the same as Eq. (2-20).

On the basis of the assumption that the eddy viscosity, eddy diffusivity and eddy conductivity are determined by the first and second differential coefficients of the mean velocity U, mean humidity q, and mean potential temp T, Björgum (6) obtained the following relations for the constant flux layer:

$$q - q_s = q_* \ln \frac{z}{z_{om}} , \tag{2.36}$$

and

$$T - T_s = T_* \ln \frac{z}{z_{ot}} , \tag{2.37}$$

in which z is measured from the effective zero plane, given by $z = z_T - d$. The zero plane displacement d is the same as in the corresponding case of velocity profile (Eq. 2.35) and z_T is measured from the base of the roughness. The quantities q_* and T_* are known as the friction humidity and friction temperature respectively; z_{om} and z_{ot} may be considered as hypothetical length parameters.

For the turbulent transport of water vapor in the constant flux region, one can write

$$E = \rho \overline{w'q'} = - \rho K_z \frac{\partial q}{\partial z} . \tag{2.38}$$

Combining Eq. (2.38) with Eqs. (2.31), (2.32), (2.33) and (2.35), one obtains

$$E = - \rho k \beta u_* q_* , \tag{2.39}$$

in which $\beta = K_z/K_M$. In an analogous fashion, the following equation can be written for the turbulent transport of heat,

$$H = \rho C_p \overline{w't'} = - \rho C_p K_h \frac{\partial T}{\partial z} = - \rho C_p \beta' k u_* T_* \ , \qquad (2.40)$$

in which t' is the potential temperature fluctuation, K_z is the eddy conductivity, C_p is the specific heat at constant pressure and β' is equal to K_h/K_M.

In regard to ratio K_z/K_M (or K_h/K_M), the experimental results obtained, both in field and laboratory, are contradictory and the question is far from settled. The work of Swinbank (84) suggests a value of 0.7 for K_h/K_M, while that of Rider (70) suggests about 1.3, for neutral conditions. Pasquill (58) found that in neutral and stable conditions, but not under unstable conditions, measured K_z and calculated K_M values were essentially equal within 10 percent. Laykhtman and Ponomareva (43) obtained the following relation, which agrees satisfactorily with the measurements of other authors,

$$\frac{K_h}{K_M} \simeq \begin{cases} 0.8 & \text{for } -0.03 < \frac{z}{L} < +0.10 \\ 3.2 \left| z/L \right|^{0.35} & \text{for } -0.8 < \frac{z}{L} < -0.03 \\ 3.0 & \text{for } \frac{z}{L} < -0.8 \end{cases} \qquad (2.41)$$

in which L is the Monin-Obukhov length.

Most of the formulae for evaporation used primarily for meteorological observations, however, rely mainly on the identity of K_z and K_M; some of these are discussed in the following text.

2.2.1 The Thornthwaite & Holzman formula (86) - By combining Eqs. (2.31), (2.32), and (2.38) and assuming $K_z = K_M$, one arrives at the equation

$$E = - \rho \frac{u_*^2}{\left(\frac{\partial U}{\partial z}\right)} \frac{\partial q}{\partial z} \ , \qquad (2.42)$$

which can be written in the constant flux layer as

$$E = \rho u_*^2 \frac{q_1-q_2}{U_2-U_1} \quad . \tag{2.43}$$

Under neutral conditions in the lower atmosphere, using the logarithmic velocity $U/u_* = (1/k)\ (\ell n\ z/z_o)$ in (2.43), we obtain

$$E = \rho k \frac{u_*(q_1-q_2)}{\ln(\frac{z_2}{z_1})} \quad , \tag{2.44}$$

which can also be written as

$$E = \rho k^2 \frac{(U_2-U_1)(q_1-q_2)}{(\ln\ z_2/z_1)^2} \quad . \tag{2.45}$$

The above formula was first derived by Thornthwaite and Holzman (86).

Similarly, if one uses the logarithmic profile $U/u_* = \left(1/k\right)\left(\ell n\ \frac{z-d}{z_o}\right)$, one can easily obtain the relation

$$E = \rho k^2 \frac{(U_2-U_1)(q_1-q_2)}{\left(\ln\ \frac{z_2-d}{z_1-d}\right)^2} \quad . \tag{2.46}$$

This equation was first suggested by Pasquill (58 and 59) and later used by Rider (69) to calculate evaporation from an oat field.

Since velocity profiles (2.34) and (2.35) are only applicable in neutral conditions, Eqs. (2.45) and (2.46) are also subject to this restriction. However, Pasquill (58) has shown that the Deacon (19) generalized wind profile law [Eq. (2.17)] provides a satisfactory basis for the modification of Eq. (2.46) for unstable conditions. The modified equation is

$$E = \frac{\rho k^2 (1-\beta_1)^2 (q_1-q_2)(U_2-U_1) z_o^{2(1-\beta_1)}}{\left[(z_2-d)^{1-\beta_1} - (z_1-d)^{1-\beta_1}\right]^2} \quad . \tag{2.47}$$

In stable conditions, Rider (63) has shown that Eq. (2-17) does not hold and its use would lead to an underestimation of the eddy diffusivity for momentum and, hence, of that for vapor.

2.2.2 Flux equations using surface conditions - The methods just discussed for measuring evaporation flux demand observations at two atmospheric levels by refined techniques and may not be used on a synoptic basis. If one level is the surface itself, large humidity differences would be available for measurement, with a reduction in errors, especially in the observations at a water surface (for land surfaces, there is always the problem of defining surface conditions accurately). Sheppard (77) used $K_z = ku_*z$ in the equation

$$E = -\rho(D + K_z)\frac{\partial q}{\partial z} \quad , \tag{2.48}$$

to obtain

$$E = \frac{\rho k u_* (q_s-q)}{\ln \frac{ku_* z}{D}} \qquad \text{for} \quad z >> \frac{D}{ku_*} \quad , \tag{2.49}$$

in which D is the molecular diffusivity of water vapor.

Sverdrup (83) decided to neglect D in Eq. (2.48) and assumed $K_z = ku_*(z+z_o)$. Thus, on integration of Eq. (2.48), he obtained:

$$E = \frac{\rho k u_* (q_s-q)}{\ln \frac{z + z_o}{z_o}} \qquad \text{for} \quad z \geq z_o \quad . \tag{2.50}$$

To estimate vertical vapor flux from hydrodynamically rough sea surface, Montgomery (51) assumed the existence of a three layer model described below:

1. a laminar layer of very small thickness, above the surface of the water.

2. an "intermediate" layer of height I (about the height of the waves), in which the stress as represented by the friction velocity u_{*k} is constant, with the velocity distribution in this layer given by Eq. (2-19), and

3. the normal turbulent boundary layer, above the "intermediate" layer, in which the friction velocity remains constant at a different value u_{*R} $(u_{*R} > u_{*k})$. By requiring continuity in wind speed, a relation between the two friction velocities was obtained. Montgomery, postulating the distribution of water vapor in the "intermediate" layer as being nearly the same as in the case of smooth water surface, expressed the humidity q_I at the top of the intermediate layer as

$$q_s - q_I = \frac{E_o}{\rho k u_{*k}} \left(\frac{\lambda_1 \nu k}{D} + \ln \frac{k u_{*k} I}{D} \right), \tag{2.51}$$

in which E_o is the rate of evaporation and λ_1 is a nondimensional constant defined by the equation

$$\delta = \frac{\lambda_1 \nu}{u_{*k}} , \tag{2.52}$$

with δ as thickness of the laminar layer. Montgomery found $\lambda_1 = 7.8$. For the turbulent layer, where the friction velocity is supposed to be equal to u_{*R}, Montgomery wrote:

$$E_o = - \rho k \, u_{*R} \, z \, \frac{dq}{dz} . \tag{2.53}$$

Integrating above equation with respect to z, between the top of the "intermediate" layer and any height z, and eliminating q_I with the

help of Eq. (2.51), Montgomery obtained

$$q_s - q = \frac{E_o}{\rho k u_{*R}} \left[\ln \frac{z}{I} + \frac{u_{*R}}{u_{*k}} \left(\frac{\lambda_1 \nu k}{D} + \ln \frac{k u_{*k} I}{D} \right) \right]. \qquad (2.54)$$

Defining, for a height b ($b > I$), the evaporation coefficient,

$$\Gamma_b \equiv \frac{1}{q_s - q_b} \frac{dq}{d\ell n z} = \left[\ln \frac{b}{I} + \frac{u_{*R}}{u_{*k}} \left(\frac{\lambda_1 \nu k}{D} + \ln \frac{k u_{*k} I}{D} \right) \right]^{-1}, \qquad (2.55)$$

we get

$$E_o = \rho k \, u_{*R} \, \Gamma_b \, (q_s - q_b) \quad . \qquad (2.56)$$

Later, Norris (53) also used the concept of three layer model to obtain evaporation rates from extensive surfaces of water, but he differed from Montgomery as far as the distribution of water vapor in the outer turbulent layer was concerned. Norris pointed out that by assuming the equality of eddy diffusivities for momentum and water vapor, except for the small difference in D & ν, one uses the same friction velocity for a rough surface for both properties [$K_z(\text{vapor}) = D + k u_{*R}(z+z_o) \simeq \nu + k u_{*R}(z+z_o) = K_M$]. Hence, once the eddy diffusivities are conceded to be the same, it follows that the distribution of water vapor and velocity must obey similar laws. Based on this argument and proceeding in Montgomery's manner, Norris arrived at the following expression for evaporation rate

$$E = \rho k \, u_{*R} \, \Gamma_b (q_s - q_b), \qquad (2.57)$$

in which

$$\Gamma \equiv \frac{1}{q_s - q_b} \frac{dq}{d\ell nz} = \left[\ln \frac{b}{I} + \frac{u_{*k}}{u_{*R}} \left(\frac{\lambda_1 \nu k}{D} + \ln \frac{k u_{*k} I}{D}\right)\right]^{-1} . \quad (2.58)$$

2.3 Some other Relevant Wind Tunnel & Field Studies

Okuda and Hayami (55) reported a series of wind-tunnel experiments on evaporation from water waves. They analyzed their results in terms of the evaporation coefficient (49) and found them independent of free stream velocity when the spray of water was not important at a fixed fetch.

Kondo (40) obtained a universal diagram by applying the theory of turbulent transfer in non-neutral conditions and using some empirical relations derived from many observations. Using this diagram, one can evaluate turbulent fluxes of water vapor, heat, and momentum from observations of wind, air temperature, and humidity at a certain level above the water surface, and of the surface temperature.

Easterbrook (21) conducted experiments in connection with the effect of waves on evaporation from a water surface. He observed that certain combinations of windspeed and wave conditions actually lead to evaporation rates somewhat less than those measured for similar wind-speeds and smaller waves. His investigations of air flow over the waves indicated the presence of dead air regions and vortices which were apparently trapped in the wave troughs and moved along with the wave system.

Miyake and McBean (50) measured the spectral shape of humidity fluctuations over a vegetated surface using a Ly - α humidiometer.

Their results showed good agreements with those obtained by a dew point hygrometer, but further experimentation is needed to determine the dependence on stability and other factors, such as horizontal variability of the surface. Regener and Aldas (66) made simultaneous measurements of the vertical fluxes of ozone and heat, together with measurements of the vertical profiles of ozone and temperature, in the first 16 meters above the earth's surface.

2.4 Dimensionless Correlations

Traditionally, data on mass transfer have been expressed in terms of the mass transfer coefficient K_c in an analogy with the corresponding problem of heat transfer. Correlations of such data have generally taken the form of empirical expressions relating the dimensionless groups Sh, Re, & Sc, in which Sh is the Sherwood number, Re the Reynolds number, and Sc the Schmidt number. Considerable amount of work has been done in an effort to develop these dimensionless correlations for mass transfer rates from aerodynamically smooth surfaces in turbulent flows. The Chilton-Colburn formula (13), which indicates a mass transfer dependency to $Re^{0.8}$, has been extensively used for obtaining mass-transfer information from smooth flat plates. Gilliland and Sherwood (27) found, for vaporization of a liquid into air in a wetted column,

$$Sh = 0.023\ Re^{0.83}\ Sc^{0.44} \quad . \tag{2.59}$$

In electrochemical mass transfer for cathode reduction at limiting current conditions, it was observed by Elder et al (23) that the mass transfer rate varied with $Re^{0.6}$; Arvia et al (3) found that it was

proportional to $Re^{0.5}$. Smolsky and Sergeyev (80) investigated heat and mass transfer by the evaporation of various liquids (water, acetone, benzol, and butanol) from a free surface into a turbulent air stream and concluded that

$$Sh = 0.094\ Re^{0.8}\ Sc^{0.33}\ Gu^{0.2}\ , \tag{2.60}$$

in which Gu is the Gukhman number given by

$$Gu = \frac{T_a - T_w}{Ta}\ , \tag{2.61}$$

with T_a and T_w the dry and wet bulb temperatures of the free stream, respectively.

Relatively little has been published to date on the effect of roughness on the rates of heat and mass transfer. Moreover, results from different investigators sometimes disagree either partly or completely. In connection with their work on flow through rough tubes, Nunner (54), Smith and Epstein (79), and Dipprey and Serbersky (20) found that the presence of roughness increased the heat (or mass) transfer rates. On the other hand, Pohl (63), and Kolar (39) found the opposite, especially at high Re.

Levich (44) proposed that if the height of roughness elements was greater than the thickness of the viscous sub-layer, but less than that of the turbulent boundary layer, the hydrodynamic situation may be modified in such a way that a decrease of the mean mass transfer would result. He came to this conclusion after considering the following. In turbulent flow, he postulated two zones in the hydrodynamic boundary layer - a viscous sublayer near the solid interface in which momentum transfer occurs mainly because of friction, and a turbulent boundary

layer further outside where the exchange of momentum takes place by turbulent eddies. In a similar fashion, a diffusion sublayer exists where mass is transferred mainly by a molecular mechanism; further outside there is a concentration boundary layer where mass transfer occurs because of turbulent mixing. The diffusion sublayer forms the main resistance to mass transfer and its thickness is related to that of the viscous sublayer. A viscous sublayer usually will develop around the roughness peaks. However, a separation in the flow over individual protrusions will also occur in the case where the roughness height is greater than the thickness of the viscous sublayer, but less than that of the turbulent boundary layer. Levich proposed a theoretical correlation for the mass transfer rate in terms of friction velocity, difference of surface and free stream concentrations, and fluid properties (for $Sc >> 1$):

$$E' = \frac{D(\Delta q)\ u_*^{1/2}\ Sc^{1/4}}{\nu^{1/2}\ h^{1/2}} = \frac{(\Delta q)\ D^{3/4}\ u_*^{1/2}}{\nu^{1/4}\ h^{1/2}} \quad , \tag{2.62}$$

in which h is the height of roughness, Δq the difference of free stream and surface concentrations, D the molecular diffusivity, and $E' = K_c(\Delta q)$. Since $u_* = (\frac{C_f}{2})^{1/2} U_\infty$, Eq. (2.62) reduces to

$$\frac{E'\ell}{D(\Delta q)} = (\frac{C_f}{2})^{1/4}\ Re^{1/2}\ Sc^{1/4}(\ell/h)^{1/2},$$

or

$$(S_h)_\ell = (\frac{C_f}{2})^{1/4}\ Re^{1/2}\ Sc^{1/4}\ (\frac{\ell}{h})^{1/2} \quad , \tag{2.63}$$

in which ℓ is a characteristic length, $(Sh)_\ell = E'\ell/D(\Delta q)$, and $Re = \ell U_\infty/\nu$.

Although Levich's model presents a basic approach of the problem of mass transfer from rough surfaces, its applicability is limited to cases which satisfy the condition $Sc >> 1$. Equation (2.63) agrees with the results obtained by Mahato and Shemilt (45) in their experiments with the corrosion of commercial iron pipe by water under isothermal turbulent flow conditions, where the concept of mass transfer is that of the transfer of a depolarizer (dissolved oxygen, $Sc \simeq 238$) to the cathodic sites on the corroding pipe. On the other hand, Lai's (42) evaporation data, from his experiments on small water waves ($Sc \simeq 0.60$), did not correlate well with Levich's equation (2.63). Lai obtained a variation of Sherwood number as $Re^{0.85}$ instead of $Re^{0.5}$.

In addition, the derivation of Eq. (2.63) does not take into account the fact that protrusions themselves extending into the boundary layer are in a somewhat favored position from the standpoint of diffusion. Therefore, equation (2.63) gives somewhat low values for the mass transfer rate. Secondly, it is to be noted that the true surface area of a rough body with a large number of protrusions may greatly exceed the apparent surface area. Thus, in computing the diffusional flux, Eq. (2.63) should be multiplied by a factor to take care of the area differences.

Kolar [(38) and (39)] presented a theoretical analysis of heat and mass transfer in the turbulent flow of fluids through smooth and rough tubes. His theoretical consideration was based on description of the hydrodynamic relations on the phase boundary employing quantities and relations derived in the statistical theory of turbulence. He assumed the following: (1) The fluid at the interface consists of vortex elements of dimension λ_o and fluid velocity $U_{\lambda o}$ with

$$\lambda_o = \left(\frac{\nu^3}{\varepsilon}\right)^{1/4} \quad \text{or} \quad \frac{\lambda_o U_{\lambda o}}{\nu} \approx 1 , \tag{2.64}$$

in which λ_o is the local degree of turbulence, $U_{\lambda o}$ is the velocity in fluctuation of dimension λ_o, ε is the energy dissipation per unit mass per unit time, and ν is the kinematic viscosity. (2) Within these vortex elements, heat (or mass) is transferred by molecular mechanisms. On solving the appropriate differential equation with relevant boundary conditions, he obtained for the heat transfer coefficient the relation

$$h = 2\left(\frac{\alpha}{\pi \tau_e}\right)^{1/2} , \tag{2.65}$$

in which α = thermal diffusivity and

$$\tau_e = \frac{\lambda_o}{U_{\lambda o}} . \tag{2.66}$$

According to assumption (1), τ_e is the period of time when part of the surface of the vortex element is in contact with the medium in which the heat transfer occurs. Thus, Eq. (2.65) indicates that the rate of heat transfer is inversely proportional to the time the vortex element is in contact with the surface. Combining Eqs. (2.64), (2.65), and (2.66), one obtains

$$\frac{hd}{k} = \frac{2}{\sqrt{\pi}} \left(\frac{d}{\lambda_o}\right) (Pr)^{0.5} . \tag{2.67}$$

Kolar, then, made use of his experimental data to evaluate λ_o and obtained the relation

$$\frac{hd}{k} \simeq \left(\frac{u_* d}{\nu}\right) (Pr)^{0.5} ,$$

or

$$Nu \simeq (Re_*)_d \, Pr^{0.5}, \tag{2.68}$$

in which $(Re_*)_d = u_* d/\nu$. He obtained good agreement between his experimental results on flow through tubes and the above relation. Thus, relation (2.68) depicts the mechanism of heat transfer, as well as mass transfer on parallel lines, for flow through smooth tubes and through tubes with various forms of surface roughness.

2.5 Some Considerations on Reynolds Analogy

Reynolds (67) suggested that in turbulent flows momentum and mass (or heat) were transferred by the same mechanism. This requires that

$$\frac{\overline{w'q'}}{(U_1-U_2)(q_1-q_2)} = \frac{\overline{u'w'}}{(U_1-U_2)^2} , \tag{2.69}$$

in which a flow parallel to the x-axis is considered with mass transfer in the positive direction of the z-axis and U_1, U_2, and q_1, q_2 are the velocity and moisture contents at a pair of corresponding reference planes. It then follows that the rate of mass transfer $E(=\rho\overline{w'q'})$ in the positive direction of the z-axis across unit area normal to this axis is related to the Reynolds shear stress $\tau(=\rho\overline{u'w'})$ as:

$$\frac{E}{\rho(U_1-U_2)(q_1-q_2)} = -\frac{\tau}{\rho(U_1-U_2)^2} . \tag{2.70}$$

In case of mass transfer from a fixed surface with moisture content q_s

and velocity $U = 0$, we obtain

$$\frac{E_o}{\rho U(q_s - q)} = \frac{1}{2} C_f \quad , \tag{2.71}$$

in which $C_f = \frac{\tau}{\frac{1}{2}\rho U_\infty^2}$. The quantity $E_o/\rho U(q_s - q)$ is analogous to the Stanton heat transfer coefficient.

The theory postulated above can be explained by the following. Conventional boundary layer equations for steady, two-dimensional mean motion in the x, z plane can be written as

$$U \frac{\partial U}{\partial x} + W \frac{\partial U}{\partial z} = - \frac{1}{\rho} \frac{\partial p}{\partial x} + \frac{\partial}{\partial z} \left[\nu \frac{\partial U}{\partial z} + K_M \frac{\partial U}{\partial z}\right] \quad , \tag{2.72}$$

and

$$U \frac{\partial q}{\partial x} + W \frac{\partial q}{\partial z} = \frac{\partial}{\partial z} \left[D \frac{\partial q}{\partial z} + K_z \frac{\partial q}{\partial z}\right] \quad , \tag{2.73}$$

in which ν and D are molecular diffusivities for momentum and mass, and K_M and K_z are the corresponding eddy diffusivities. Inspection of these equations shows that Eq. (2.73) has a solution for which $(q - q_1)$ is proportional to $(U - U_1)$, provided that the condition $\partial p/\partial x = 0$ and $Sc = \nu/D = 1$ are satisfied, in addition to the condition $K_z = K_M$, provided also that the boundary conditions for q and U are analogous. With the above restrictive assumptions, Eqs. (2.69) and (2.70) may be valid when the rate of mass transfer E, per unit area, and the shear stress are given by

$$\left.\begin{aligned} E &= - D \frac{\partial q}{\partial z} - \rho K_z \frac{\partial q}{\partial z} \\ \text{and} \qquad \tau &= \mu \frac{\partial u}{\partial z} + K_M \frac{\partial U}{\partial z} \end{aligned}\right\} . \tag{2.74}$$

Therefore, Reynolds hypothesis holds only under special conditions. The main reasons for difference in the transport of mass (or heat) and momentum can be briefly described as follows. Momentum is destroyed at a surface by skin friction and by form drag (the bluff body effects), and only the former has an analogy in mass (or heat) transfer. In addition, the molecular diffusion coefficient D (or α) is not equal numerically to the analogous kinematic viscosity ν. Hence, it seems that the Reynolds analogy between the transport of mass (or heat) and momentum may or may not apply within the fluid flow, but it can never apply right up to the surface.

Owen and Thomson (56) used a dimensionless number B, called the sublayer Stanton number, to measure the discrepancy between the transport of mass (or heat) and momentum to the surface. The authors defined B in terms of the rate of mass transfer, the friction velocity, and the difference in moisture concentration across the lowest part of the boundary layer (the sublayer); but for convenience, the following relation [based on a similar method used by Squire (81)] can be derived

$$K_g^{-1} = \frac{\rho U(z)(q_s - q)}{E} = \frac{U(z)}{u_*} \left[\frac{U(z)}{u_*} + B^{-1}\right] , \qquad (2.75)$$

in which K_g is analogous to the Stanton heat transfer coefficient.

If $q(z)$ is the moisture content of the air at height z above a surface (or effective zero plane) and E is the flux (which is assumed to be constant with height), the resistance to transport of water vapor from (or to) a surface to (or from) the air stream is given by

$$r(z) = \frac{\rho[q_s - q]}{E} . \qquad (2.76)$$

The analogous resistance for momentum can be written as

$$f(z) = \frac{[U(z)-U(o)]}{\tau} = \frac{U(z)}{u_*} . \tag{2.77}$$

It is convenient to make both of these resistances dimensionless by multiplying by the friction velocity u_*. Hence, the nondimensional resistances are

$$r_+(z) = \frac{\rho u_*(q_s-q)}{E} , \tag{2.78}$$

and

$$f_+(z) = \frac{\rho u_* U(z)}{\rho u_*^2} = \frac{U(z)}{u_*} . \tag{2.79}$$

Multiplying both sides of Eq. (2-75) by $u_*/U(z)$, we get

$$r_+(z) = f_-(z) + B^{-1} . \tag{2.80}$$

On theoretical grounds and by analysis of their experiments on mass and heat transfer in flow over rough surfaces, such that $u_* h_1/\nu > 100$ where $h_1 = 30\, z_o$ = the equivalent sand roughness, Owen and Thomson postulated that

$$B^{-1} = \alpha_1 \left(\frac{u_* h_1}{\nu}\right)^m \sigma^n , \tag{2.81}$$

in which $\sigma = \nu/D$(or α), m and n are constants to which values of 0.45 and 0.8 were assigned, and α_1 was suggested to be a constant for each experimental arrangement, but varied according to the type of roughness. In connection with these considerations, it might be worthwhile to quote from Owen and Thomson's paper,

"It must be emphasized that our purpose has not been to establish a unique relation between B, $u_* h_1/\nu$ and σ for we are convinced

that one does not exist -- but to test whether the experimental data are consistent with the simple model proposed and, more particularly, with the Eq. (2.81) for the sublayer Stanton number B, at least over the limited range of the variables explored."

Chamberlain (10 and 11) conducted some wind tunnel experiments on the transport of a radioactive vapor of thorium B and water vapor, to and from some rough surfaces. He analyzed his results in the light of the empirical formula, (2.81), derived by Owen and Thomson.

Using a similar procedure, Cowan (14) gave an expression for the ratio of the resistances to mass and momentum transfer between plants and the atmosphere above, which emphasizes the important difference between the momentum dissipation and mass transfer due to the break down of Reynolds analogy near the surface.

The foregoing discussion has summarized major investigations connected with mass transfer from smooth and rough surfaces. The information on mass transport from rough surfaces is very limited. In view of this and because of the difficulty of controlling the variables encountered in field research and because of the great amount of time and money involved, laboratory investigation of this problem was initiated at the Fluid Dynamics and Diffusion Laboratory of Colorado State University.

CHAPTER III

Equipment and Measurement Procedures

This chapter briefly describes the equipment and measuring techniques used in this study. Methods of measuring evaporation are emphasized. Calibration procedures are described and various errors involved in the measurements are discussed.

3.1 Wind Tunnel

Experiments were conducted in the low speed wind tunnel (Fig. 1) located in the Fluid Dynamics and Diffusion Laboratory at Colorado State University. This recirculating tunnel can generate wind speeds ranging from 5 ft per second to about 70 ft per second. The test section is about 30 ft long and has approximately a 6 ft by 6 ft cross section. The turbulent intensity in the free stream is kept low by providing damping screens and a 4:1 ratio entrance contraction. A carriage system, built inside the wind tunnel, moves along the wind tunnel on rails, which are attached to the vertical walls of the tunnel. The carriage boom, intended for mounting probes, has independent lateral and vertical movements. The carriage has an outside remote control box, and the position of the carriage boom is determined from the output of potentiometers through a digital voltmeter. The accuracy of the positional measurements can reach about 0.005 in. with 10 volts input of the potentiometer.

3.2 Physical Arrangements in the Experiment

Figure 2 shows the layout of the experimental set up used in this study. The measurements were taken on sinusoidal waves cut in three

sizes (λ = 4.2 in. and h = 1.70 in., 1.0 in. and 0.50 in.)[1]. These waves were cut from styrofoam[2] blocks with a single shaper blade on a horizontal milling machine at the Engineering Research Center workshop. Figure 3 shows photographs of the three different sizes of waves and the shaper blades used to cut these waves. The styrofoam waves were laid in aluminum pans (Figs. 2 and 4), which were of sizes convenient for moving. Aluminum channel supports were spot welded to the bottom of these pans; the waves were later screwed down in sets to these channel supports to keep them from floating when the pans were filled with water. An assembly of six pans was used (Figs. 2 and 4). The first pan contained a set of 4½ waves, the next four contained 5 waves each, and the last pan contained 3½ waves, in addition to a specially built wave, called the evaporation metering wave (described in Section 3.6). These pans were placed adjacent to each other in the wind tunnel (as shown in Fig. 2), and a sheet of felt was positioned very carefully over the waves, following their contour. Small stainless steel pins were used to tack the felt to the waves. The ends of the waves toward the walls of the wind tunnel were sealed. When positioning the individual styrofoam waves in the pans, care was taken to leave a small (about 1/32 in. wide) crack between each wave to allow water to flow up from the bottom of the pans (Fig. 4); thus the continuity of the wavy surface was not disturbed. Once the pans containing the waves were assembled, they could be conveniently moved in or out of the wind tunnel. Distilled water was supplied from a reservoir (shown in Fig. 4) to the bottom of each pan. The water level was maintained so that water came

---

[1] λ and h denote the wave length and height of a wave.

[2] Styrofoam is the commercial name for polystyrene foam.

to the top of the crack in the troughs of the waves (Fig. 4). Before beginning a run, the felt surface was saturated with water; it was observed that the felt remained wet everywhere as long as the desired water level in the pans was maintained.

The surface upstream of the waves was raised by the addition of a false floor (4 3/16 in. high) level with the mean height of the waves. Also, just upstream of the false floor, a 6 ft wide aluminum sheet was placed to provide a smooth transition from the contraction section to the false floor (Fig. 2). A 9½-in. wide strip of steel brushes were positioned across the entire width of the wind tunnel between the aluminum sheet and the false floor at a distance of about half an inch from the leading edge; the brushes were used for tripping the turbulent flow and thickening the boundary layer. Downstream, at the end of the pan assembly, 2½ styrofoam waves and a 6 ft wide sloping plank were located to provide a smooth transition from the end of the waves to the wind tunnel floor (Fig. 2).

3.3 Measurement of Mean Velocity

Mean velocity profiles, on the floor and wave crests, were measured by a pitot tube. A set of two hot wires was employed to cross-cleck the values obtained by the pitot tube measurements.

3.3.1 Pitot tube for mean velocity - A special pitot tube (see Figs. 9 and 10) was built with the dynamic and static taps located on two parallel arms 5/8 in. apart. The arms were held in a horizontal plane parallel to the mean stream. Near roughness elements, significant pressure gradients exist both in x and z directions (41), with the pressure gradient in the lateral direction being zero because of the

assumed two-dimensionality of the flow. The velocity measured by a conventional pitot tube must involve an error because of the presence of the above mentioned pressure gradients. In view of this, both the dynamic and static taps were put on two different arms held along the y-axis in order to obtain zero pressure gradient between the two taps. The output of this pitot tube was checked against that of a standard pitot tube in free stream.

Both the total and static heads were measured by connecting the dynamic and static taps to the P_x and $P_{Ref.}$ pressure terminals, respectively, of the M.K.S. Baratron (TM Type 77) electronic pressure meter. The D.C. output of this pressure meter was proportional to the pressure difference $(P_x - P_{Ref.})$ in mm Hg. An integrator (built at the Fluid Dynamics and Diffusion Laboratory at Colorado State University (41)), in conjunction with a D.C. amplifier (Dynamics, Model 1250) and a digital voltmeter (Hewlett Packard, Model 3440A), was used to obtain averages of the pressure meter outputs.

Both the integrator and the D.C. amplifier were calibrated by introducing non-fluctuating voltages from a power supply. Figures 12 and 13 show these calibrations. The pressure meter was also calibrated, along with the integrator, the D.C. amplifier, and digital voltmeter, against a standard Merium Micromanometer (model 34FB2TM) for all the meter scales of interest. A typical calibration curve is shown in Fig. 14. A check of this calibration was made by putting two identical pitot tubes, separately connected to the pressure meter and the micromanometer, in the wind tunnel to measure the velocity simultaneously at the same flow height.

3.3.2 Mean velocity by hot wires - The hot wire measurements were taken simultaneously with two different probes. The first one, a Disa type F13 miniature hot-wire probe, had right angle tips with a 3.4×10^{-4} in. diameter platinum coated tungsten wire mounted parallel to the probe axis. Because of its size and design, this probe could take measurements near surfaces that are not readily accessible. This probe was used, with its wire vertical, to measure the horizontal component of the mean velocity (within 3 to 4 percent). The second probe, a Disa type 55A22 general purpose hot wire probe, also with a platinum coated tungsten wire, was used with the wire held parallel to the floor and perpendicular to the main flow to measure the total velocity. Two Disa (type 55A01) constant temperature hot wire anemometers were used. The outputs of these anemometers were printed on digital printers (Hewlett Packard type H75562A) for a suitable time interval; later, averages were obtained from the printed records. These hot wires were calibrated against a standard pitot tube in free stream. These calibrations were taken before and after every run of the experiment. Figure 15 shows a typical hot wire calibration curve.

3.4 Measurement of Moisture Content

The moisture content of the air flow was measured by sampling the gas stream through a specially built sampling probe (Figs. 9 and 10), connected to a dew point hygrometer (Cambridge Systems, Model 992), at a constant flow rate maintained by a vacuum pump built in the hygrometer. During an experimental run, the background humidity changed, although very slowly, with time because the recirculating air gradually absorbed additional moisture. Also, the surface air humidity changed slightly.

Two stainless steel sampling probes were used simultaneously to measure both the local moisture content in the boundary layer and the free stream moisture content (see the arrangement of the probes in Fig. 11). The sampling lines connecting the sampling probes to the dew point hygrometer consisted of ¼ O.D. teflon tubing with stainless steel swagelok fittings and a three-way stainless steel valve. The surface air humidity was determined by measuring the surface air temperature, T_s by a copper constantan thermocouple (see Fig. 11), after assuming that it was equal to the saturated humidity at temperature T_s .

The dew point hygrometer, utilizing a thermoelectrically cooled optically sensed mirror, directly measures the temperature at which the vapor adjacent to a surface of water is in equilibrium with the vapor in the sample gas. This is the dew point temperature of the gas; the moisture content of the gas can be determined from this using some standard relations (see Appendix A). A simplified block diagram of the hygrometer along with an interior view of the instrument is shown in Figs. 16 and 17. In addition to the thermoelectrically cooled mirror which has an internal thermometer, the dew point sensor contains an optical sensing bridge for sensing the dew formation. The amplifier unit consists of solid state amplifiers and control components for amplifying the output of the optical sensing bridge, and controlling the mirror. The temperature of the mirror, representing the dew point temperature, is determined by a platinum resistance thermometer.

To measure the moisture content, a sample of air is drawn, at a flow rate of two cubic feet per hour, through a sampling probe and is directed on the mirror inside the hydgrometer. Because the mirror is

exposed to the moist air, the optical sensing bridge, which is supposed to maintain a constant surface reflectance, becomes unbalanced and a sufficient signal from the bridge is supplied to the amplifier so that cooling commences. The output from the unbalanced optical bridge is amplified and used to control the output of a D.C. power supply and hence control the thermoelectric module cooling current. As the mirror cools down to the dew point, formation of dew on the mirror causes attenuation of a directly reflected light beam, and an increase in the light received by the "bias" photoresistor (in the optical sensing bridge). This forces the bridge toward the balance point, while proportionally decreasing the current supplied to the cooler, until a stable current is attained, whereby a thin film of dew is maintained on the mirror surface. The temperature of the mirror, once it stabilizes at the dew point, represents the dew point temperature.

The instrument tracks changes in dew point by increasing or decreasing the D.C. cooler current about the stable point in proportion to the thickness of the dew deposit on the mirror. If the sample happens to have a lower dew point, the dew layer tends toward thinning. This causes an increase in the cooling current and a lowering of the mirror temperature to the new dew point. On the other hand, if the sample has a higher dew point, the dew layer tends to thicken, causing a decrease in the cooling current, with the mirror warming to the higher dew point. In this fashion, true proportional control of the dew point mirror is obtained at all times. The maximum response, or the tracking rate, of the instrument is approximately $3^{o}F$ per second. There is no known hysteresis associated with the evaporation or condensation of water so that any change in mirror surface humidity,

however slight, will immediately upset the equilibrium condition and begin to increase or decrease the mass of water present on the mirror surface. The hygrometer was calibrated against another standard hygrometer (N.B.S. certified). A calibration curve is shown in Fig. 18.

3.5 Measurement of Temperature

All temperature measurements were taken with copper constantan thermocouples. A precision potentiometer (Leeds-Northrup Co., type K-3), in conjunction with an accurate galvanometer, a standard cell and a set of batteries, was used to measure the output of each thermocouple.

In the temperature profile ($T-T_s/T_\infty-T_s$ vs height) measurement, three thermocouples were simultaneously used, to measure the local temperature in the boundary layer, the free stream temperature, and the surface air temperature, respectively. The free stream and surface air temperatures had to be measured along with the local temperature at every point of measurement so that the changes in ambient and surface temperatures could be taken into account. The surface thermocouple was positioned very carefully on the surface of the wave at each measurement station.

Every thermocouple used in this study was calibrated in a temperature calibrator. This calibrator consists of an insulated oil bath equipped with a heater, a cooling coil, a thermostat, and a set of precision thermometers. A typical calibration curve is shown in Fig. 19. All thermocouples were calibrated before and after the experimental runs in the wind tunnel. This was done to check for any suspected drift in the stability of the batteries or the standard cell used. No appreciable differences were noted.

3.6 Measurement of Local Evaporation Rates

Local mass transfer coefficients were determined by measuring the actual volume of water that had evaporated from different sections of a saturated wavy surface in a given time. These measurements were taken from a specially designed "evaporation metering wave", in an approximately fully developed boundary layer, located about 10 ft from the initial upstream wave (Fig. 2). This special wave facilitated the direct measurements of local evaporation rates. These rates could be determined with the aid of an automatic feed and metering system. Both the "evaporation metering wave" and the automatic feed and metering system are described subsequently.

3.6.1 Evaporation metering wave - A detailed drawing of the evaporation metering wave is shown in Fig. 5. Taken from a top view, the wave (of wavelength = 4.2 in.) was divided into eight sections of equal width with thin (0.020 in.) copper baffles comprising both the sides and the bottom of each section. The copper channels (which consisted of the above mentioned copper baffles) were fixed to an aluminum block with the top edges of the channels forming the desired sinusoidal profiles. The dimensions of these copper channels and the aluminum block were computed so that when combined they resulted in a sinusoidal-shaped wave of desired amplitude and wavelength (Fig. 5 and 6). Strips of blotter paper (0.022 in. thick) were cut to fit vertically in these channels; the tops of the blotter papers were carefully sanded to form a continuous surface. Water from separate burettes, belonging to the automatic feed and metering system described later, was supplied to the bottom of these sections through brass tubings. It was carried to the top of the blotters by capillary action. Thus, the blotter surface was

kept completely wet as long as the water supply was maintained. Brass screens (18 x 14 mesh, 0.011 in. dia. wire) were placed at the bottom of each section to keep the blotter papers in position. The dimensions of these screens were designed so that the water travelled equal distances through the blotter capillaries at every part of the wave. Figure 5 shows the relative positions of the screens, tubings, copper channels, etc., in the wave. The presence of the thin copper walls prevented the longitudinal transport of water from one section of the wave to another. From a top view, the measuring wave was 2 ft long. Two additional waves (called the buffer waves), each also 2 ft long, were provided on each end of the measuring wave (Fig. 2). These buffer waves were also kept wet to minimize lateral diffusion of water vapor. Care was taken to seal the ends and sides of the metering wave to avoid any leaks. To measure the surface air temperatures, copper constantan thermocouples were mounted on the wave surface in each section. The thermocouple beads were placed in the center of the top surface of the blotters; their leads ran ¼ in. downward from the surface and then along the horizontal length of the wave between two blotter layers, to minimize conduction errors.

Metering waves of three sizes, namely λ = 4.2 in. and a = 0.85 in., 0.5 in., and 0.25 in., were built separately. Figure 5 shows the dimensions for a typical case.

3.6.2 Automatic feed and metering system - A photograph of the automatic feed and metering system is shown in Fig. 7. This system maintains and measures the supply of water to each of the eight sections of the metering wave; it is similar to the one used by Cermak and Lin (9), and Nelson (52). Figure 8 shows the arrangement needed for

one typical wave section. Each wave section was linked to a graduated burette, which in turn was connected to its own water bottle. These burettes were closed by rubber stoppers at the top; two brass tubes (0.092 in. O.D.) were inserted in each through holes in the rubber stoppers. The bottom end of tube A (Fig. 8) was used to control the water level in the corresponding wave section. The pressure difference, created by the water loss from evaporation at the top of the wave section, was compensated for by drawing water from the burette automatically. This volume of water drawn from the burette was replaced by the ambient air coming through tube A. Thus, the evaporation of water from each wave section took place at ambient pressure and the amount of water that evaporated from each section in a given time was measured from the drop of water level in the corresponding graduated burette. Burette readings were corrected to account for the volume occupied by the brass tube A in each burette.

3.7 Measurement of Pressure Distribution and Drag Force

3.7.1 Measurement of pressure distribution - The pressure distribution on the surface of the waves was measured by a special pressure tapped wave, placed at the 27^{th} wave postion. This pressure tapped wave had the same shape and dimensions as the other styrofoam waves except that 17 equispaced pressure holes were drilled across the mid-section of the wave. Each pressure tap was in turn connected to a MKS Baratran (TM type 77) pressure meter. The meter measured the difference in the wall pressure at that point on the wave and the static pressure at a reference height in the free stream. Figure 66 shows the wall pressure distributions along the surface of the waves.

3.7.2 Measurement of the drag force on the waves - The drag force on the waves was determined in two ways; first, by integrating the wall pressure distribution, and secondly, by using a shear plate.

So that drag force could be directly measured on different kinds of surfaces, Hsi and Nath (33) had previously designed a special shear plate. This shear plate is aluminum with dimensions of 0.635 cm x 59.6 cm x 59.0 cm. This plate was separated from the foundation plate by three chrome-steel balls (0.635 cm diameter). Two stainless steel restoring arms, 0.317 cm x 1.27 cm x 45.6 cm each, were used. One end of the arm was attached to the shear plate and the other to the foundation plate. Four semi-conductor strain gages, one on each side of the restoring arm, were installed at 1.27 cm from the end of the restoring arm which was attached to the foundation plate. The shear plate moved back and forth in a horizontal plane only; it had a natural frequency of six cycles per second. The construction of the shear plate has been described in detail in (33).

If a horizontal force was applied to the shear plate, the plate would be displaced according to the spring constant of the restoring arms and the magnitude of the applied force. The shear plate would return to its original position after the applied force was removed. An 8 volt D.C. power supply and a D.C. micro-ammeter in conjunction with a digital voltmeter and a digital printer were used to measure the shear plate readout.

Three 23.5 in. pieces of styrofoam wave were attached by masking tape to the top of the shear plate. The shear plate was put in the wind tunnel so that the above wave pieces would occupy the 26^{th}, 27^{th}, and 28^{th} wave positions; other styrofoam waves were put on each side

and at each end of these pieces to maintain the continuity of the wavy surface. Care was taken to properly seal the ends and sides of these pieces. The shear plate was calibrated on location by applying a known horizontal force to the plate and recording the bridge output. These measurements were conducted on all the wave sizes.

3.8 Visualization of Flow Pattern

To get a qualitative picture of the flow pattern in the troughs of the waves, a visualization study was made. Air motions were traced by releasing smoke near the waves, and visible records were obtained by means of pictures taken from a 35 mm still camera. The smoke was produced by passing moist air through a container of titanium-tetrachloride located outside the wind tunnel floor by means of a tygon tube terminating at suitable locations near the waves. Figures 63 and 64 show some of the photographs taken during this study.

3.9 Experimental Procedure

The main aspects of the experimental procedure can be divided into two parts. The first part consisted of measuring velocity, temperature, and humidity profiles; the second part consisted of directly measuring the local evaporation rates. A systematic procedure of these measurements, using the apparatus (see Fig. 20) previously detailed, is presented below.

3.9.1 Velocity, temperature, and humidity profiles - As mentioned, local measurements of mean velocity, temperature, and moisture content of the air flow were simultaneously made by a pitot tupe, a set of two hot wires, a thermocouple, and a sampling probe connected to a dew point hygrometer. In addition, the free stream and the surface air temperatures

and humidities were also monitored (see probe arrangement in Fig. 12). A typical run was conducted according to the following procedure.

1. First, water levels in the pan as well as in the water tank (see Fig. 4) were checked to make sure the waves were completely wet. Barometric pressure was also noted.

2. A thermocouple was carefully positioned on the wavy surface at the station where profile measurements were to be made. Positions of all the other probes on the carriage were checked.

3. Checks and adjustments of balance, zero, and full scale, etc., were made on all the instruments. The hot wire anemometers were balanced and put into operation. Flow was initiated. A set of measurements were taken for the calibration of the hot wires against the pitot tube in free stream.

4. All the probes for taking local measurements were lowered, with the help of the carriage control, near (say about 0.1 in.) the surface; the distance between the probe and the surface was noted. After the wind tunnel was adjusted for the desired free stream speed, the wind tunnel was left running for about half an hour before actual measurements were taken.

5. The carriage output voltage was noted. The pitot tube output was amplified 250 times and then integrated for three minutes. At the same time the outputs from both hot wires were printed on two digital printers. Local and free stream humidities were also noted during the same duration. Because the local humidity values were fluctuating, the output was recorded every 5 seconds for 2½ minutes so that an average value could be computed later. The values of free stream humidity both before and after this duration were noted. Also the outputs of the

three thermocouples (namely, surface, local, and free stream) were measured on the potentiometer in the same interval. Before taking each reading, the potentiometer was balanced against the standard cell.

6. After completing the above set of measurements, the carriage was raised step by step and the same measurements were made until all the instruments indicated outputs independent of height.

7. Finally, another set of calibrations were taken for the hot wires. The barometric pressure was again noted.

All these measurements just mentioned were taken at various longitudinal positions on the waves.

3.9.2 Local evaporation rates - Measurements of local evaporation rates were made by directly measuring the volume of water evaporated from the different sections of the metering wave (Fig. 5). As previously described, the automatic feed and metering system was used to supply water to the metering wave and also to measure the amount of evaporated water. A typical evaporation run proceeded in the following manner.

1. The seals around the metering wave and the water levels in the aluminum pans were checked. The buffer waves were put into position.

2. All the burettes and the connecting tubings were filled with water. The wave sections were then individually filled with water. These sections were then flushed to dislodge any air pockets. Water levels in the sections were checked to prevent overflowing into the other sections and the thermocouple positions were checked. The carriage was positioned slightly downstream of the metering wave to monitor the free stream velocity, temperature, and humidity. The air flow in the wind tunnel was set at the desired speed and the wind tunnel was run for about

15 minutes before the actual measurements were taken. Again, the barometric pressure was noted.

3. Initial water levels in the burettes, one after another, were noted at 1 minute intervals. At the same time, outputs of the thermocouples on the corresponding sections were noted. Free stream humidity was also recorded. After an interval of time, which varied from 8 to 16 minutes, the final water levels in the burettes, the final thermocouple outputs, and the values of free stream humidity were again recorded.

Thus, at a particular speed, the amount of water that evaporated in a certain time from each section of the metering wave was obtained with the values of surface and free stream air temperatures and humidities. These measurements were taken several times at each speed to obtain a check on their repeatability. These measurements, in most cases, were obtained at wind speeds of 10, 20, and 40 ft per second. These experiments were also conducted with all the waves both up and downstream of the metering wave dry.

As a check, these measurements were also made with the metering wave turned around.

3.10 Uncertainty Analysis

Systematic errors in the study were minimized by suitable corrections and frequent checks on the calibration of the various instruments. Estimates of the random errors are presented here with regard to all the basic measurements, based on the principle proposed by Kline and McClintock (1953):

(i) probable error in velocity measurements:

$$\frac{\Delta U}{U} = \pm \text{ 2 to 3 percent;}$$

(ii) probable error in humidity measurements:

$$\frac{\Delta q}{q} = \pm \text{ 3 to 4 percent;}$$

(iii) probable errors in the mean evaporation rates are estimated as ± 2 percent for the best cases and ± 5 to 7 percent for the worst ones.

Chapter IV

Results and Discussion

The results of evaporation measurements on the waves in the low speed wind tunnel are presented. Emphasis is placed on the region far downstream from the leading wave, because at this location the momentum boundary layer is approximately fully developed and equilibrium boundary layer conditions are obtained. The analysis has been divided into two parts. The first deals with the average evaporation characteristics from a rough surface. The second part concentrates on the local variation of mass transfer coefficient along the curvature of the wave in the far downstream region. The mass transfer results are compared with certain other pertinent investigations on this subject. Mean velocity, humidity, and temperature profiles on the waves in the approach flow (or the transition region) are also presented and their broad characteristics considered. Applications of this study in practical situations are discussed.

Two dimensionality of the flow near the centerline of the wind tunnel was checked by taking horizontal traverse measurements across the wind tunnel at several heights above the wave crests. Deviations from the center line velocity of not more than 2 to 3 per cent were observed within 6 in. of both sides of the centerline. However, there may be significant corner effects and secondary circulation at low speeds. Therefore, ambient velocities smaller than 10 fps were not used.

4.1 Mean Velocity Distributions and Drag Measurements

4.1.1 Mean velocity - Table 1 summarizes the measured mean velocity profiles at different stations. The dimensionless velocity profiles $(\frac{U}{U_\infty}$ vs $\frac{z_c}{\delta})$ at different crest positions (1, 3, 6, 12, 18, 23, 24, and 25) are plotted in Figs. 21, 22, and 23, in which z_c is the height measured above the respective wave crest and δ is the boundary layer thickness, where δ is defined by $U_\delta = 0.99\ U_\infty$. The velocity profile measured above the false floor 1.6 ft upstream of the leading wave is shown in Fig. 24. Figure 25 shows the corresponding wall law plot at that station, with the equation

$$\frac{U}{u_*} = 5.76 \log \frac{zu_*}{\nu} + 5.68 \qquad (4.1)$$

correlating the data reasonably well. This assures a well defined turbulent airflow approaching the waves.

Figures 21, 22 and 23 clearly show the changes in the velocity profiles above the waves proceeding downstream. But for stations downstream of the 22nd crest, all the nondimensional velocity profiles approximately collapse into a single curve. In addition, the quantities $\frac{u_*}{U_\infty}$ (described in Section 4.1.3) and $\frac{dp_\infty}{dx}$ became almost constant for $x \geq 7$ ft, where x is measured from the start of the leading wave (See Figs. 31 and 29). This means that the boundary layer reached its equilibrium condition for $x \geq 7$ ft (74). Plots of relevant boundary layer parameters, e.g., boundary layer thickness δ, displacement thickness δ^*, momentum thickness θ and form factor H, are shown in Figs. 26, 27, and 28. When the smooth wall boundary layer (on the false floor upstream of the waves) encounters a series of waves, the

form drag of the waves introduces an increase in the wall shear stress (as shown in Fig. 31). The increase in wall shear stress causes a loss in momentum and therefore, δ, δ^* and θ are increased at a faster rate in the beginning (Figs. 26, 27 and 28). Shortly however, the flow adjusts itself to a normal boundary layer development; about 7 ft downstream of the leading wave the equilibrium boundary layer conditions are obtained. Figure 30 shows typical wall law plots for the velocity profiles, for all three wave cases, in the far downstream region. The wall law is found to be

$$\frac{U}{u_*} = 5.76 \log \frac{zu_*}{\nu} + C \quad , \tag{4.2}$$

in which C varies from -8.0 to -13.15. These values of C are comparable to the values obtained by Kung (41) in his wall law plots for velocity profiles above equally spaced fences in the far downstream region.

4.1.2 Drag measurements - Measuring form drag on the waves by two different methods, namely integrating wall pressure distributions, and using a shear plate, was discussed in Sections (3.7.1) and (3.7.2). Table 3 gives the values of the effective average skin friction coefficient C_f obtained from both methods in the far downstream region. The agreement of results from these two different methods in most cases is within 20 to 25 percent. Details of the computation are given in Appendix B.

4.1.3 Friction velocity (u_*) and roughness parameter (z_o) -

Friction velocities were obtained primarily from the measurements of velocity profiles. The results from drag force measurements were used to cross-check these values. In order to obtain u_* and z_o, it was assumed that the velocity distributions followed the logarithmic profile

$$\frac{U}{u_*} = \frac{1}{k} \ln \frac{z}{z_o} \qquad z > z_o \qquad (4.3)$$

for nearly neutral conditions (see page 53). In Eq. (4.3), z is the effective zero plane given by $z = z_T - d = z_c + \varepsilon$ and $\varepsilon = h - d$, where z_T is the height measured from the bottom of the waves, z_c is the height measured above the respective wave crest, d is the zero plane displacement, and h the wave height. The value of d was estimated by a method similar to the one used by Perry et al. (61). The velocity profiles on wave crests in the far downstream region were first plotted on the $\frac{U}{U_\infty}$ vs z_c axes. An estimate of the required slope of the final logarithmic distribution ($2.5 \ln \frac{C_f}{2}$) was then calculated using values from the drag measurement results. Values of ε were then added to the abscissa of the raw profile in a trial and error process until a value of ε was obtained that gave a straight line, in the lower part, with a slope close (within 10 to 15 percent) to the above predetermined value of $2.5 \ln \frac{C_f}{2}$. The values of $d(= h - \varepsilon)$ so obtained are given by $\frac{d}{h} = 0.5$, 0.25 and 0 for waves A, B, and C, respectively, with $\frac{h}{\lambda} = 0.41$, 0.24 and 0.12. This means, from the bottom of the waves, the effective zero plane is raised by a half and a quarter of the wave height for the steepest and the intermediate waves, but remains unchanged for the shallowest one, which seems reasonable.

Considering the above and using Eq. (4.3), values of u_* were computed for different longitudinal positions assuming d constant with fetch. Figure 31 shows the variation of friction velocity with fetch for all three wave situations. The results indicate the friction velocity initially undergoes a rapid change when the air first encounters the change of roughness, and then adjusts itself in the far downstream region. This type of response in the wall shear stress has been predicted by many investigators and is consistent with that measured by Yeh (89) as shown in Fig. 32.

Having obtained the u_* values, values of z_o were obtained by using equation (4.3). In the far downstream region, the values of z_o varied from 0.03 to 0.175 in. for the three wave sets, which are comparable, at least with regard to the order of magnitude, to the results obtained in investigations above similar surfaces [e.g. Chamberlain (11), and Owen and Thomson (56)].

In the evaporation experiments, a temperature gradient was set up as heat was transferred from the air to the evaporating surface (see Section (4.3) also). However, the gradient of windspeed in the lowest few inches (above the wave crests) was large, and a typical value of the Richardson number $= \frac{g}{T} \frac{\frac{\partial T}{\partial z}}{(\frac{\partial U}{\partial z})^2}$ for 1 in. $< z_c <$ 4 in. was found of the order of 10^{-3}. The Monin Obukhov parameter $L = \frac{u_*^3}{k\frac{g}{T}(\frac{H_o}{\rho C_p})}$ (with $H_o \simeq L_e E$, see Section 4.3), was of the order of order of 10^3 cm. This means that an error of about 2 to 3 percent is involved in estimating u_* by using the relation (4.3). Thus, the effect of stability on the velocity profile could be neglected.

4.2 Mean Humidity Distributions

Profiles of mean humidity at various stations were obtained by simultaneously measuring local, free stream, and surface air humidities. It has been shown (e.g., Chamberlain (10)) that evaporation from saturated surfaces is equivalent to evaporation from a free liquid surface; so, the air humidity at the evaporating surface can be determined by assuming that it is equal to the saturated humidity q_s at T_s where T_s is the surface temperature.

Table 2 summarizes humidity profile measurements. To account for variation in free stream and surface humidities, the humidity profiles were plotted in terms of $\frac{q-q_\infty}{q_s-q_\infty}$ vs height z_c, where q, q_∞, and q_s are the local, the free stream, and the surface air humidities, respectively. Figures 33, 34, and 35 show plots of $\frac{q-q_\infty}{q_s-q_\infty}$ vs height for various crest positions. These plots indicate that variations of humidity at various stations have been obtained with reasonable accuracy and relatively little data scatter. The value of the nondimensional humidity $\frac{q-q_\infty}{q_s-q_\infty}$ at a particular height, encounters a noticeable increase with fetch downstream as expected, because of more and more water vapor effluxing from the wave in the boundary layer. The thickness of the mass (or humidity) boundary layer, δ_m can be defined as the height where the non dimensional humidity $\frac{q-q_\infty}{q_s-q_\infty}$ becomes equal to 0.01. The development of a typical mass boundary layer is shown in Fig. 36.

The vertical distributions of humidity at different longitudinal positions were plotted in semi logarthmic form, as shown in Figs. 37,

38, and 39. Except for large heights, most of the data points, taken at a station, form a straight line indicating that these humidity profiles follow logarithmic distributions. This result is consistent with the observations made in both field and laboratory experiments by Montgomery (51), Pasquill (58), and Lai (42). The humidity profiles in the far downstream region were then plotted with $\frac{q-q_s}{q_*}$ vs $\frac{z}{z_{om}}$ axes (Figs. 40, 41 & 42), in which z is again the height measured from the effective zero plane, which is the same as for velocity profiles. The experimental data seem to be well correlated by the line

$$q-q_s = q_* \ln \frac{z}{z_{om}} \tag{4.4}$$

in which z_{om} is a length parameter, and q_* is the friction humidity (Section 2.2.1). The values of q_* computed for various longitudinal positions are given in Table 4.

In the far downstream region, vertical humidity profiles were also measured at various positions inside the troughs of the waves. Figures 43, 44, and 45 show these humidity distributions. Shown in Figs. 46, 47, and 48 are the enlarged views of the lower portion of the corresponding profiles near the surface of the wave. This is presented to display contrast in behavior of humidity variation at different positions on the wave surface. Using these profiles, isoconcentration lines (i.e. lines of $\frac{q-q_\infty}{q_s-q_\infty}$ = constant) were drawn inside the troughs of each wave in the far downstream region (shown in Figs. 49, 50, and 51). From these isoconcentration plots, one can conclude the following: the humidity gradient is relatively high just upstream of a crest and it starts decreasing quite rapidly downstream of the crest along

the curvature of the wave. In the middle of the trough, the humidity gradient is relatively small, but passing this region it again starts increasing until just before the next crest. This result facilitates understanding the effect of the flow structure on the variation of local evaporation rates along the surface of waves (Section 4.5).

4.3 Mean Temperature Distributions

Nondimensional temperature profiles $(\frac{T - T_s}{T_\infty - T_s})$ vs height) at various crest positions were computed and some typical results are plotted in Fig. 52. As mentioned, free stream and surface air temperatures, T_∞ & T_s respectively, were measured along with the local temperature $T(z)$ to account for changes in ambient and surface temperatures. Figure 36 shows a typical development of temperature boundary layer, where δ_t is defined by $\frac{T_\delta - T_s}{T_\infty - T_s} = 0.99$. From Fig. 52 it appears that these temperature distributions follow logarithmic variation except for the outer region. In case of temperature profiles also, one can define a friction temperature T_* given by the equation

$$T - T_s = T_* \ln \frac{z}{z_{ot}} \quad , \tag{4.5}$$

in which z is the height above the effective zero plane, with the same definition as used in the velocity and humidity profiles, and z_{ot} is a hypothetical length parameter (6). Values of T_* were computed for various longitudinal positions; results for a typical case are tabulated in Table 5.

An estimate of the flux of sensible heat H can be obtained by using the equation

$$H = - \rho C_p k u_* T_* \quad , \tag{4.6}$$

in which u_* and T_* are the friction velocity and the friction temperature respectively, ρ is the density, C_p the specific heat and $\beta' = \frac{K_h}{K_M}$ has been assumed to be unity (Eq. (2.42)). If no heat is conducted below or radiated from above to the waves, H should be equal to $L_e E$, where L_e is the latent heat of vaporization, and E is the evaporation rate per unit area. A relatively small amount of heat was conducted upwards through the floor of the wind tunnel and this was calculated (in a typical case) to be about 10 percent of the heat lost by vaporization $L_e E$. The long wave radiation downward from the roof of the tunnel was estimated to be about 6 percent of $L_e E$, by assuming black body radiation. Using Eq. (4.6), the sensible heat was computed to be approximately equal to 84 percent of the heat transferred by vaporization.

Vertical temperature profiles were also measured at various positions inside the troughs of the waves in the far downstream region. Figures 53 and 54 show a typical case of these temperature distributions. From these profiles, isotherms (i.e., the line of constant $\frac{T - T_s}{T_\infty - T_s}$) were also drawn inside the troughs (Fig. 55). The variation of temperature gradients, along the wave surface, is quite similar to the corresponding variation of humidity gradients.

4.4 Average (Mean) Evaporation Rates

Average evaporation rates, in the fully developed region, were obtained by direct measurements (by averaging the results of local evaporation measurements - Section 4.5). Knowing the velocity and

humidity profiles, two other methods were employed to compute evaporation rates for various longitudinal positions. Variation of evaporation rate with fetch in the approach flow was obtained. The reliability of these two methods was cross-checked with the directly measured values, at least in the fully developed region.

The first method, which may be called the mass balance method, makes possible the evaluation of evaporation rates by using the equation

$$E = \frac{d}{dx} \int_0^{\delta} \rho U(z) \, [q(z) - q_\infty] \, dz \ . \tag{4.7}$$

This equation can be obtained by considering a mass balance on a control volume in the air (22), or by simply integrating the two-dimensional diffusion equation with respect to z and neglecting the vertical velocity at the interface. To find the experimental values of evaporation rates from the above equation, values of $\rho U[q-q_\infty]$ were plotted vs height z_c. Curves for a typical case are shown in Fig. 56. An optical planimeter was used to obtain the value of the integral $\int_0^{\delta} \rho U[q-q_\infty]dz$. The value of evaporation rates were obtained by using Eq. (4.7).

This method requires measuring slopes of the curve $\int_0^{\delta} \rho U[q-q_\infty]dz$ vs x; therefore, measurments at a number of closely spaced longitudinal positions are needed to obtain the evaporation rates accurately. In view of this, this method was used to evaluate the evaporation rates in the fully developed (far downstream from the leading wave) region only. In order to obtain the estimates of evaporation rates at different longitudinal positions in the approach flow, the following method was used.

The second method, which may be called the profile method, is based on Eq. (2.39), described in Chapter II. The values of friction velocity u_* and friction humidity q_* can be obtained from measured mean velocity and mean humidity profiles as described in previous sections. The vapor flux at the surface can be obtained from Eq. (2.39) by assuming the validity of the assumption $K_z \simeq K_M$ near the surface.

Figures 57, 58, and 59 show the variation of evaporation rates with fetch for all of the three cases. In general, the evaporation rate, in the beginning, increases rapidly to a maximum near the fourth or fifth crests and then decreases, leveling off in the far downstream region. When the air first encounters the presence of waves, there is a sudden increase in the shear (as exhibited by the u_* variation in Fig. 31), which causes an increase in the evaporation rates in the beginning. Also, when the relatively dry air contacts the first few waves, it absorbs much more moisture than it does in the downstream region. The evaporation rate later decreases and becomes constant in the far downstream region, in a fashion similar to that seen in the friction velocity variation. This kind of variation is compatible with results reported in some other studies, e.g., Marciano and Harbeck (47).

In the far downstream region, the results obtained from the first and second methods of evaluating evaporation rates were compared with direct measurements; the first method agreed within 10 percent and the second, for most cases, within 20 percent (Table 6). Considering that these two methods used entirely different sets of measurements than those used for direct evaporation measurements, the agreement is encouraging.

4.5 Local Mass Transfer Coefficients

In this section, results of measurements on local mass transfer coefficients over wavy surfaces is presented, along with other relevant experimental observations. Flow inside the troughs of the waves is very complex, and is characterized by high turbulent intensities. Measurements of various flow characteristics in such flows are delicate and difficult to interpret. However, to facilitate future research it was considered worthwhile to attempt to measure the local mass transfer behavior. The mass transfer data reported in this study reveal some interesting features. An explanation of the behavior inside the troughs primarily in a qualitative sense is presented and some practical aspects of the results discussed.

Local evaporation rates were measured from various positions on the surface of the specially designed wave located in the far downstream (approximately fully developed) region (Section 3.6). These measurements were taken with all upstream waves completely wet, at various ambient air speeds for waves of all three sizes. The ambient and surface air humidities were also simultaneously measured. The mass transfer coefficients were defined as $\frac{E}{q_s - q_\infty}$, in which E is the local evaporation rate per unit area, and $(q_s - q_\infty)$ is the difference of surface and ambient air humidities.

The result for all cases are shown in Table 7 and are plotted in Figs. 60, 61 and 62. As discussed in Section 3.5, actual measurements were conducted on only one evaporation metering wave of each size. Therefore, results in Figs. 60, 61 and 62 have been projected to the next consecutive wave to facilitate a better understanding of the process. The nature of local mass transfer distribution for air speeds

ranging from 10 to 40 fps, for each of the three wave sets, is essentially the same, indicating that the flow pattern for each wave remains unchanged in the corresponding range of Reynolds numbers. In each case, the evaporation rate shows a maximum just upstream of a crest and undergoes a minimum slightly downstream of that crest. At a given ambient speed (e.g. 20 fps), the ratio of maximum to minimum mass transfer rates varies approximately from 3.6 in wave A to 2.40 and 2.10 in waves B and C, respectively. After reaching the minimum, the evaporation rates show relatively little variation inside the trough in the case of steeper waves (A and B) as compared to the shallowest wave (C). Before explaining this behavior, some other pertinent results should be considered.

Photographs taken for visual studies are shown in Figs. 63, and 64. The most noticeable feature of the flow is the vortex (or roller) seen in the troughs of the waves; this vortex is more significant in the steeper wave (Wave A). In general, certain distinct characteristics of the flow can be identified (Fig. 65). In addition to the presence of vortex region 'v', one can also see that the region marked 's' is the place where the flow separates. It is also noticed that the region 'a' is the approximate vicinity where the airflow contacts the wave surface. As seen in the photographs (Figs. 63 and 64), the flow on the upstream portion of the wave trough is much quieter than on the downstream portion where certain degree of unsteadiness is observed, especially near the place where the flow contacts the wave surface.

Also, the results of wall pressure measurements, for all three wave sets, are shown in Fig. 66. A general feature noticed is a maximum in all these curves upstream of a wave crest approximately near region

'a' where the flow contacts the surface and a minimum near region 's' where the flow possibly separates. Also, pressure in the trough of wave A remains relatively constant as compared to the shallower waves (B and C).

In light of what has just been presented, an explanation of the local mass transfer behavior can be attempted. The variations of local mass transfer coefficients for all three wave sets, at a given ambient speed (≃20 fps), have been plotted together in Fig. 67 to facilitate comparison. The minimum in evaporation rate distribution occurs in region 's' where the flow is suspected of separating; this is the same region where the minimum of pressure distribution is also exhibited (Fig. 66). Right after this minimum, in region 'v', the evaporation rate for steeper waves is found to be smaller than for shallower waves. Also, in the case of waves A and B, the evaporation rates are relatively constant in region 'v' as compared to the situation in wave C. As displayed in the visualization pictures, the vortex in the steeper wave (A) is much better defined than the vortex in the shallower wave (C). In case of steeper waves, a given particle of air in region 'v' tends to remain in that region for a relatively longer time and keeps on picking up more and more moisture, thus reducing the evaporation rates, than in the corresponding case of shallower waves. Thus, it is felt that the build up of high humidity in the vortices, which are bigger for steeper waves, tends to reduce the moisture transfer more effectively in the case of waves A and B than in wave C. As mentioned before, flow on the upstream portion of a trough is much quieter than on the downstream portion where a certain degree of unsteadiness is noticed, especially near the place

where air flow contacts the wave surface (Figs. 63, 64 & 65). The evaporation rates become significantly larger on the downstream portion of wave troughs and peak at a maximum in the vicinity of region 'a'. In this region, the incoming air directly contacts the wave surface, thereby absorbing larger amounts of moisture. Another distinct feature noticed in Fig. 67 is the shift in the maxima of evaporation rates of the shallower waves in the upstream direction. The corresponding shift in the wall pressure maxima can also be noted (Fig. 66). This indicates that the region where the fresh air comes in contact with the wave surface is reached sooner for the shallower waves than the steeper ones, which is reasonable. After this maximum, the evaporation rate decreases sharply and drops to a minimum in region 's'. This can be attributed to a relatively low shear occurring there and also to the fact that the fresh air coming in contact with the wave surface in region 'a' picks up relatively more moisture flowing along the wave before reaching the region 's' and so is left with lesser capacity to hold the moisture.

To reiterate with regard to humidity distribution in wave troughs, as discussed in Section 4.2 (see Figs. 49, 50, and 51), a typical set of isoconcentration lines can be drawn as shown in Fig. 68. This figure reveals, as also indicated in Section 4.2, that the humidity gradient is fairly low in region 'v', but later it increases toward region 'a', reaching a maximum just upstream of a crest. After this maximum, the humidity gradient again starts decreasing rapidly downstream of the crest. This presentation substantiates the conclusions drawn previously in connection with the variation of local mass transfer coefficients.

Measurements of local evaporation rates from the "evaporation metering wave" were also taken when all upstream waves were kept completely dry. Typical results are shown in Fig. 69. For this dry condition also, the local evaporation rates exhibited almost the same behavior discussed previously. An overall increase in evaporation by 10 to 15 percent resulted because the upstream was dry instead of wet.

The above measurements were repeated with the measuring wave turned around. The results matched within 5 to 10 percent, indicating that the effect of a possible texture difference of surfaces of different wave sections is negligible.

An important conclusion to be drawn from the results reported in this section is that the various sets of independent measurements, e.g., the local evaporation rates, the wall pressure distributions, the vertical humidity profiles inside the troughs, and the visualization studies, are self consistent. The results of this study are of importance in agricultural applications, especially in connection with using furrows to reduce moisture loss. A model of a field furrow is shown in Fig. 70. For the furrow orientation, as shown in this figure, the moisture loss is fairly low $\left([E/\Delta q - (E/\Delta q)_{min}] / [E/\Delta q)_{max} - (E/\Delta q)_{min}] < 0.25\right)$ in the region D; so, from an evaporational point of view, this region would be favorable for planting seeds. Another important consideration in connection with seed germination is the availability of reasonably moderate soil temperatures. A typical set of distributions of surface temperature over the wavy surfaces of this study is shown in Fig. 71. As expected, the surface temperature is relatively higher in the region for planting seeds, which is quite favorable for seed germination and seedling establishment.

As previously indicated the evaporation losses from the bottom of waves A and B are respectively 30 to 40 percent and 20 to 25 percent less than the evaporation loss from the bottom of the shallowest wave C. This result is consistent with the results of a set of field experiments conducted by McGinnies (49). His results indicated that furrows, if deep enough, can have a pronounced effect on increasing soil moisture content and improving the seedling stand. The increase in moisture content (and thus a proportional decrease in evaporation loss), as found in his experiments, by increasing the depth to width ratio of the furrows, was of the same order of magnitude as the results of this study.

Improvements in the sense of reducing moisture loss by furrowing the field is so significant that the method deserves careful examination for range seeding, especially when soil moisture is critical for seed germination and seedling emergence.

4.6 Correlation of Evaporation Data

Evaporation from a saturated surface may be influenced by certain variables:

(1) physical properties, dynamic and vapor characteristics of the ambient air,

(2) characteristics of the evaporating surface, and

(3) properties of the evaporating liquid.

For a fully developed boundary layer under near neutral conditions, with no lateral diffusion present, a dimensional analysis of the evaporation problem leads to

$$\frac{E\,\ell}{\rho D(q_s - q_\infty)} = f\left[\frac{u_* \ell}{\nu}, \frac{\nu}{D}\right] , \qquad (4.8)$$

in which E is the evaporation rate per unit of projected area, ρ is the density, D is the molecular diffusivity, ν is the kinematic viscosity, u_* is the friction velocity, (q_s-q_∞) is the difference of surface and ambient air humidities, and ℓ is a characteristic length.

As shown in Section (4.1), an approximately fully developed boundary layer was obtained near the evaporation metering wave. The effect of lateral diffusion was minimized by keeping the buffer waves, located at both ends of the metering wave, completely wet during the course of an experimental run. It also has been shown in Section (4.1) that conditions in this study can be treated as nearly neutral with a negligible effect of stability on u_*. Thus, the evaporation data of the present study can be correlated on the basis of Eq. (4.7). As the first step for correlating the evaporation data, the height h of a wave was taken as the characteristic length. The computed values of Sherwood numbers, $(Sh)_h = -\frac{Eh}{(q_s-q_\infty)}$, and the corresponding Reynolds numbers, $(Re_*)_h = \frac{u_* h}{\nu}$, for all three wave sets at different free stream speeds are given in Table 8. Figure 72 shows a plot of $(Sh)_h$ vs $(Re_*)_h$ and the data is correlated by the line

$$(Sh)_h = 0.10\ (Re_*)_h^{0.84} \tag{4.9}$$

where $\frac{\nu}{D}$ (=Sc) is included in the constant 0.10. In connection with the above relation there have been numerous values proposed for the exponent to the Reynolds number for the transport of mass or heat from different kinds of surfaces. Based on their heat transfer measurements for flow through rough tubes, Kolar (39) and Nunner (54) found values of 0.986 and 1.0, respectively, for the exponent to the Reynolds number

formed from the friction velocity and diameter of the tube. On the other hand, Levich (44) obtained [rewriting Eq. (2.62)]

$$\frac{Eh}{\rho D(q_s - q_\infty)} \simeq \left(\frac{u_* h}{\nu}\right)^{1/2} (Sc)^{1/4} \simeq (Re_*)_h^{1/2} (Sc)^{1/4} , \quad (4.10)$$

in which h is the height of the protrusions. It should be noted that Levich's analysis is restricted only to cases where $Sc >> 1$; his results are in agreement with Mahato and Shemilt's (45) results (with $Sc \simeq 238$). In trying to correlate his data on evaporation from water waves ($Sc \simeq 0.6$) with Levich's correlation (2.63), Lai (42) reports a $Re^{0.85}$ dependence on the Sherwood number. In view of these various dependences reported in the literature, the relation $(Sh)_h \simeq (Re_*)_h^{0.84}$ of Eq. (4.9) can be considered reasonable.

The applicability of relation (4.9) is restricted to wavy surfaces. In an attempt to make the correlation more general, roughness parameter z_o was used as the characteristic length. Using the average values of u_* and z_o in the far downstream region, the values of $(Sh)_o = \frac{Ez_o}{\rho D(q_s - q_\infty)}$ and $(Re_*)_o = \frac{u_* z_o}{\nu}$ were computed for all the three sets at different free stream speeds; they are tabulated in Table 9. Figure 73 shows a plot of these values, and the relation

$$(Sh)_o = 0.055 \ (Re_*)_o^{0.90} \quad (4.11)$$

gives the best fit correlation for all the different sets of data. The advantage of this correlation is that it is applicable to evaporation from any type of surface, some examples of which are considered in the next few sections.

4.7 Comparison with Evaporation Data from Water Waves

Lai (42) measured evaporation from small amplitude wind generated water waves at different ambient conditions. He reported his evaporation data along with the corresponding values of the friction velocity u_* and the roughness parameter z_o obtained from the relation

$$\frac{U}{u_*} = \frac{1}{k} \ln \frac{z}{z_o} \quad , \tag{4.12}$$

where U is the air speed, k is the Karman constant, and z is the height above mean level. In attempting to correlate Lai's data with the data obtained in the present study, the following considerations can be made. Consider the simplified case of a long train of waves of constant form with amplitude a and length λ moving at a constant speed or celerity c. The wind blows over these waves with a velocity U which varies with height z, i.e., $U = U(z)$, but remains constant with time and direction. The flow is unsteady and the boundary conditions are different from those of a fixed set of solid waves. To reduce this situation to a steady one, a coordinate system moving at the same speed as the waves is introduced. When viewed from the moving coordinate system, the wave profile is stationary, so this transformation makes boundary condition correspond approximately to the rigid waves. The introduction of this moving coordinate system does not affect the values of u_* reported by Lai (42), but it does modify the roughness parameter:

$$\frac{(z_o) \text{ moving coordinate}}{(z_o) \text{ fixed coordinate}} = e^{\frac{kc}{u_*}} \quad . \tag{4.13}$$

Using this modification, values of $(Sh)_o = \frac{Ez_o}{\rho D(q_s - q_\infty)}$ & $(Re_*)_o = \frac{u_* z_o}{\nu}$ were computed from the set of data, (taken in the approximately fully developed region), reported by Lai (32). The results are shown in Fig. 74. As shown, the evaporation data from the water waves and those from the fixed waves are reasonably well correlated by Eq. (4.11). Therefore, this relation can be used to obtain estimates of evaporation rates from water waves, provided necessary modifications are made.

4.8 Comparison with Evaporation Data from a Flat Plate

Cermak and Lin (9) reported evaporation results from their experiments on a smooth flat plate. To correlate their data with that of the present study, one needs the values of the friction velocity u_* and the roughness parameter z_o corresponding to each evaporation run.

The values of u_* reported by the authors were based on the relation

$$\frac{U}{u_*} = \frac{1}{k} \ln \frac{zu_*}{\nu} + \text{constant} \quad . \tag{4.14}$$

For a smooth flat plate, designating z_o as the roughness parameter may be misleading. However, for the sake of evaluating Eq. (4.11), z_o may be assumed to have that value of z for which the extrapolated value of U is zero. This procedure for obtaining z_o for a flat plate has been previously used by Cermak and Koloseus (8) and Chamberlain (11). Using the values of u_* and z_o thus obtained, along with the evaporation data obtained from a flat plate located in a fully developed boundary layer (9), the values of Sherwood number = $\frac{Ez_o}{\rho D(q_s - q_\infty)}$ and Reynolds number = $\frac{u_* z_o}{\nu}$ were computed; the results

are shown in Fig. 75. The line representing Eq. (4.11), which correlated the data from the solid and water waves, can be extrapolated to correlate the evaporation data from a flat plate reasonably well.

4.9 Comparison with Sublimation Data from Different Rough Surfaces

Owen and Thomson (56, p. 327) measured sublimation rates of camphor from surfaces roughened by two types of glass: "one was mottled by irregular pyramids in relief and the other reeded, with the generators of the reed running perpendicular to the stream...". To correlate their sublimation data with the evaporation data, one must account for the difference in molecular diffusivities of the camphor and water vapors which can be incorporated in the non dimensional Schmidt number, $Sc = \frac{\nu}{D}$, analogous to the Prandtl number in the corresponding heat transfer case. Thus a correlation of the type

$$(Sh)_o \simeq (Re_*)_o^m \ (Sc)^n \qquad (4.15)$$

can be attempted, in which $(Sh)_o = \frac{Ez_o}{\rho D(\Delta q)}$ where E is the mass transfer rate per unit area and Δq is the difference of the surface and ambient concentrations. A variety of values, ranging from 0.25 to 0.5, for the exponent n have been used in the literature.

From their experiments on evaporation of various liquids, Smolsky and Sergeyev (80) reported a value of 0.44 for n as did Gilliland and Sherwood (27). Levich (44) and Mahato and Schmilt (45) used $Sc^{0.25}$ in their correlation. In heat transfer experiments, Chilton and Colburn (13), Reynolds et al. (68), and many others report a $Pr^{0.33}$ dependence, whereas Kolar (39) obtained a $Pr^{0.5}$ dependence on

the Nusselt number. In this study, $n = 0.33$ has been chosen for correlating the sublimation data with the evaporation data. Figure 76 shows a plot of $\frac{(Sh)_o}{(Sc)^{0.33}}$ vs $(Re_*)_o$ for the sublimation data of Owen and Thomson (56) with the evaporation data of this study. The line

$$\frac{(Sh)_o}{(Sc)^{0.33}} = 0.064\ (Re_*)_o^{0.90} \tag{4.16}$$

correlates both of these data well.

The foregoing presentation indicates that the mass transfer parameter $(Sh)_o$ for a wide variety of uniformly saturated surfaces, may be considered as uniquely determined by the surface Reynolds number $(Re_*)_o$ and the Schmidt number Sc. This implies that the roughness of the surface can influence $(Sh)_o$ only insofar as u_* and z_o are influenced. The importance of this result is embodied in the fact that by knowing the velocity profile above a surface, one can predict the mass transfer rates with reasonable accuracy for different ambient conditions, provided the surface and ambient concentrations are known.

4.10. Comparison with Some Results based on Field Observations

4.10.1 Norris' results (53) - Norris (53) investigated the problem of evaporation from extensive surfaces of water. As mentioned previously, his analysis was based on the three-layer model which was also used by Montgomery (51). On physical grounds Norris differed from Montgomery concerning the distribution of water vapor in the outer turbulent layer above rough surfaces. For evaporation from a rough surface, Norris presented the relation

$$E = \rho k\, u_{*R}\, \Gamma_b (q_s - q_b)\ , \tag{4.17}$$

in which

$$\Gamma_b = [\ell n \frac{b}{I} + \frac{u_{*k}}{u_{*R}} (\frac{\lambda_1 \nu k}{D} + \ell n \frac{k u_{*k} I}{D})]^{-1} \qquad (4.18)$$

Equations (4.17) and (4.18) have previously been presented as Eqs. (2.57) and (2.58). Equation (4.18) could be simplified to

$$\Gamma_b = [\ell n \frac{b}{\alpha z_o}]^{-1} , \qquad (4.19)$$

in which $\ell n\alpha = 1.76 \frac{u_{*k}}{u_{*R}}$ with u_{*k} and u_{*R} being the friction velocities in the intermediate and turbulent layers of the three-layer model over a hydrodynamically rough surface. From actual calculations for many wind profile data, Norris reported an approximate value of 0.88 for $\ell n\alpha$.

In connection with estimating evaporation losses from lakes, reservoirs, or any other water surfaces of finite extent, let us assume that the value of mean humidity measured at 10 meters above the water surface is approximately representative of the ambient humidity. This assumption is compatible with the considerations made in (47).

Determinations of wind profile over the sea (73) indicate that the sea surface is hydrodynamically rough at wind velocities exceeding 6 m/sec as measured at a height 6 to 12 meters above the sea surface. The roughness length z_o of the sea surface has been found to be about 0.6 cm, regardless of wind velocity. On the other hand, for hydrodynamically rough lake surface, z_o was found to vary from 0.55 to 1.55 cm for the wind velocity ranging from 1 m/sec to 15 m/sec measured at an 8 meter level from the water surface (47). For

computation of Γ_b in Eq. (4.19), an average value of z_o equal to 0.8 cm was chosen.

Using the above assumptions, the values of $\frac{Ez_o}{\rho D(q_s - q_{amb})}$ were computed for various values of $\frac{u_* z_o}{\nu}$ from Norris' results. A line representing these values is shown in Fig. 77, along with the correlation

$$\frac{E\ z_o}{\rho D(q_s - q_{amb})} = 0.055\ (\frac{u_* z_o}{\nu})^{0.90} \quad . \tag{4.20}$$

Agreement is within 10 to 15 percent for the range of $\frac{u_* z_o}{\nu}$ considered.

It turns out that Norris' results are not very sensitve to the chosen level for measuring ambient humidity. For example, a change of this level from 10 to 20 meters makes a difference of 5 to 8 percent only in the values of $\frac{E}{q_s - q_{amb}}$.

4.10.2 Kondo's (40) results - Based on empirical relations derived from field observations, Kondo (40) obtained estimates of evaporation losses from natural water surfaces for various ambient conditions. Kondo (40) tabulated the values of $\frac{E}{q_s - q_{10m}}$ with the corresponding U_{10m} , u_* and z_o values for various stability conditions, where q_{10m} and U_{10m} are the humidity and velocity measured at 10 m above the water surface. Again, assuming that q_{10m} approximately represents the ambient humidity over a lake or reservoir surface, the values of $\frac{Ez_o}{\rho D(q_s - q_{amb})}$ and $\frac{u_* z_o}{\nu}$ were computed from Kondo's results for near neutral conditions. Figure 77 shows a line representing these values plotted along with relation (4.20). Except for low $\frac{u_* z_o}{\nu}$ values, the agreement is reasonable. For example, the

evaporation losses predicted by the relation (4.20) are within 10 to 15 percent of Kondo's results for $200 < \frac{u_* z_o}{\nu} < 500$.

The preceding comparisons indicate relation (4.20) is of considerable practical significance. With the help of simple meteorological measurements, namely, windspeeds at a few levels, surface temperature and ambient humidity, using relation (4.20), one can reliably estimate the evaporation losses from field situations, e.g. lakes, reservoirs irrigated areas, etc. Marciano and Harbeck (47) concluded, as did Holzman (32), that evaporation can be accurately predicted by neglecting stability, that is, by exclusively using adiabatic equations. Therefore, it appears that the application of relation (4.20) may also be extended to stratified conditions.

4.11 Comparison with Some Results Related to Reynolds Analogy

The rate of mass transfer immediately near a surface, regardless of the regularity of the surface, is controlled by a purely molecular property (i.e. molecular diffusivity in the flowing fluid) of the substance (e.g. water vapor). However, the stream-wise pressure forces (the bluff body effect) acting on individual roughness elements of the surface, in case of an aerodynamically rough flow, are large enough to render the simultaneous transfer of momentum independent of the molecular viscosity of the fluid. A dimensionless number B^{-1} given by (see Section 2.5 also)

$$B^{-1} = r_+(z) - f_+(z) = \frac{\rho u_* [q_s - q]}{E} - \frac{U(z)}{u_*} \qquad (4.21)$$

has been used [Chamberlain (10), Chamberlain (11) and Owen and Thomson

(56)] to measure the discrepancy between the transport of mass and momentum transfer to, or from, a surface. Based on dimensional analysis and experimentation, Owen and Thomson (56) presented a relation for B^{-1} given by (Section 2.5)

$$B^{-1} = \alpha_1 \left(\frac{30u_* z_o}{\nu}\right)^m \quad (\nu/D)^n \quad \text{for} \quad \left(\frac{30u_* z_o}{\nu}\right) > 100 \ , \qquad (4.22)$$

where m and n were assigned the values 0.45 and 0.8, respectively, and α_1 was suggested to be a constant for each experimental arrangement, but varied according to the type of roughness.

Values of B^{-1} and $u_* z_o/\nu$ were computed from the experimental data obtained in this study. Figure 78 shows a plot of these values for $u_* z_o/\nu > 40$, along with the data points from Chamberlain's wind-tunnel experiments on evaporation from artificial grass (10) and various other surfaces with cylindrical and wavelike roughness elements (11). The results show that, for the range of $u_* z_o/\nu$ considered, B^{-1} is always positive, indicating that the resistance to momentum transfer is usually less than the resitance to a simultaneous mass transfer to, or from, a surface. Although, for a given value of $u_* z_o/\nu$ the value of B^{-1} will depend upon the type of roughness elements, the B^{-1} values obtained in this study are of the same order of magnitude as the values obtained by Chamberlain (11), especially in the case of his evaporation experiments with cylindrical and wavelike surfaces. In the range $50 < u_* z_o/\nu < 400$, B^{-1} values, in this study, do not seem to vary with $u_* z_o/\nu$, as much as indicated by Owen-Thomson's model (Eq. 4.22). A similar observation can be made from most of Chamberlain's data [(10) and (11)], especially when one chooses to examine the variation of $u_* z_o/\nu$ for one type of roughness elements at a time.

4.12 Vertical Exchange Coefficient K_z

The diffusion equation can be solved to obtain useable results provided the distribution of the exchange coefficient K_z is known. Many efforts have been made to determine K_z in various situations. Poreh (64) assumed a form for the concentration distribution, and then integrated the diffusion equation to find a relation between K_z and some functions, which were evaluated from experimental data. These functions, however, are extremely sensitive to scatter in the data. Chaudhry (12), using the method developed by Perdreauville and Goodson (60), integrated the two-dimensional diffusion equation w.r.t. x and z, after multiplying both sides of this equation by a weighting function. This weighting function was chosen such that the derivatives of concentration were eliminated. This method could not be used in this study because it would require an interpolation, between two crests, for the values of concentration and velocity. In this study, a method, similar to that used by Al Saffar (1), Ellison and Turner (24) etc., was used. The two-dimensional diffusion equation, in conjunction with the continuity equation, can be integrated to give

$$K_z = \left[\frac{\partial}{\partial x} \int_z^{\delta} U(q-q_\infty)\, dz - W(q-q_\infty)\right] \Big/ \frac{\partial q}{\partial z}\,, \qquad (4.23)$$

in which δ is the boundary layer thickness. This method suffers from the inaccuracies involved in measuring the slopes of curves, e.g. $\int_z^{\delta} U(q-q_\infty)\, dz$ vs x, unless the values of the integral is known at quite a few closely spaced x- positions. An attempt to obtain an approximate behavior is worthwhile, since it may stimulate future research. From experimental data, plots of $U(q-q_\infty)$ vs z were constructed for various

longitudinal positions as shown in Fig. 56. Then the values of the integral $\int_z^\delta U(q-q_\infty)dz$, for various heights z , were obtained by planimetering the $U(q-q_\infty)$ vs z curves between z and δ . From this information, the $\frac{\partial}{\partial x}\int_z^\delta U(q-q_\infty)dz$ values at various heights were obtained in the far downstream region. The humidity derivatives $\frac{\partial q}{\partial z}$ were computed from the measured humidity profiles. Using these computations, the distribution of K_z was obtained from Eq. (4.23) in the far downstream region. Figure 79 shows a typical distribution of K_z along with the values of K_M (vertical exchange coefficient for momentum transfer) measured by Beebe (5), for the corresponding case. The ratio K_z/K_M is approximately equal to 1 up to about 0.75 in. above the crest, but later it decreases and becomes about 0.75 at 2 in. above the crest; beyond this the K_M values could not be determined accurately. In view of the uncertainties involved in these measurements of K_z and K_M , it is difficult to conclude anything definitely, so further study in this direction is recommended.

Chapter V

Summary and Conclusions

A systematic experimental study of the problem of mass transfer (evaporation) from rough surfaces was conducted in a wind tunnel. Wavy (sinusoidal) surfaces were chosen to represent a controlled and defined shape of roughness. In the wind tunnel, air flowed from a flat and dry surface toward a series of saturated waves. The mean velocity, humidity and temperature distributions were measured simultaneously at various stations over the saturated wavy surface. The variation of evaporation rates with fetch, measured from the leading wave, was computed.

A technique was developed to measure the distribution of local mass transfer coefficients $E/(q_s-q_\infty)$ on the wavy surface. Local mass transfer rates E were determined by measuring the actual volume of water evaporated from different sections of a saturated wavy surface in a given time. These measurements were taken from specially designed "evaporation metering waves" with the aid of an "automatic feed and metering system". Investigation of flow structure revealed the presence of vortex regions inside the wave troughs. The vortices were better defined in case of the steeper waves. In the vortex region, the mass transfer coefficients for steeper waves, on the average, were found to be smaller than for the shallower ones. Also, in case of the steeper waves, the mass transfer coefficients remained relatively constant in the vortex region, as compared to the shallower ones. The minimum of local mass transfer coefficient distribution occurred immediately downstream of a wave crest where the flow was suspected to

separate. This coefficient showed a maximum just upstream of a crest where incoming air directly contacted the wavy surface, thereby absorbing relatively larger amounts of moisture.

In the region far downstream from the leading wave, where the equilibrium boundary-layer conditions were achieved, the average evaporation rates computed from the profile method ($E = - \rho k\, u_* \, q_*$) and the mass balance method ($E = \frac{d}{dx} \int_0^{\delta} \rho U(q-q_\infty)dz$) compared well with the direct measurements. In this region, the mass-transfer parameter $(Sh)_o/(Sc)^{1/3}$ was found to be a simple power function of the surface Reynolds number $(Re_*)_o$, given by the equation

$$\frac{(Sh)_o}{(Sc)^{1/3}} = 0.064\ (Re_*)_o^{0.90} \quad . \tag{5.1}$$

This relation was found to satisfactorily correlate mass-transfer data from various types of surfaces, e.g., evaporation data from water waves, evaporation data from flat plate and sublimation data from surfaces roughened with irregular pyramids and spanwise humps.

Estimates of the reciprocal sublayer Stanton number B^{-1} of Owen-Thomson (56) were obtained and compared with the results from other pertinent mass transfer investigations.

For equilibrium boundary layer situations, the following can be concluded:

1. For uniformly saturated surfaces, the mass-transfer parameter $(Sh)_o$, for a wide variety of geometrical characteristics, depends primarily upon the surface Reynolds number $(Re_*)_o$ and the Schmidt

number Sc. This implies that the roughness of the surface can influence mass transfer (evaporation, sublimation etc.) rates only insofar as the aerodynamic parameters u_* and z_o are influenced.

2. Based on the experimental data of this study, the following relation is proposed for obtaining estimates of evaporation losses from lakes, reservoirs or irrigated areas:

$$\frac{E\, z_o}{\rho D(q_s - q_{amb})} = 0.055 \left(\frac{u_* z_o}{\nu}\right)^{0.90} . \tag{5.2}$$

3. The vertical humidity profiles over wave crests were found to follow a logarithmic distribution and the results indicated that one could obtain reasonable estimates of humidity by using the relation:

$$q - q_s = q_* \ \ell n \ \frac{z}{z_{om}} . \tag{5.3}$$

4. With the knowledge of velocity and humidity distributions, evaporation rates can be satisfactorily estimated by either of the following relations:

$$E = \frac{d}{dx} \left[\int_o^{\delta} \rho U \ (q - q_\infty) dz \right] , \tag{5.4}$$

or

$$E = - \rho k \ u_* \ q_* . \tag{5.5}$$

5. The mass-transfer rates from various locations on the wavy surface are intimately related with the flow structure inside the wave-troughs. The buildup of high humidity in the vortices formed in the

troughs, tends to reduce the moisture transfer. These vortices are significantly more effective in reducing the evaporation loss from the bottom of the steeper waves as compared to the shallower ones. This substantiates that furrows, if deep enough, can have pronounced effects on decreasing the moisture loss. Furrowing the field offers another advantage in terms of providing relatively higher soil temperature at the bottom, which is favorable for seed germination.

6. In case of an aerodynamically rough surface, the resistance to momentum transfer $(f_+(z) = \frac{U(z)}{u_*})$ is usually less than the resistance to a simultaneous transfer of mass $(r_+(z) = \frac{\rho u_* [q_s - q(z)]}{E})$ to, or from a surface.

REFERENCES

REFERENCES

1. Al-Saffar, A. M. (1964), "Eddy diffusion and mass transfer in open channel flow," Ph.D. Dissertation, Civil Engineering Department, University of California.

2. Aris, R. (1956), "On dispersion of a solute in a fluid flow through a tube," Proceedings Royal Society, Vol. A235.

3. Arvia, A. J., J. S. W. Carrozza and S. L. Marchiano (1964), "On the mechanism of turbulent flow in mass transfer controlled electrochemical reactions," Electrochemical Acta, Vol. 9, No. 11.

4. Atesman, K. M. (1970), "The dispersion of matter in turbulent shear flows," Ph.D. Dissertation, Colorado State University, Fort Collins, Colorado.

5. Beebe, P. S. (1971), "Turbulent flow over a wavy boundary," Ph.D. Dissertation (to be published), Colorado State University, Fort Collins, Colorado.

6. Björgum, O. (1953), "On the velocity temperature and humidity profiles in the lower atmosphere," Quarterly Journal of Royal Meteor. Soc., Vol. 79.

7. Calder, K. L. (1949), "Eddy diffusion and evaporation in flow over aerodynamically smooth and rough surfaces," Quarterly Journal of Mechanics and Applied Mathematics, Vol. 2.

8. Cermak, J. E. and H. J. Koloseus (1953), "Lake Hefner Model Studies on wind structure and evaporation," Report No. 54JEC20, Department of Civil Engineering, Colorado State University, Fort Collins, Colorado.

9. Cermak, J. E. and P. N. Lin (1955), "Vapor transfer by forced convection from a smooth, plane boundary," Report No. 55JEC1, Colorado State University, Fort Collins, Colorado.

10. Chamberlain, A. C. (1966), "Transport of gases to and from grass and grass-like surfaces," Proceedings of Royal Society Vol. A290.

11. Chamberlain, A. C. (1968), "Transport of gases to and from surfaces with bluff and wavelike roughness elements," Quarterly Journal of Royal Meteor. Soc., Vol. 94.

12. Chaudhry, F. H. (1969), "Turbulent diffusion in a stably stratified shear layer," Ph.D. Dissertation, Colorado State University, Fort Collins, Colorado.

13. Chilton, T. H. and A. P. Colburn (1934), "Mass Transfer (Absorption) Coefficients -- Prediction from data on heat transfer and fluid friction," Ind. Eng. Chem., 26.

14. Cowan, I. R. (1968), "Mass, heat and momentum exchange between stands of plants and their atmospheric environment," Quarterly Journal of Royal Meteor. Soc., Vol. 94.

15. Davies, D. R. (1947), "Turbulence and diffusion in the lower atmosphere with particular reference to lateral effect," Proceedings of Royal Society, 190.

16. Davies, D. R. (1950a), "Three dimensional turbulence and evaporation in lower atmosphere I," Quarterly Journal of Mechanics and Applied Mathematics, Vol. 3.

17. Davies, D. R. (1950b), "Three dimensional turbulence and evaporation in lower atmosphere II, Quarterly Journal of Mechanics and Applied Mathematics, Vol. 3.

18. Davies, D. R. (1952), "On diffusion from a continuous point source at ground level into a turbulent atmosphere," Quarterly Journal of Mechanics and Applied Mathematics, Vol. 5.

19. Deacon, E. L. (1948), "Vertical Profiles of mean wind velocity in the surface layers of the atmosphere," Porton Technical Paper No. 39, British Ministry of Supply, London.

20. Dipprey, D. F. and R. H. Sebersky (1963), "Heat and momentum transfer in smooth and rough tubes at various Prandtl Numbers," International Journal of Heat and Mass Transfer, Vol. 6.

21. Easterbrook, C. C. (1968), "A study of the effects of waves on evaporation from free water surface," Cornell Aeronautical Laboratory Report No. RM-2151-P-1.

22. Eckert, E. R. G. and R. M. Drake, Jr. (1959), "Heat and mass transfer," McGraw Hill Book Company, Inc., New York.

23. Elder, J. P. and G. Wranglen (1964), "Mass transfer at plane plate electrodes," Electrochemical Technology, Vol. 2, No. 1-2.

24. Ellison, T. H., and J. S. Turner (1960), "Mixing of dense fluid in a turbulent pipe flow," Journal of Fluid Mechanics, Vol. 8, Part 4.

25. Fischer, H. B. (1964), "Longitudinal dispersion by velocity gradients in open channel flow," Technical Memo 64-4, W. M. Keck Laboratory, California Institute of Technology.

26. Frost, R. (1946), "Turbulence and diffusion in lower atmosphere," Proceedings Royal Society, Vol. A186.

27. Gilliland, E. R., and T. K. Sherwood (1934), "Diffusion of vapors into air streams," Ind. Eng. Chem., 26.

28. Goff, J. A. and S. Gratch (1948), "The humidity ratio (mixing ratio) of moist air at saturation," Special Report, University of Pennsylvania Thermodynamics Research Laboratory, Navy Contract NOBS-2477.

29. Goldstein, S. (1939), "A note on the boundary layer equations," Proceedings Camb. Phil. Soc., 35.

30. Himus, G. (1929), "The evaporation of water in open pans," presented at conference on Vapor Absorption and Adsorption sponsored by Inst. of Chem. Eng., London.

31. Hine, T. B. (1924), "Rate of evaporation of liquids in a current of air," Physical Review, Vol. 24.

32. Holzman, B. (1943), "Influence of stability on evaporation," Annals New York Academy of Science, Vol. 44.

33. Hsi, G. and J. H. Nath (1968), "Wind drag within a simulated forest canopy field, Colorado State University Report No. CER68-69 GH-JHN6.

34. Jeffreys, H. (1918), "Some problems of evaporation," Philosophical Magazine, Vol. 35.

35. von Kármán, T. (1939), "The analogy between fluid friction and heat transfer," Trans. American Society of Mechanical Engineers, 61.

36. Kline, S. J. and F. A. McClintock (1953), "Describing uncertainties in single sample experiments," Mech. Eng., Vol. 75.

37. Kohler, H. (1950), "On evaporation from snow surfaces," Arkiv für Geofysik. Bandl, nr. 8.

38. Kolar, V. (1961), "Heat and mass transfer in a turbulent medium," Collection of Czechoslovak Chemical Communications, Vol. 26.

39. Kolar, V. (1965), "Heat transfer in turbulent flow of fluids through smooth and rough tubes," International Journal of Heat and Mass Transfer, 8.

40. Kondo, J. (1962), "Evaporation from extensive surfaces of water," The Science Reports of Tôhuko University, 5th Series, Vol. 14, No. 3, The Faculty of Science, Tôhuko University, Sendai, Japan.

41. Kung, R. J. (1970), "Boundary layer development over equally spaced fences," Ph.D. Dissertation, Colorado State University, Fort Collins, Colorado.

42. Lai, J. (1969), "Evaporation from small wind waves," Ph.D. Dissertation, Colorado State University, Fort Collins, Colorado.

43. Laykhtman, D. L. and S. M. Ponomareva (1969), "On the ratio of the turbulent transfer coefficients for heat and momentum in the surface layer of the atmosphere," Izv. Atmos. and Oceanic Phys. Vol. 5, No. 12.

44. Levich, V. G. (1962), "Physicochemical Hydrodynamics," Prentice-Hall, Inc., Englewood Cliffs, N.J.

45. Mahato, B. K. and L. W. Shemilt (1968), "Effect of surface roughness on mass transfer," Chem. Eng. Sci., Vol. 23.

46. Mangler, W. (1943), "Die ahnlichen Lösungen der Prandtlschen Grenzsich--tgleichungen," Zeitsch. Ang. Math. und Mech., Vol. 23.

47. Marciano, J. J. and G. Earl Harbeck, Jr. (1952), "Mass-transfer studies," Water Loss Investigations: Vol. 1 - Lake Hefner Studies Technical Report, Geological Survey Circular 229, U.S. Department of Interior.

48. Marlatt, W. and D. Hyder (1969), "The effect of microridging and wind erosion from grass seedbeds," Presented at the Eighth National Conference on Agricultural Meteorology of the American Meteorological Society, May 21-23, 1968, Ottawa, Canada.

49. McGinnies, W. J. (1959), "The relationship of furrow depth to moisture content of soil and to seedling establishment on a range soil," Agronomy Journal, Vol. 51.

50. Miyake, M. and G. McBean (1970), "On the measurement of vertical humidity transport over land," Boundary Layer Meteorology, Vol. 1, No. 1.

51. Montgomery, R. B. (1940), "Observations of vertical humidity distribution above the ocean surface and their relation to evaporation," Papers in Physical Oceanography and Meteorology, Vol. VII, No. 4, Massachusetts Institute of Technology and Woods Hole Oceanographic Institution, Cambridge and Woods Hole, Massachusetts.

52. Nelson, D. F. (1957), "The effect of shape of a plane, smooth saturated surface on evaporation rate," M.S. Thesis, Colorado State University, Fort Collins, Colorado.

53. Norris, R. (1948), "Evaporation from extensive surfaces of water roughened by waves," Quarterly Journal of Royal Meteorol. Soc., Vol. 74.

54. Nunner, W. (1956), "Heat transfer and pressure drop in rough tubes," V.D.I. Forsch. Series B, 22.

55. Okuda, S. and S. Hayami (1959), "Experiments on evaporation from wavy water," Records Oceanog. Works, Japan (N.S.), 5.

56. Owen, P. R. and W. R. Thomson (1963), "Heat transfer from rough surfaces," Journal of Fluid Mechanics, 15.

57. Pasquill, F. (1943), "Evaporation from a plane, free-liquid surface into a turbulent air," Proceedings Royal Society, Vol. A182.

58. Pasquill, F. (1949a), "Eddy diffusion of water vapor and heat near ground," Proceedings Royal Society, Vol. 198A.

59. Pasquill, F. (1949b), "Some estimates of the amount and diurnal variation of evaporation from a clayland pasture in fair spring weather," Quarterly Journal of Royal Meteorol. Soc., Vol. 75.

60. Perdreauville, F. J., and R. E. Goodson (1966), "Identification of systems described by partial differential equations," Trans. American Society of Mechanical Engineers, Journal of Basic Engineers, pp. 463-468.

61. Perry, A. E., W. H. Schofield and P. N. Joubert (1969), "Rough wall turbulent boundary layers," Journal of Fluid Mechanics, Vol. 37, Part 2.

62. Phillip, J. R. (1959), "The theory of local advection: I," Journal of Meteorology, 16.

63. Pohl, N. (1933), "Einfluss der Wnadrauhig--keit auf den wäermeÜbergang an Wasser," Forsch. Ing., Vol. 4, No. 5.

64. Poreh, M. (1961), "Diffusion from a line source in a turbulent boundary layer," Ph.D. Dissertation, Colorado State University, Fort Collins, Colorado.

65. Powell, W. and E. Griffith (1935), "The evaporation of water from plane and cylindrical surfaces," Trans. Inst. Chem. Eng., London, Vol. 13.

66. Regener, V. H. and L. Aldaz (1969), "Turbulent transport near the ground as determined from the measurements of the ozone flux and the ozone gradient," Journal of Geophysical Research, Vol. 74.

67. Reynolds, O. (1874), "On the extent and action of the heating surface for steam boilers," Proc. Manchester Lit. and Phil. Soc., Vol. 14, p. 7.

68. Reynolds, W. G., W. M. Kays and S. J. Kline (1958), "Heat transfer in the turbulent incompressible boundary layer, II -- the step temperature distribution," N.A.S.A. Memo 12-2-58W.

69. Rider, N. E. (1954a), "Evaporation from an oat field," Quarterly Journal of Royal Meteorol. Soc., Vol. 80.

70. Rider, N. E. (1954b), "Eddy diffusion of momentum, water vapor and heat near the ground," Phil. Trans., Royal Society, Vol. A246.

71. Rider, N. E., J. R. Phillip and E. F. Bradley (1963), "The horizontal transport of heat and moisture -- a micrometeorological study," Quarterly Journal of Royal Meteorol. Soc., Vol. 89.

72. Roberts, O. F. T. (1923), "The theoretical scattering of smoke in a turbulent atmosphere," Proceedings Royal Society of London, Vol. A104.

73. Rossby, C. G. (1936), "On the momentum transfer at the sea surface," Papers in Physical Oceanography and Meteorology, 4, No. 3.

74. Rotta, J. C. (1962), "Turbulent boundary layer in incompressible flow," Progress in Aero. Sci., Vol. 2, Pergamon Press, the MacMillan Co., New York.

75. Saffman, P. G. (1962), "The effect of wind shear on horizontal spread from an instantaneous ground source," Quarterly Journal of Royal Meteorol. Soc., Vol. 88.

76. Sayre, W. M. (1967), "Dispersion of mass in open channel flow," Ph.D. Dissertation, Colorado State University, Fort Collins, Colorado.

77. Sheppard, P. A. (1958), "Transfer across the earth's surface and through the air above," Quarterly Journal of Royal Meteorol. Soc., Vol. 84.

78. Smith, F. B. (1957), "The diffusion of smoke from a continuous elevated point source into a turbulent atmosphere," Journal of Fluid Mechanics, Vol. 2.

79. Smith, J. W. and N. Epstein (1957), "Effect of wall roughness on convective heat transfer in commercial pipes," American Institute of Chemical Engineers Journal, Vol. 3.

80. Smolsky, B. M. and G. T. Sergeyen (1962), "Heat and mass transfer with liquid evaporation," International Journal of Heat and Mass Transfer, Vol. 5.

81. Squire, H. B. (1953), "Modern Developments in Fluid Dynamics High Speed Flow Vol. II," (edited by L. Howarth), Oxford at the Clarendon Press.

82. Sutton, O. G. (1934), "Wind structure and evaporation in a turbulent atmosphere," Proceedings Royal Society, Vol. A146.

83. Sverdrup, H. V. (1946), "The humidity gradient over the sea surface," Journal of Meteorology, Vol. 3.

84. Swinbank, W. C. (1955), "Eddy transport in the lower atmosphere," Commonwealth Scientific and Industrial Research Organization, Division of Meteorological Physics (Melbourne), Technical Paper No. 2.

85. Thiesenhausen, R. (1930), "Untersuchungen über die Wasserverdungstungs-geschwindigkeit in Abhangigkeit von der Temperatur des Wassers, der Luftfeuchtigkeit und Windgeschwineligkeit," Gesundheits Ingenieur, Vol. 53.

86. Thornthwaite, C. W. and B. Holzman (1939), "The determination of evaporation from land and water surfaces," Monthly Weather Review, Vol. 67.

87. Threlkeld, J. L. (1962), "Thermal environmental engineering," Prentice Hall, Inc., Englewood Cliffs, N.J.

88. Yih, C. S. (1952), "On a differential equation of atmospheric diffusion," Trans. AGU, Vol. 33, No. 1.

89. Yeh, F. F. (1970), "Air flow over roughness discontinuity," Ph.D. Dissertation, Colorado State University, Fort Collins, Colorado.

APPENDIXES

APPENDIX A

Dew point temperature t_d is a saturation temperature of moist air defined (87) mathematically by the solution $t_d(p,q)$ of the equation:

$$q_s(p,t_d) = q, \tag{A-1}$$

in which p is the barometric pressure, q is the humidity ratio or the weight of water vapor associated with unit weight of dry air, and q_s is the humidity ratio of saturated air. Practically speaking, t_d is the temperature of incipient condensation when moist air is cooled at constant pressure. It is the lowest temperature at which a given humidity ratio q may exist for a certain barometric pressure.

The humidity ratio at saturation q_s is defined (25) by

$$q_s = 0.62197 \frac{f_s p_s}{p - f_s p_s}, \tag{A-2}$$

in which p_s is the saturation pressure of pure water, and f_s is a coefficient. The coefficient f_s differs only moderately from unity and varies more or less slowly with pressure p and temperature T so that it is a quantity that is amenable to easy interpolation. Goff and Gratch (25) presented a chart representing the coefficient f_s as a function of temperature T (^oF) for each of a number of equally spaced pressures p (in. Hg); the part of the chart that is pertinent to this study is given in Table 10.

APPENDIX B

Measurement of drag on waves was discussed in Sections (3.7.1), (3.7.2), and (4.1.2). The form drag D (per ft of wave in the lateral direction) is given by (Fig. B-1)

$$D = \int_{-\lambda/2}^{\lambda/2} (-p_w) \sin\theta \, ds \ , \qquad \text{(B-1)}$$

in which p_w is the wall pressure at a point on the wave surface, θ is the angle that the normal to the curve at that point makes with the vertical direction and ds is the elemental curve length as shown in Fig. B-1.

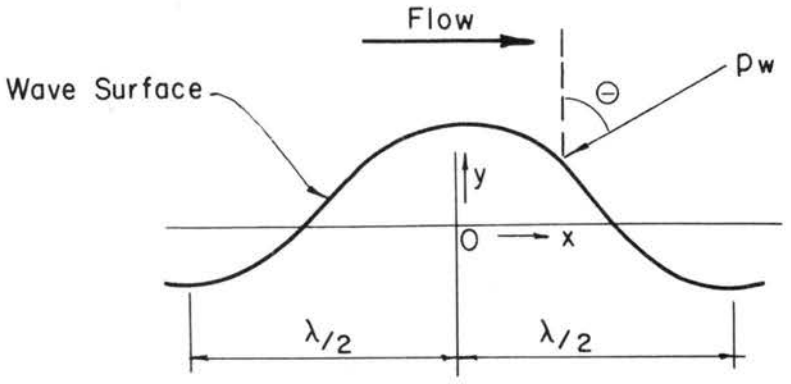

Figure B-1

The equation of the curve representing the wavy surface is

$$y = a \cos \frac{2\pi x}{\lambda} \ , \qquad \text{(B-2)}$$

in which a and λ are the amplitude and wavelength respectively.

Then the quantities ds and $\sin\theta$ (Eq. B-1) can be estimated by

$$\left.\begin{aligned} ds &= \sqrt{1+\left(\frac{dy}{dx}\right)^2}\,dx \quad ds = \sqrt{1+\left(\frac{2a\pi}{\lambda}\right)^2 \sin^2\frac{2\pi x}{\lambda}}\,dx \\ \sin\theta &= \frac{\left(\frac{2a\pi}{\lambda}\right)\sin\left(\frac{2\pi x}{\lambda}\right)}{1+\left(\frac{2a\pi}{\lambda}\right)^2\sin^2\frac{2\pi x}{\lambda}} \end{aligned}\right\} \qquad \text{(B-3)}$$

Using Eqs. (B-3) in Eq. (B-1), one obtains

$$D = -\frac{2a\pi}{12\lambda}\left[\int_0^{\lambda/2} p_w \sin\frac{2\pi x}{\lambda}\,dx + \int_{-\lambda/2}^{0} p_w \sin\frac{2\pi x}{\lambda}\,dx\right], \qquad \text{(B-4)}$$

in which ds is in inches.

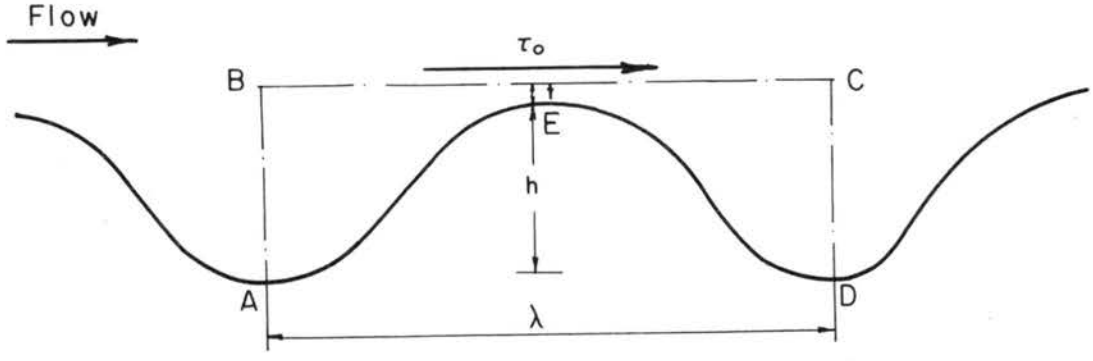

Figure B-2

The effective skin friction coefficient C_f was determined by considering a force balance on a control volume ABCDE around a single wave as shown in Fig. B-2. This method is primarily based on the procedure

Perry et al. (61) used for evaluating wall shear stress in case of flow over a series of cavities. As shown in Fig. B-2, the effective wall shear stress τ_o is assumed to act along a surface BC positioned at a distance t above the crest of the waves, where t is small compared with h. The shear on the surface AED is assumed to be negligible as compared with the acting pressure forces. Flow patterns in successive troughs are assumed to be negligibly different, and, hence, streamwise momentum in through face BA equals the momentum efflux through CD. Pressure patterns along the centerlines of two adjacent troughs are assumed to be similar. However, the values of the pressure distributions on the centerline of one trough will be lowered below that in the preceding trough by the amount the free stream static pressure has decreased in that wavelength. Neglecting the change in free stream static pressure over a wavelength, the force balance leads to

$$\frac{D}{2a\left(\frac{1}{2}\rho U_\infty^2\right)} = \frac{\tau_o \lambda}{2a\left(\frac{1}{2}\rho U_\infty^2\right)} \quad . \tag{B-5}$$

Using Eq. (B-4) in Eq. (B-5), the effective skin friction coefficient C_f $\left(= \frac{\tau_o}{\frac{1}{2}\rho U_\infty^2}\right)$ was determined. A difference of 2 to 3 percent was obtained in the value of C_f if the change in static pressure over a wavelength were taken into account. The values of C_f were also cross checked with the shear plate measurements, again by using the concept of force balance just described.

TABLES

TABLE 1 (A)

Mean Velocity Profiles

Wave A

Station: 1st Crest		Station: 3rd Crest		Station: 6th Crest		Station: 12th Crest	
Height (from crest) (in.)	U (ft/sec)	Height (from crest) (in.)	U (ft/sec)	Height (from crest) (in.)	U (ft/sec)	Height (from crest) (in.)	U (ft/sec)
0.08	17.88	0.08	12.24	0.08	10.56	0.08	10.06
0.12	18.32	0.11	12.42	0.11	10.88	0.11	10.52
0.16	18.30	0.14	12.43	0.20	10.94	0.14	10.83
0.20	18.18	0.18	12.59	0.24	11.11	0.19	10.90
0.28	18.10	0.22	12.80	0.27	11.34	0.22	11.05
0.36	18.18	0.28	13.18	0.31	11.50	0.25	11.19
0.50	18.28	0.36	13.70	0.35	11.69	0.29	11.33
0.59	18.39	0.47	14.61	0.42	12.21	0.33	11.48
0.74	18.56	0.62	15.69	0.50	12.69	0.37	11.79
0.94	18.67	0.81	16.87	0.59	13.24	0.43	12.05
1.27	18.83	1.02	17.29	0.70	13.98	0.50	12.39
1.63	19.00	1.67	18.35	0.85	14.79	0.59	12.85
2.33	19.17	2.24	18.89	1.07	15.88	0.68	13.23
3.77	19.64	3.24	19.45	1.29	16.76	0.80	13.77
5.91	19.90	4.83	19.99	1.60	17.48	0.93	14.16
8.80	20.13	7.32	20.33	1.96	18.21	1.17	14.94
12.36	20.14	10.49	20.37	2.49	18.84	1.35	15.67
				3.19	19.36	1.67	16.51
				4.50	19.89	2.04	17.53
				6.64	20.29	2.38	17.76
				9.41	20.46	2.92	18.59
				12.63	20.48	3.63	19.21
						4.33	19.74
						5.39	20.00
						8.60	20.33
						10.72	20.49

Station: 18th Crest		Station: 24th Crest		Station: 25th Crest	
0.08	10.13	0.08	10.16	0.08	10.80
0.24	10.21	0.13	10.36	0.14	10.76
0.28	10.36	0.22	10.41	0.27	10.78
0.32	10.66	0.26	10.54	0.32	10.87
0.36	10.72	0.40	10.99	0.36	11.05
0.40	10.99	0.47	11.37	0.43	11.44
0.46	11.18	0.58	11.67	0.50	11.69
0.53	11.72	0.71	12.12	0.61	12.11
0.64	12.24	0.86	12.62	0.72	12.56
0.76	12.64	1.06	13.38	0.87	12.95
0.88	13.18	1.29	13.97	1.07	13.58
1.02	13.59	1.57	14.77	1.28	14.13
1.23	14.25	1.94	15.57	1.57	14.87
1.44	14.89	2.31	16.41	1.93	15.66
1.75	15.70	3.02	17.20	2.27	16.44
2.22	16.83	3.73	18.14	2.85	17.01
2.58	17.63	4.81	19.27	3.58	17.99
3.30	18.35	6.43	20.18	4.57	19.19
4.00	19.02	8.23	20.53	6.00	20.13
5.07	19.74	10.73	20.68	7.79	20.60
6.49	20.13	13.20	20.68	10.04	20.73
8.25	20.48			12.56	20.85
10.40	20.50				
12.85	20.64				

TABLE 1 (B)

Mean Velocity Profiles

Wave B

Station: 1st Crest		Station: 3rd Crest		Station: 6th Crest		Station: 12th Crest	
Height (from crest) (in.)	U (ft/sec)	Height (from crest) (in.)	U (ft/sec)	Height (from crest) (in.)	U (ft/sec)	Height (from crest) (in.)	U (ft/sec)
0.08	13.42	0.08	12.86	0.08	11.20	0.08	10.96
0.10	14.24	0.11	12.88	0.11	11.76	0.11	11.34
0.14	14.44	0.16	12.88	0.13	11.80	0.14	11.47
0.23	14.76	0.20	12.94	0.21	11.72	0.18	11.31
0.26	15.05	0.24	13.08	0.31	11.90	0.30	11.51
0.30	15.17	0.28	13.31	0.35	12.04	0.35	11.60
0.35	15.43	0.33	13.59	0.42	12.42	0.41	11.74
0.41	15.73	0.38	13.93	0.51	12.74	0.48	12.09
0.53	16.15	0.48	14.64	0.65	13.47	0.59	12.63
0.72	16.44	0.64	15.67	0.86	14.63	0.74	13.22
0.96	16.90	0.87	16.58	1.16	15.94	0.90	13.75
1.28	17.21	1.15	17.34	1.52	17.13	1.11	14.55
1.82	17.80	1.50	17.76	1.98	18.05	1.39	15.56
2.97	18.63	2.07	18.34	2.91	18.69	1.74	16.68
4.64	19.13	3.50	19.17	4.33	19.36	2.34	17.56
7.09	19.73	5.27	19.74	6.35	19.83	3.45	18.88
10.61	19.86	7.75	20.14	9.20	20.09	5.23	19.61
		11.30	20.19	12.73	20.08	7.70	20.07
						11.25	20.21
						14.81	20.20

Station: 18th Crest		Station: 23rd Crest		Station: 25th Crest	
0.08	10.79	0.08	9.50	0.08	10.53
0.13	11.02	0.11	9.68	0.11	10.88
0.17	11.14	0.19	9.67	0.22	10.90
0.20	11.11	0.23	9.73	0.26	10.92
0.32	11.16	0.39	10.25	0.30	10.96
0.35	11.32	0.46	10.60	0.36	11.09
0.41	11.49	0.69	11.24	0.43	11.19
0.45	11.68	0.87	12.20	0.50	11.64
0.52	11.85	1.16	12.55	0.57	11.75
0.56	12.18	1.50	13.64	0.71	12.30
0.61	12.28	1.86	14.22	0.89	12.71
0.69	12.47	2.50	15.38	1.07	13.19
0.76	12.84	3.23	16.49	1.25	13.69
0.92	13.20	4.63	18.06	1.43	14.22
1.19	13.93	6.18	19.18	1.72	14.90
1.57	15.08	8.27	19.55	2.09	15.56
1.91	15.90	11.67	19.79	2.45	16.14
2.46	16.95			2.81	16.75
3.36	17.55			3.51	17.73
4.45	18.[illegible]			4.59	18.96
6.49	19.51			6.42	20.05
9.07	19.80			9.98	20.52
12.19	19.87			13.83	20.61

TABLE 1 (C)

Mean Velocity Profiles

Wave C

Station: 1st Crest		Station: 6th Crest		Station: 12th Crest		Station: 18th Crest	
Height (from crest) (in.)	U (ft/sec)	Height (from crest) (in.)	U (ft/sec)	Height (from crest) (in.)	U (ft/sec)	Height (from crest) (in.)	U (ft/sec)
0.08	13.90	0.08	12.49	0.12	13.40	0.08	12.41
0.12	14.31	0.11	12.97	0.16	13.74	0.12	12.94
0.15	14.96	0.14	13.01	0.20	13.80	0.16	13.05
0.19	15.50	0.17	13.21	0.24	13.84	0.20	13.06
0.23	15.95	0.21	13.34	0.27	13.91	0.27	13.26
0.30	16.46	0.24	13.56	0.33	14.01	0.34	13.45
0.40	17.06	0.30	13.79	0.40	14.15	0.40	13.55
0.49	17.11	0.49	14.65	0.46	14.17	0.46	13.85
0.58	17.25	0.60	15.30	0.54	14.43	0.53	14.04
0.69	17.44	0.72	15.63	0.61	14.60	0.61	14.20
0.81	17.66	0.86	16.15	1.00	15.60	0.69	14.46
1.01	17.83	0.97	16.56	1.28	16.27	0.81	14.67
1.23	18.01	1.17	17.12	1.64	16.97	0.96	15.05
1.43	18.26	1.53	17.82	2.00	17.54	1.24	15.63
1.87	18.52	2.04	18.41	2.42	18.17	1.58	16.30
2.48	18.99	3.14	19.20	3.09	18.79	1.95	16.54
3.17	19.39	4.63	19.83	3.81	19.34	2.39	17.19
4.39	19.71	6.77	20.29	4.53	19.57	2.87	17.97
6.16	20.03	8.52	20.46	5.96	19.95	3.40	18.54
7.97	20.21	11.27	20.55	7.77	20.19	4.22	19.24
9.65	20.32			10.43	20.32	4.78	19.57
				13.66	20.33	5.88	19.97
						7.44	20.22
						10.28	20.47
						13.22	20.48

Station: 23rd Crest		Station: 24th Crest	
0.14	13.40	0.08	13.70
0.21	13.43	0.10	14.07
0.33	13.39	0.13	14.10
0.40	13.63	0.17	14.23
0.46	13.92	0.24	14.31
0.52	14.31	0.35	14.47
0.70	14.45	0.39	14.56
1.05	14.75	0.54	14.54
1.23	15.36	0.70	14.66
1.44	15.54	0.81	14.86
1.78	16.10	0.93	14.89
2.14	16.77	1.04	14.94
2.52	17.56	1.21	15.50
3.23	18.27	1.54	16.17
4.32	19.43	1.91	16.55
5.75	20.29	2.29	17.27
7.48	20.71	2.68	17.54
10.28	20.86	3.41	18.69
		4.60	19.42
		6.38	20.39
		8.16	20.80
		10.35	20.94
		13.18	20.99

TABLE 2 (A)

Mean Humidity Profiles

Wave A

Station: 1st Crest		Station: 3rd Crest		Station: 6th Crest		Station: 12th Crest	
Height (from crest) (in.)	$\frac{q - q_\infty}{q_s - q_\infty}$	Height (from crest) (in.)	$\frac{q - q_\infty}{q_s - q_\infty}$	Height (from crest) (in.)	$\frac{q - q_\infty}{q_s - q_\infty}$	Height (from crest) (in.)	$\frac{q - q_\infty}{q_s - q_\infty}$
0.08	0.141	0.08	0.108	0.08	0.170	0.08	0.120
0.12	0.050	0.11	0.095	0.11	0.131	0.11	0.112
0.16	0.043	0.14	0.090	0.16	0.116	0.14	0.109
0.20	0.040	0.18	0.085	0.20	0.111	0.19	0.106
0.24	0.033	0.22	0.081	0.24	0.106	0.22	0.103
0.28	0.030	0.28	0.070	0.28	0.102	0.25	0.100
0.32	0.027	0.36	0.065	0.31	0.098	0.29	0.098
0.36	0.022	0.47	0.053	0.35	0.091	0.33	0.097
0.42	0.017	0.62	0.038	0.42	0.085	0.37	0.094
0.50	0.011	0.81	0.025	0.50	0.078	0.43	0.091
0.59	0.006	1.02	0.014	0.59	0.073	0.50	0.086
0.74	0.002	1.32	0.005	0.70	0.062	0.59	0.081
0.94	0.0015	1.67	0.003	0.85	0.053	0.68	0.077
1.27	0.0014	2.24	0.001	1.07	0.040	0.80	0.071
1.63	0.0007	3.24	0.001	1.29	0.030	0.93	0.064
3.77	0.0007	4.82	0.001	1.60	0.018	1.17	0.055
				1.96	0.009	1.35	0.048
				2.49	0.004	1.67	0.039
				3.19	0.001	2.04	0.029
				4.50	0.001	2.38	0.021
				9.40	0.001	2.92	0.011
						3.62	0.0059
						4.33	0.0026
						5.39	0.0012
						6.81	0.0011
						8.59	0.0010

Station: 18th Crest		Station: 23rd Crest		Station: 24th Crest		Station: 25th Crest	
0.08	0.169	0.08	0.225	0.10	0.216	0.08	0.294
0.09	0.164	0.10	0.214	0.15	0.210	0.10	0.257
0.12	0.154	0.13	0.210	0.19	0.207	0.15	0.250
0.14	0.153	0.17	0.201	0.29	0.202	0.18	0.244
0.17	0.147	0.22	0.201	0.32	0.196	0.22	0.240
0.21	0.143	0.26	0.194	0.36	0.194	0.27	0.232
0.24	0.142	0.29	0.193	0.40	0.191	0.32	0.226
0.28	0.140	0.33	0.187	0.46	0.187	0.36	0.227
0.32	0.135	0.37	0.185	0.54	0.181	0.44	0.212
0.36	0.132	0.42	0.185	0.66	0.171	0.53	0.208
0.40	0.130	0.47	0.180	0.74	0.165	0.63	0.199
0.45	0.126	0.54	0.177	0.82	0.160	0.74	0.188
0.53	0.121	0.62	0.170	0.98	0.153	0.88	0.177
0.64	0.113	0.73	0.165	1.18	0.141	1.13	0.164
0.76	0.109	0.86	0.156	1.34	0.131	1.36	0.150
0.88	0.101	0.97	0.147	1.54	0.120	1.62	0.135
1.02	0.096	1.12	0.136	1.92	0.105	1.99	0.119
1.23	0.087	1.28	0.129	2.34	0.086	2.37	0.101
1.44	0.079	1.47	0.121	3.06	0.063	2.91	0.083
1.75	0.066	1.67	0.111	3.84	0.042	3.62	0.060
2.21	0.052	1.94	0.099	4.94	0.021	4.33	0.043
2.58	0.040	2.20	0.087	6.10	0.0092	5.40	0.025
3.30	0.024	2.54	0.072	7.02	0.0045	6.87	0.011
4.00	0.013	2.90	0.063	9.02	0.0025	8.45	0.0030
5.07	0.006	3.61	0.043			10.71	0.0015
6.49	0.003	4.32	0.027				
8.25	0.002	5.39	0.012				
10.40	0.001	6.43	0.0060				
		8.20	0.0023				
		9.98	0.0018				

TABLE 2 (B)

Mean Humidity Profiles

Wave B

Station: 1st Crest		Station: 3rd Crest		Station: 6th Crest		Station: 12th Crest	
Height (from crest) (in.)	$\frac{q - q_\infty}{q_s - q_\infty}$	Height (from crest) (in.)	$\frac{q - q_\infty}{q_s - q_\infty}$	Height (from crest) (in.)	$\frac{q - q_\infty}{q_s - q_\infty}$	Height (from crest) (in.)	$\frac{q - q_\infty}{q_s - q_\infty}$
0.08	0.150	0.08	0.207	0.08	0.202	0.08	0.230
0.10	0.100	0.11	0.151	0.11	0.184	0.11	0.216
0.14	0.078	0.16	0.138	0.13	0.174	0.14	0.205
0.23	0.048	0.20	0.120	0.18	0.162	0.18	0.197
0.26	0.032	0.24	0.111	0.21	0.155	0.22	0.183
0.30	0.026	0.28	0.098	0.26	0.150	0.26	0.179
0.35	0.017	0.34	0.088	0.31	0.139	0.30	0.176
0.41	0.011	0.38	0.076	0.35	0.130	0.35	0.168
0.53	0.004	0.48	0.062	0.42	0.120	0.41	0.165
0.72	0.002	0.64	0.038	0.51	0.106	0.48	0.153
0.96	0.0014	0.87	0.018	0.65	0.089	0.59	0.147
1.28	0.0007	1.15	0.0073	0.86	0.068	0.74	0.129
1.82	0.0007	1.50	0.0029	1.16	0.041	0.90	0.118
		2.07	0.0022	1.52	0.022	1.11	0.100
		3.50	0.0015	1.98	0.0082	1.39	0.078
				2.91	0.0022	1.74	0.058
				4.33	0.0015	2.34	0.033
						3.45	0.0027
						5.23	0.0013

Station: 18th Crest		Station: 23rd Crest		Station: 25th Crest		Station: 28th Crest	
0.08	0.257	0.08	0.301	0.08	0.394	0.08	0.317
0.11	0.246	0.11	0.253	0.11	0.325	0.11	0.295
		0.15	0.241	0.14	0.296	0.14	0.293
0.17	0.246	0.19	0.236	0.18	0.283	0.18	0.284
0.20	0.239	0.23	0.228	0.22	0.273	0.22	0.281
0.24	0.230	0.30	0.220	0.26	0.258	0.25	0.269
0.28	0.228	0.34	0.217	0.29	0.258	0.29	0.268
0.32	0.216	0.39	0.216	0.33	0.248	0.32	0.265
0.41	0.211	0.46	0.202	0.43	0.243	0.38	0.257
0.45	0.206	0.53	0.202	0.49	0.235	0.43	0.256
0.56	0.186	0.69	0.187	0.56	0.224	0.49	0.245
0.76	0.164	0.87	0.174	0.64	0.214	0.56	0.240
0.92	0.155	1.16	0.150	0.76	0.208	0.62	0.230
1.19	0.136	1.50	0.133	0.93	0.189	0.77	0.222
1.57	0.110	1.86	0.118	1.19	0.171	0.92	0.210
1.91	0.094	2.50	0.090	1.56	0.152	1.19	0.193
2.46	0.068	3.23	0.065	1.92	0.129	1.56	0.167
3.35	0.035	4.63	0.023	2.45	0.100	1.91	0.143
4.45	0.012	6.18	0.0075	3.38	0.072	2.45	0.119
6.49	0.0027	8.27	0.0015	4.79	0.031	3.35	0.084
9.07	0.0020	11.67	0.0015	7.09	0.0054	4.42	0.051
12.19	0.0014			9.82	0.0023	7.05	0.010
				13.45	0.0022	9.70	0.0028
						13.25	0.0015

TABLE 2 (C)

Mean Humidity Profiles

Wave C

Station: 1st Crest		Station: 6th Crest		Station: 12th Crest		Station: 23rd Crest	
Height (from crest) (in.)	$\frac{q - q_\infty}{q_s - q_\infty}$	Height (from crest) (in.)	$\frac{q - q_\infty}{q_s - q_\infty}$	Height (from crest) (in.)	$\frac{q - q_\infty}{q_s - q_\infty}$	Height (from crest) (in.)	$\frac{q - q_\infty}{q_s - q_\infty}$
0.08	0.133	0.08	0.239	0.08	0.268	0.08	0.304
0.12	0.068	0.11	0.200	0.12	0.210	0.11	0.246
0.15	0.048	0.14	0.175	0.16	0.198	0.14	0.236
0.19	0.033	0.17	0.168	0.20	0.194	0.18	0.223
0.23	0.022	0.21	0.155	0.24	0.182	0.22	0.213
0.30	0.010	0.24	0.150	0.27	0.179	0.26	0.210
0.40	0.0014	0.30	0.132	0.33	0.163	0.29	0.205
0.49	0.0017	0.37	0.127	0.40	0.157	0.33	0.202
0.58	0.0012	0.42	0.117	0.46	0.148	0.40	0.187
0.69	0.0009	0.49	0.110	0.54	0.137	0.46	0.182
0.81	0.0010	0.60	0.091	0.61	0.131	0.52	0.175
1.01	0.0013	0.72	0.071	0.69	0.124	0.59	0.166
1.23	0.00078	0.86	0.063	0.80	0.115	0.70	0.159
1.42	0.00065	0.97	0.050	1.00	0.091	0.88	0.145
3.17	0.00065	1.17	0.035	1.28	0.073	1.05	0.134
4.39	0.00065	1.53	0.017	1.64	0.054	1.23	0.127
		2.04	0.0054	2.00	0.037	1.44	0.105
		3.14	0.0018	2.42	0.025	1.78	0.092
		4.63	0.0012	3.09	0.011	2.14	0.079
		6.77	0.0018	3.81	0.004	2.52	0.071
				4.53	0.003	3.23	0.045
				5.96	0.001	4.32	0.021
				7.76	0.001	5.73	0.0094
						7.48	0.0019
						10.28	0.0019

Station: 24th Crest		Station: 25th Crest	
0.08	0.337	0.08	0.376
0.10	0.298	0.11	0.321
0.13	0.252	0.14	0.280
0.17	0.241	0.18	0.264
0.20	0.236	0.23	0.258
0.24	0.232	0.26	0.250
0.28	0.218	0.30	0.242
0.31	0.216	0.35	0.233
0.35	0.211	0.39	0.228
0.39	0.201	0.43	0.219
0.43	0.194	0.46	0.212
0.48	0.191	0.51	0.206
0.54	0.190	0.55	0.203
0.63	0.176	0.60	0.203
0.70	0.173	0.66	0.189
0.81	0.164	0.75	0.190
0.93	0.150	0.83	0.174
1.04	0.137	0.92	0.172
1.21	0.131	1.01	0.161
1.54	0.109	1.09	0.153
1.91	0.094	1.17	0.152
2.29	0.077	1.29	0.146
3.41	0.045	1.50	0.129
4.60	0.020	1.86	0.113
6.38	0.0042	2.29	0.087
8.16	0.0025	3.48	0.052
10.35	0.0006	4.57	0.030
		6.17	0.0097
		8.00	0.0013
		13.29	0.0013

TABLE 3

Effective Average Skin Friction Coefficient C_f

(Far Downstream Region)

	U_∞ (ft/sec)	Wall Pressure Integration	Shear Plate
Wave A	39.70	0.0210	0.0205
	19.60	0.0218	0.0175
Wave B	40.1	0.0195	------
Wave C	39.70	0.0110	0.0160
	19.80	0.0126	0.0170

TABLE 4

Variation of q_*

Position (Distance from the start of waves) (incnes)	Wave A q_*/q_s-q_∞	Wave B q_*/q_s-q_∞	Wave C q_*/q_s-q_∞
2.1	-----	-0.333	-0.320
10.5	-0.135	-0.202	-----
23.1	-0.121	-0.162	-0.147
48.3	-0.077	-0.138	-0.126
73.5	-0.0874	-0.134	-----
94.5	-0.110	-0.124	-0.110
98.7	-0.112	-0.130	-0.115
102.9	-0.119	-0.137	-0.123
115.5	-0.125	-0.137	-----

TABLE 5

Variation of T_*

Position (Distance from the start of waves) (inches)	Wave A $\frac{T_*}{T_\infty-T_s}$
2.1	0.091
10.5	0.163
23.1	0.143
94.5	0.142
115.5	0.150

TABLE 6

Comparison of Average Evaporation rates $(E/q_s-q_\infty)^*$ obtained from Different Methods

(Far Downstream Region) (Upstream Waves Wet)

Waves	U_∞ cm/sec	Direct Measurements	First Method (Mass Balance Method) $E = \frac{d}{dx}\int_0^\delta \rho U(q-q_\infty)dz$ x 10^3	Second Method (Profile Method) $E = -\rho k u_* q_*$ x 10^3
A	596.49	3.900	3.620	3.280
B	595.58	3.265	3.160	3.315
C	595.27	3.450	3.320	2.240

* E (gm/cm^{2}sec) = Average evaporation rate (based on projected area)

q_s-q_∞ ($\frac{\text{gm water vapor}}{\text{gm dry air}}$) = Difference of surface and ambient air humidities

TABLE 7

Local Mass Transfer Coefficients (E/q_s-q_∞)

Wave A

(Far Downstream Region) $(E/q_s-q_\infty)^* \times 10^3$ Upstream waves completely wet

Sections**	U_∞ = 3.03 m/sec	U_∞ = 5.97 m/sec	U_∞ = 12.08 m/sec
1	0.561	2.376	3.757
2	1.072	3.005	4.276
3	1.502	4.514	5.357
4	3.168	6.528	8.250
5	0.894	2.934	4.321
6	0.555	1.948	2.722
7	0.780	2.147	2.928
8	0.784	2.633	4.341

Wave B

$(E/q_s-q_\infty)^* \times 10^3$

Sections**	U_∞ = 3.04 m/sec	U_∞ = 5.96 m/sec	U_∞ = 9.15 m/sec	U_∞ = 12.05 m/sec
1	1.020	2.713	3.925	4.984
2	2.000	3.549	5.033	6.239
3	2.507	4.499	6.039	7.427
4	2.568	4.485	6.090	7.181
5	1.020	2.021	3.157	4.124
6	0.893	2.206	3.428	4.378
7	1.090	2.252	3.200	4.100
8	1.161	2.831	4.147	5.399

Wave C

$(E/q_s-q_\infty)^* \times 10^3$

Sections**	U_∞ = 3.02 m/sec	U_∞ = 5.95 m/sec	U_∞ = 12.11 m/sec
1	1.995	4.200	6.578
2	2.538	4.390	6.917
3	2.250	4.090	6.029
4	2.099	3.774	5.637
5	1.311	2.290	3.629
6	0.826	2.362	5.013
7	1.150	2.898	5.039
8	1.776	3.322	5.244

* E = Local evaporation rate per unit of curved area $(gm/cm^2 sec)$

q_s-q_∞ = Difference of surface and ambient air humidities $\left(\frac{gm\ water\ vapor}{gm\ dry\ air}\right)$

** The evaporation metering wave consisted of 8 sections of equal width with section 1 being upstream.

TABLE 8

Data for Correlation $(Re_*)_h$ vs $(Sh)_h$

Waves	U_∞ cm/sec	u_* cm/sec	h=2a cm	$(Re_*)_h = \frac{u_* h}{\nu}$	$(Sh)_h = \frac{En}{\rho D(q_s - q_\infty)}$
A	302.97	32.72	4.318	856.27	25.95
A	596.49	64.42	4.318	1685.85	62.49
A	1208.23	130.49	4.318	3414.88	92.13
B	304.19	29.81	2.54	458.89	14.85
B	595.58	58.37	2.54	898.54	30.77
B	915.01	89.67	2.54	1380.37	43.68
B	1204.87	118.08	2.54	1817.72	54.07
C	301.75	22.18	1.27	170.72	8.20
C	595.27	43.75	1.27	336.74	16.26
C	1210.97	89.01	1.27	685.11	26.30

TABLE 9

Data for Correlation $(Re_*)_o$ vs $(Sh)_o$

Waves	U_∞ cm/sec	u_* cm/sec	z_o cm	$(Re_*)_c = \frac{u_* z_o}{\nu}$	$(Sh)_o = \frac{E z_o}{\rho D(q_s - q_\infty)}$	$\frac{(Sh)_o}{(Sc)^{1/3}}$
A	302.97	32.72	0.4445	88.15	2.47	2.90
A	596.49	64.42	0.4445	173.54	6.43	7.54
A	1208.23	130.49	0.4445	351.53	9.48	11.11
B	304.19	29.81	0.358	64.68	2.09	2.45
B	595.58	58.37	0.358	126.65	4.34	5.09
B	915.01	89.67	0.358	194.56	6.157	7.22
B	1204.87	118.08	0.358	256.20	7.62	8.93
C	301.75	22.18	0.0813	10.92	0.525	0.615
C	595.27	43.75	0.0813	21.56	1.04	1.22
C	1210.97	89.01	0.0813	43.86	1.68	1.97

TABLE 10

Values of f_s [Goff and Gratch (28)]

$T^{o}F/p$	23 in. Hg	24 in. Hg	25 in. Hg
32	1.003484	1.003616	1.003749
42	1.003497	1.003623	1.003751
52	1.003543	1.003666	1.003789
62	1.003626	1.003745	1.003864
72	1.003749	1.003865	1.003979
82	1.003909	1.004021	1.004134
92	1.004104	1.004216	1.004326

FIGURES

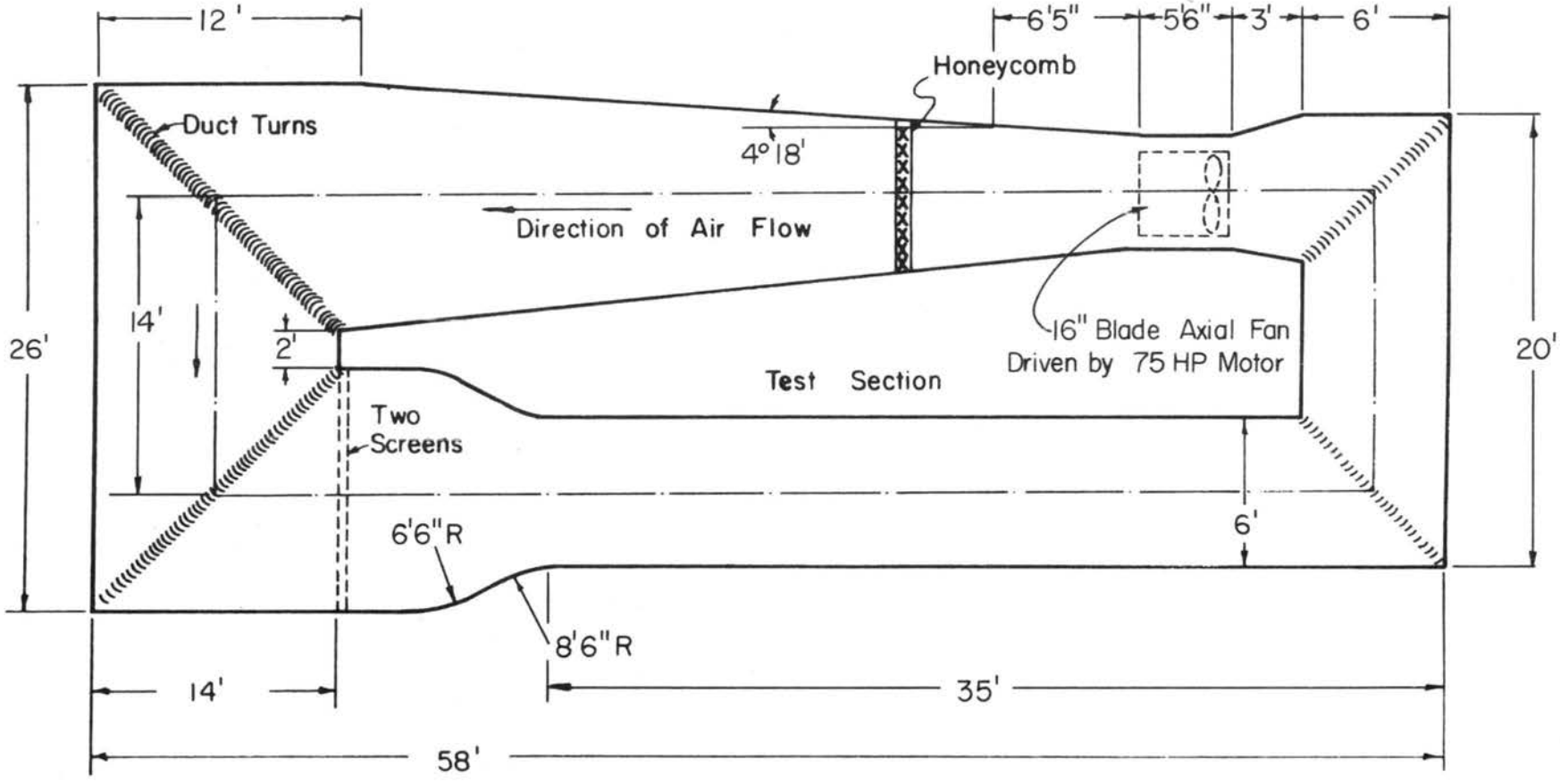

Fig. 1. Wind tunnel: Plan view.

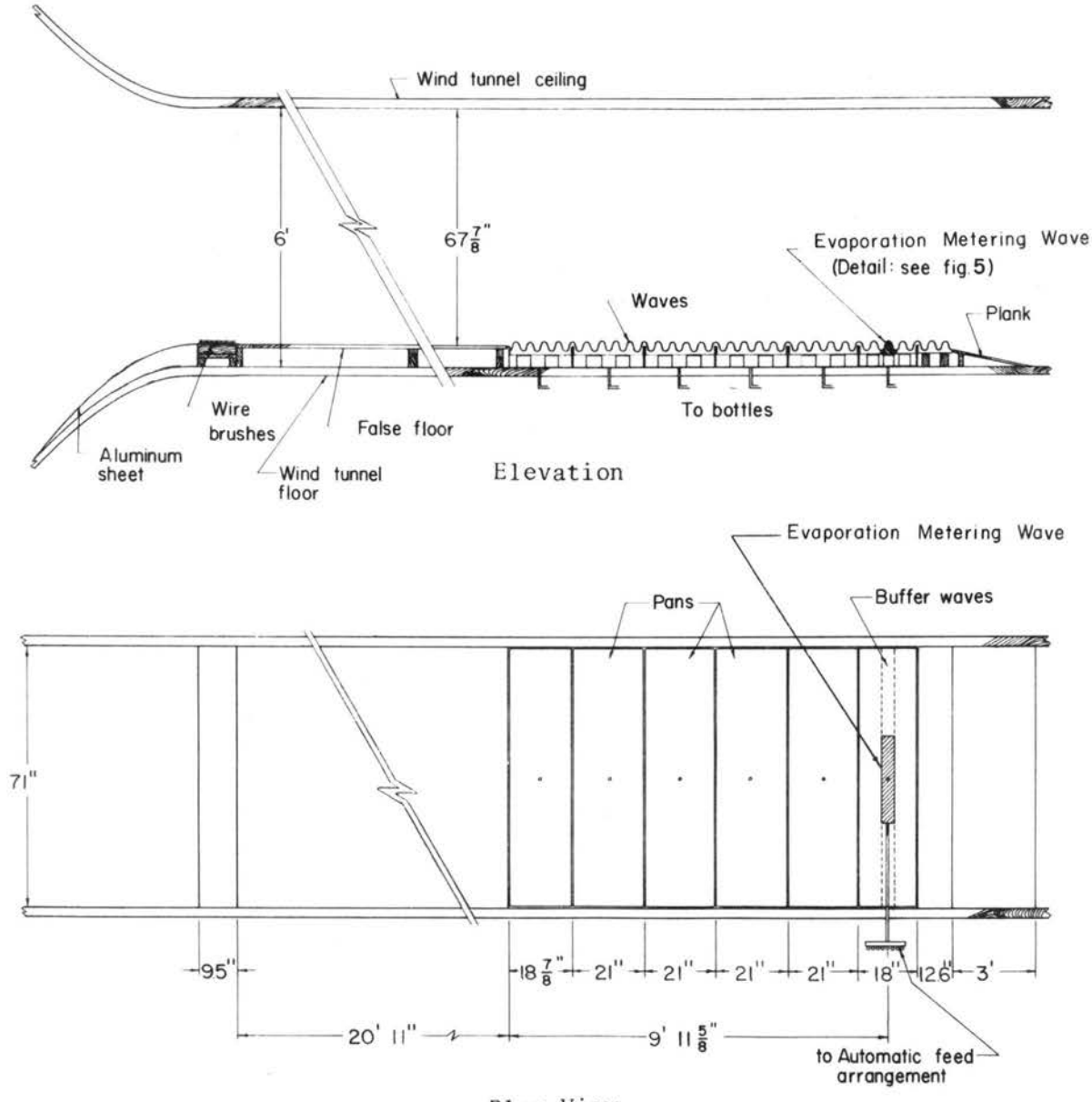

Fig. 2. Experimental set up in wind tunnel.

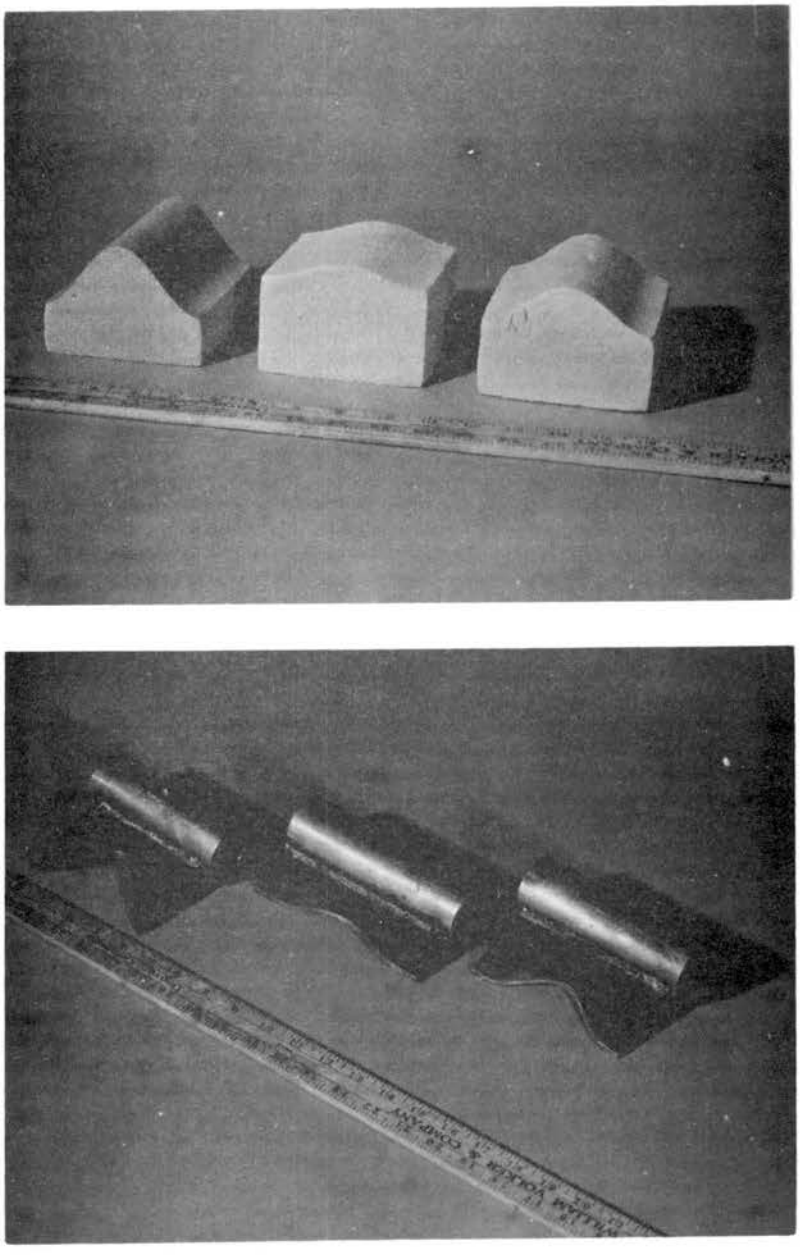

Fig. 3. Waves and shaper blades.

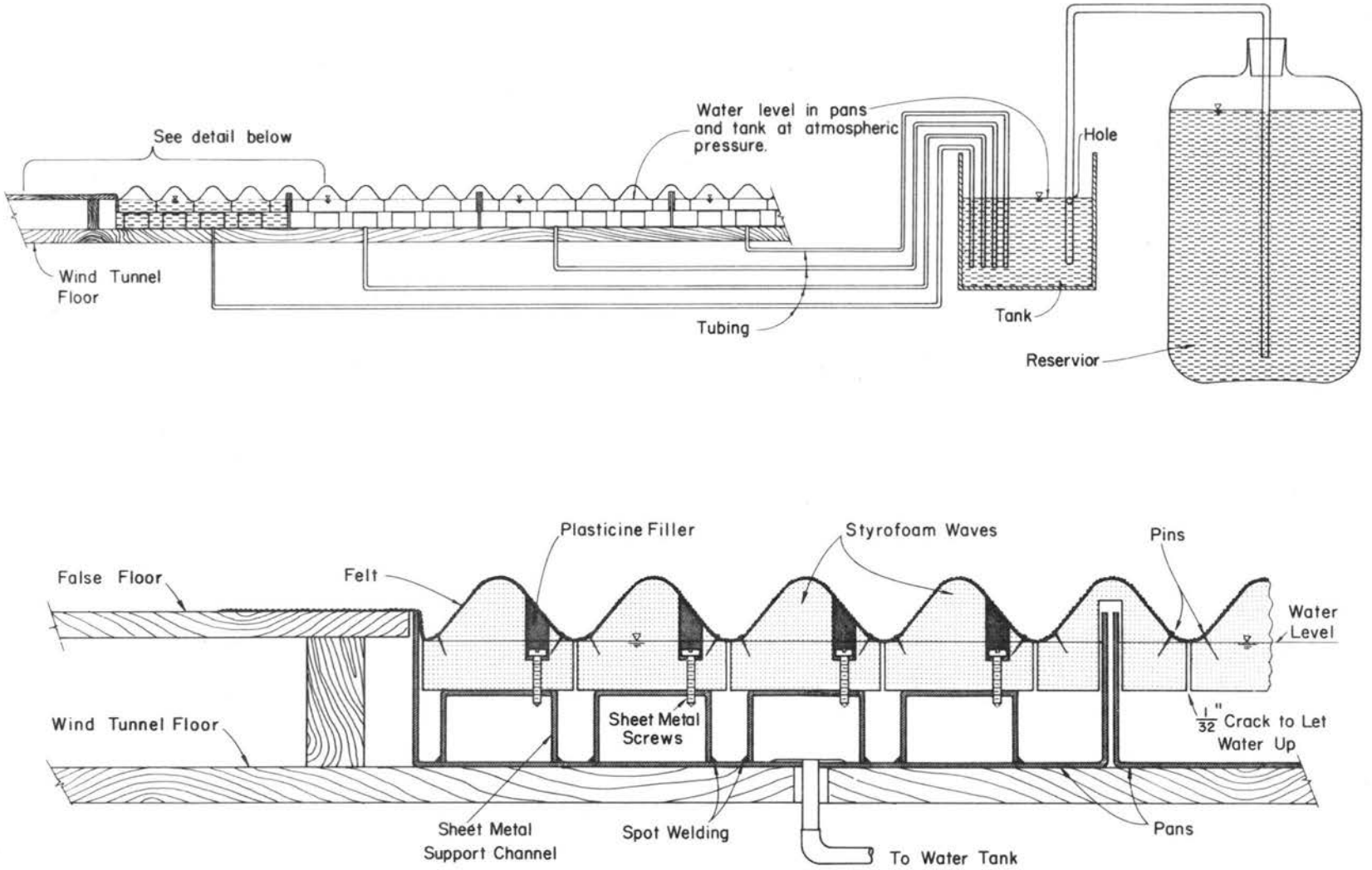

Fig. 4. Details of Figure 2 (schematic).

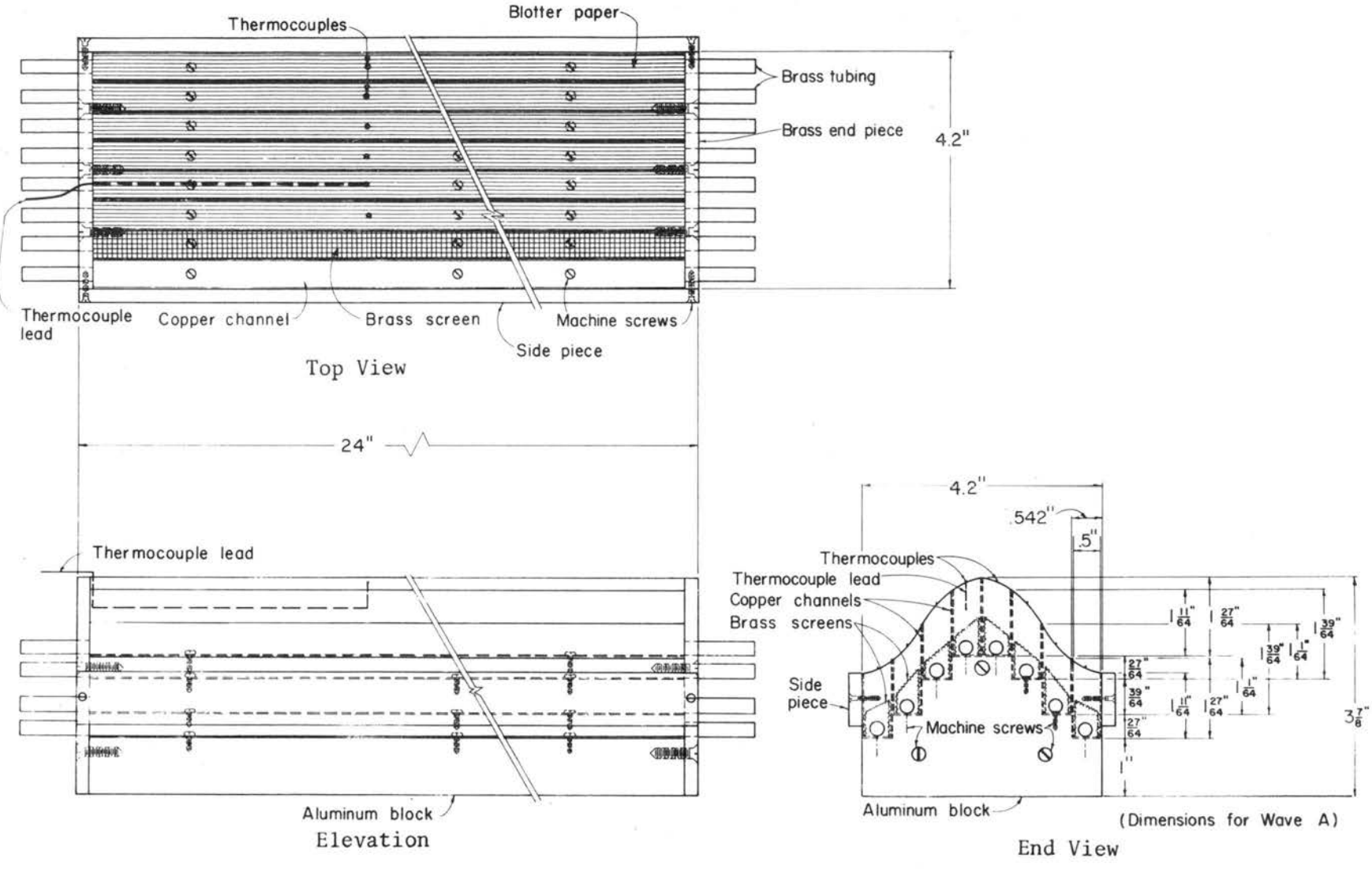

Fig. 5. Evaporation metering wave.

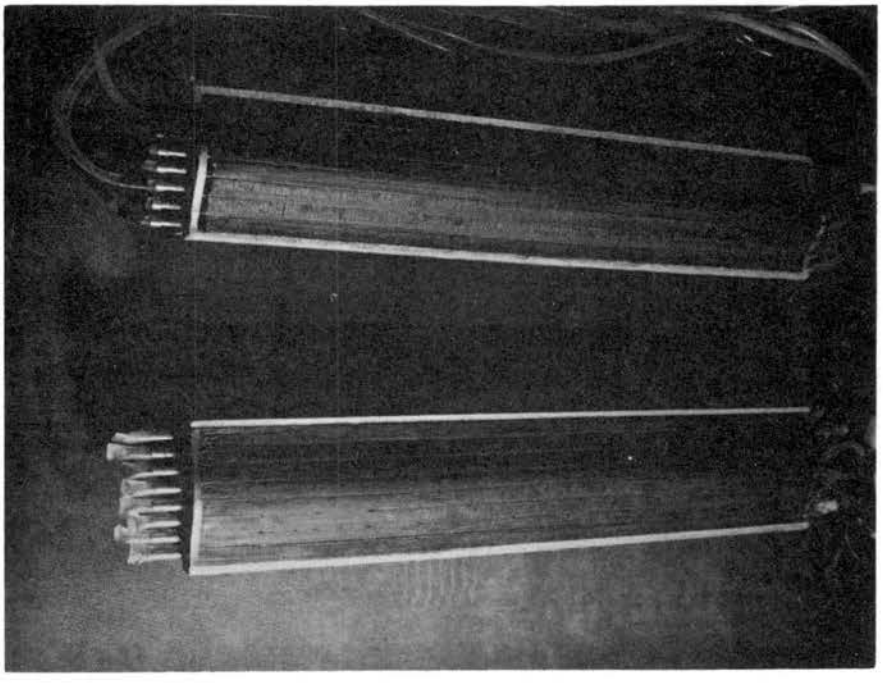

Fig. 6. Photograph of evaporation metering waves B and C.

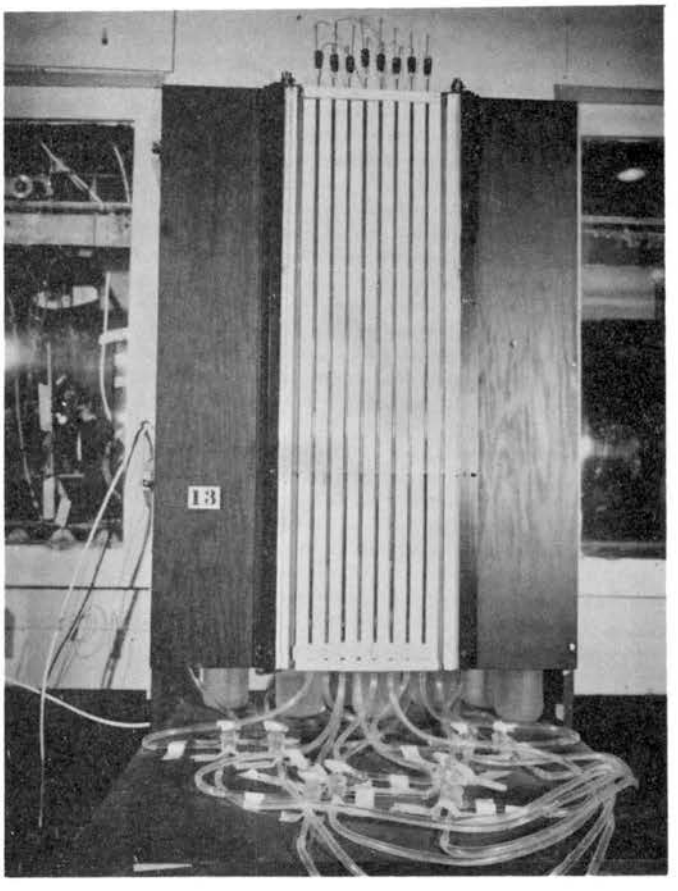

Fig. 7. Photograph of automatic feed and evaporation metering system.

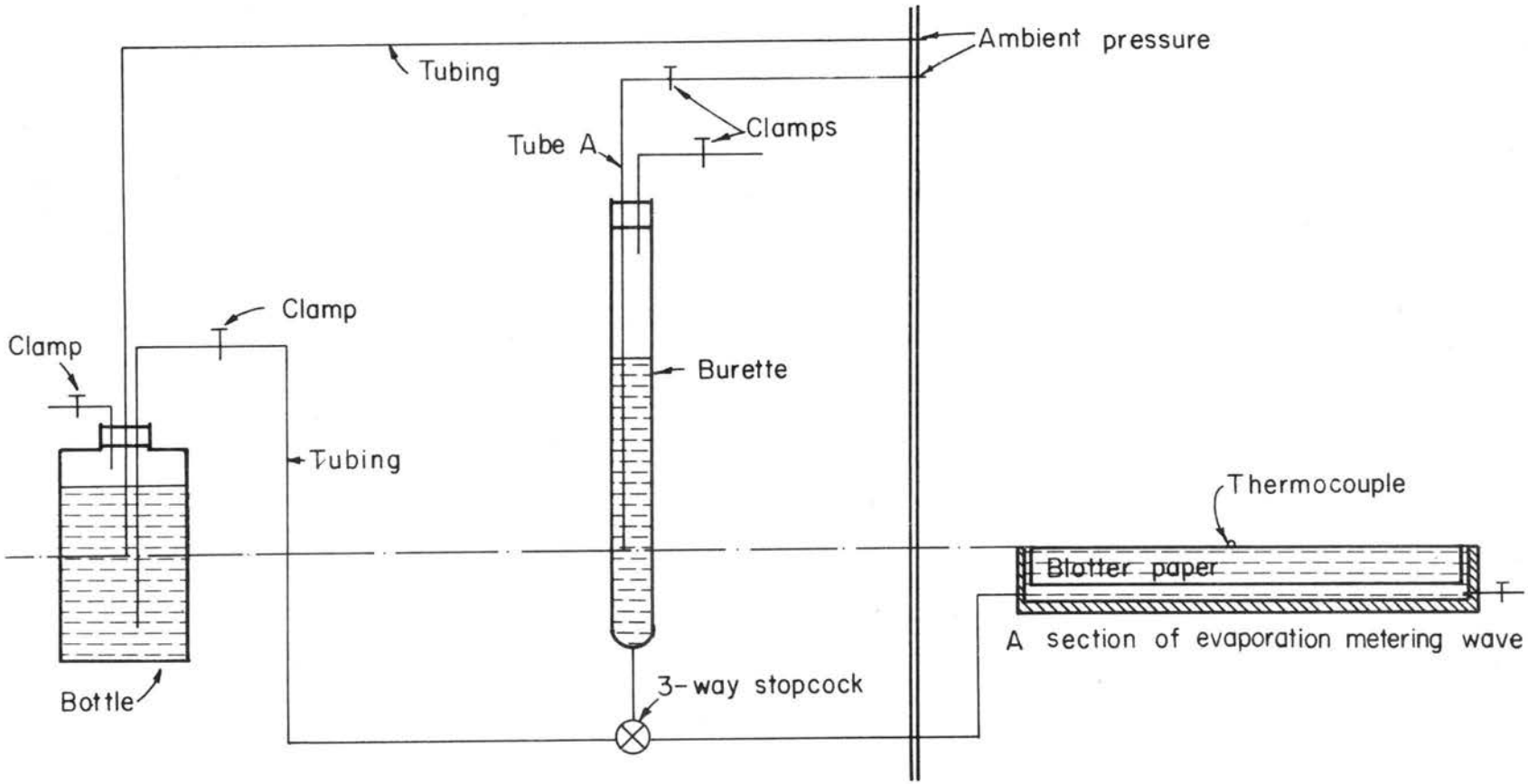

Fig. 8. Part of automatic feed and metering system (Typical for each wave section).

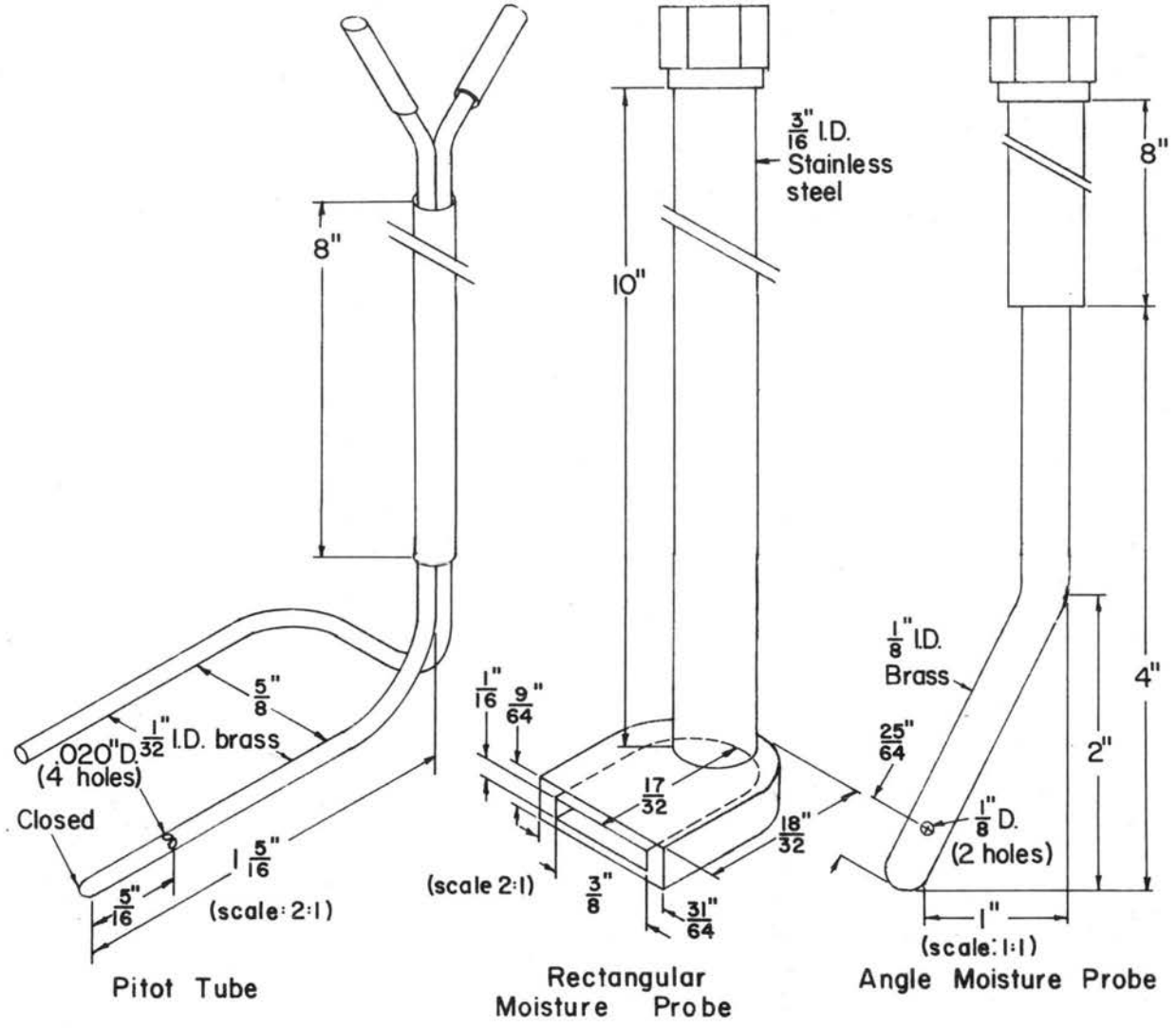
8"
5/8"
1/32" I.D. brass
.020" D.
(4 holes)
Closed
1 5/16"
5/16"
(scale: 2:1)
Pitot Tube
3/16" I.D.
Stainless
steel
10"
1/16"
9/64"
17/32
18/32"
(scale 2:1)
3/8"
31/64"
Rectangular
Moisture Probe
8"
1/8" I.D.
Brass
4"
25/64"
2"
1/8" D.
(2 holes)
1"
(scale: 1:1)
Angle Moisture Probe

Fig. 9. Probes

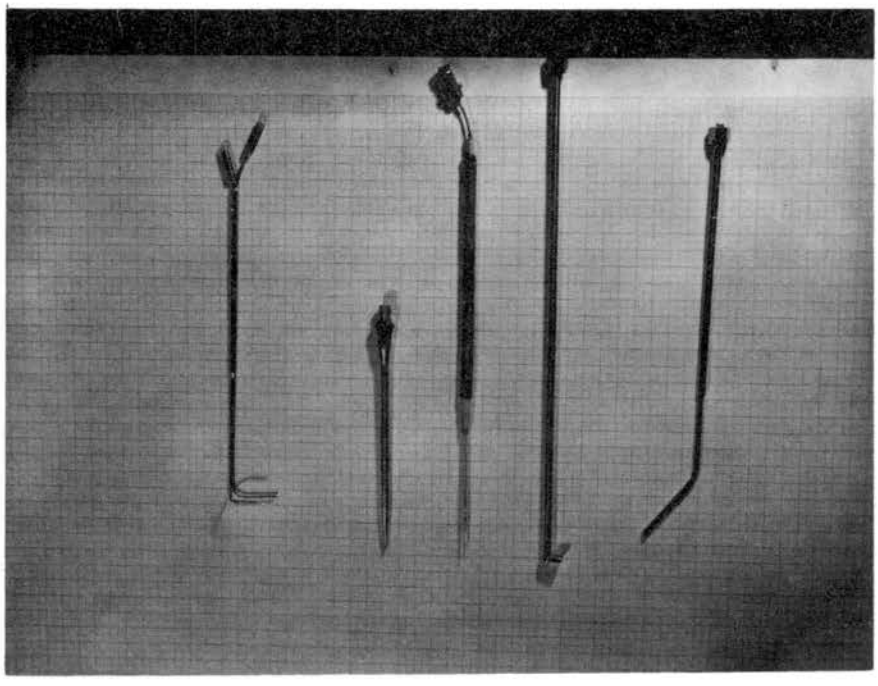

a b c d e

a: Pitot tube, b: Disa Type F13 Hot Wire Probe c: Disa Type 55A22 Hot Wire Probe, d: Moisture Probe, e: Reference Moisture Probe

Fig. 10. Photograph of Probes

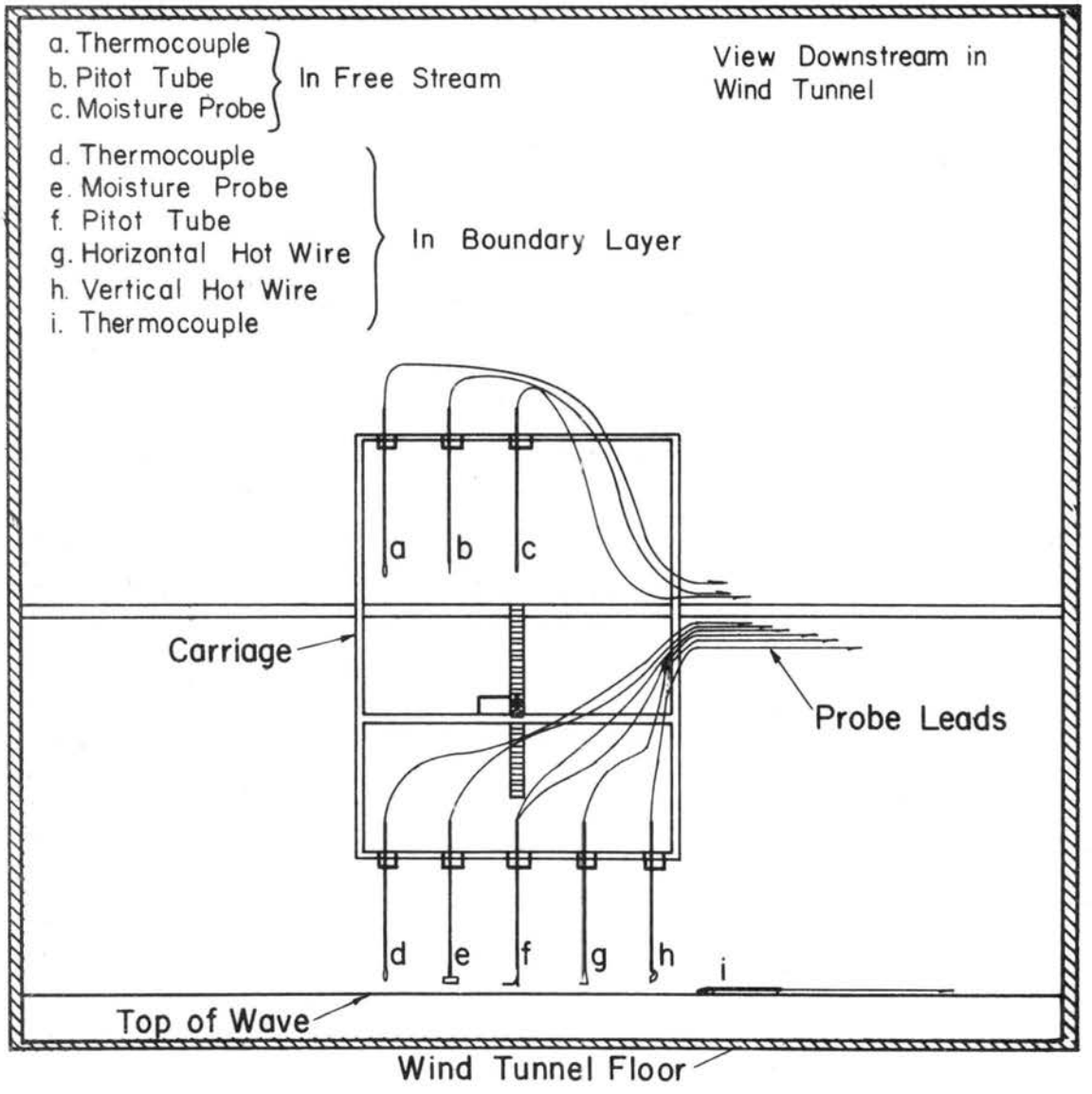

Fig. 11. Probe arrangement.

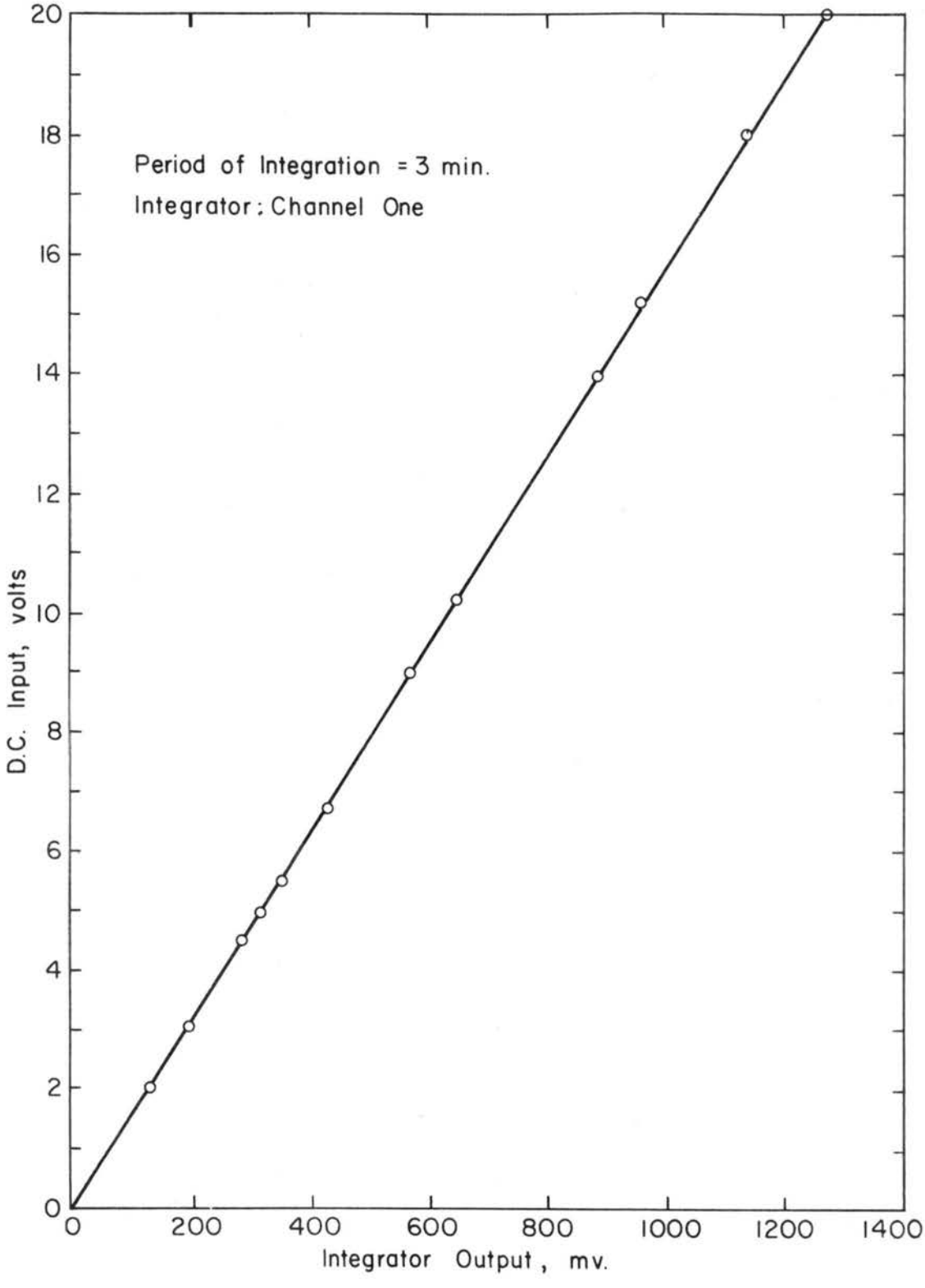

Fig. 12. Typical calibration of the integrator [built at Colorado State University, (41)].

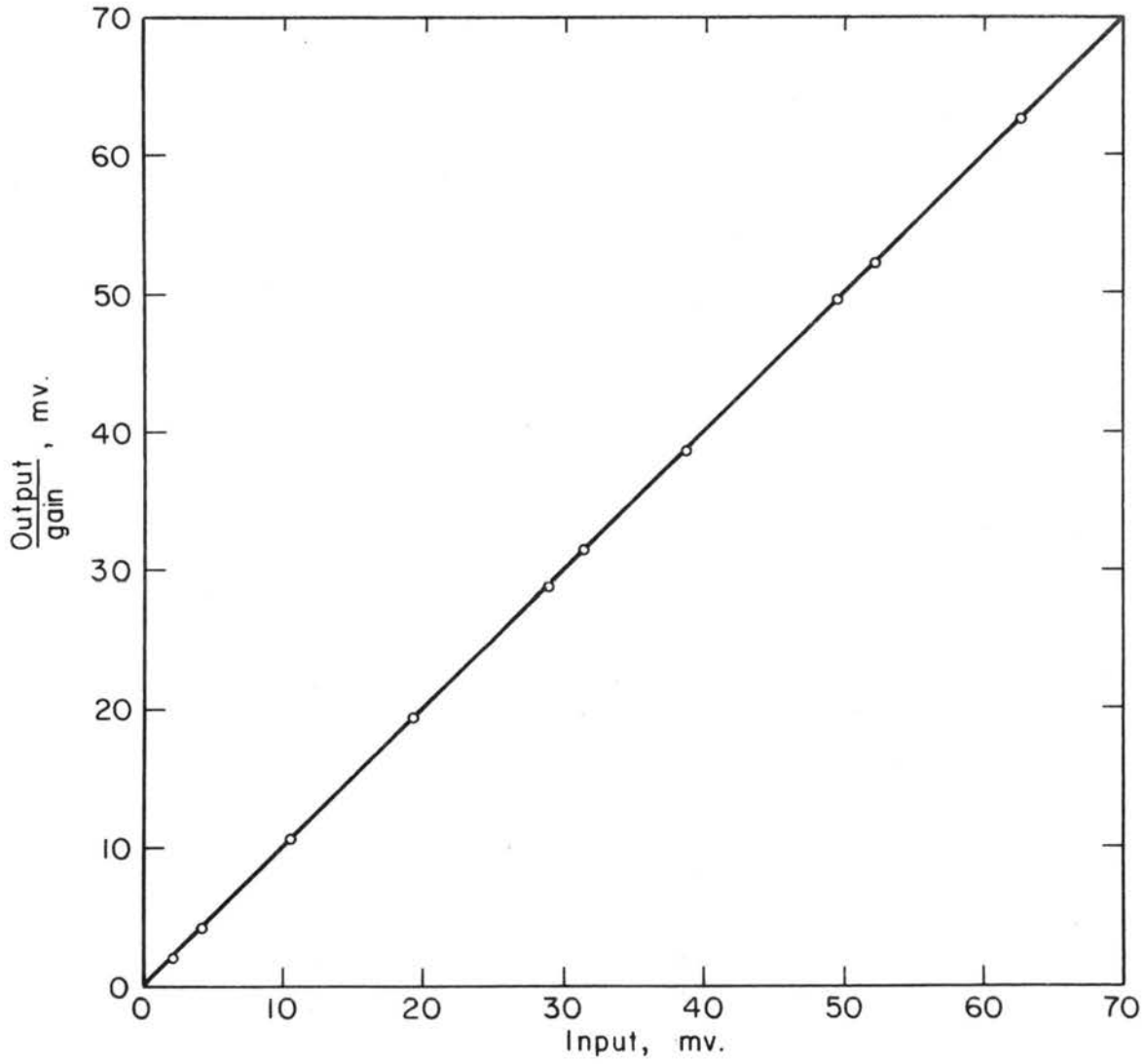

Fig. 13. Typical calibration of D.C. Amplifier (Dynamics Model 1250).

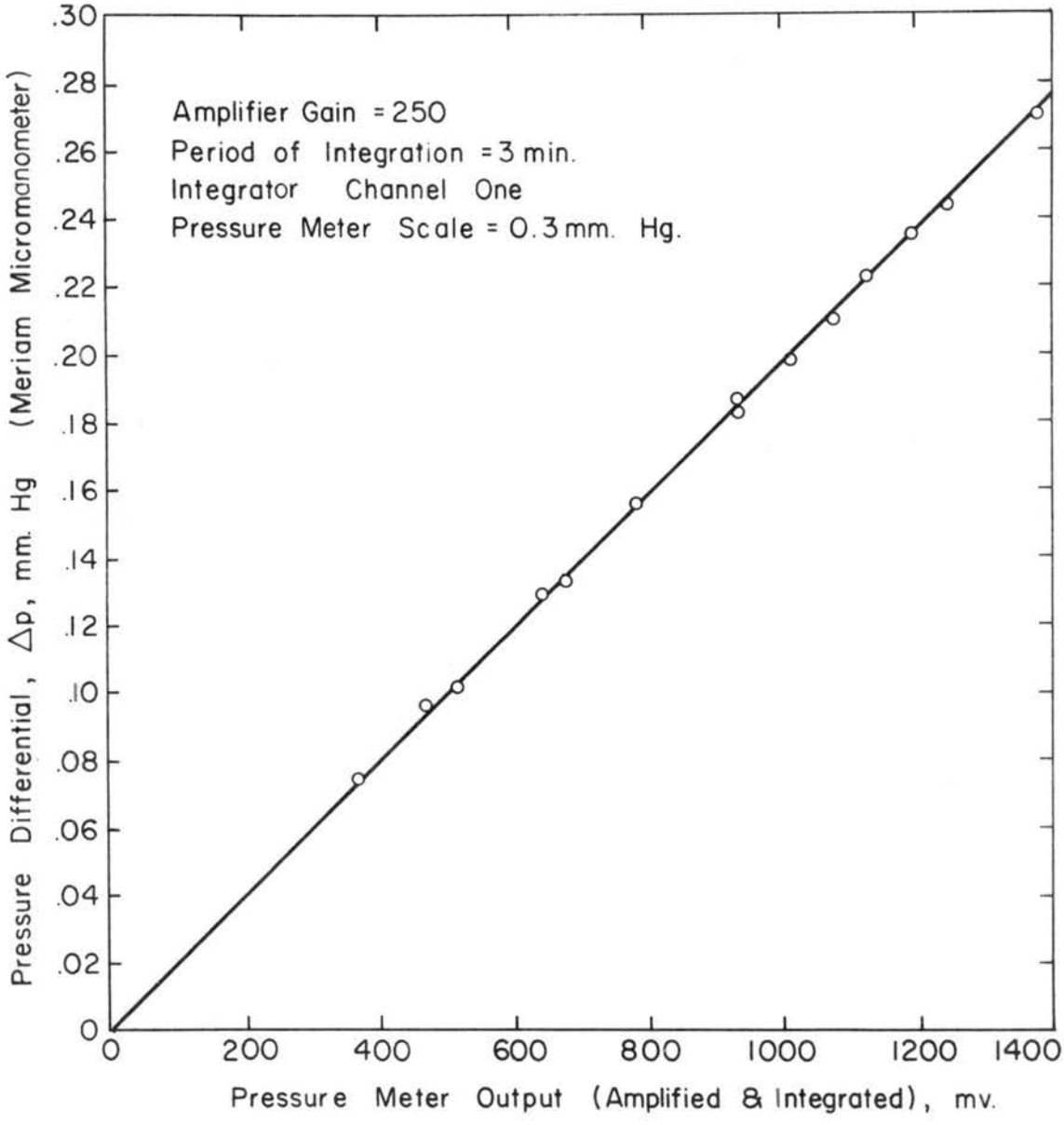

Fig. 14. Typical calibration of the pressure meter (M.K.S. Baratron TM type 77).

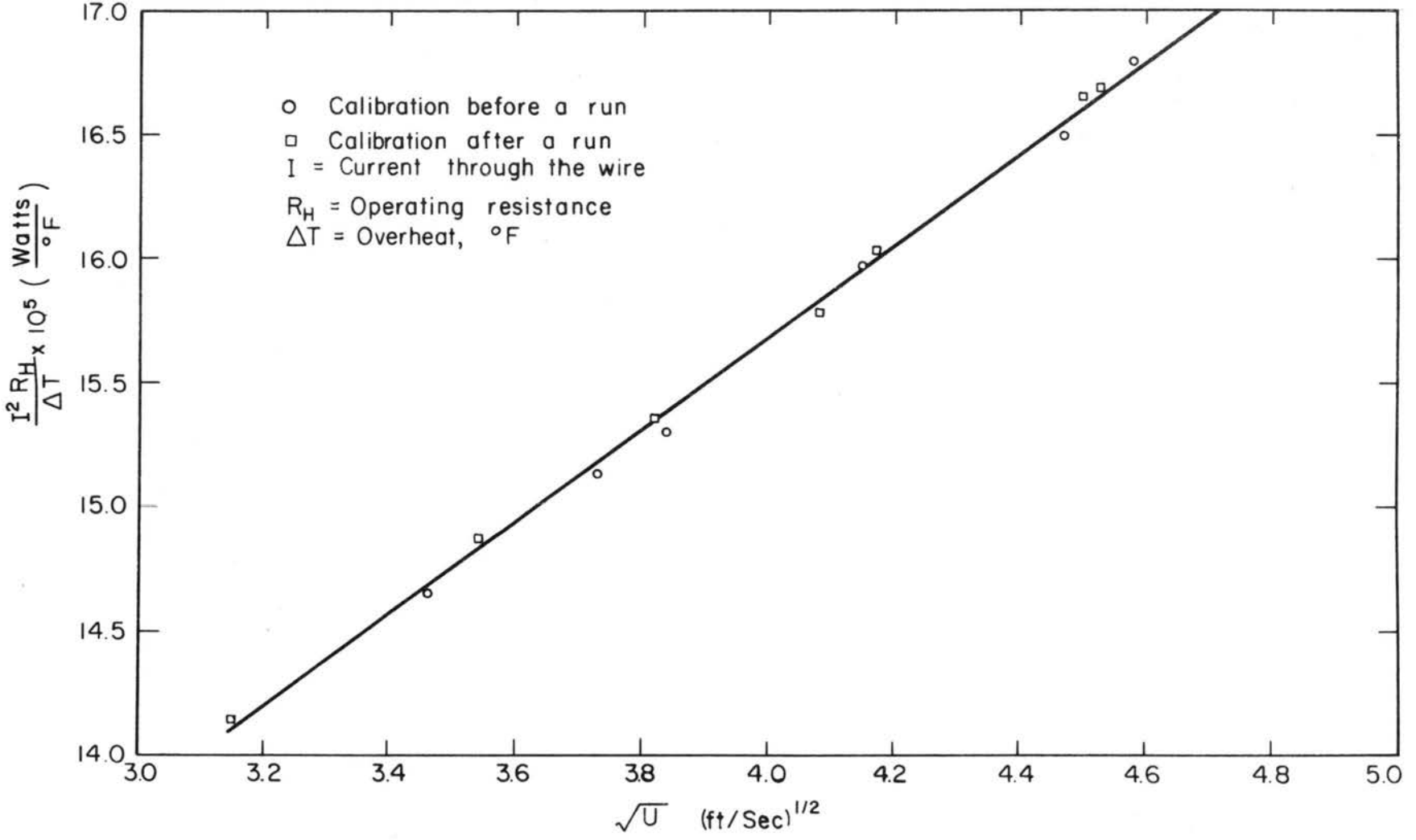

Fig. 15. Typical hot wire calibration.

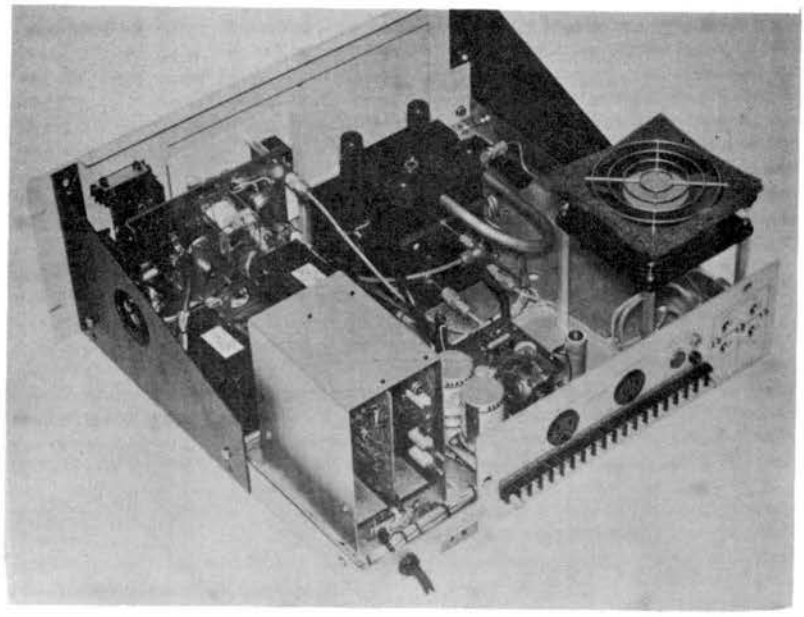

Fig. 16. Interior view of the dew point hygrometer (Cambridge Systems Model 992).

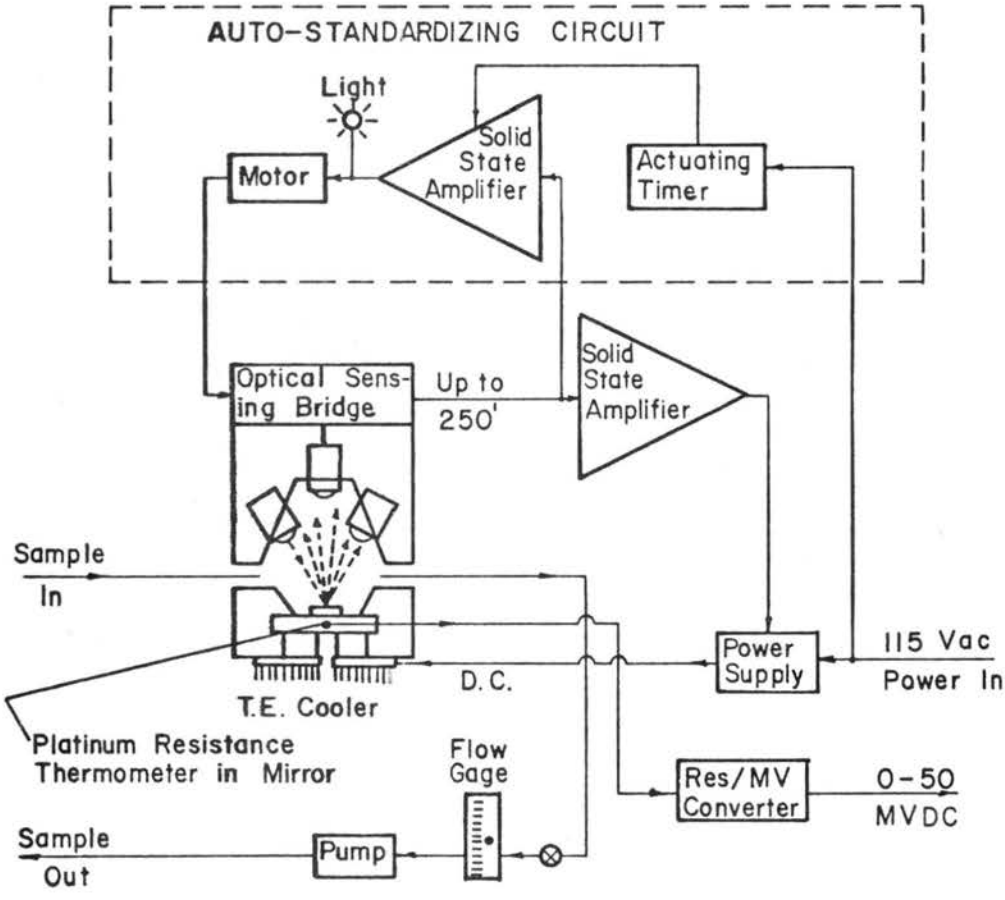

Fig. 17. Simplified block diagram of the dew point hygrometer (Cambridge Systems Model 992).

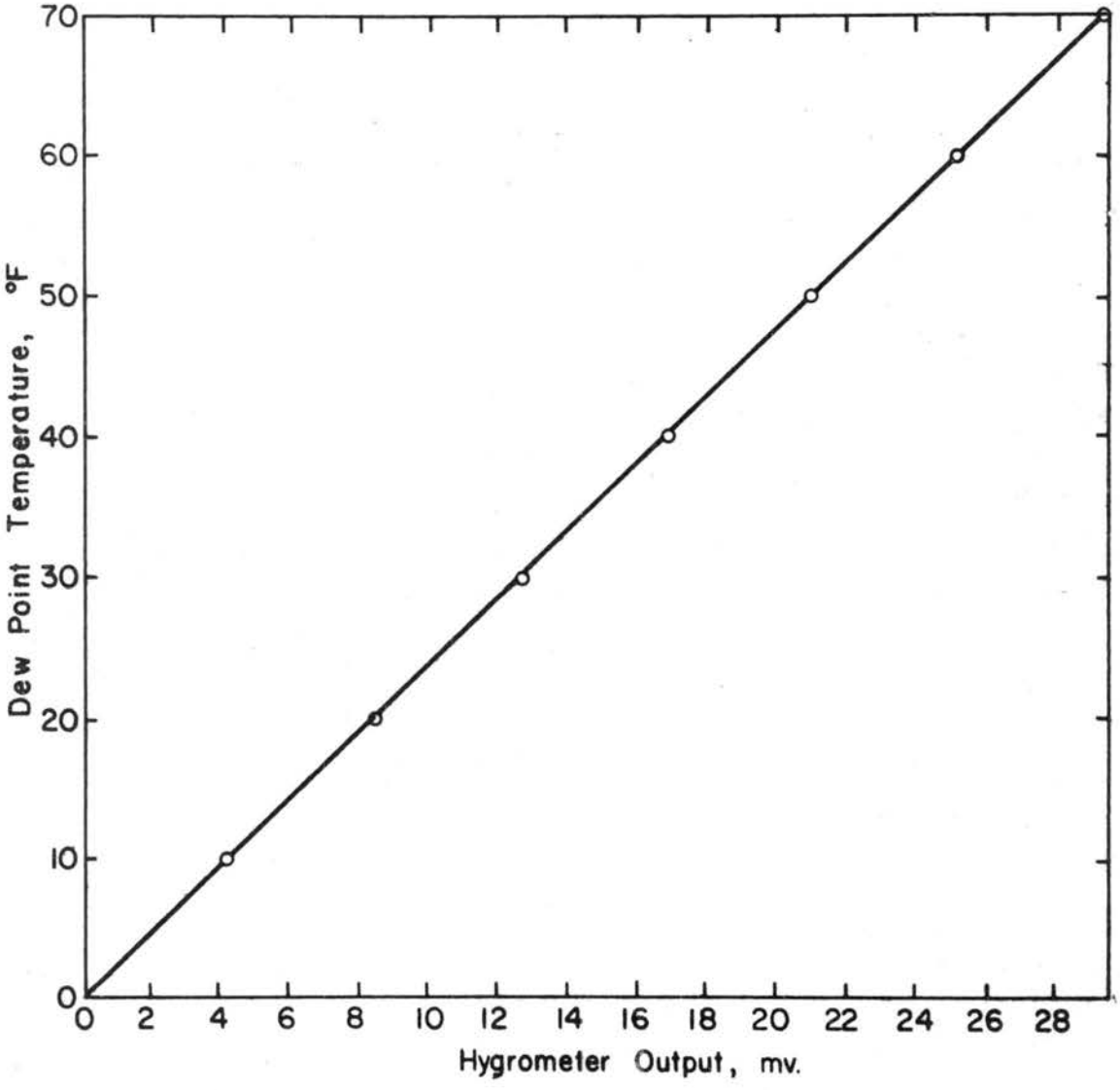

Fig. 18. Calibration of the dew point hygrometer (Cambridge Systems Model 992).

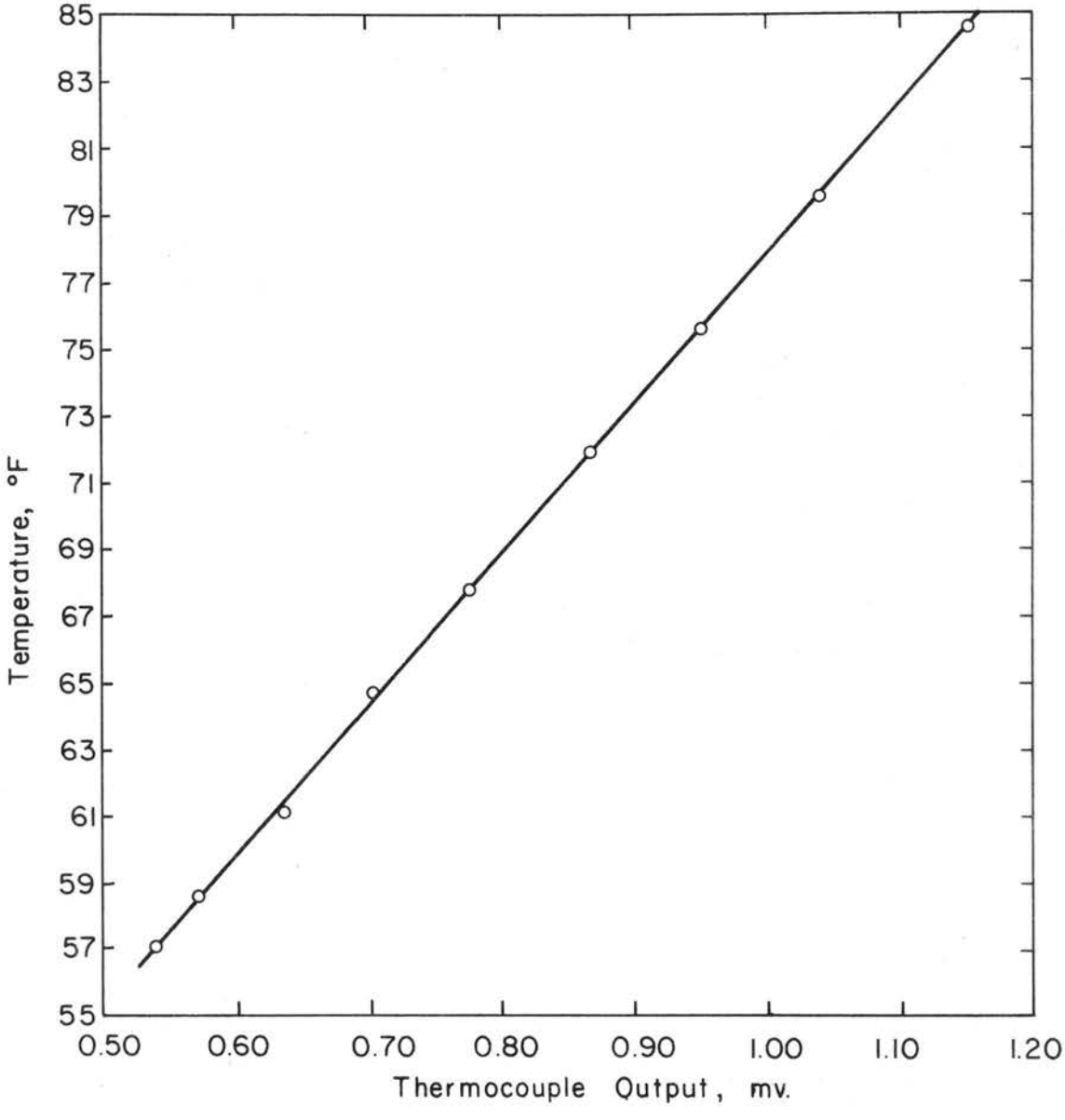

Fig. 19. Typical calibration of a copper constantan thermocouple.

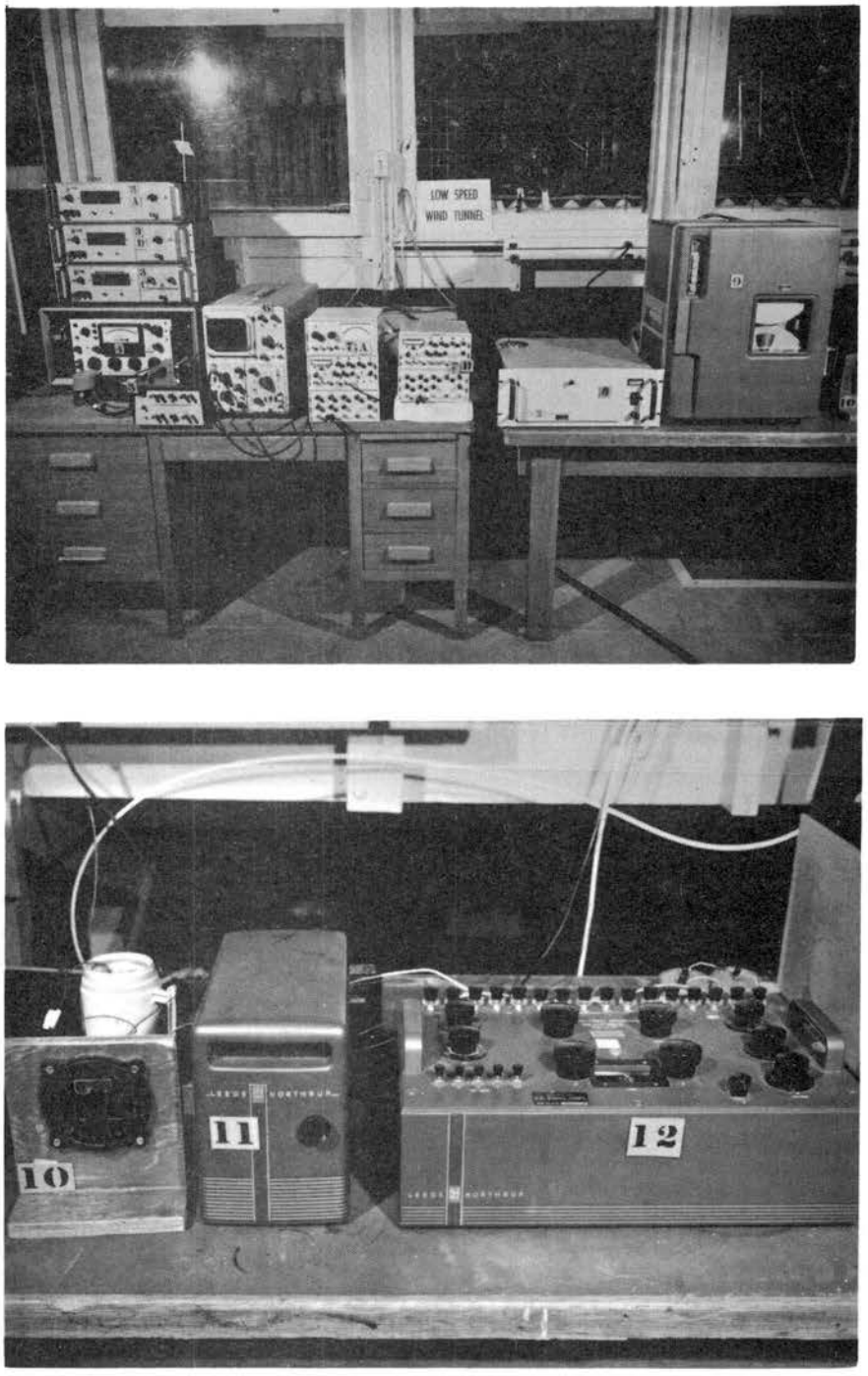

3A,B and C	Digital voltmeters	9	tape recorder
4	pressure meter	10	thermocouple switch
5	integrator	11	galvanometer
6	oscilloscope	12	potentiometer
7 A and B	hot wire anemometers		
8	dew point hygrometer		

Fig. 20. Instrumentation display.

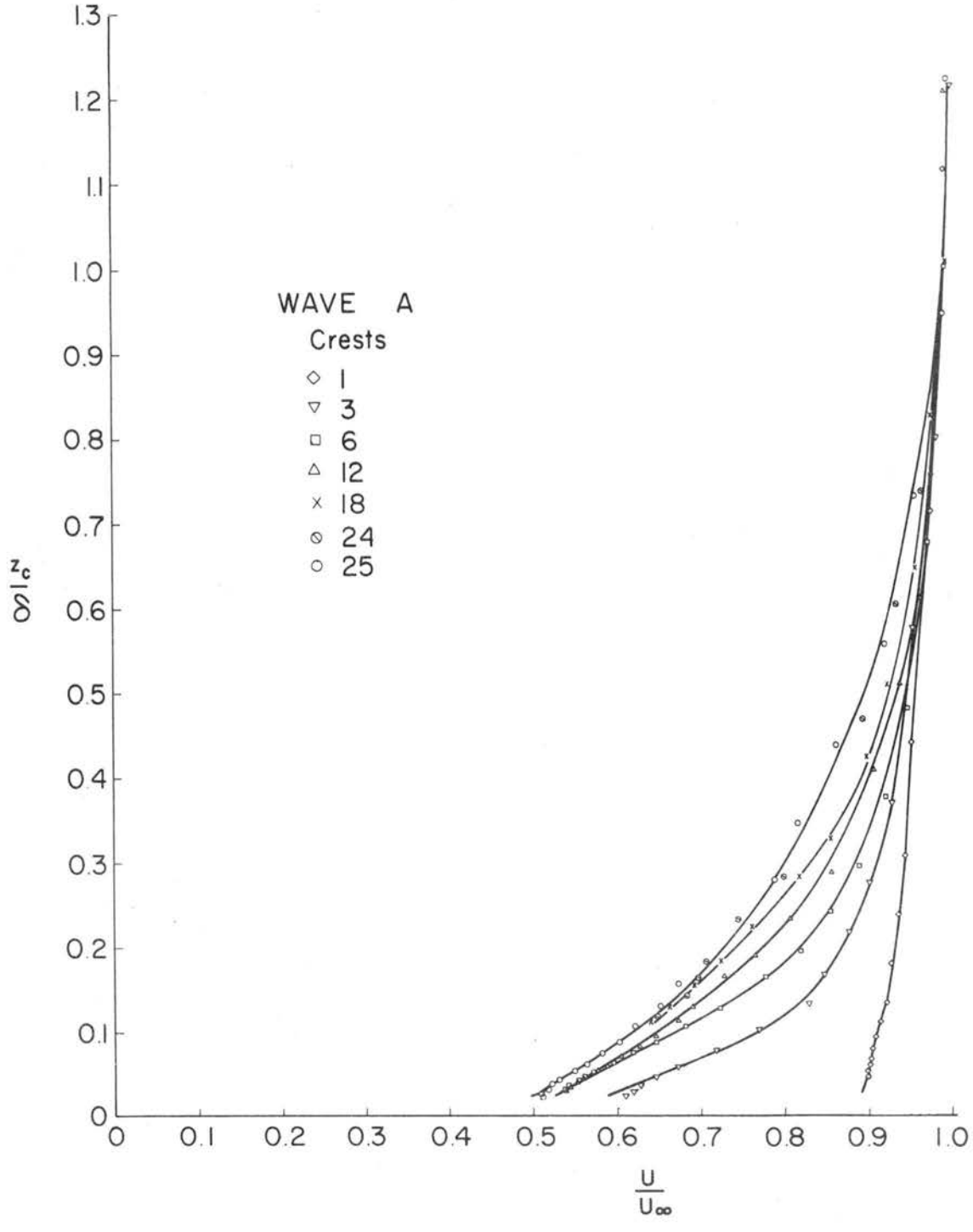

Fig. 21. Mean velocity profiles, Wave A.

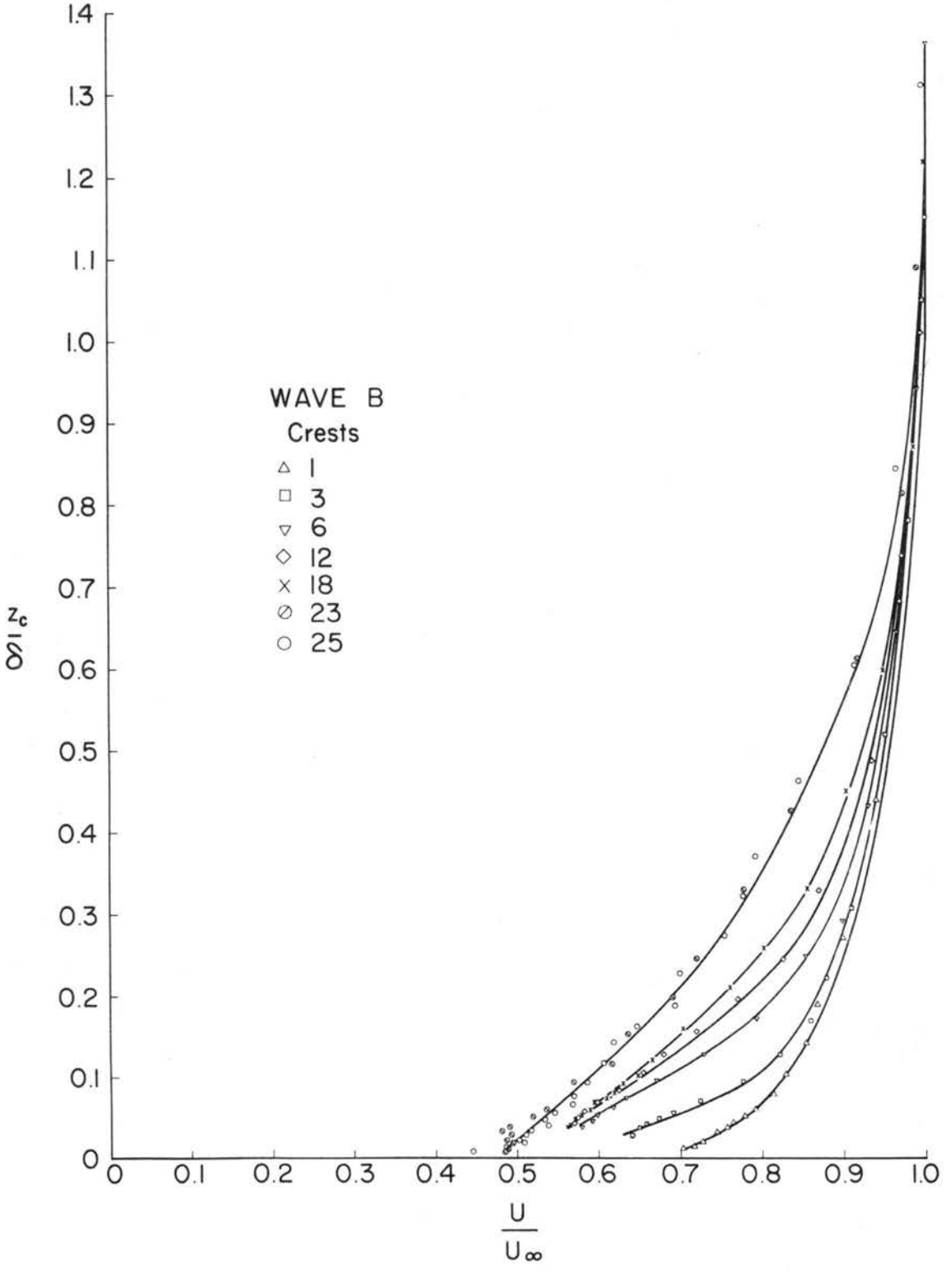

Fig. 22. Mean velocity profiles, Wave B.

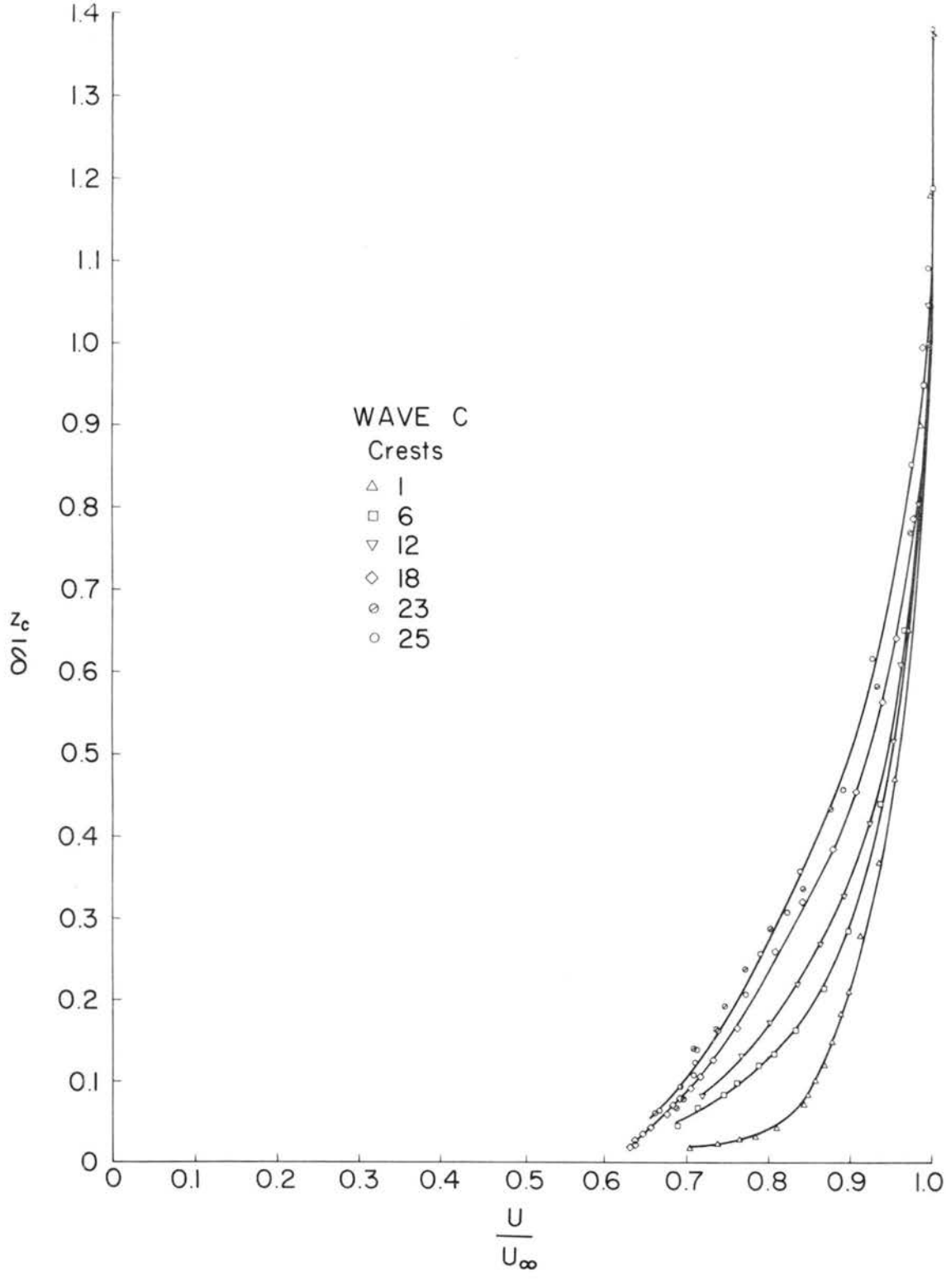

Fig. 23. Mean velocity profiles.

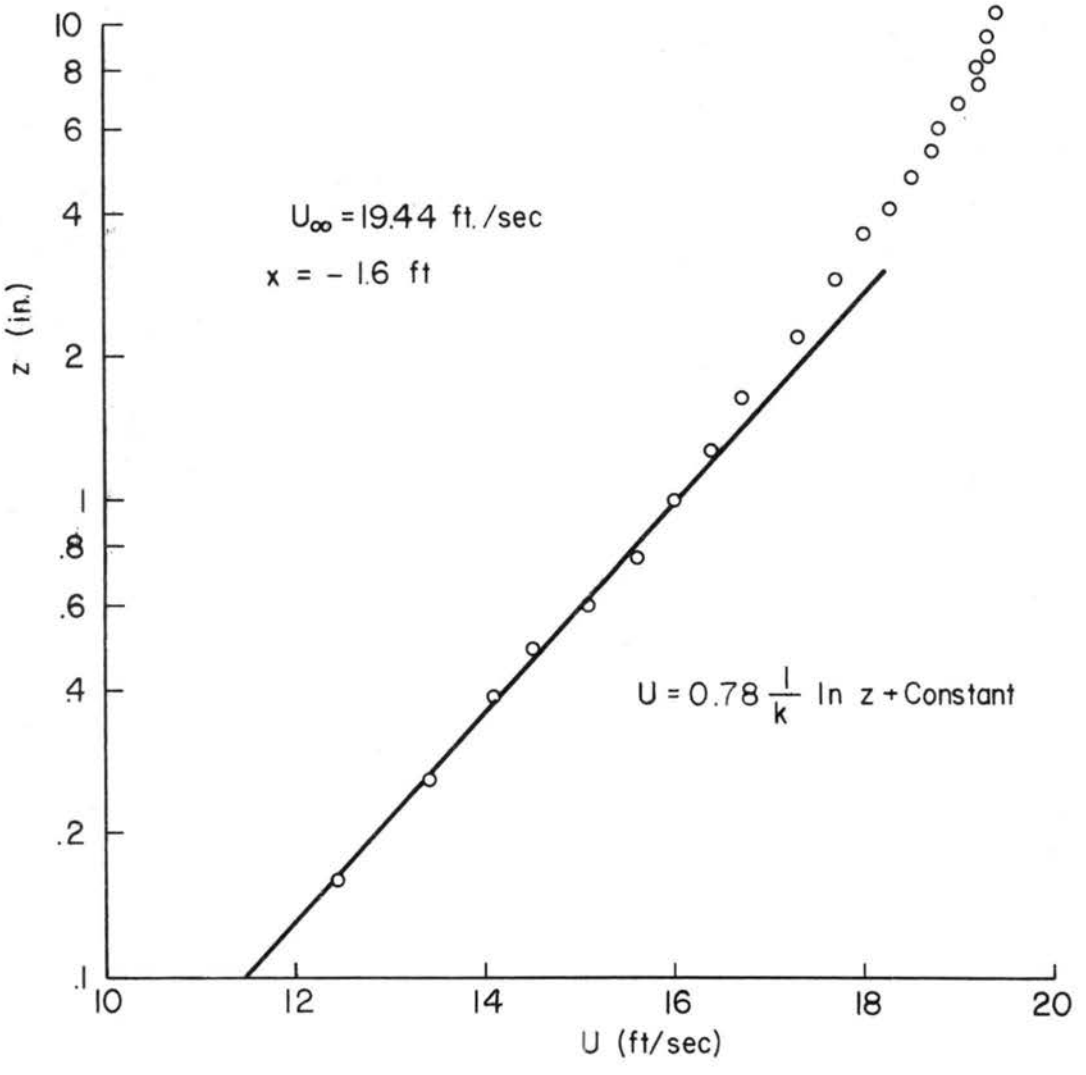

Fig. 24. Mean velocity profile at station x = - 1.6 ft.

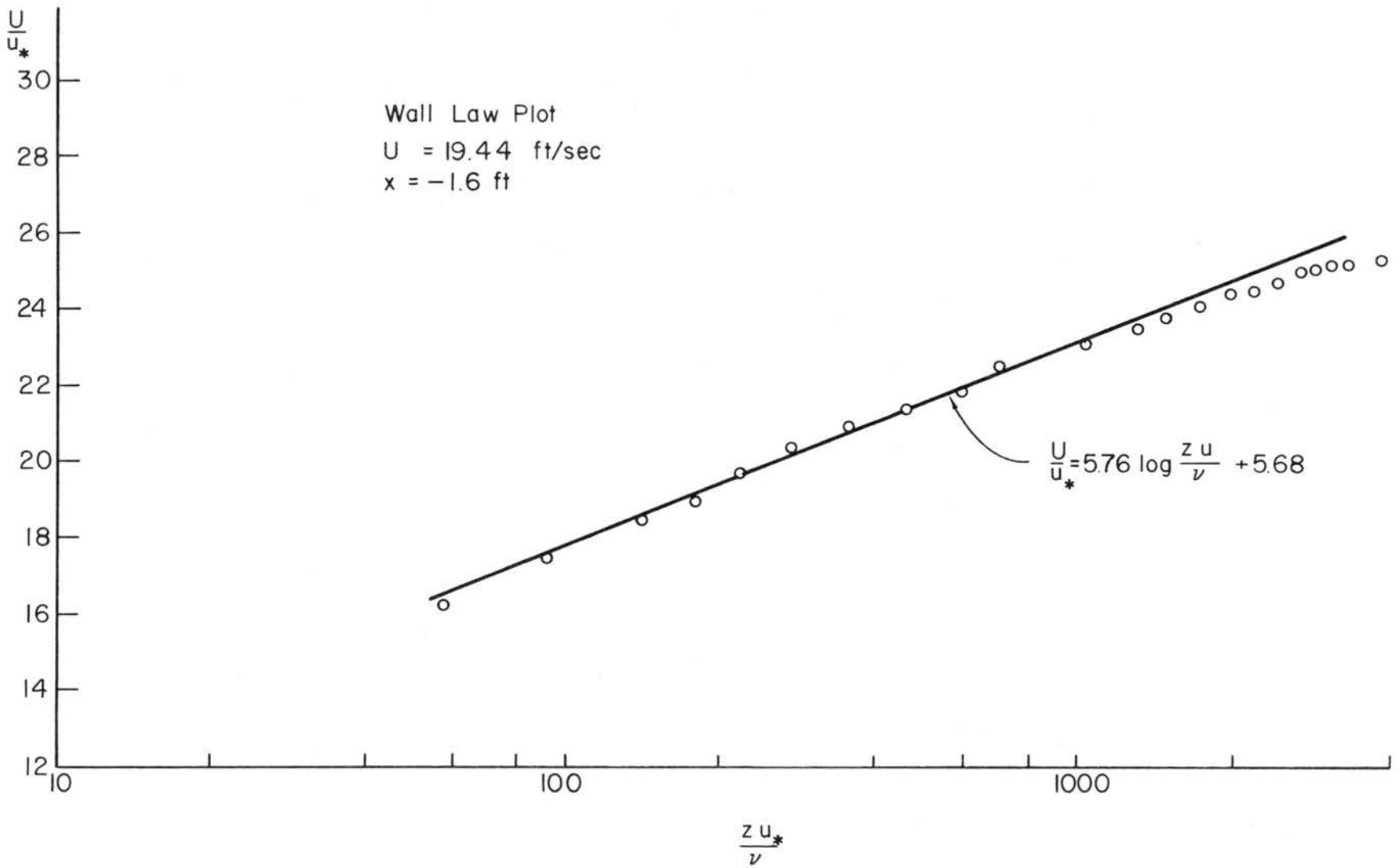

Fig. 25. Wall law plot for mean velocity profile at station x = - 1.6 ft.

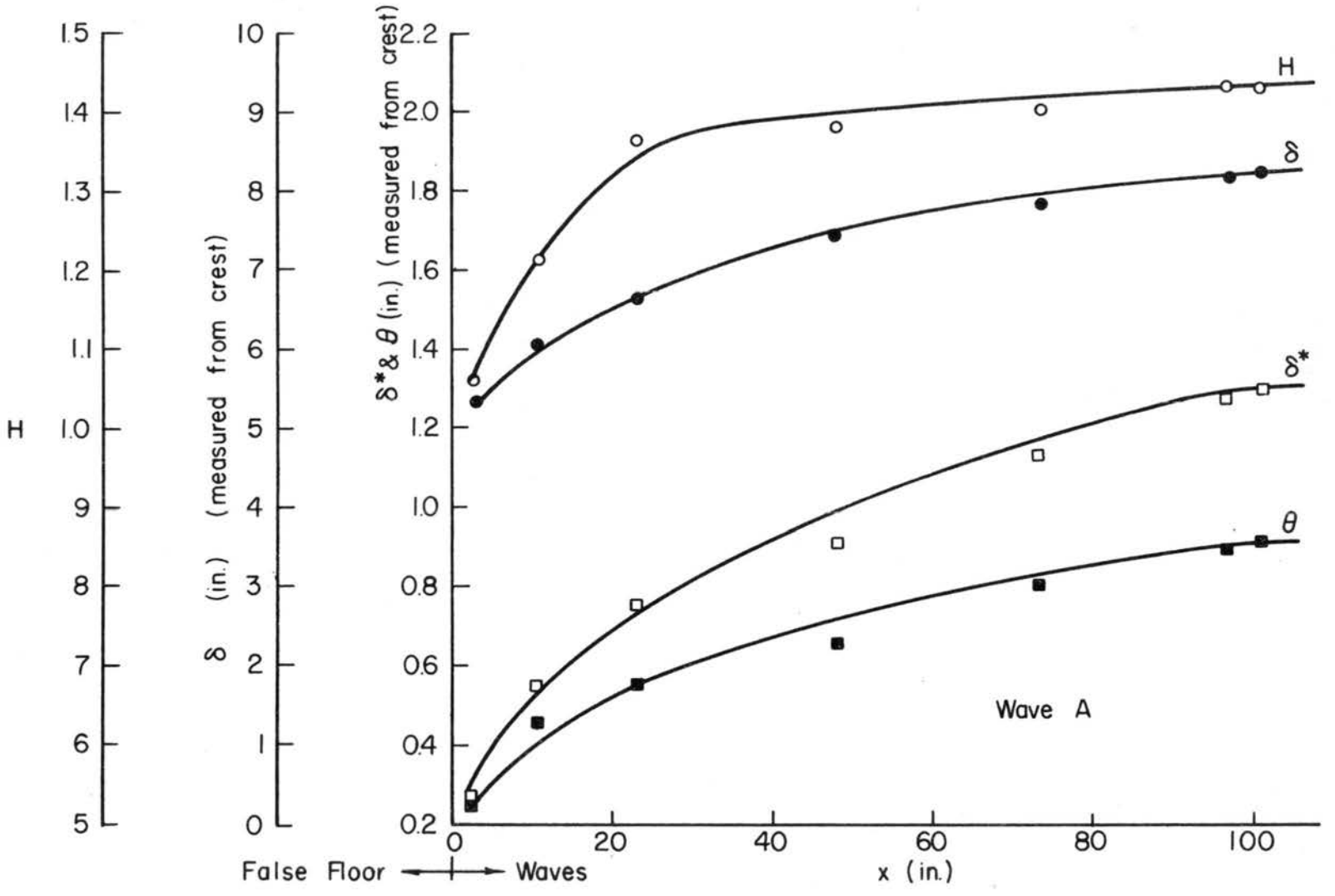

Fig. 26. Plots of δ, δ^*, Θ and H, Wave A.

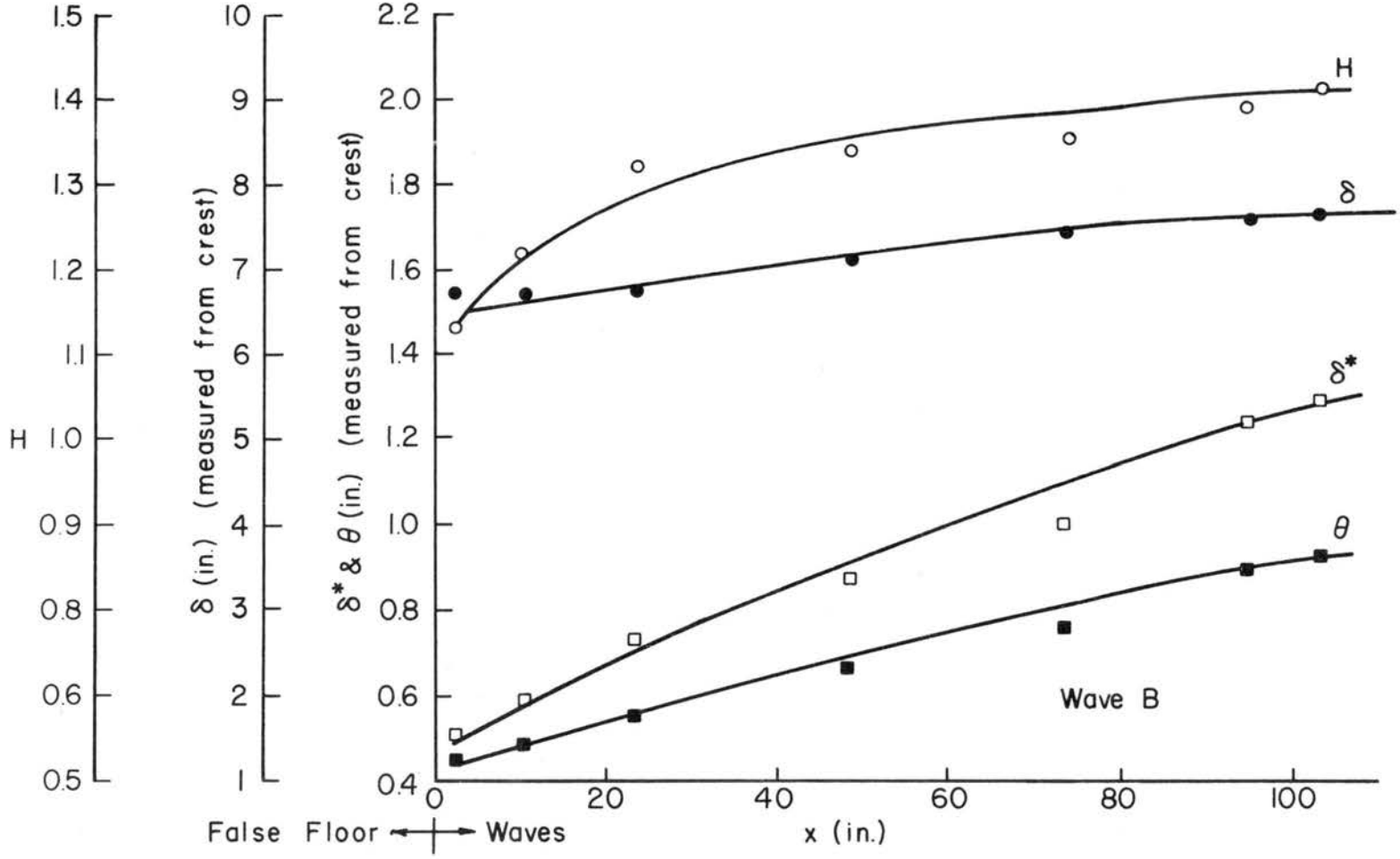

Fig. 27. Plots of δ, δ^*, Θ and H, Wave B.

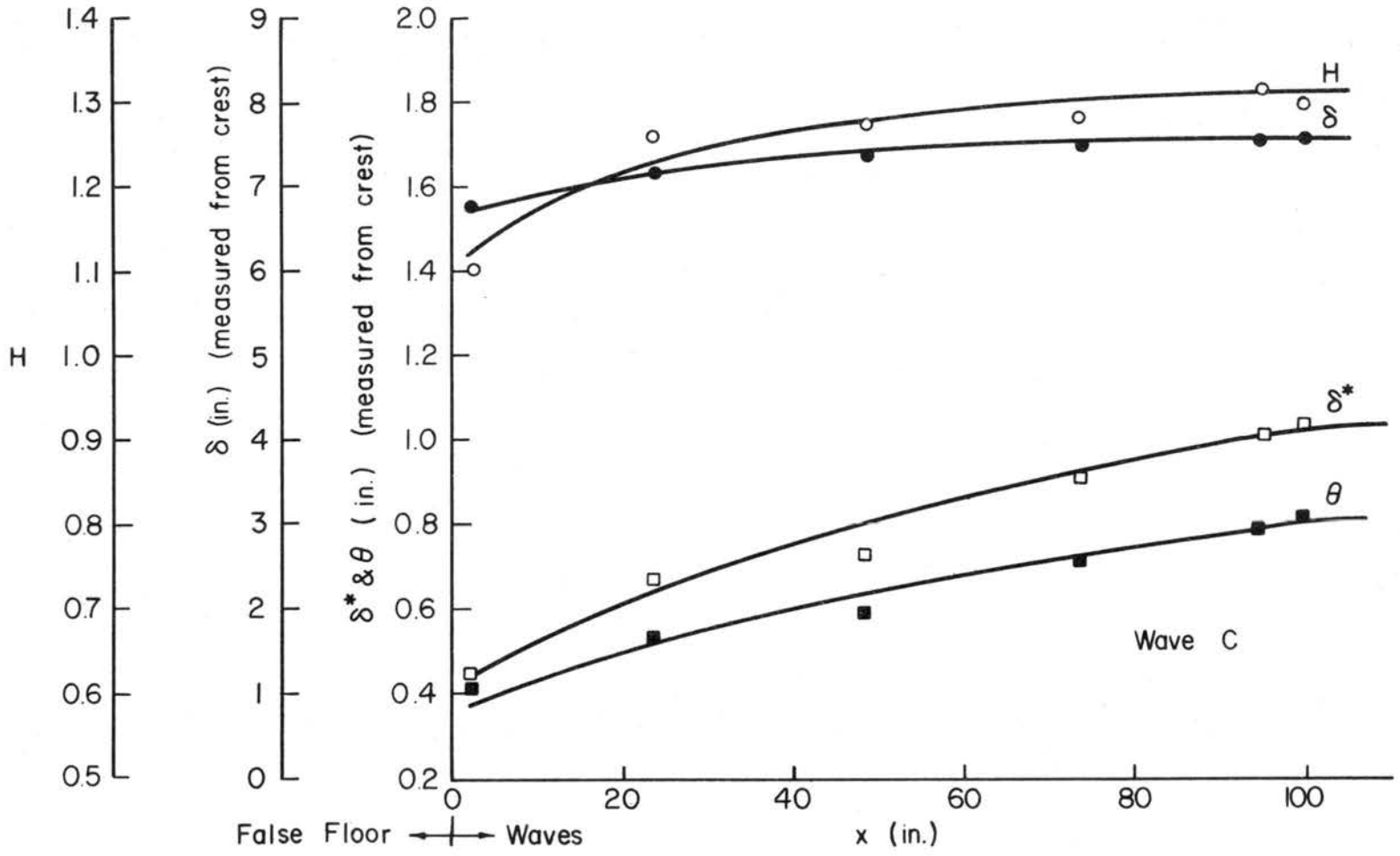

Fig. 28. Plots of δ, δ^*, Θ and H, Wave C.

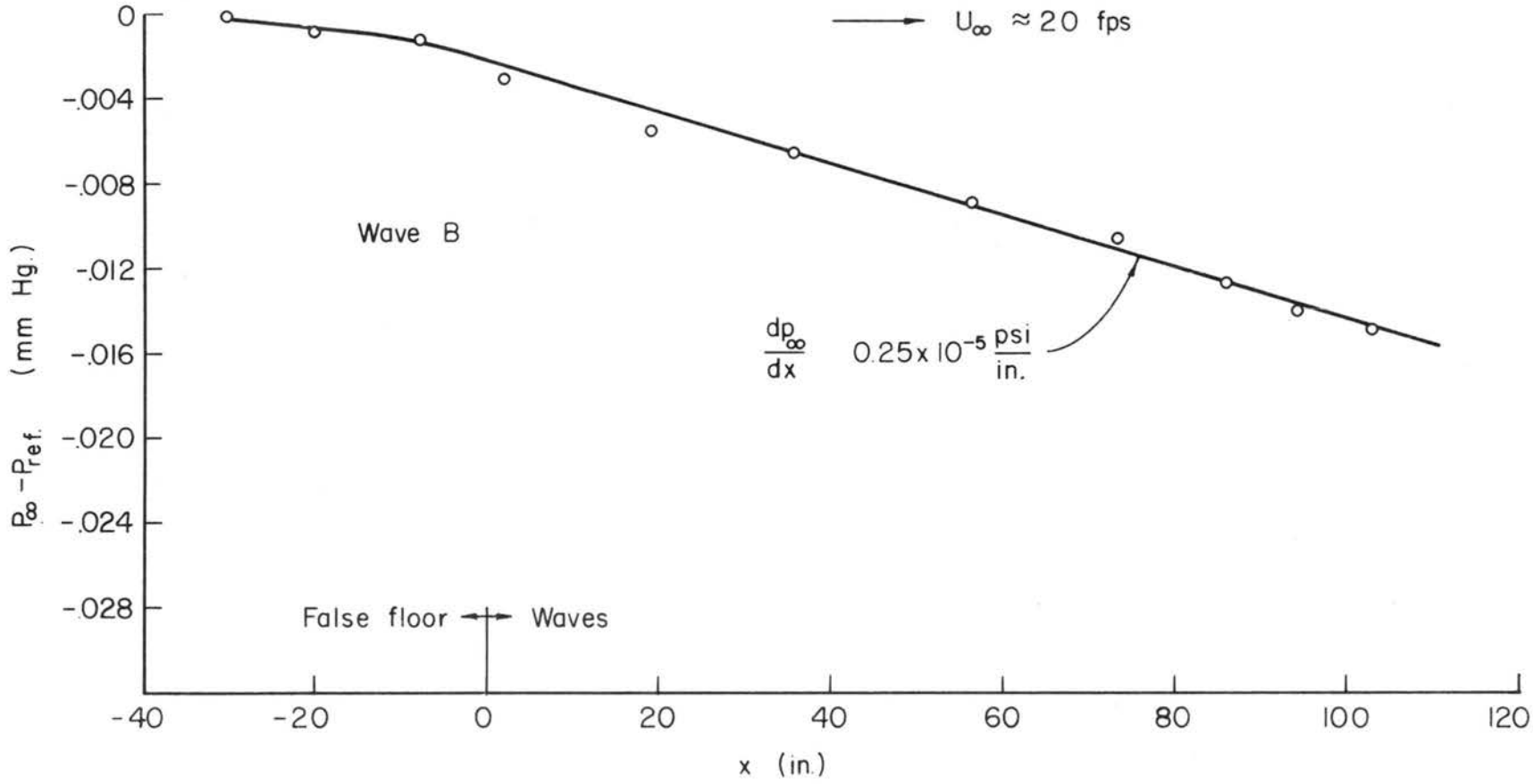

Fig. 29. Free stream static pressure distribution (Typical case).

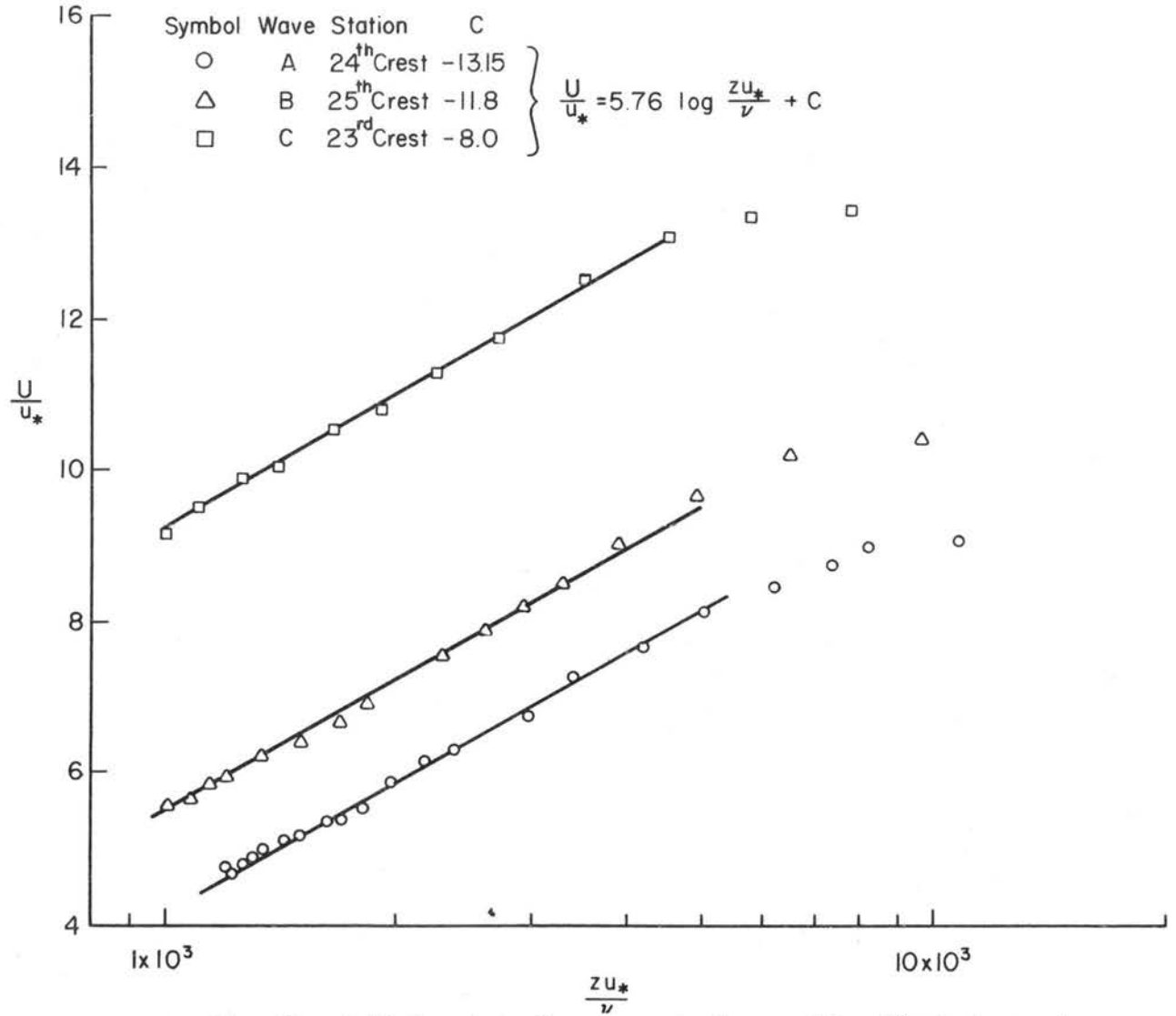

Fig. 30. Wall law plots for mean velocity profiles (Typical cases).

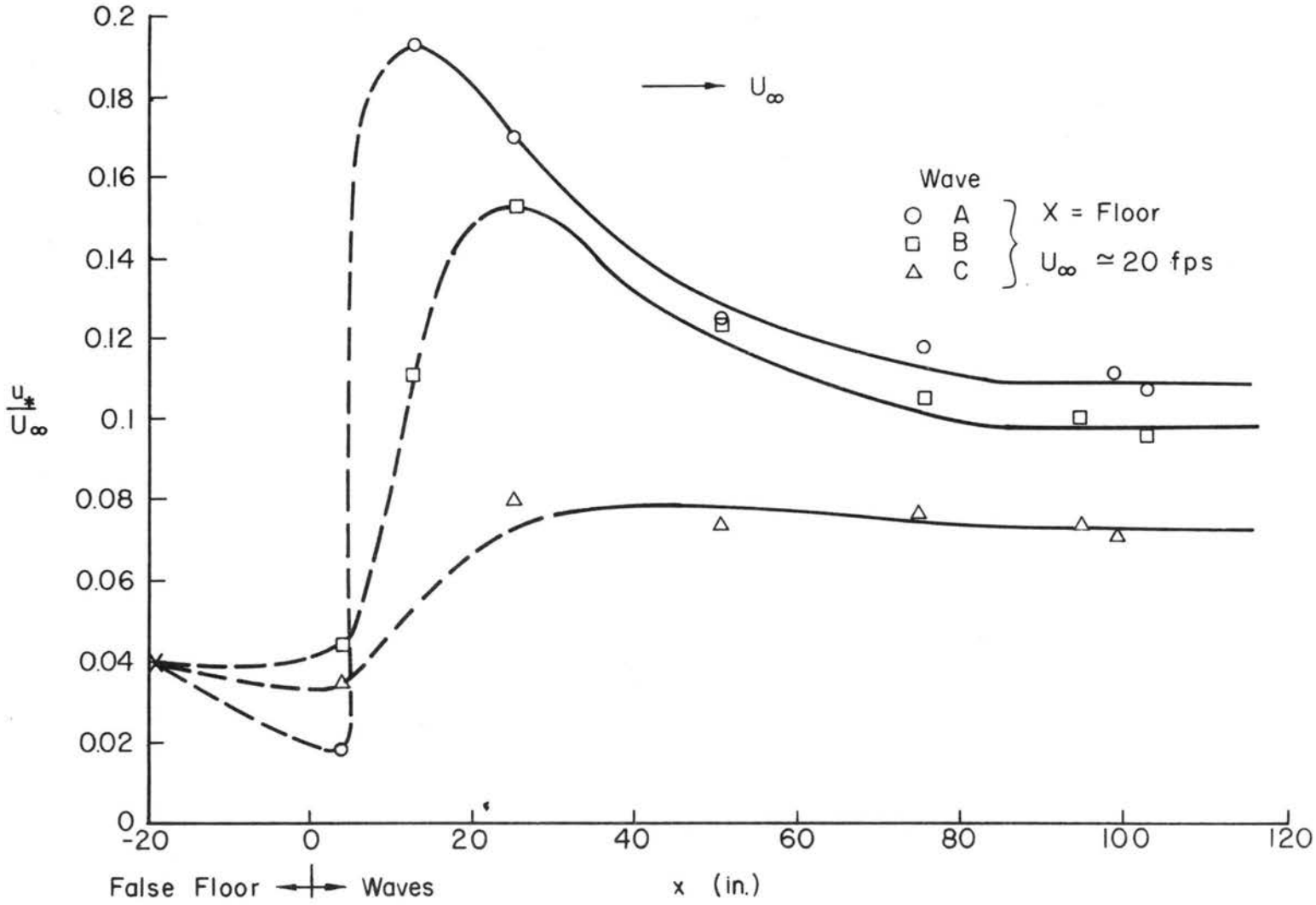

Fig. 31. Variation of friction velocity u_* with fetch.

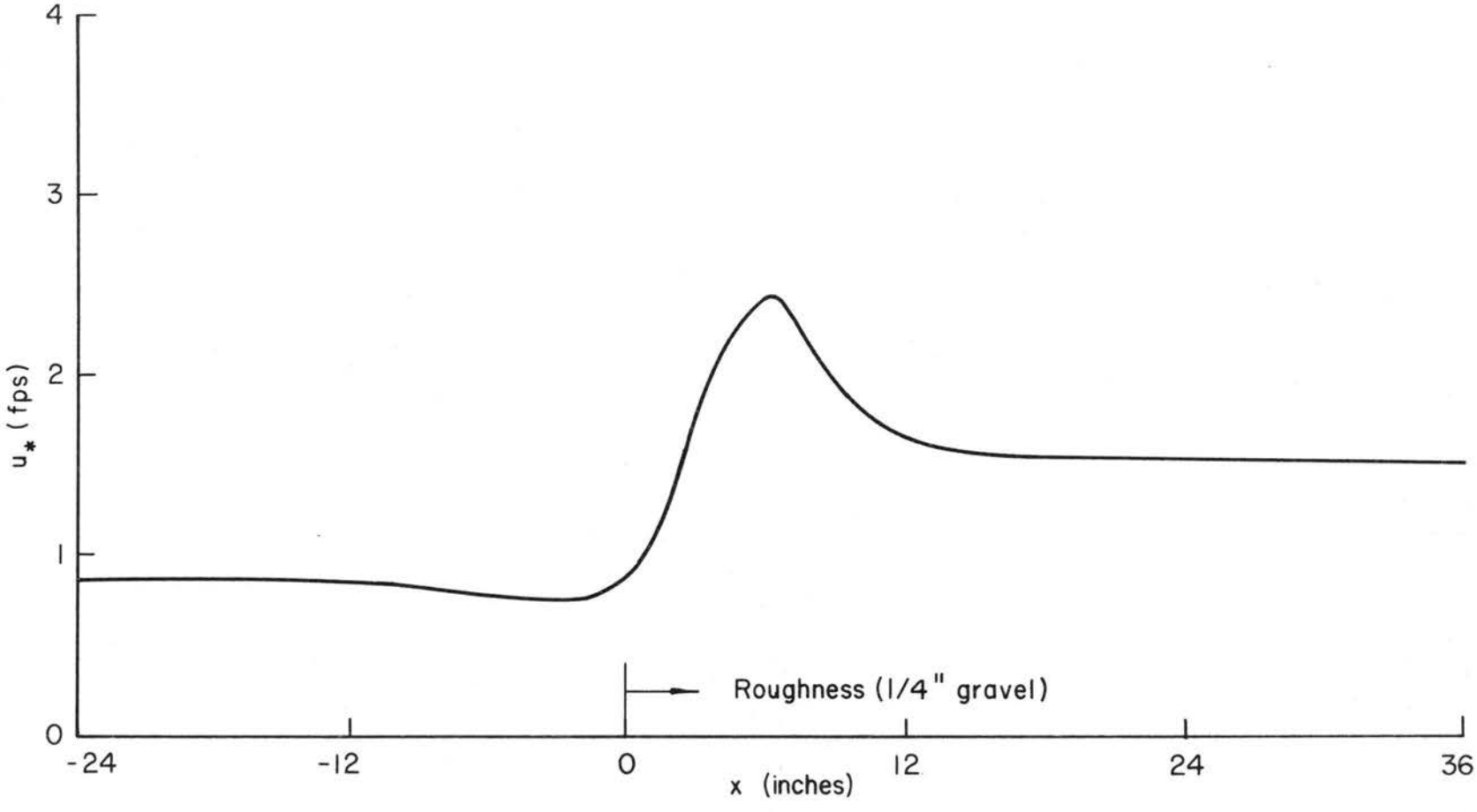

Fig. 32. Variation of friction velocity with fetch [Yeh (89) - Fig. 19].

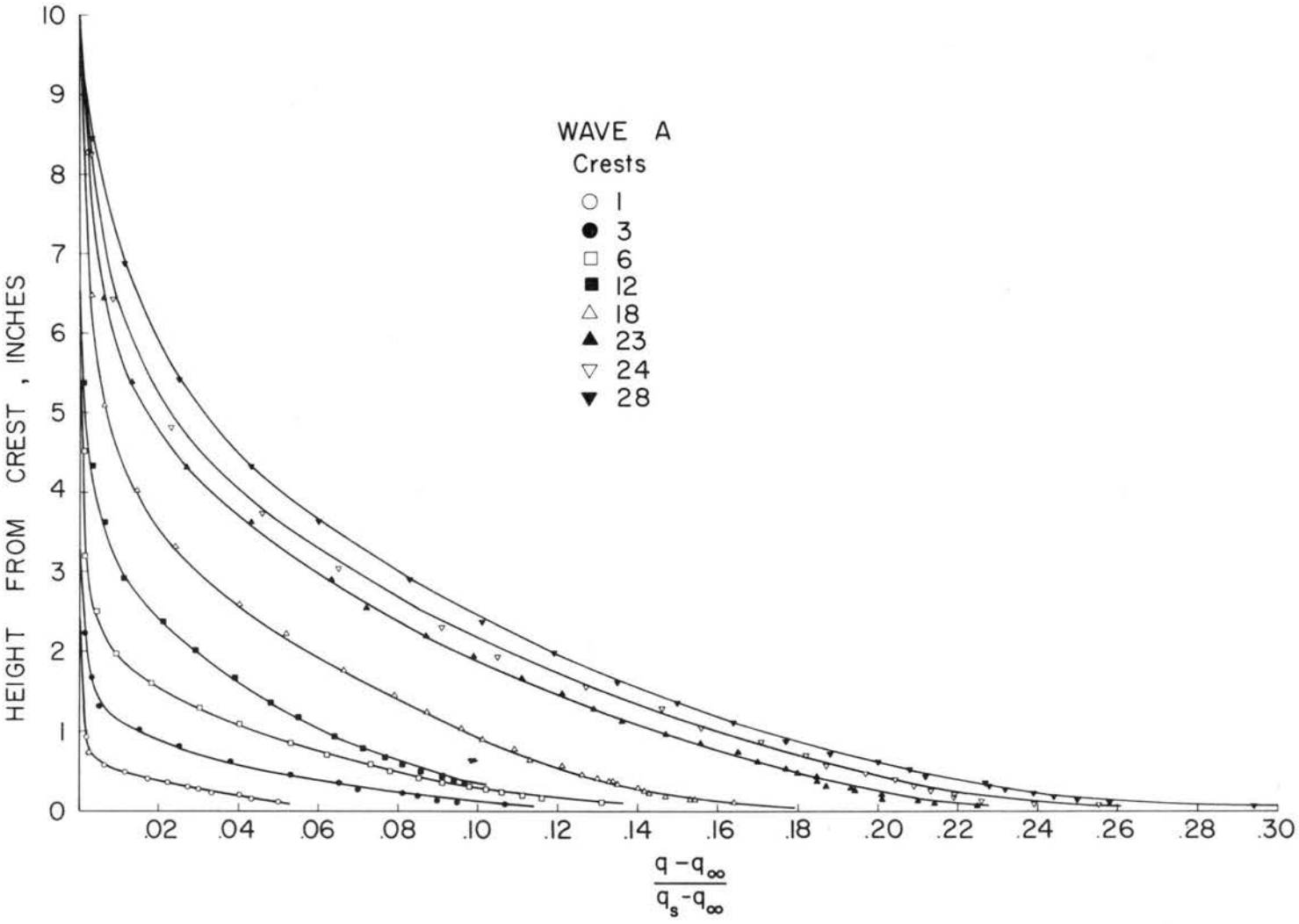

Fig. 33. Mean humidity profiles at various longitudinal positions, Wave A.

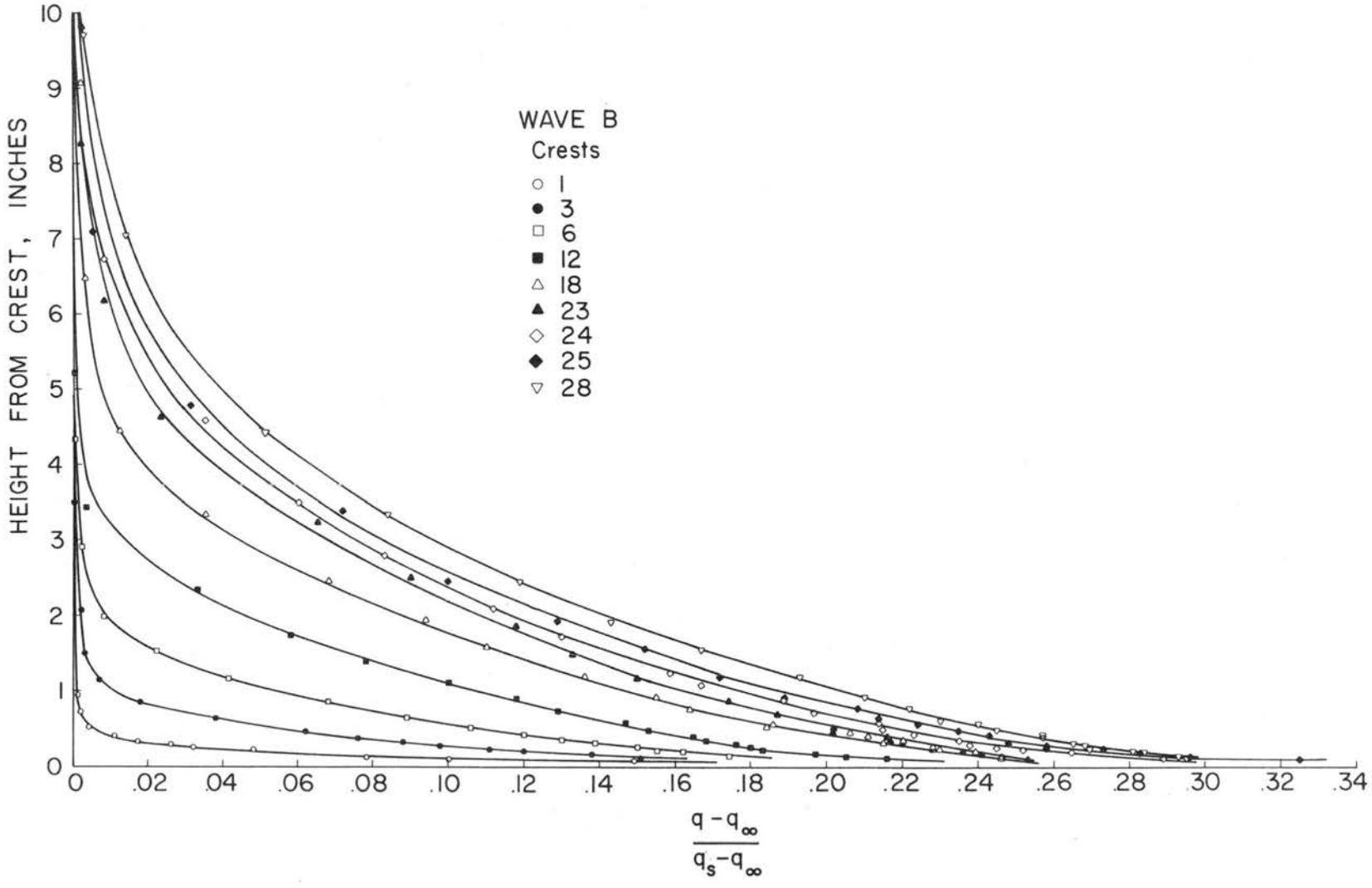

Fig. 34. Mean humidity profiles at various longitudinal positions, Wave B.

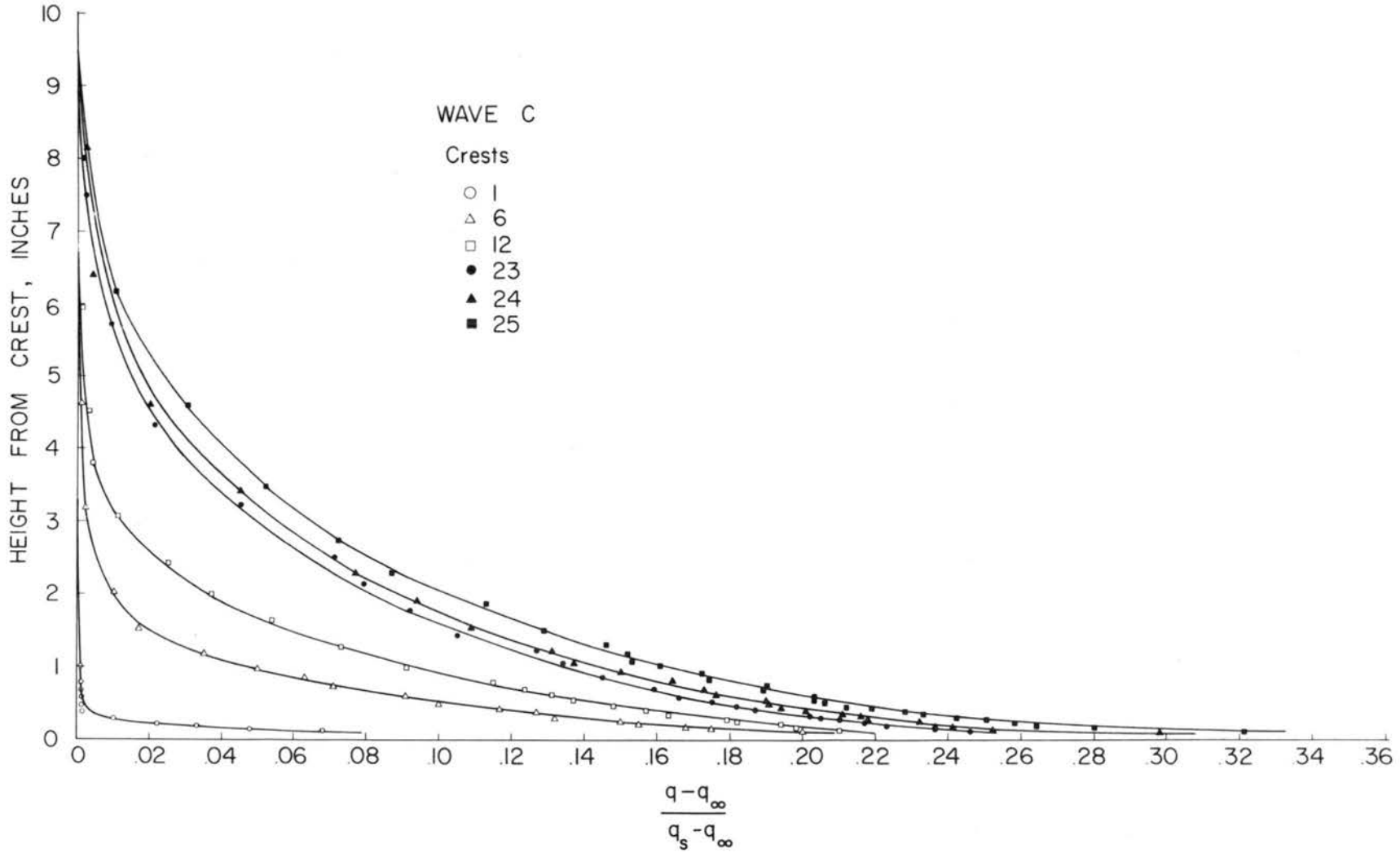

Fig. 35. Mean humidity profiles at various longitudinal positions, Wave C.

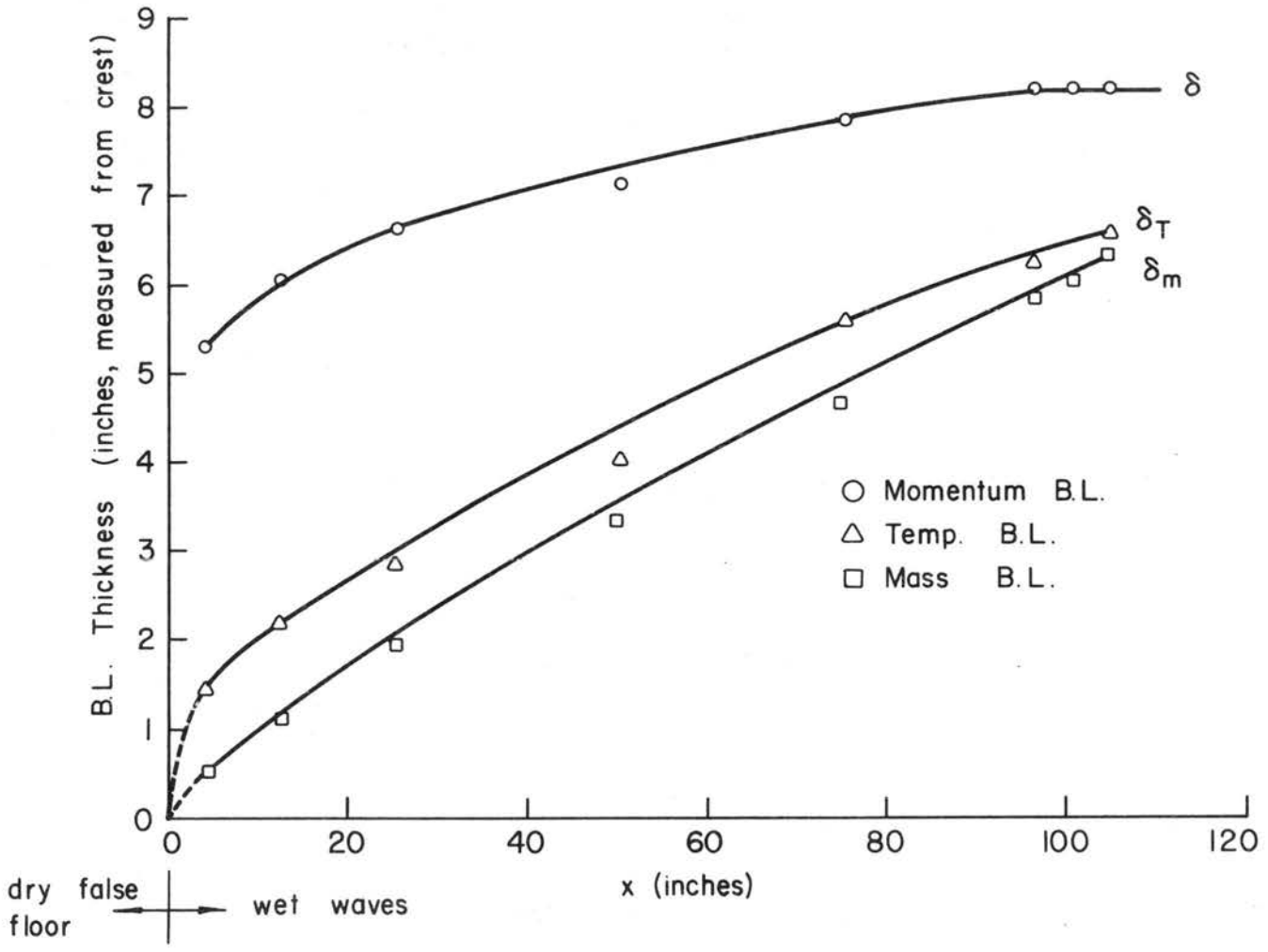

Fig. 36. Development of mass, momentum & temperature boundary layers (Typical case).

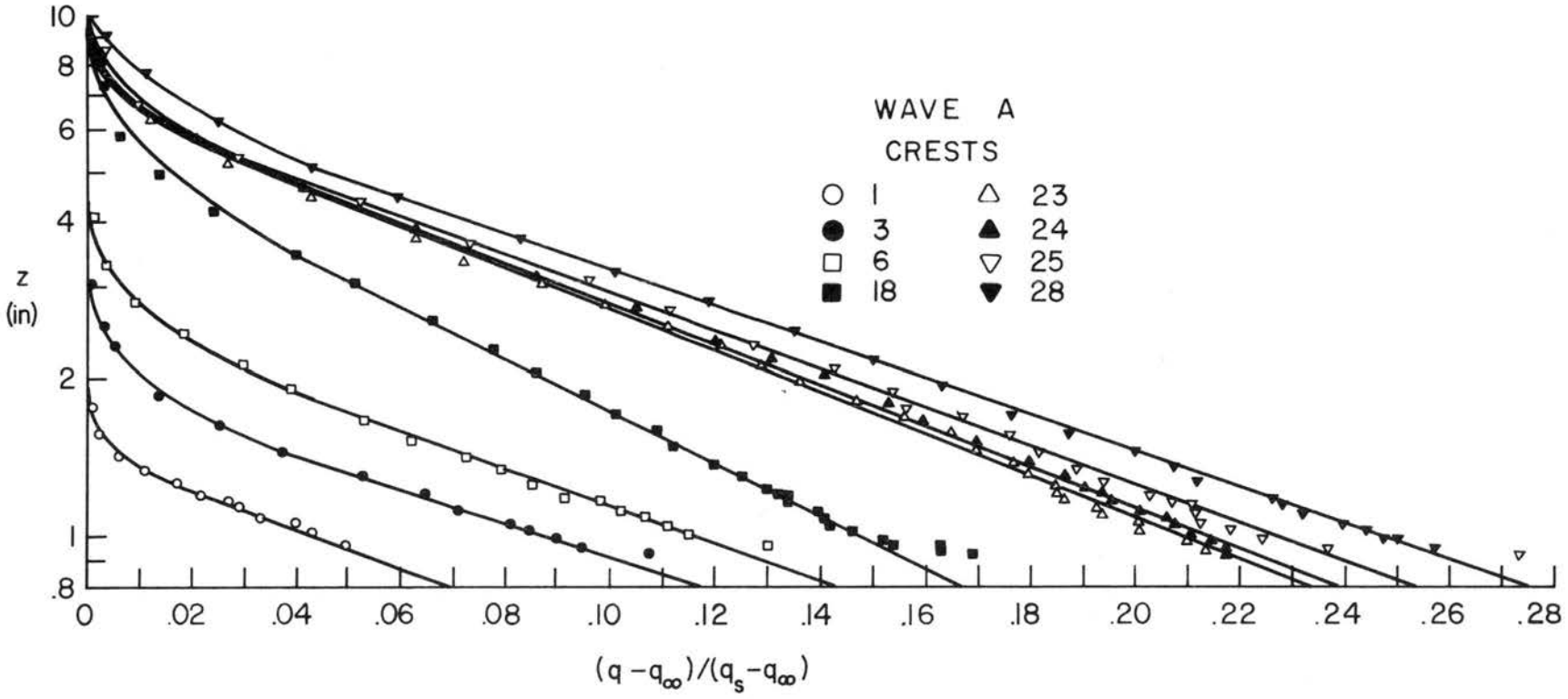

Fig. 37. Semilogarithmic plots of humidity distributions, Wave A.

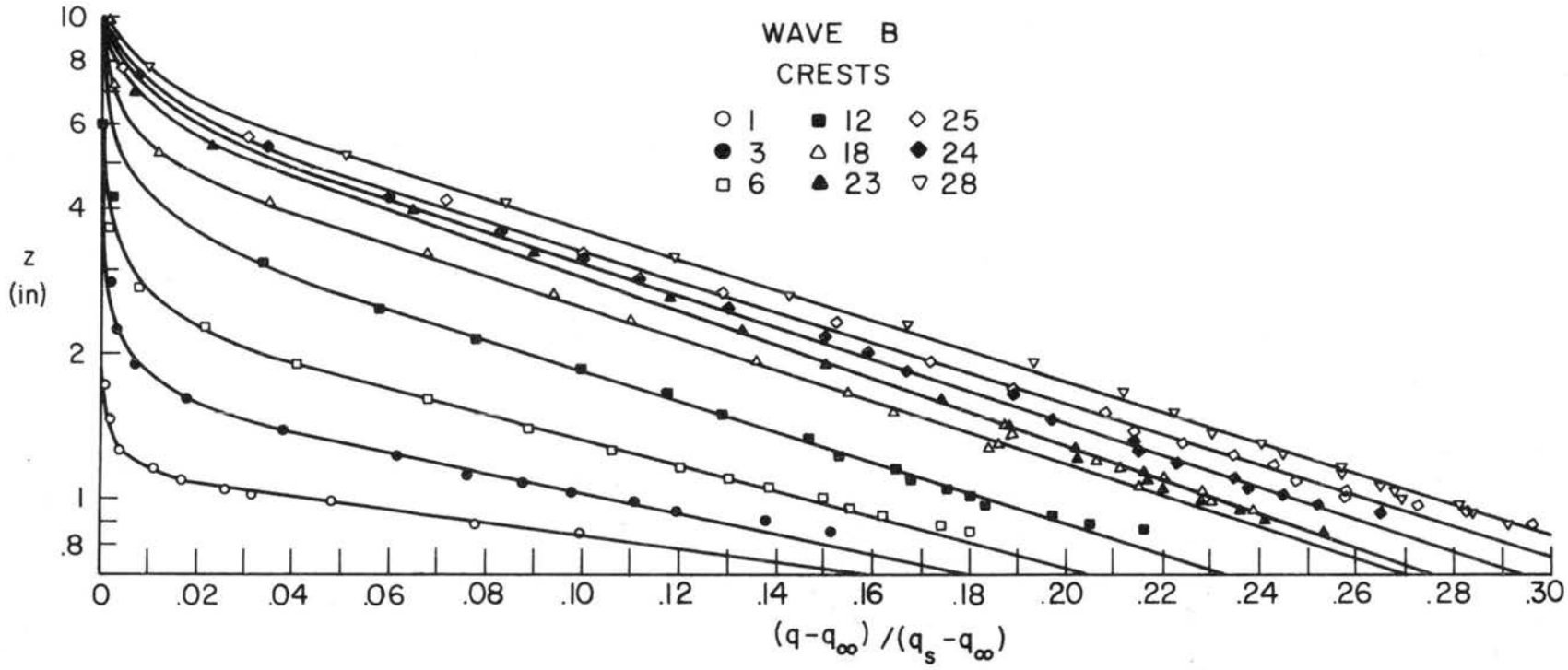

Fig. 38. Semilogarithmic plots of humidity distributions, Wave B.

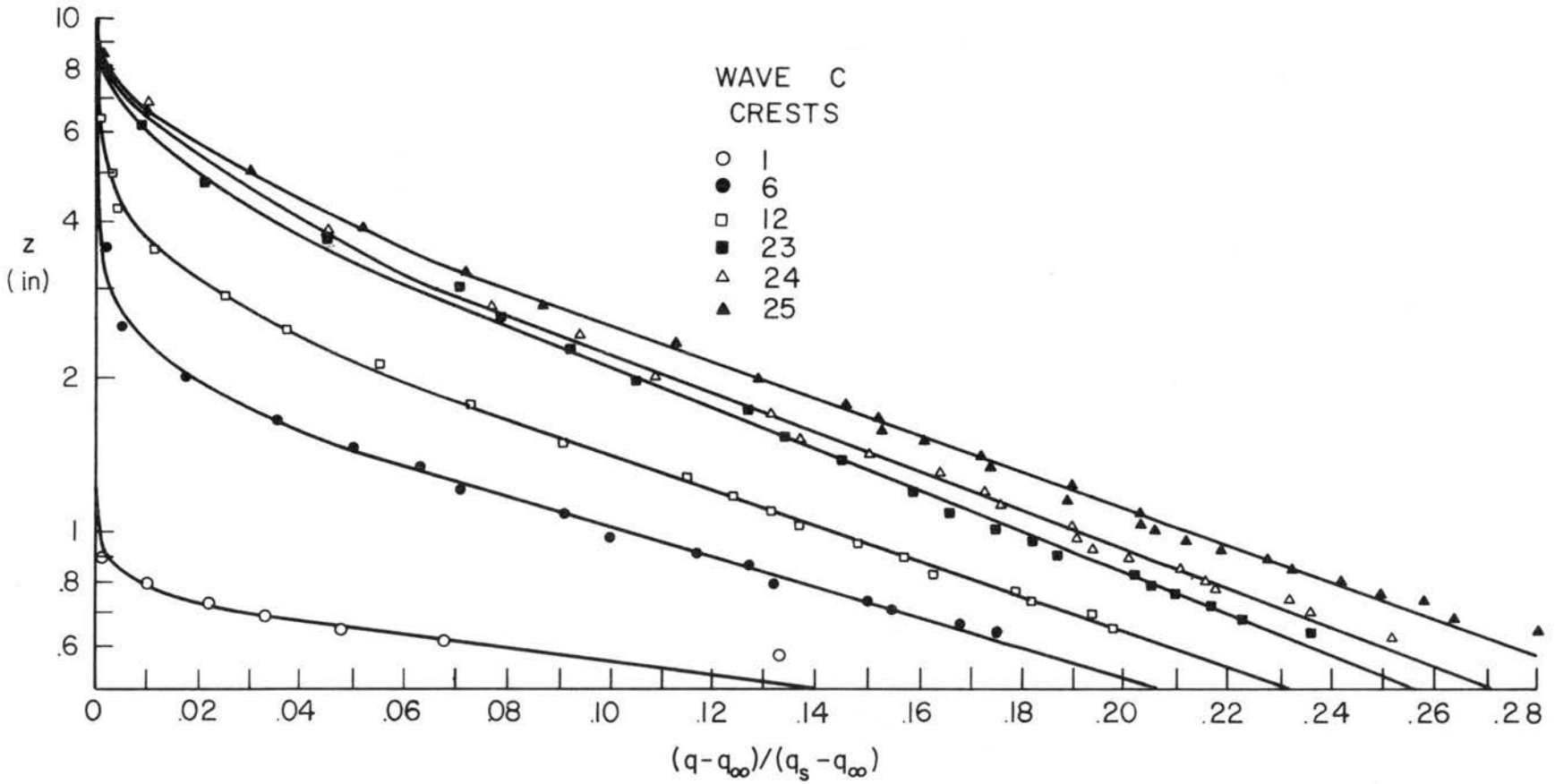

Fig. 39. Semilogarithmic plots of humidity distributions, Wave C.

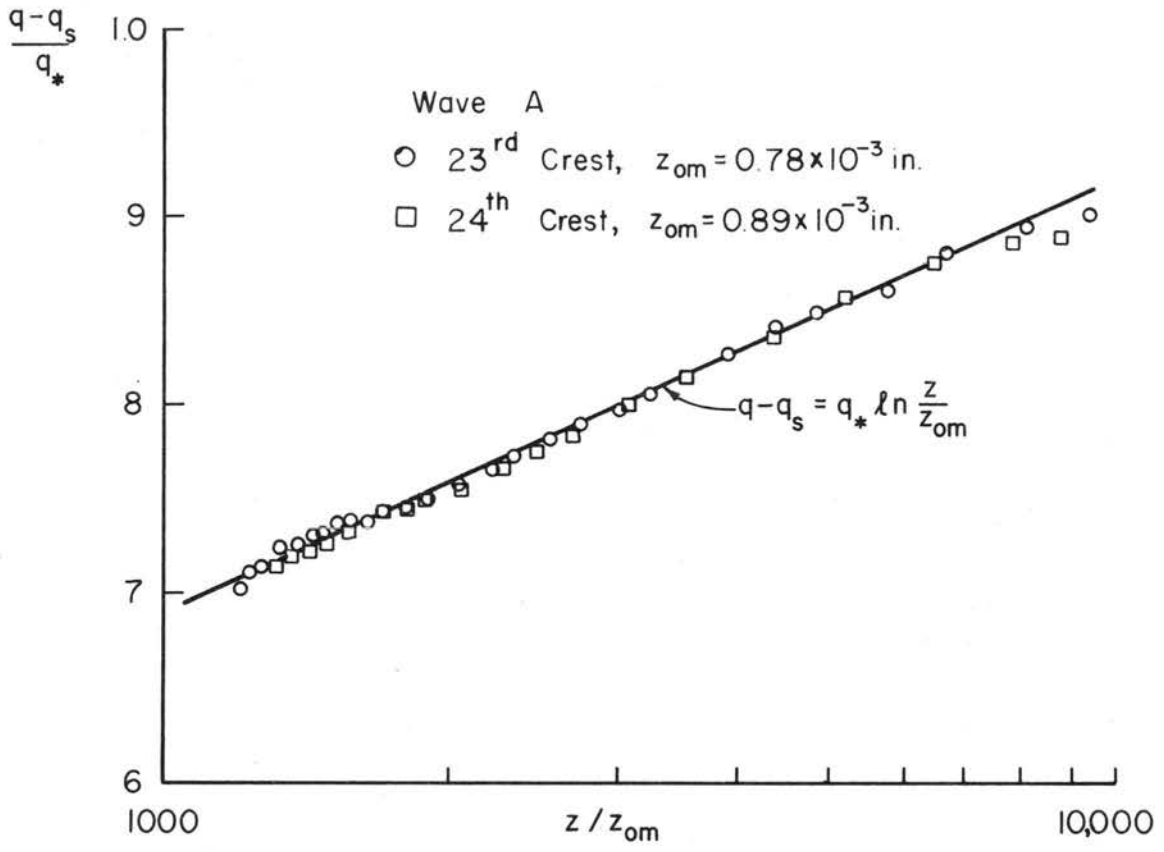

Fig. 40. Plots of $\frac{q-q_s}{q_*}$ vs $\frac{z}{z_{om}}$ (far downstream region), Wave A.

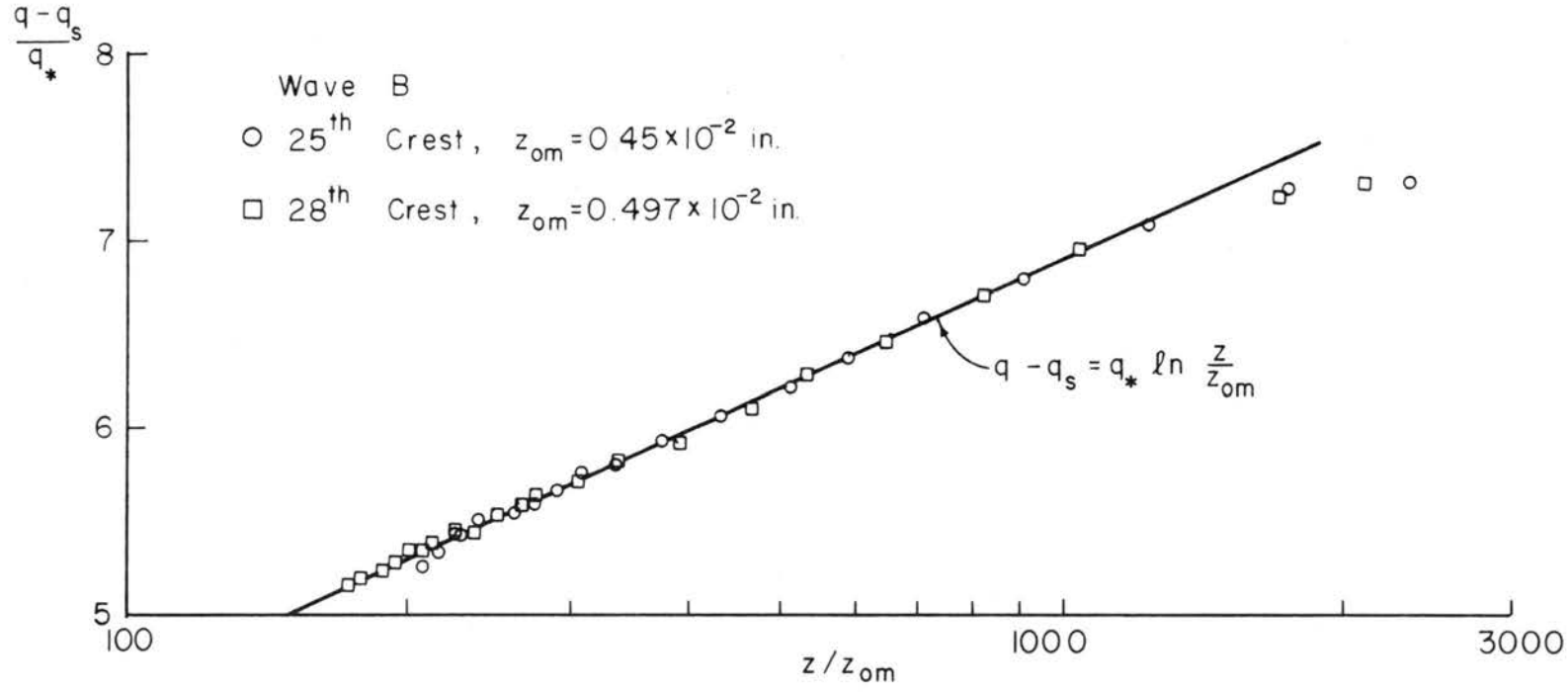

Fig. 41. Plots of $\frac{q-q_s}{q_*}$ vs $\frac{z}{z_{om}}$ (far downstream region), Wave B.

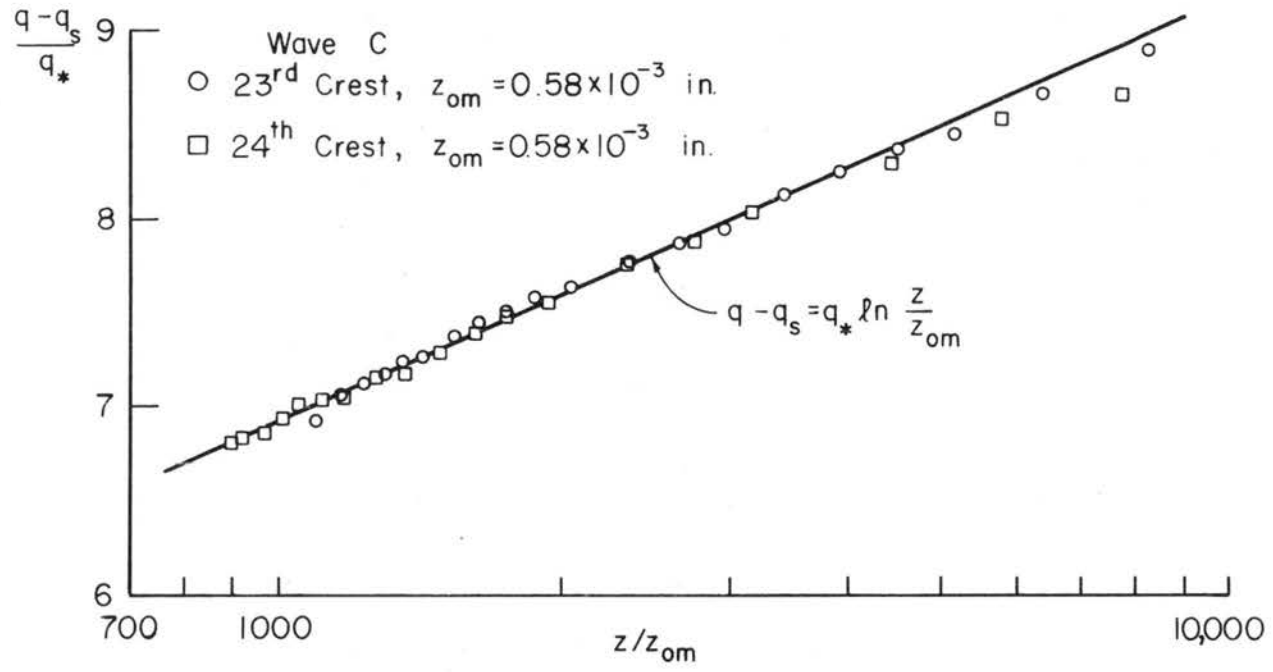

Fig. 42. Plots of $\frac{q-q_s}{q_*}$ vs $\frac{z}{z_{om}}$ (far downstream region), Wave C.

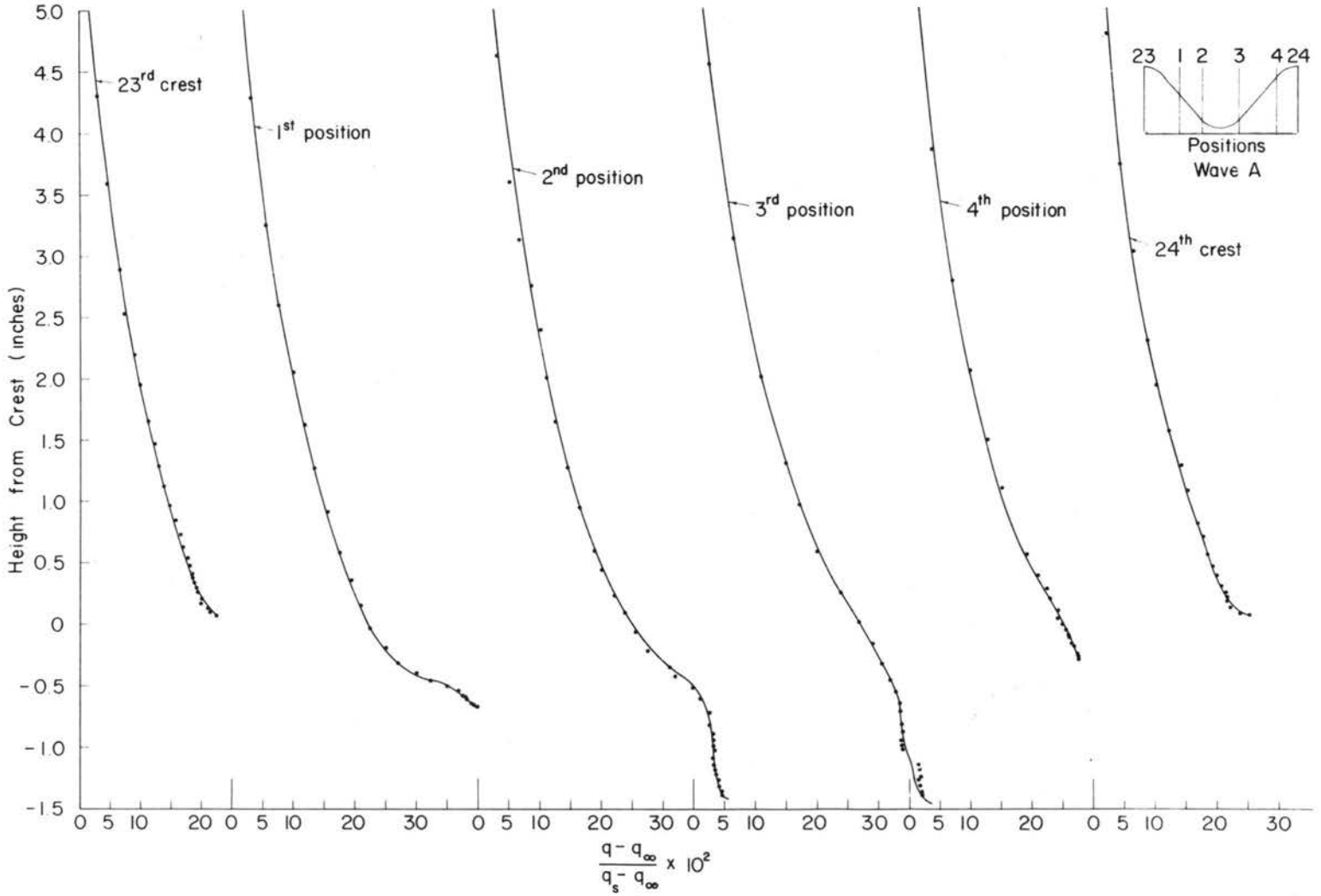

Fig. 43. Vertical humidity profiles at various positions inside a wave trough, Wave A.

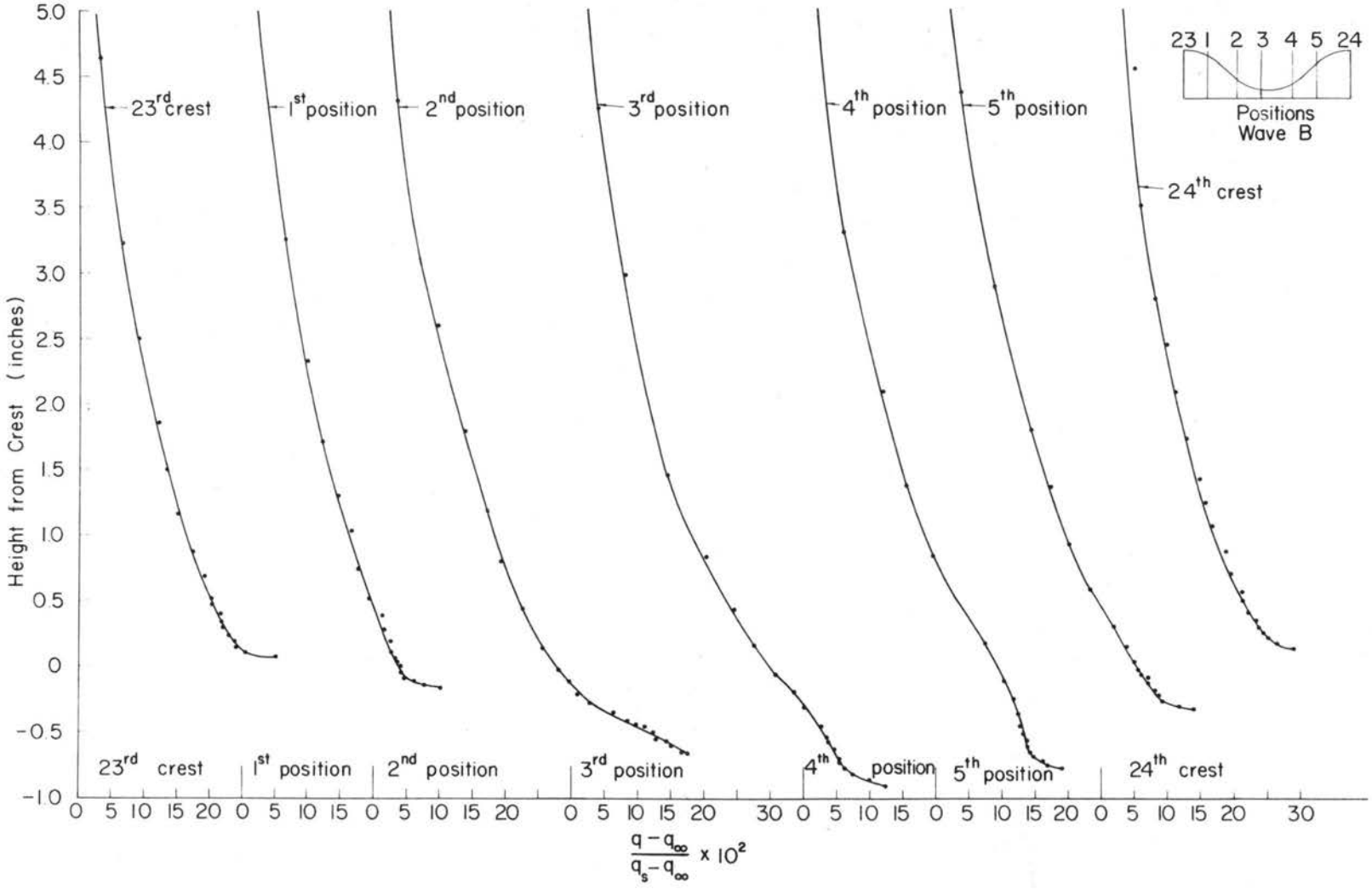

Fig. 44. Vertical humidity profiles at various positions inside a wave trough, Wave B.

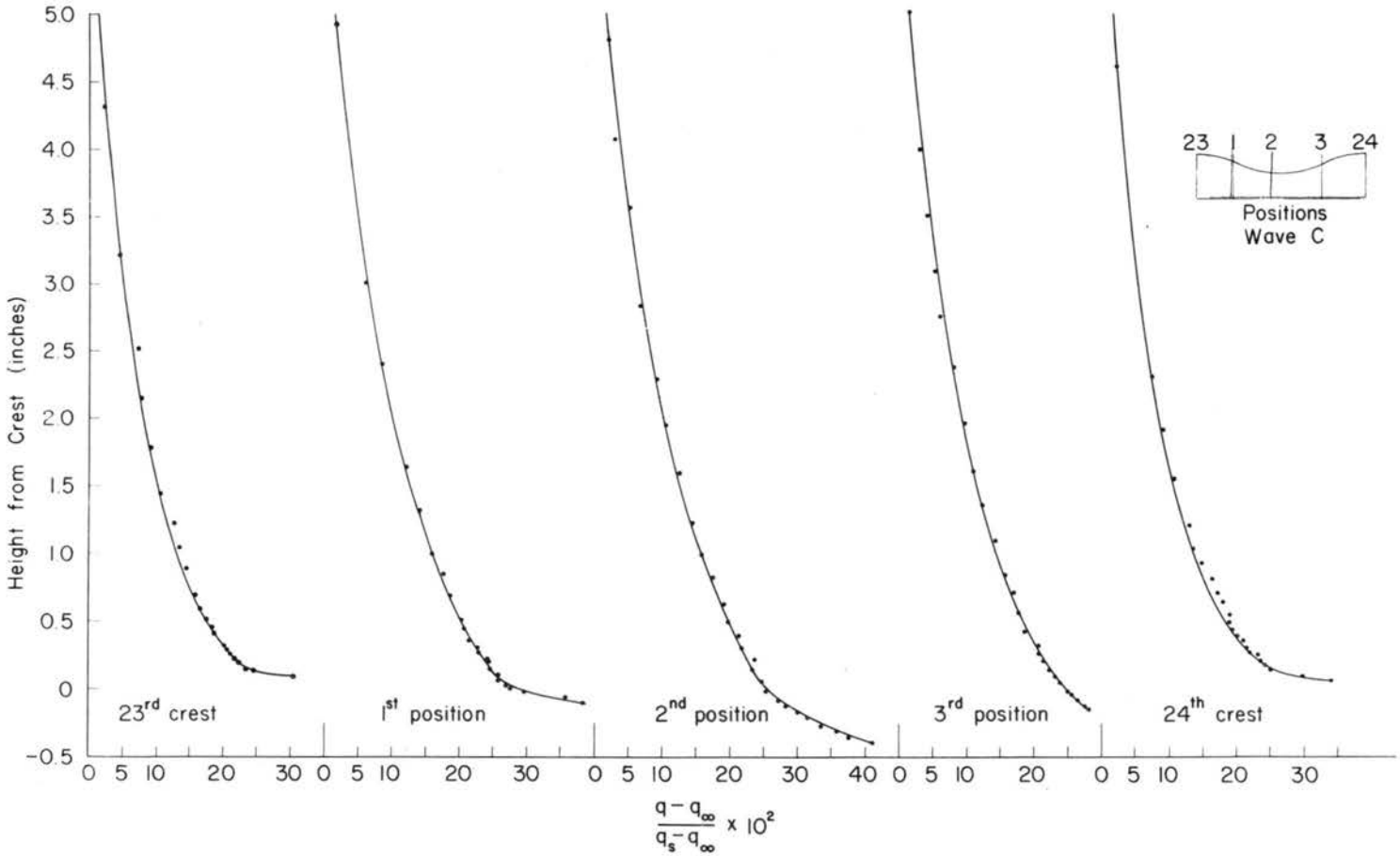

Fig. 45. Vertical humidity profiles at various positions inside a wave trough, Wave C.

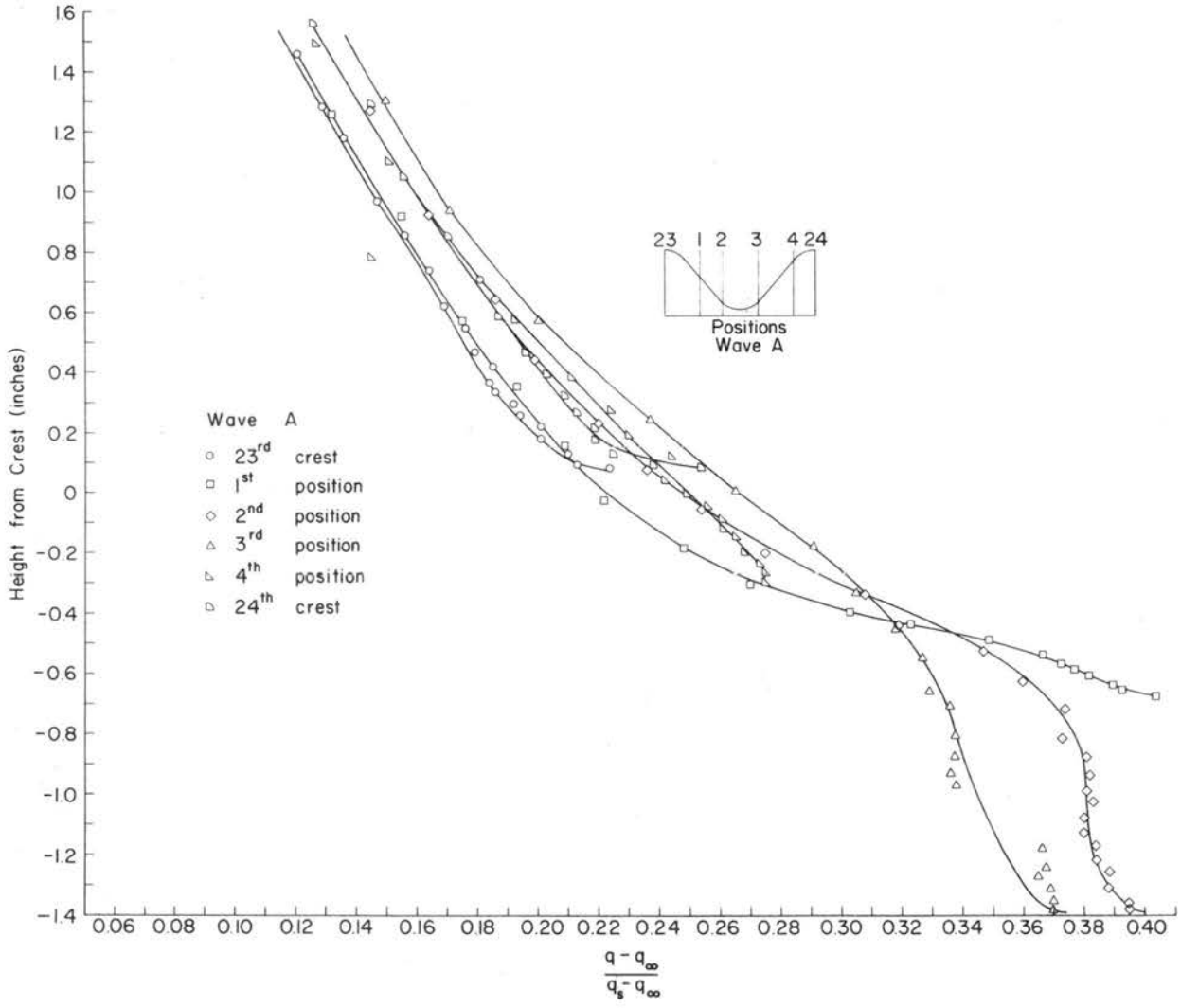

Fig. 46. Enlarged view of lower portion of humidity distributions in Fig. 43.

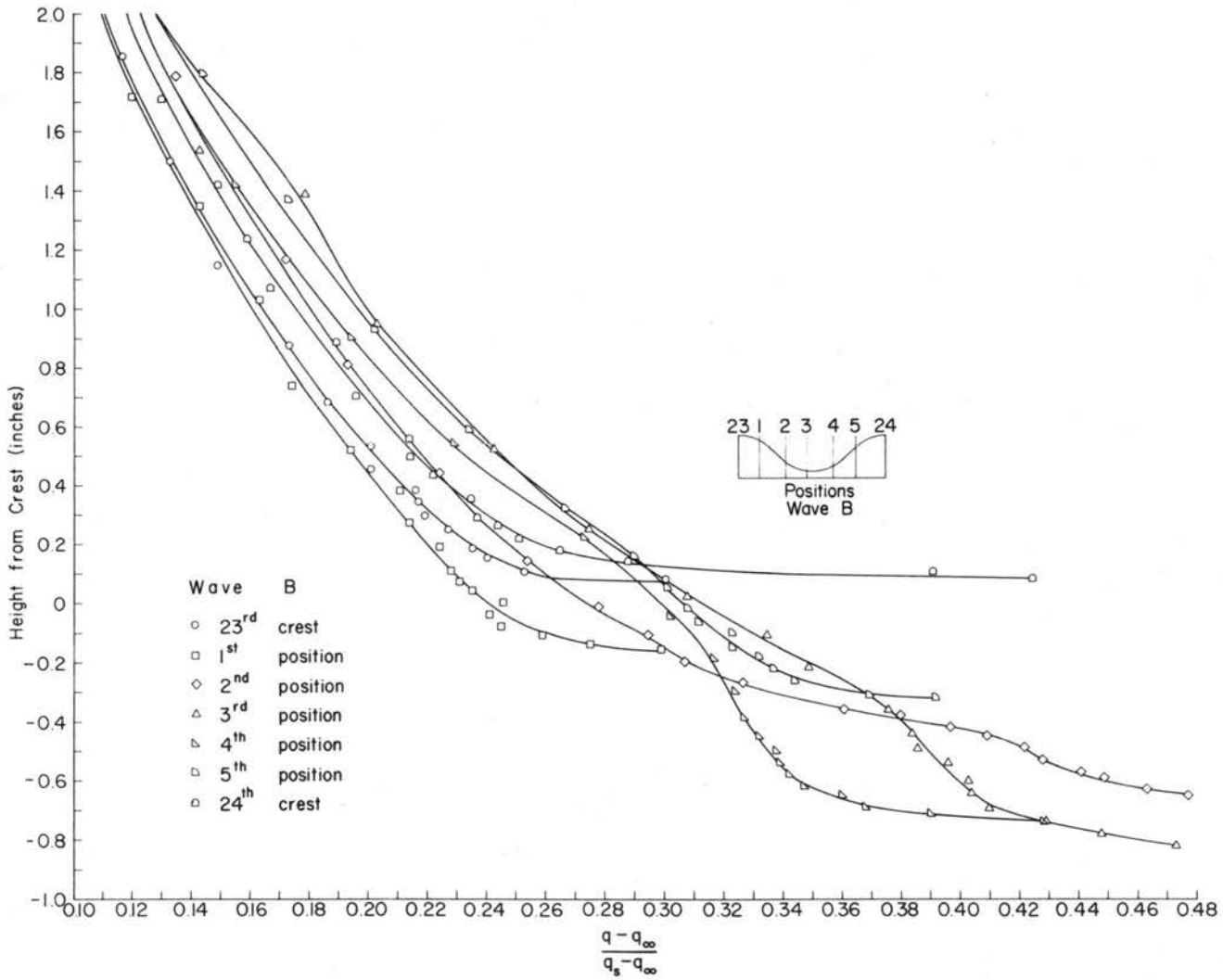

Fig. 47. Enlarged view of lower portion of humidity distributions in Fig. 44.

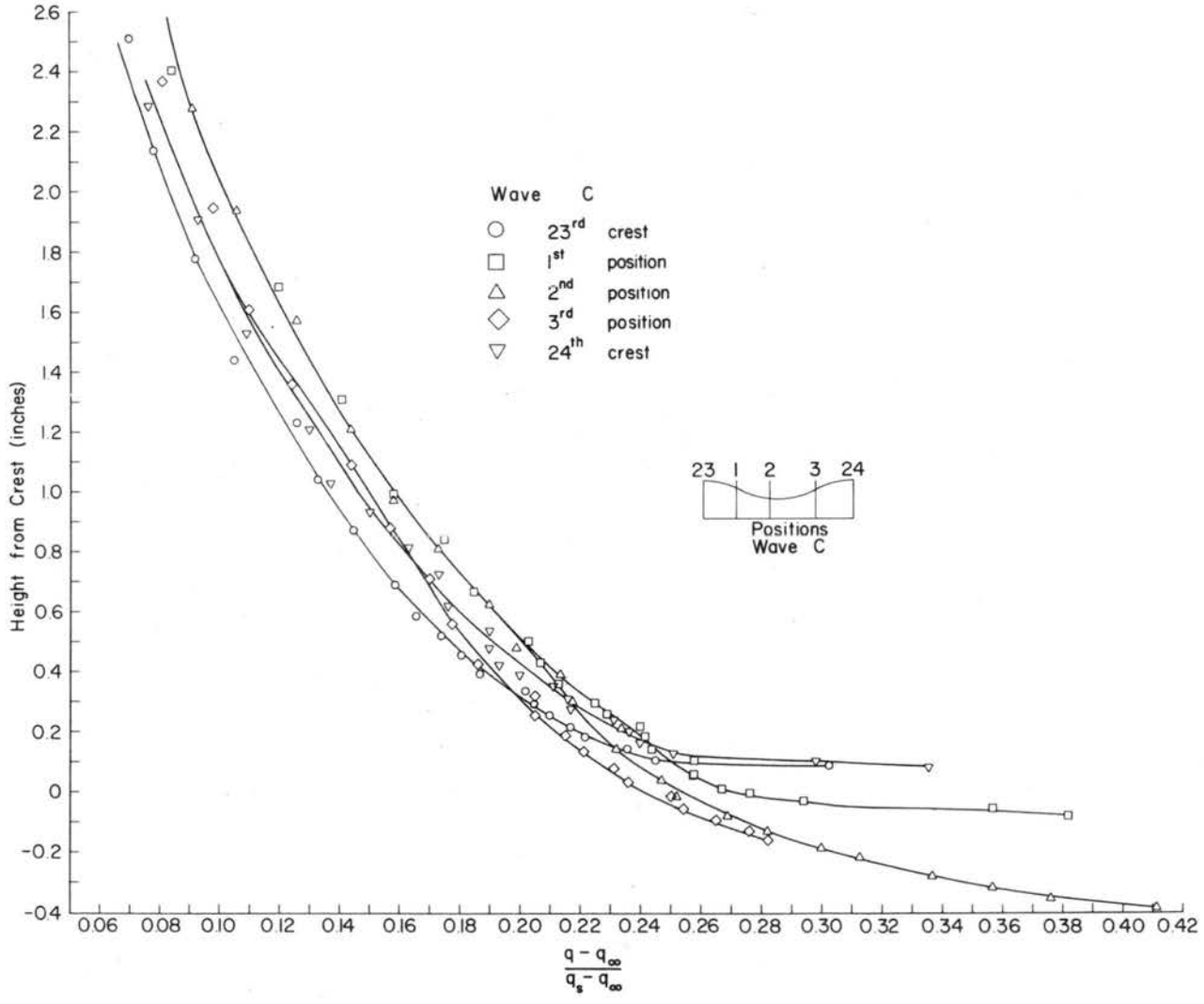

Fig. 48. Enlarged view of lower portion of humidity distributions in Fig. 45.

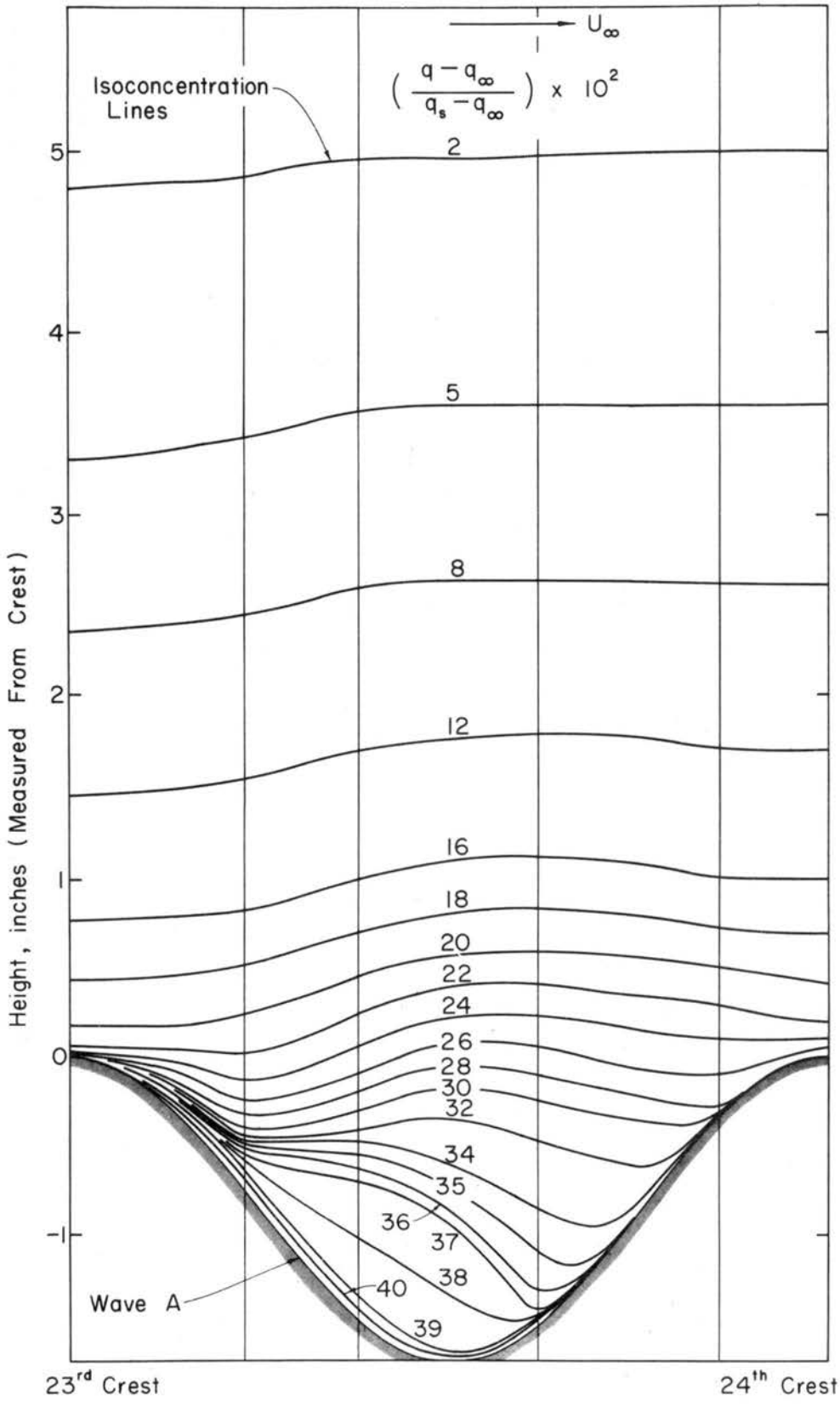

Fig. 49. Isoconcentration lines inside a wave trough, Wave A.

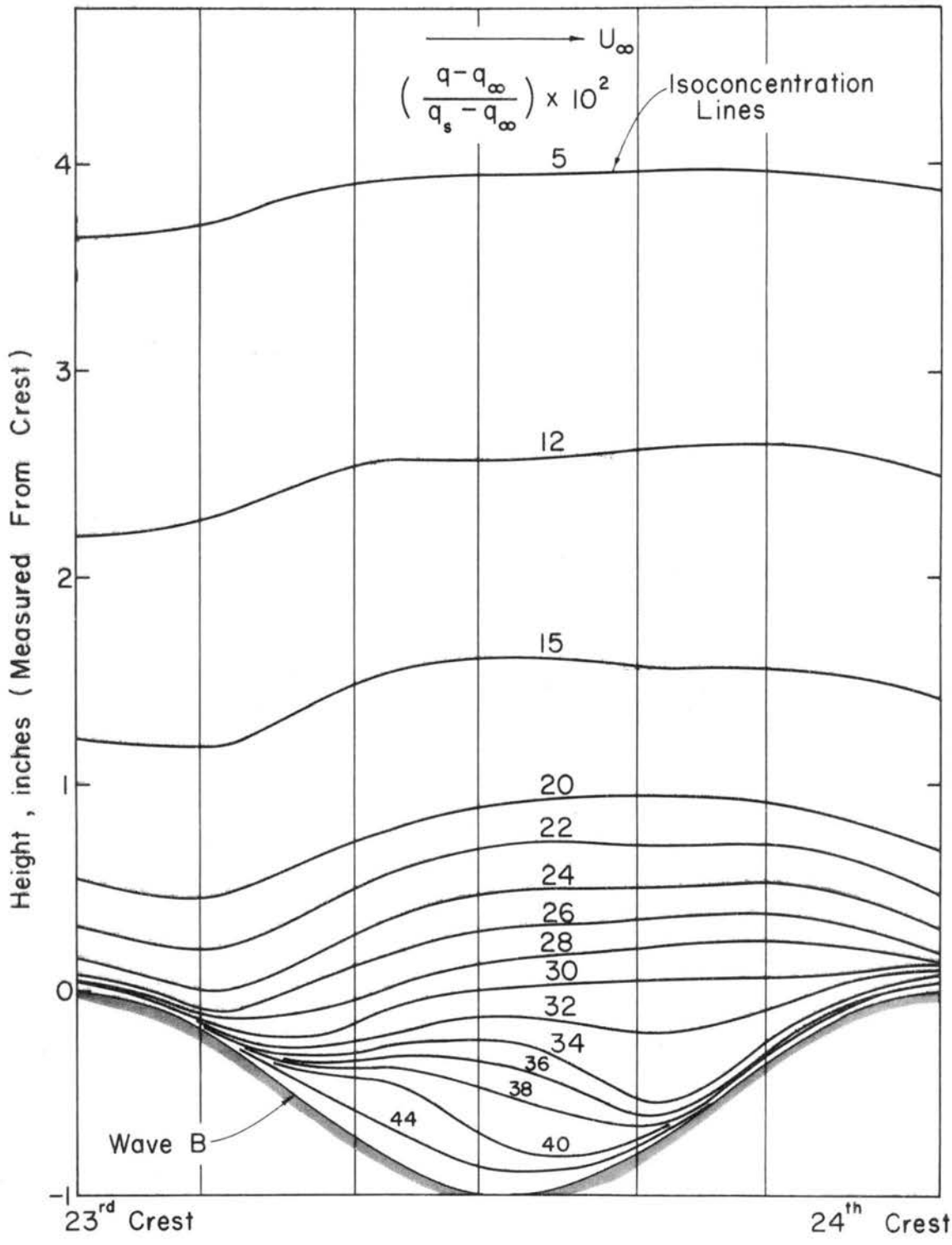

Fig. 50. Isoconcentration lines inside a wave trough, Wave B.

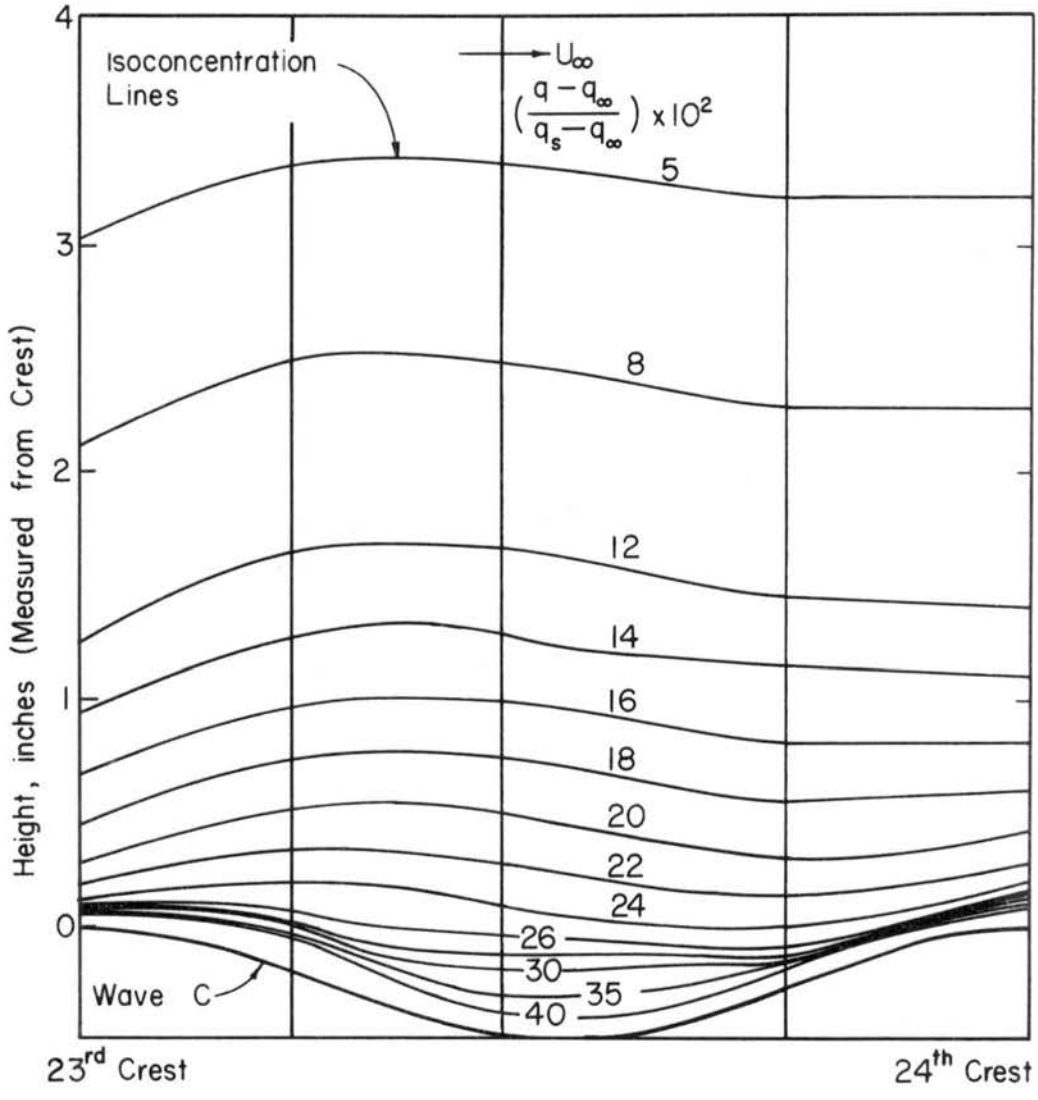

Fig. 51. Isoconcentration lines inside a wave trough, Wave C.

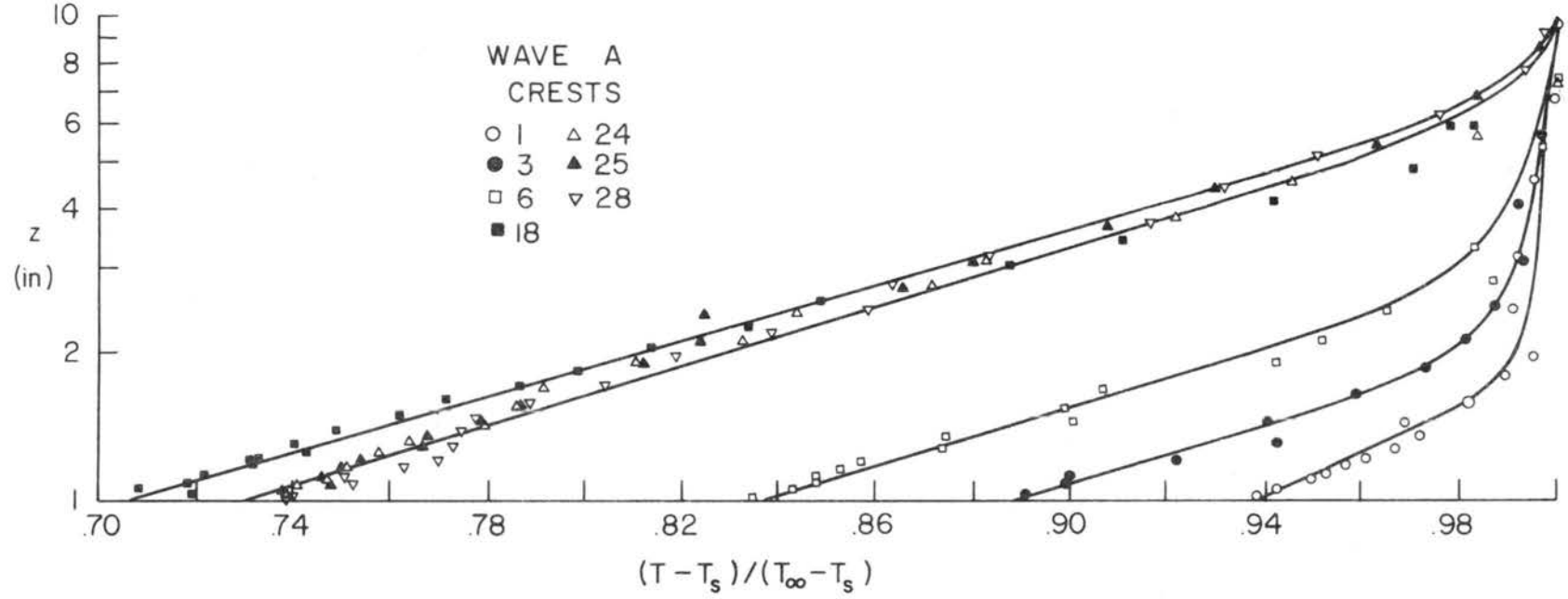

Fig. 52. Mean temperature distributions at various longitudinal positions (Typical case).

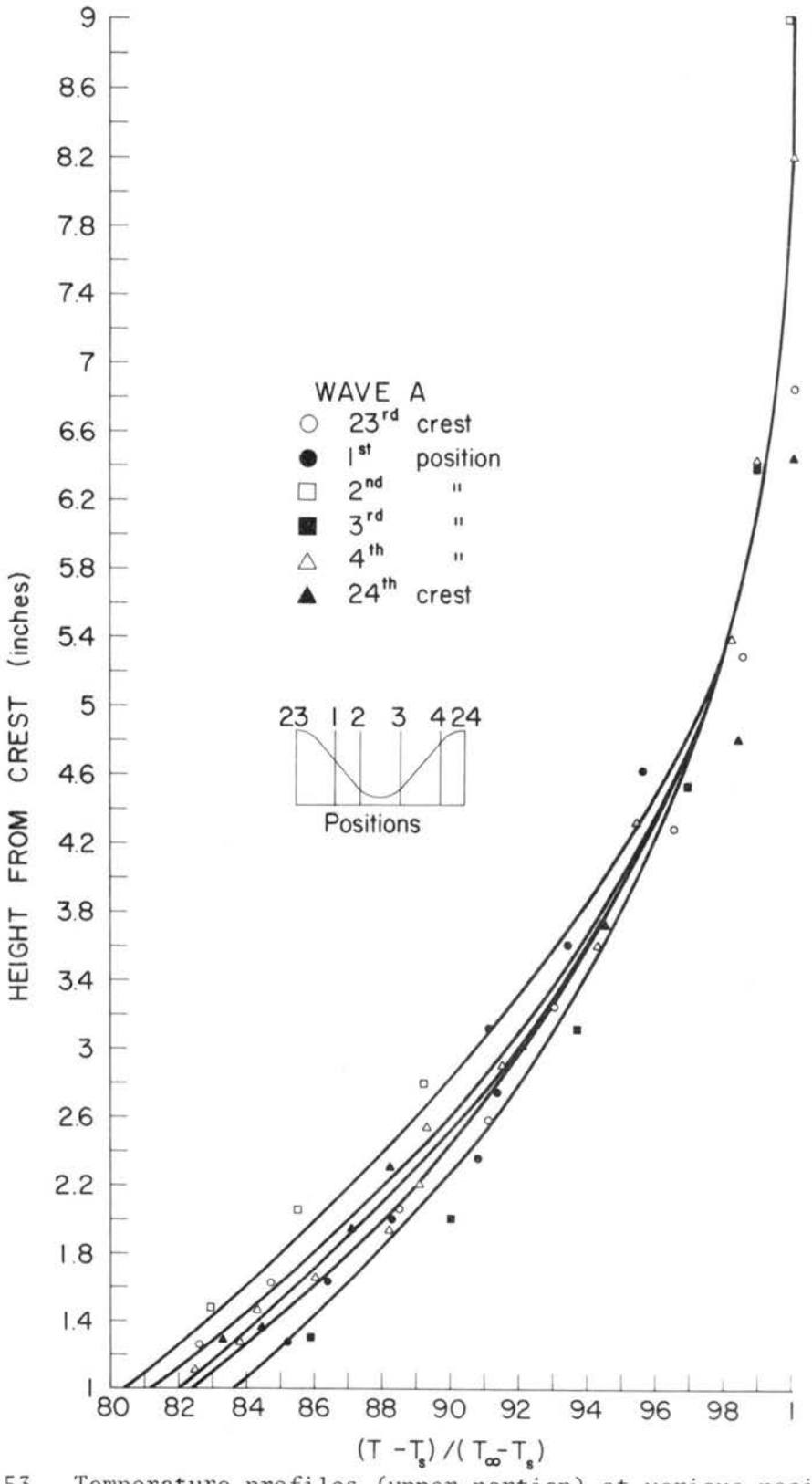

Fig. 53. Temperature profiles (upper portion) at various positions inside a wave trough (Typical case).

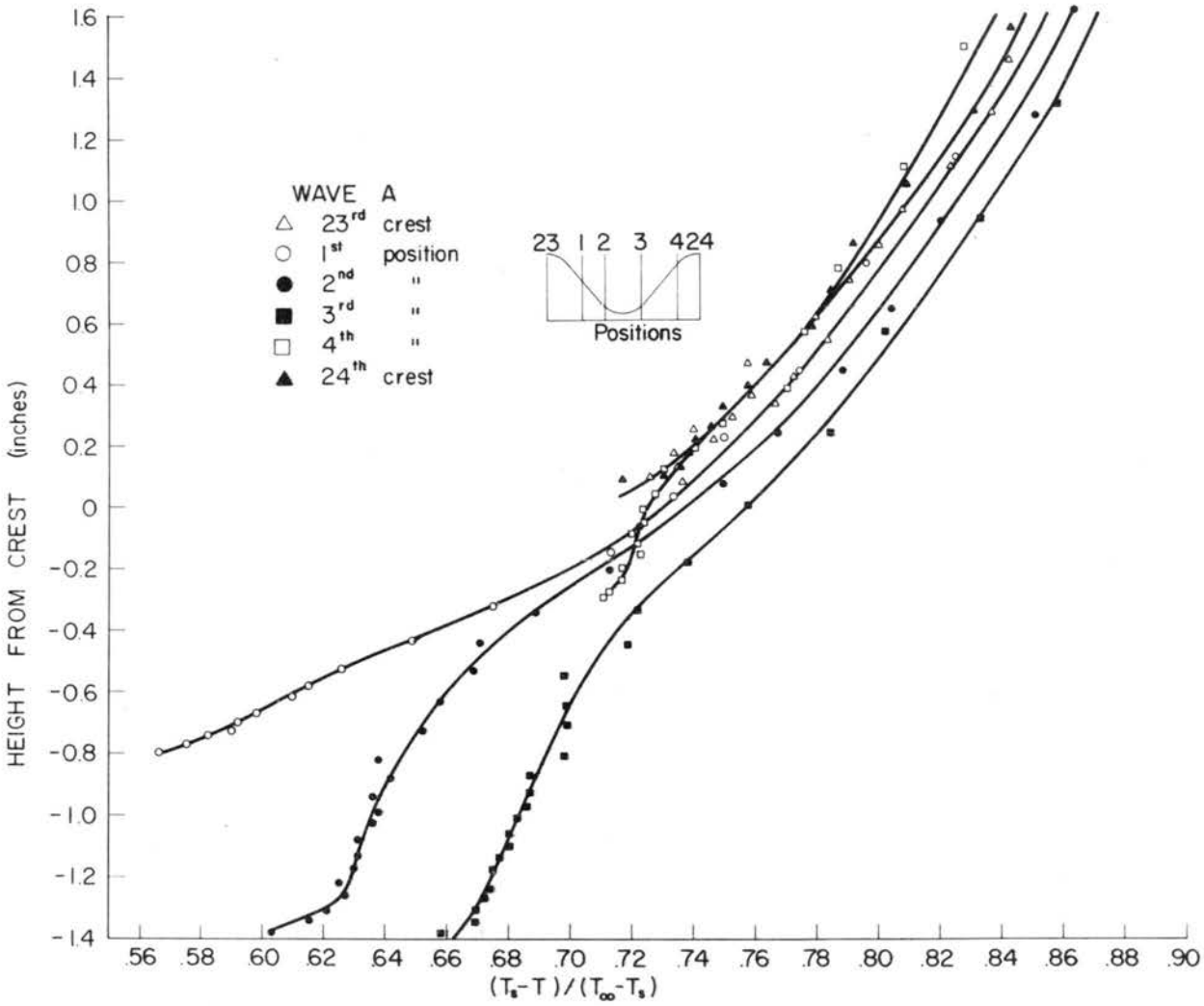

Fig. 54. Enlarged view of lower portion of temperature profiles in Fig. 53.

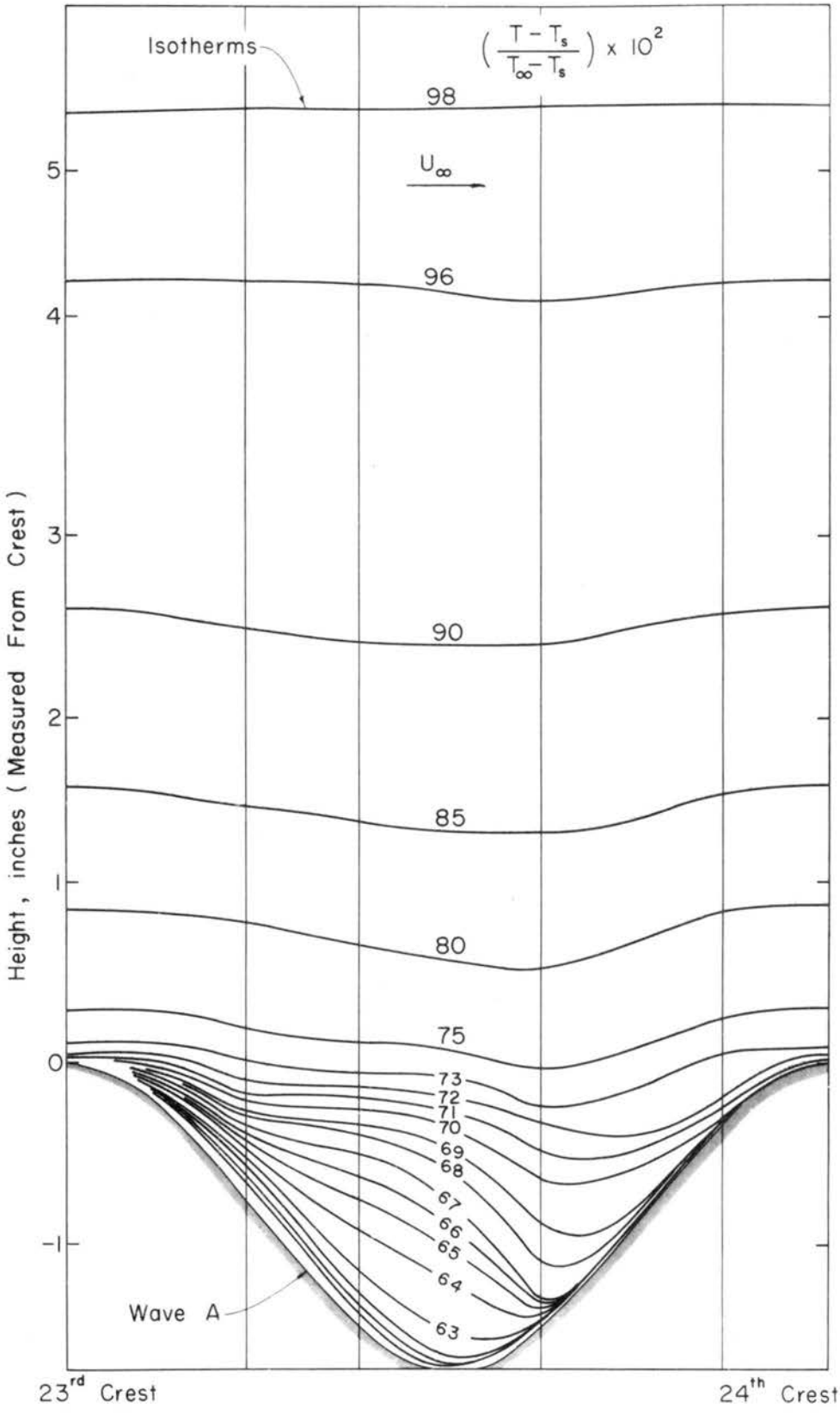

Fig. 55. Isotherms inside a wave trough (Typical case).

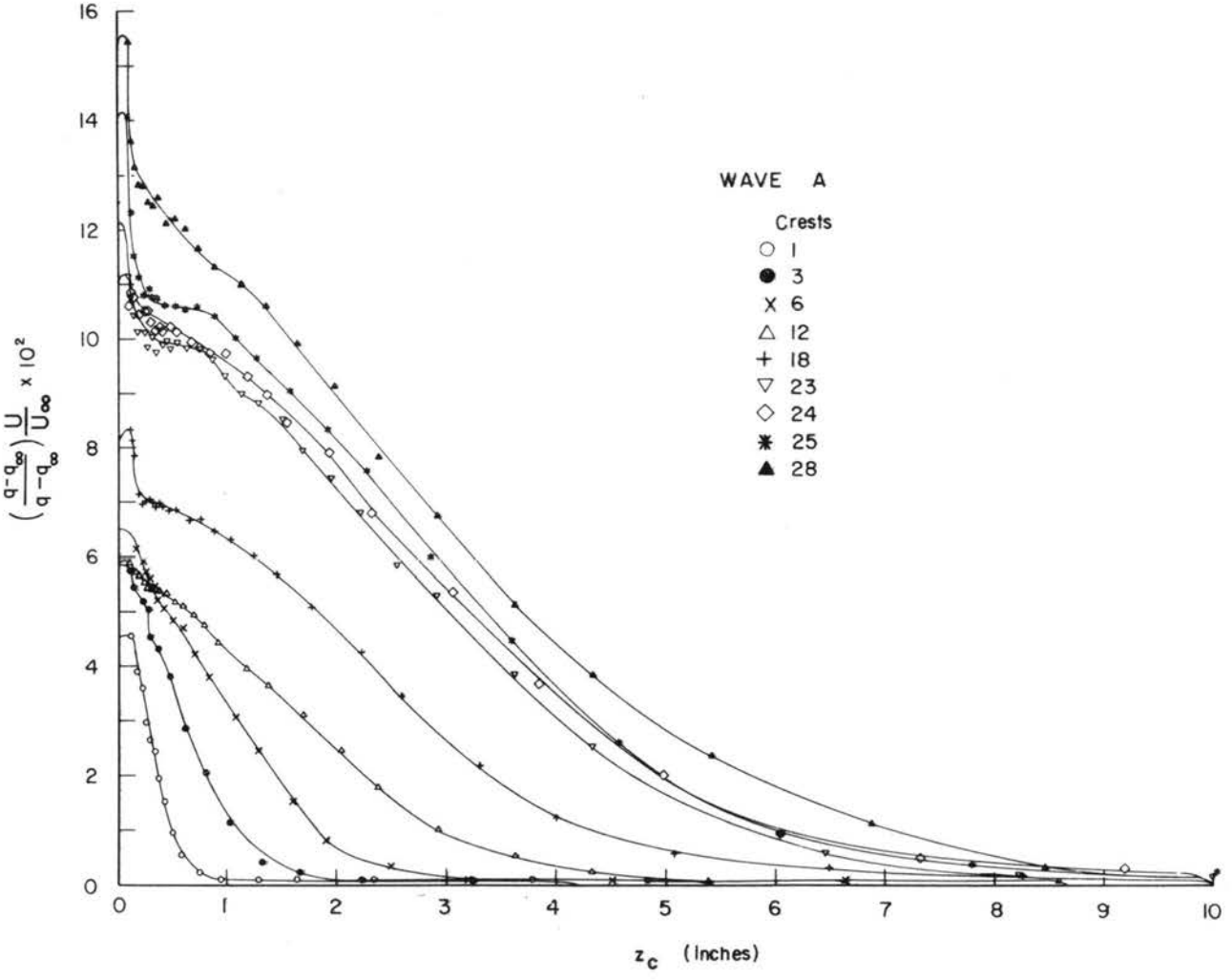

Fig. 56. Variation of $\left(\frac{q-q_\infty}{q_s-q_\infty}\right)\ \frac{U}{U_\infty}$ vs z_c (Typical case).

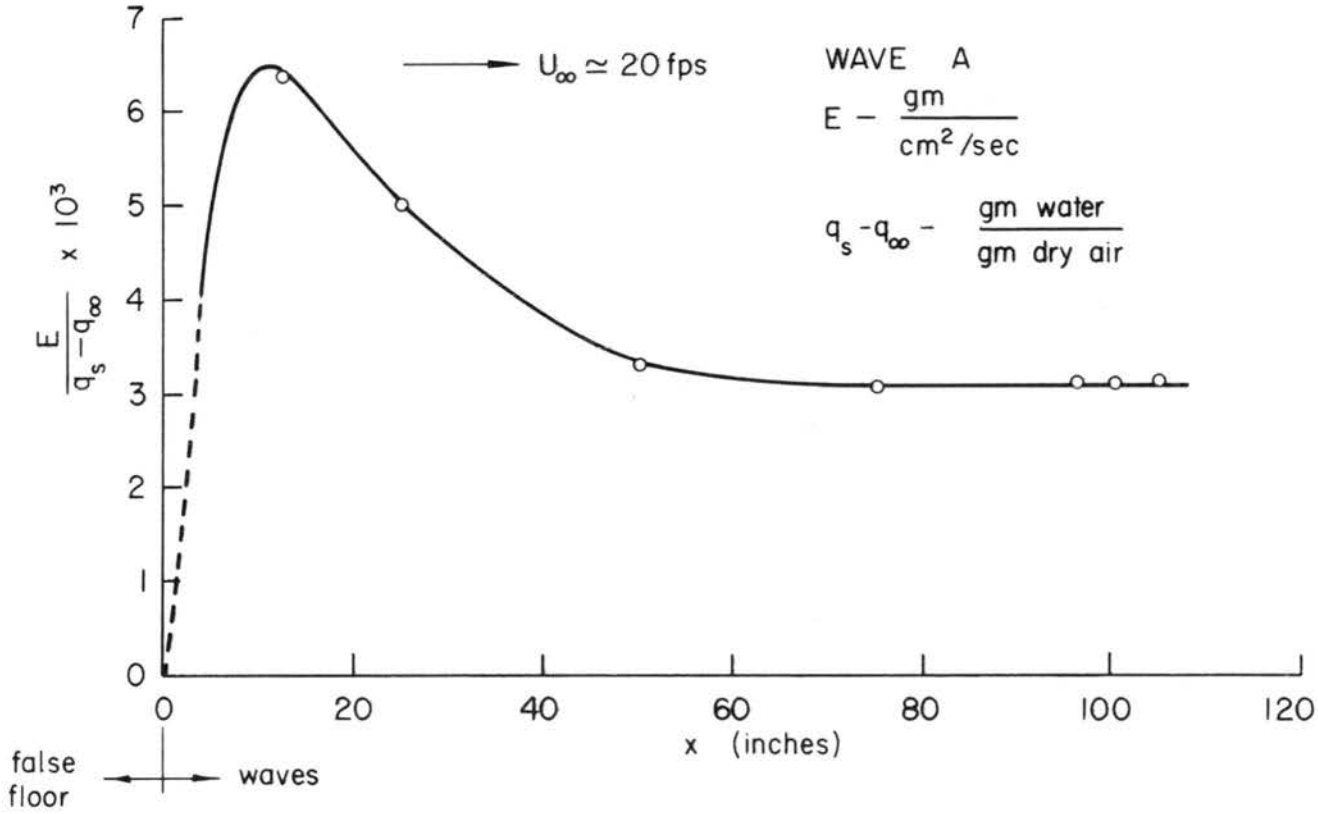

Fig. 57. Variation of average evaporation rates with fetch, Wave A.

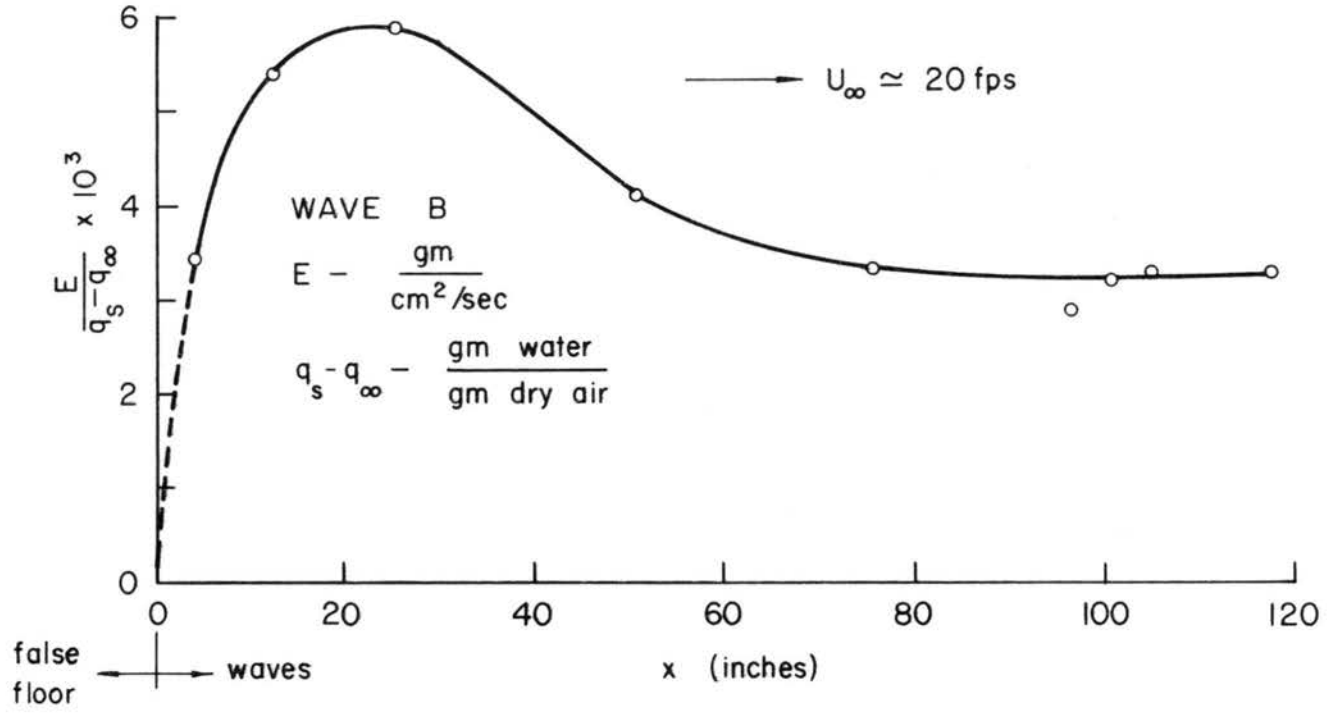

Fig. 58. Variation of average evaporation rates with fetch, Wave B.

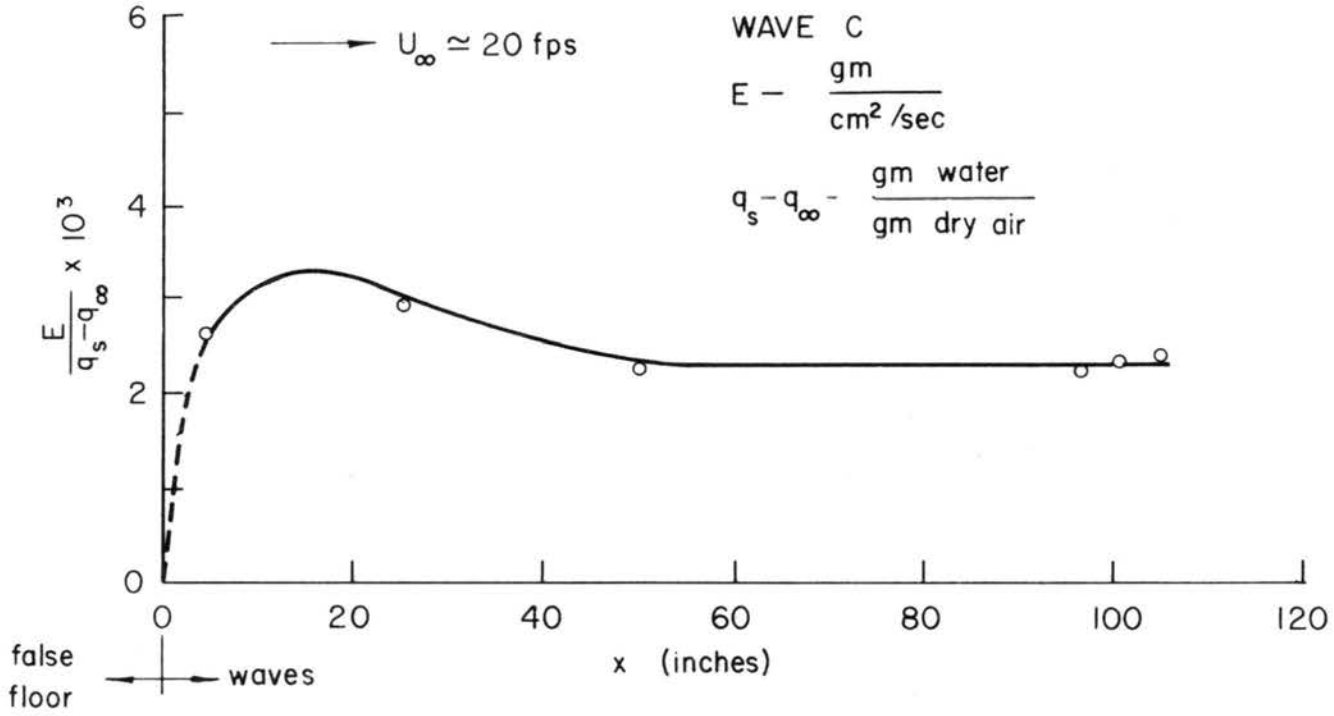

Fig. 59. Variation of average evaporation rates with fetch, Wave C.

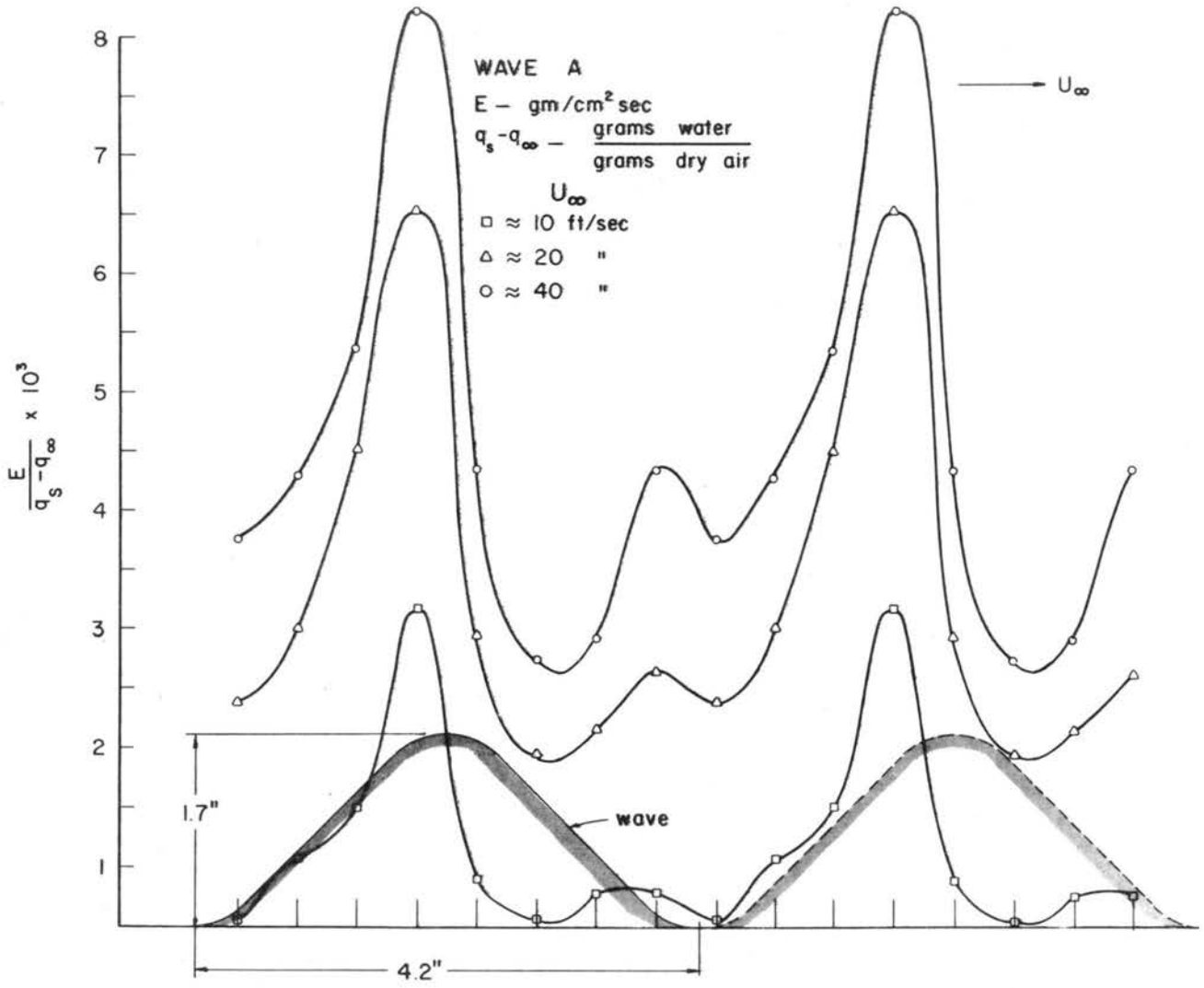

Fig. 60. Distribution of local mass transfer coefficients, Wave A.

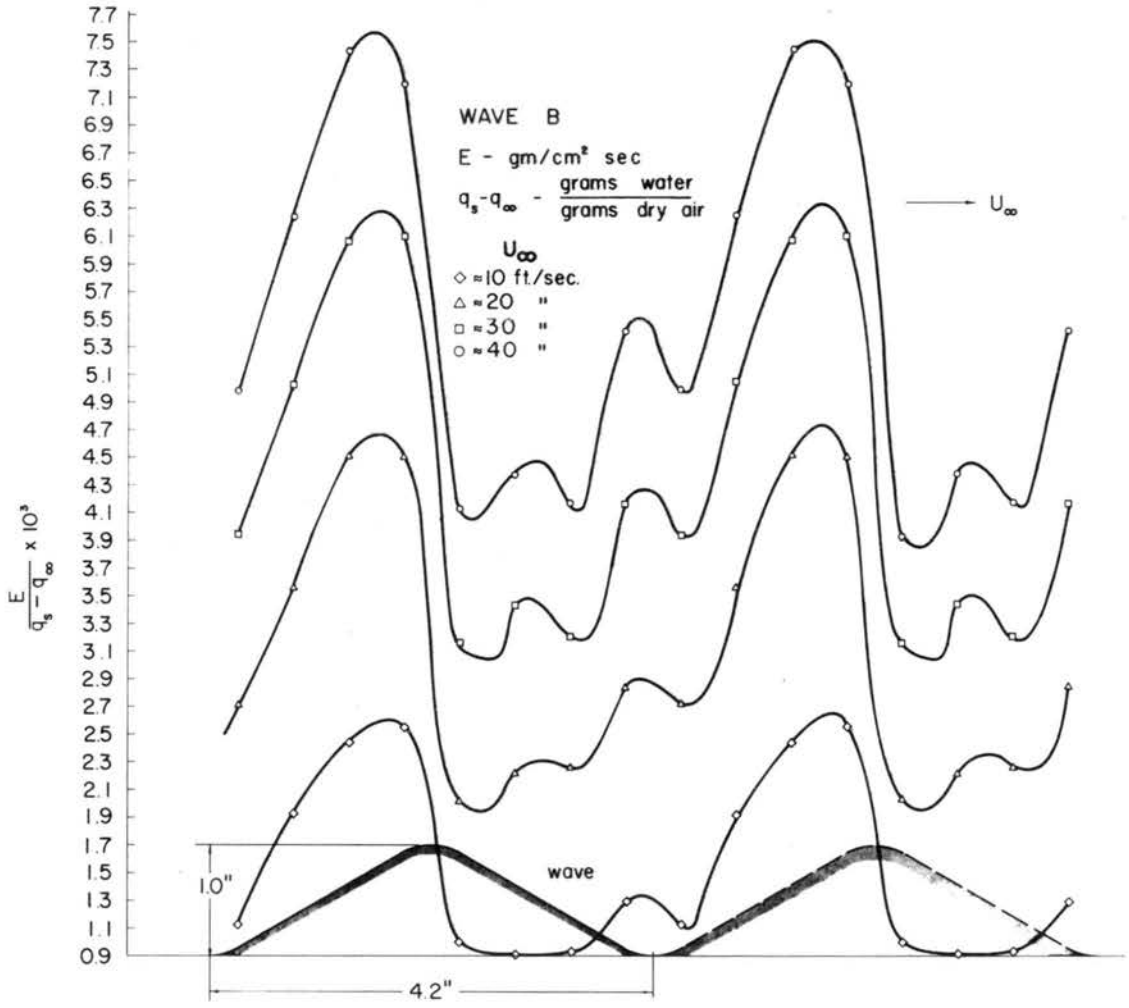

Fig. 61. Distributions of local mass transfer coefficients, Wave B.

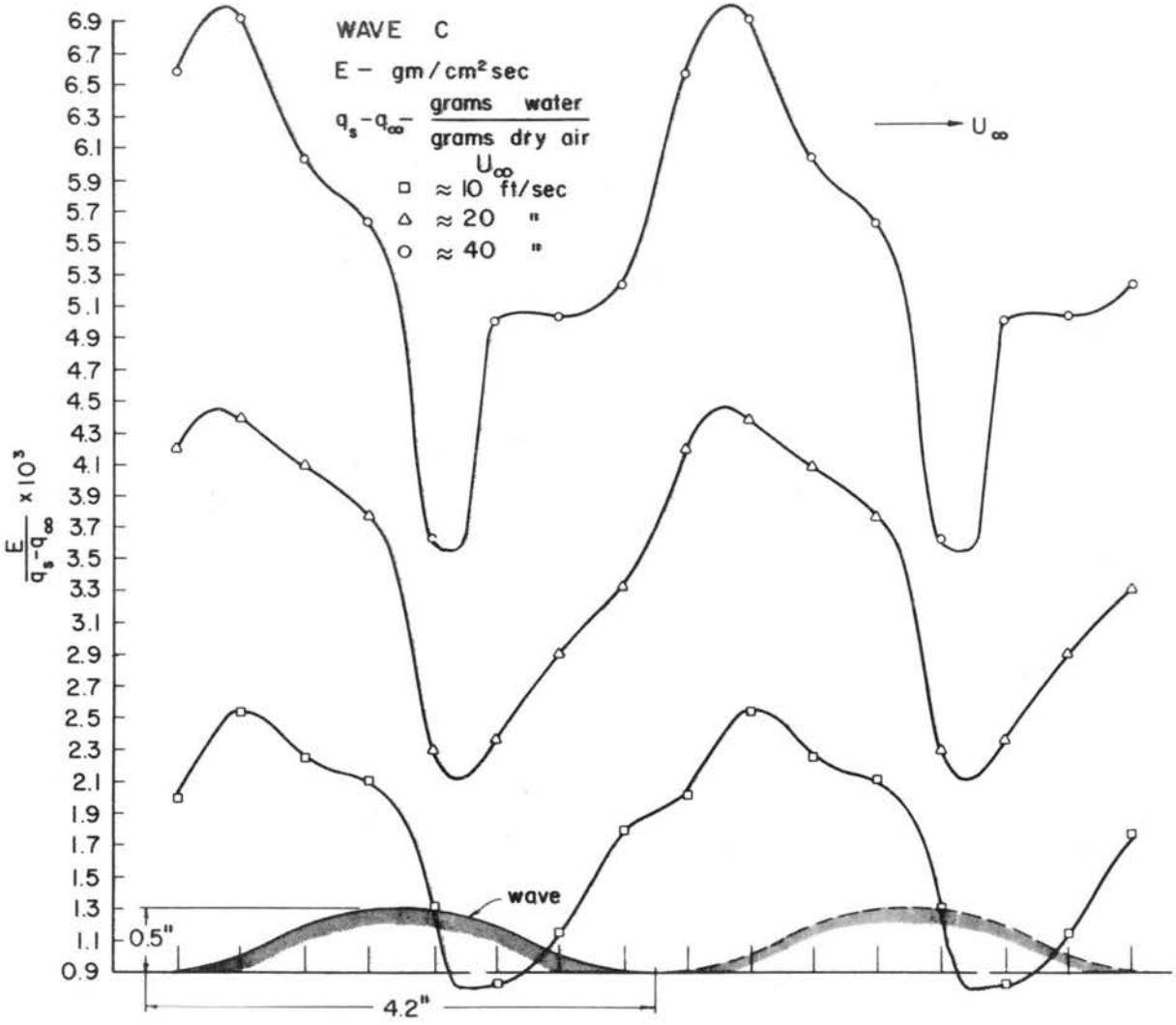

Fig. 62. Distribution of local mass transfer coefficients, Wave C

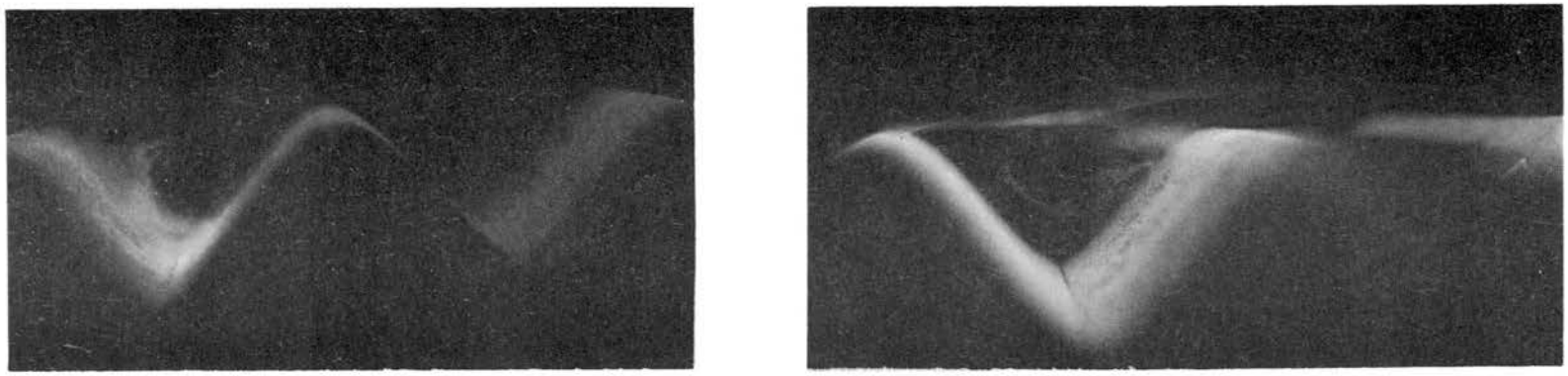

Fig. 63. Photographs of visualization study, Wave A.

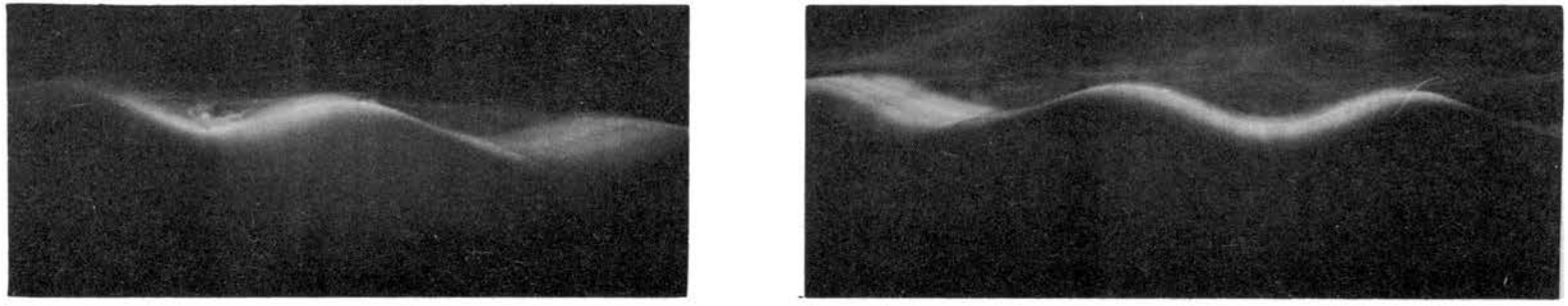

Fig. 64. Photographs of visualization study, Wave C.

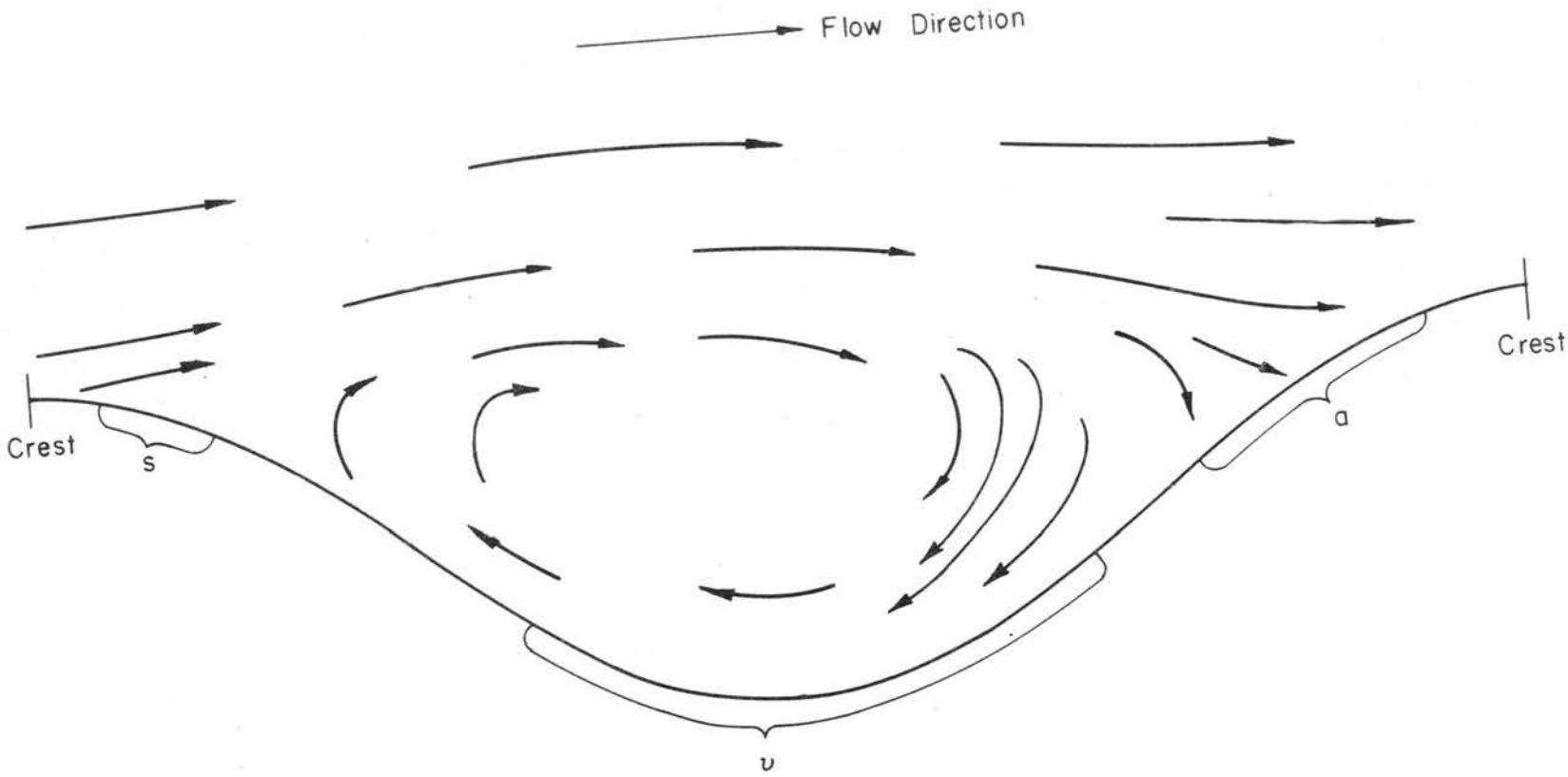

Fig. 65. Approximate flow pattern.

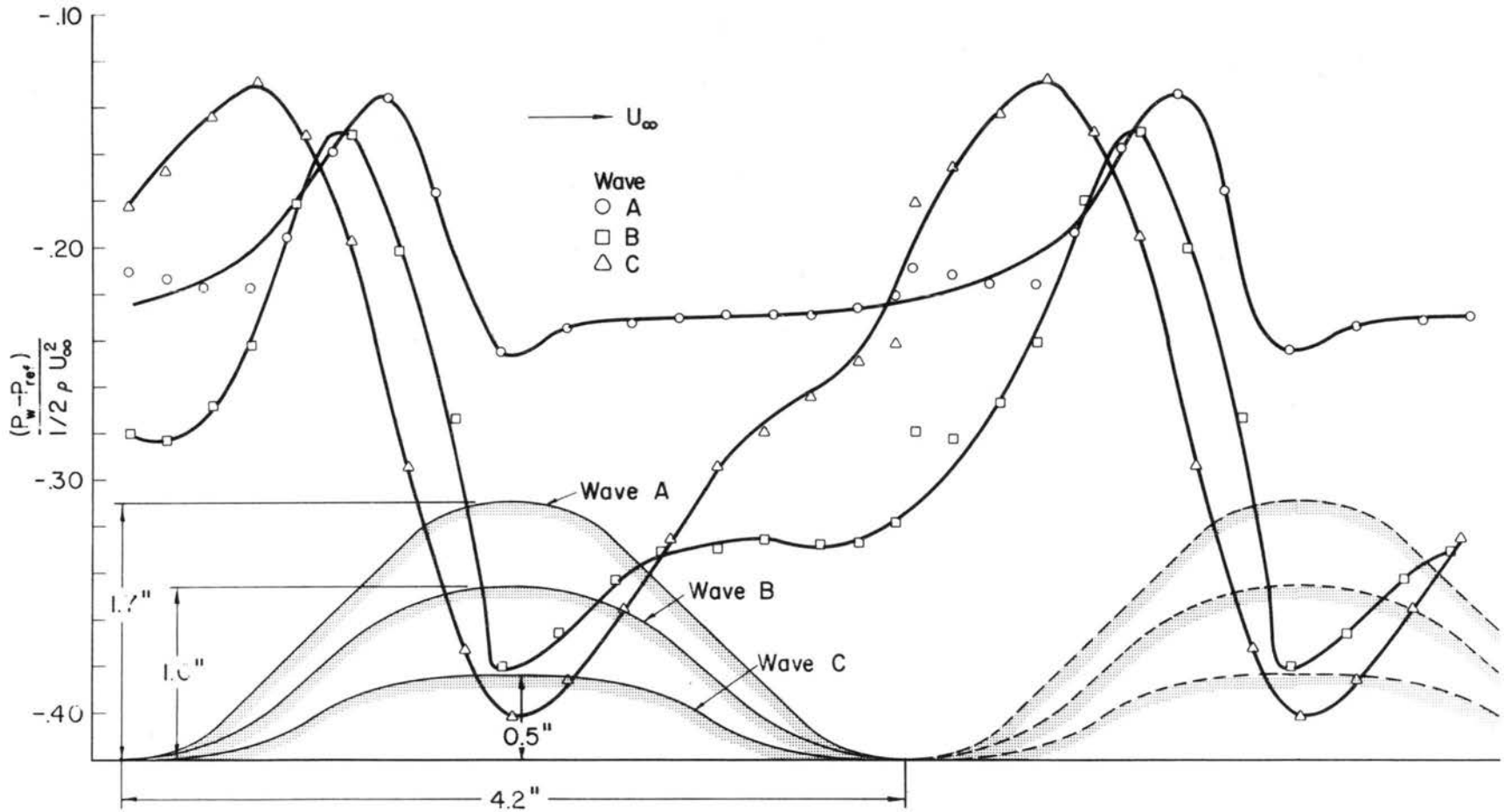

Fig. 66. Wall pressure distributions, waves A, B, & C.

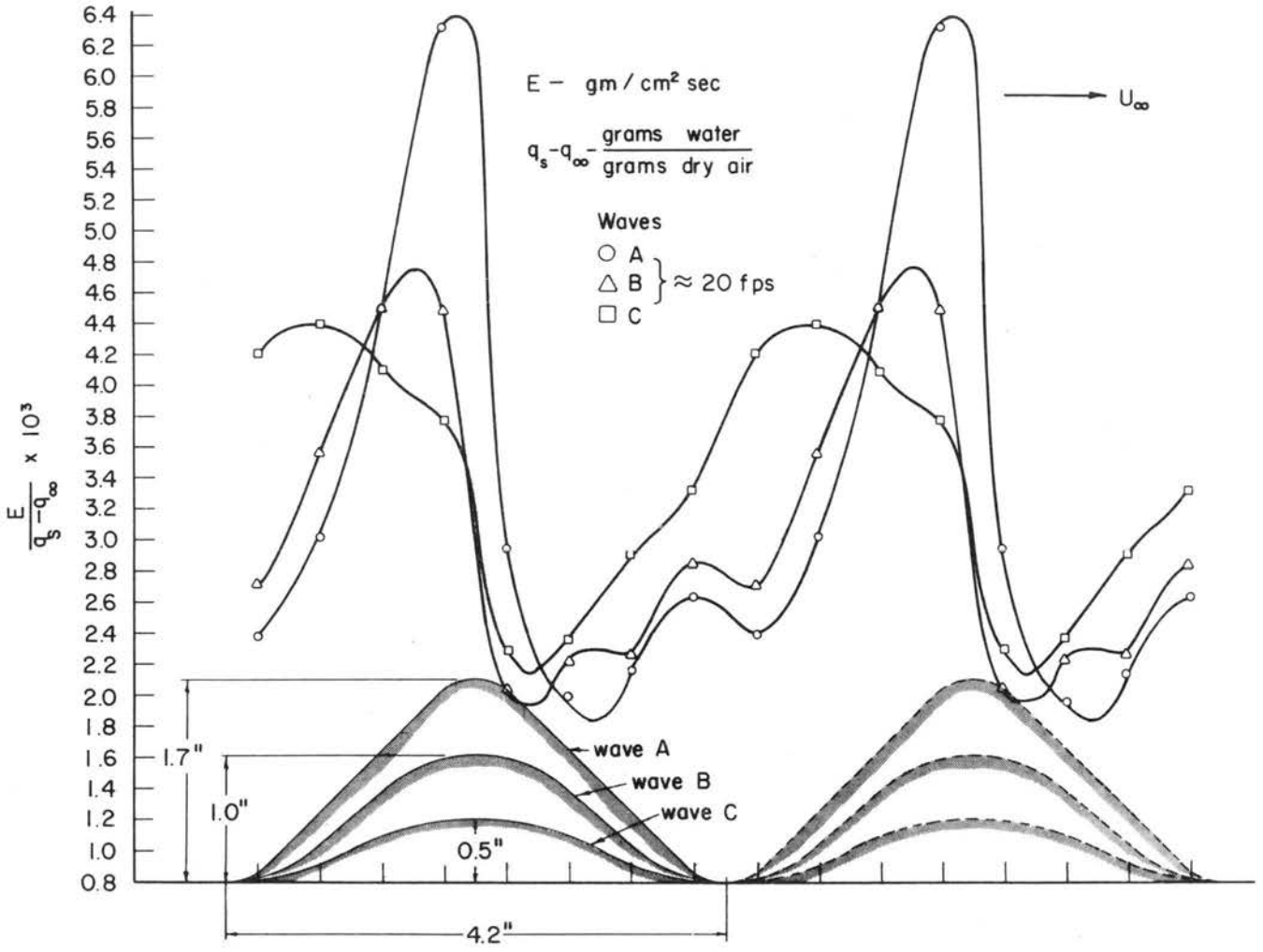

Fig. 67. Comparison of distributions of local mass transfer coefficients for the three wave sets.

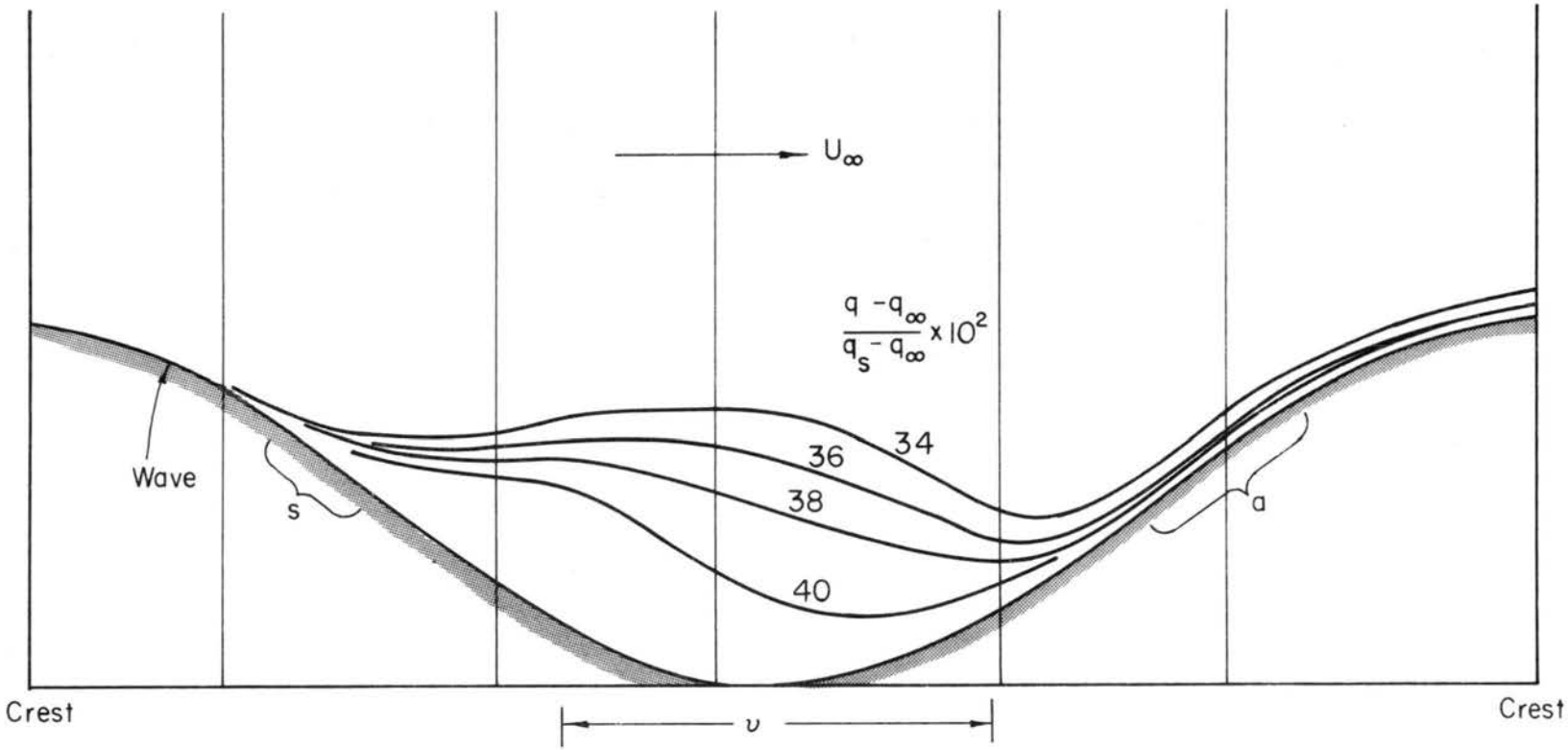

Fig. 68. Typical set of isoconcentration lines in a wave trough.

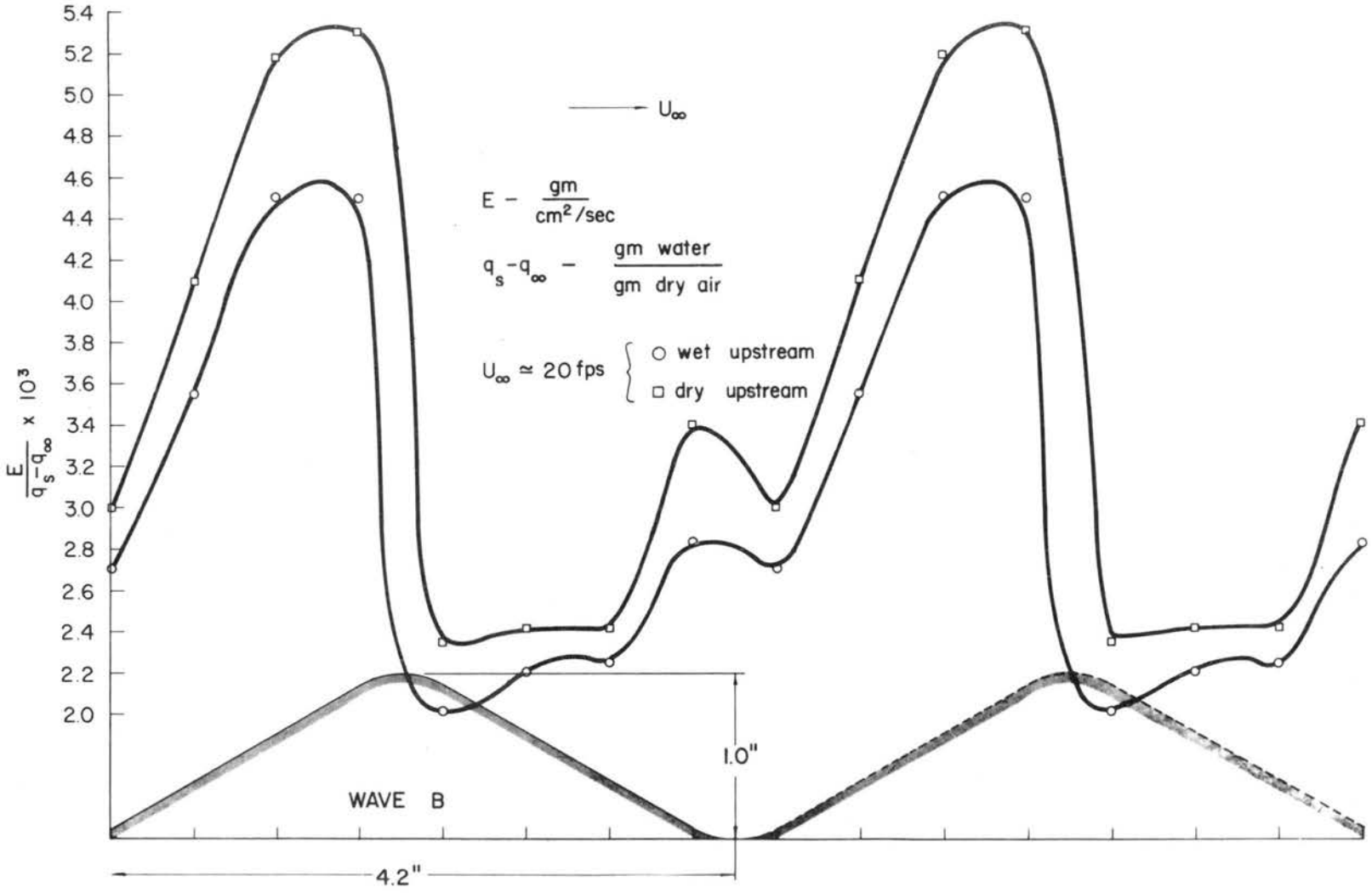

Fig. 69. Comparison of local mass coefficient distributions for wet and dry upstream cases, (Typical case).

Wave	h/λ	Region D
A	0.41	-0.43λ to 0.15λ
B	0.24	-0.46λ to 0.08λ
C	0.12	-0.48λ to 0.17λ

$U_\infty \approx 20$ ft./sec

Region D ≈ Region Over Which $\dfrac{(\frac{E}{\Delta q}) - (\frac{E}{\Delta q})_{min.}}{(\frac{E}{\Delta q})_{max.} - (\frac{E}{\Delta q})_{min.}} < 0.25$

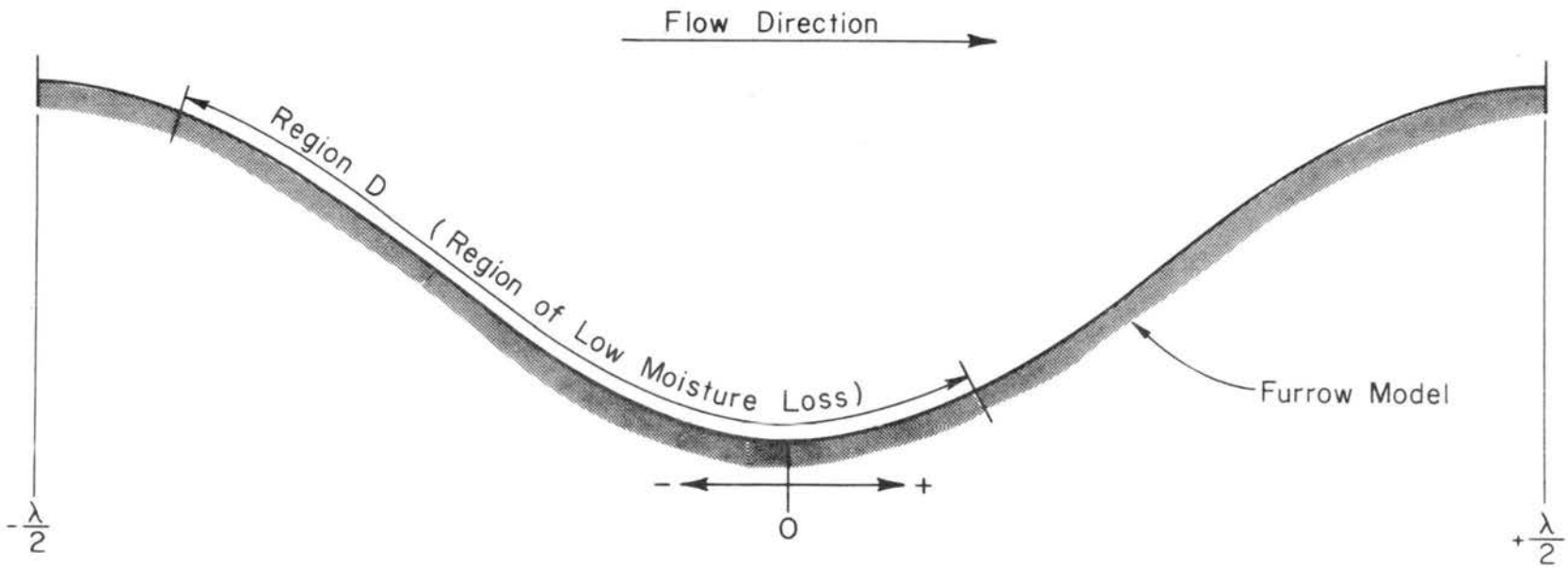

Fig. 70. Model of a field furrow

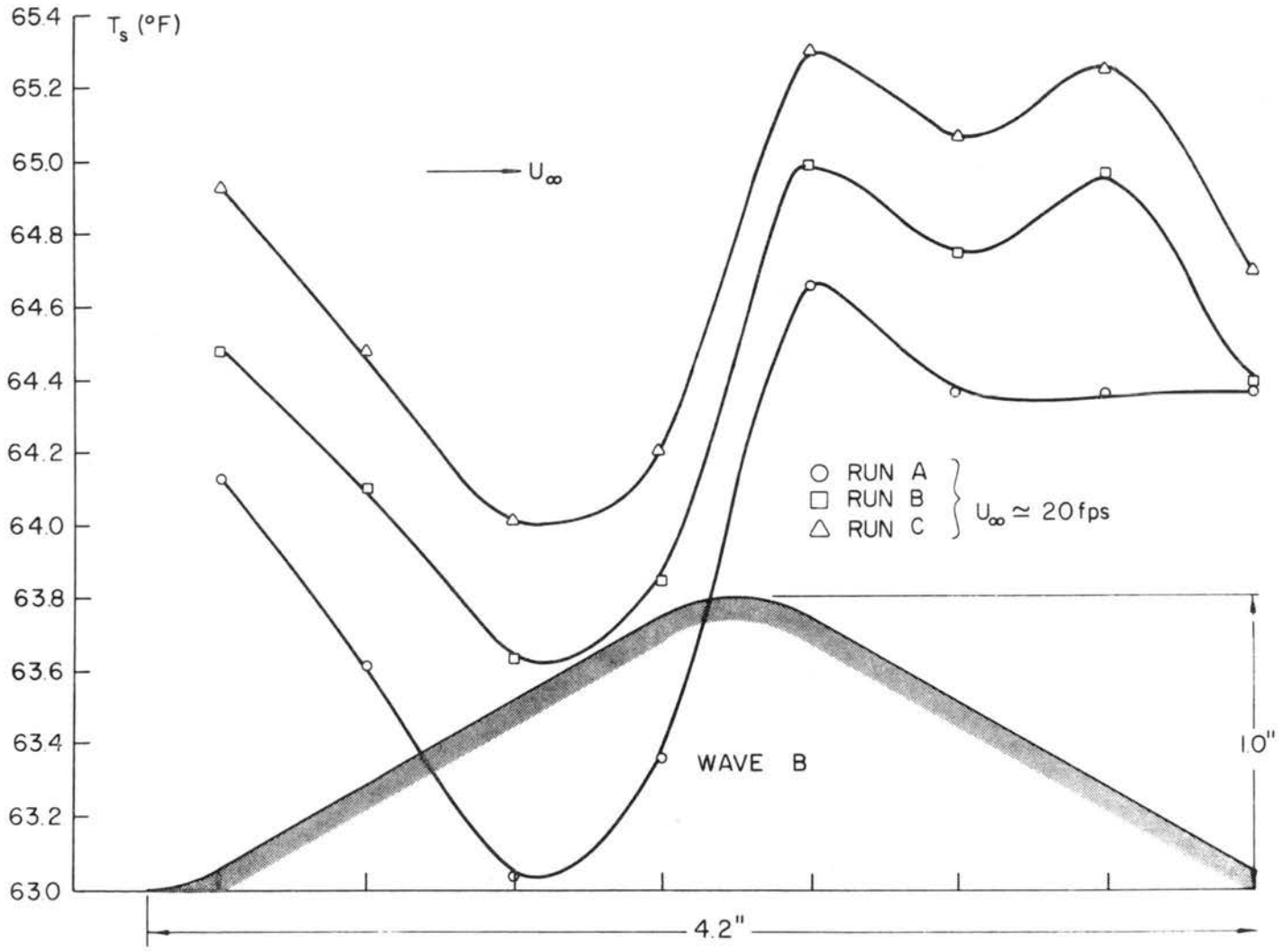

Fig. 71. Variation of surface temperature on a saturated wavy surface (Typical case).

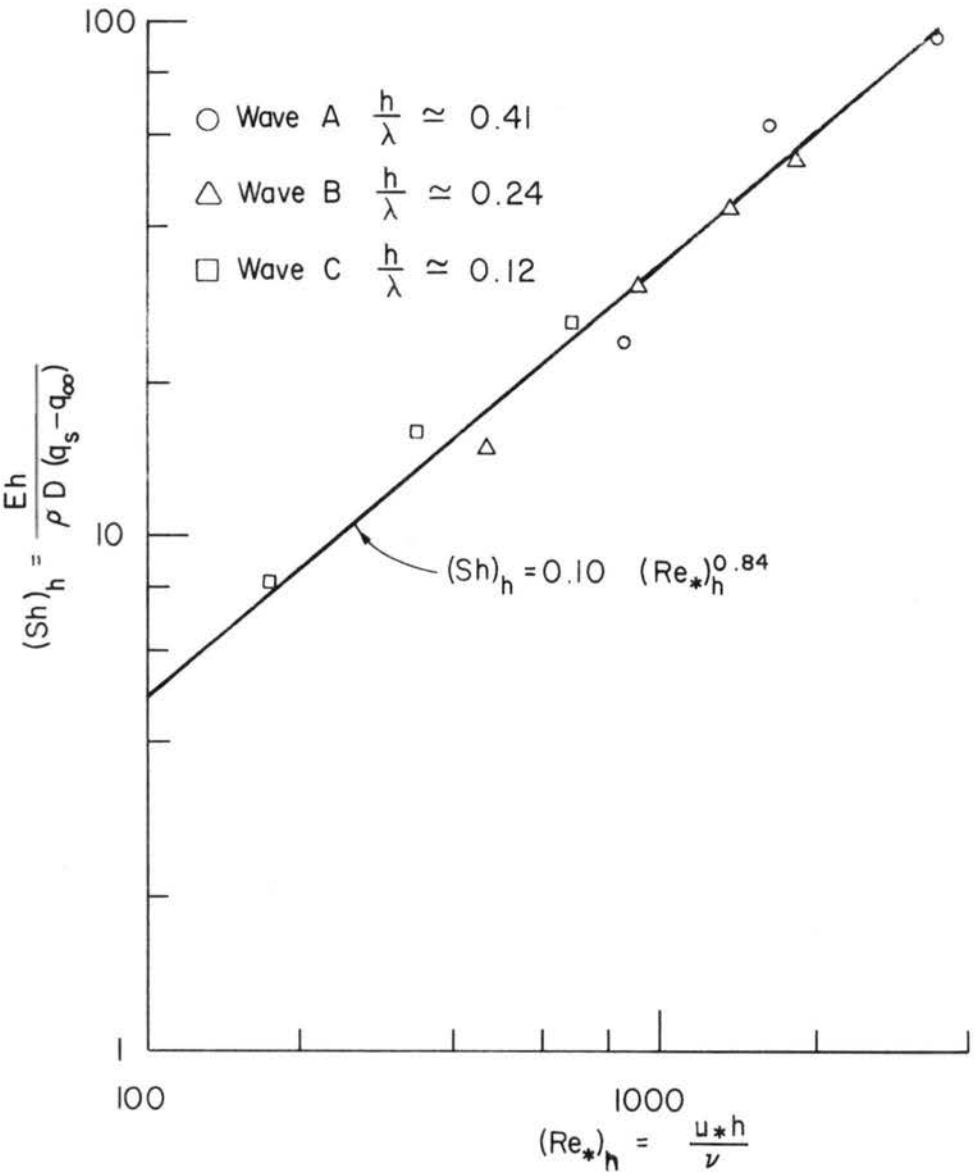

Fig. 72. Correlation of evaporation data with h as the characteristic length.

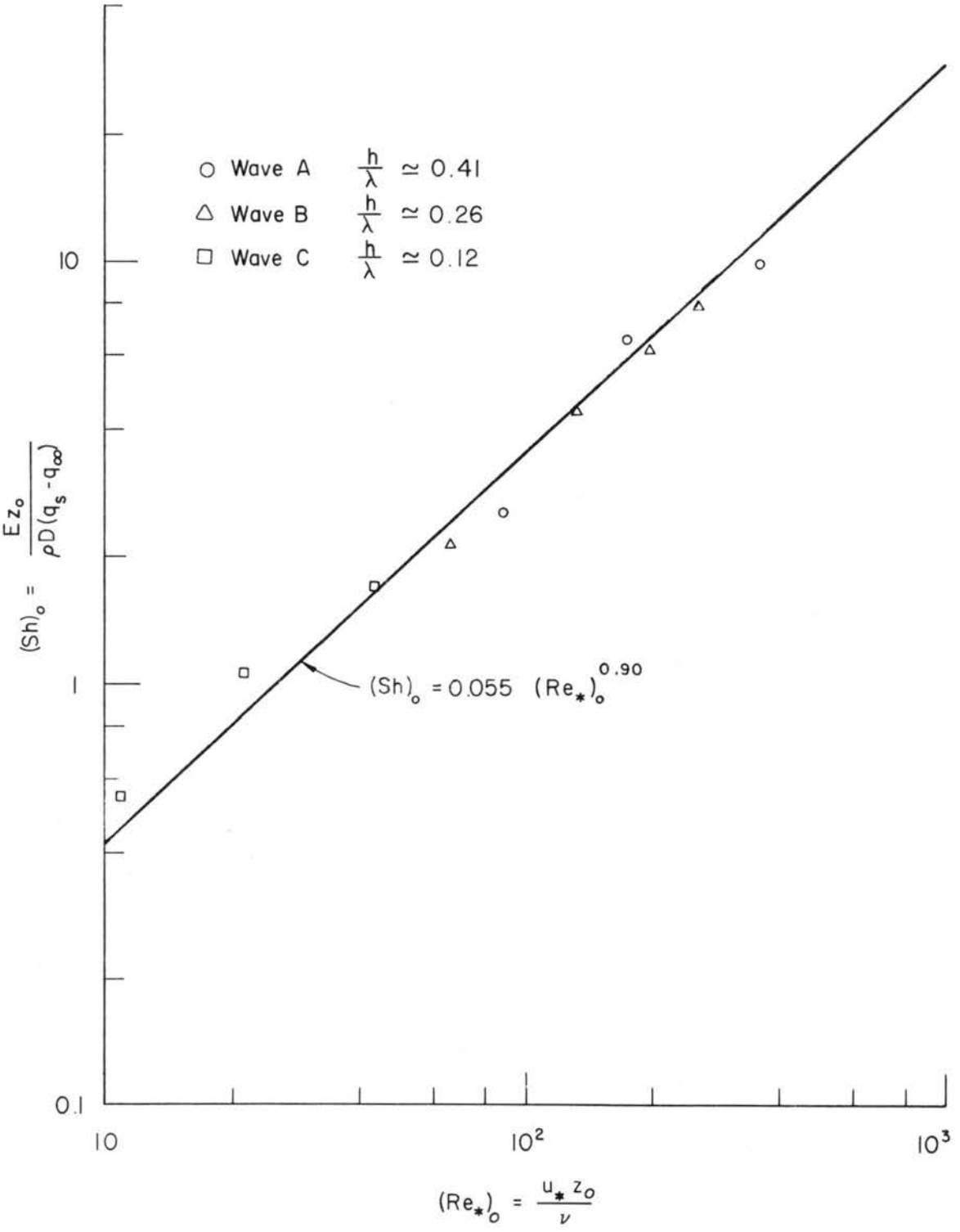

Fig. 73. Correlation of evaporation data with z_o as the characteristic length.

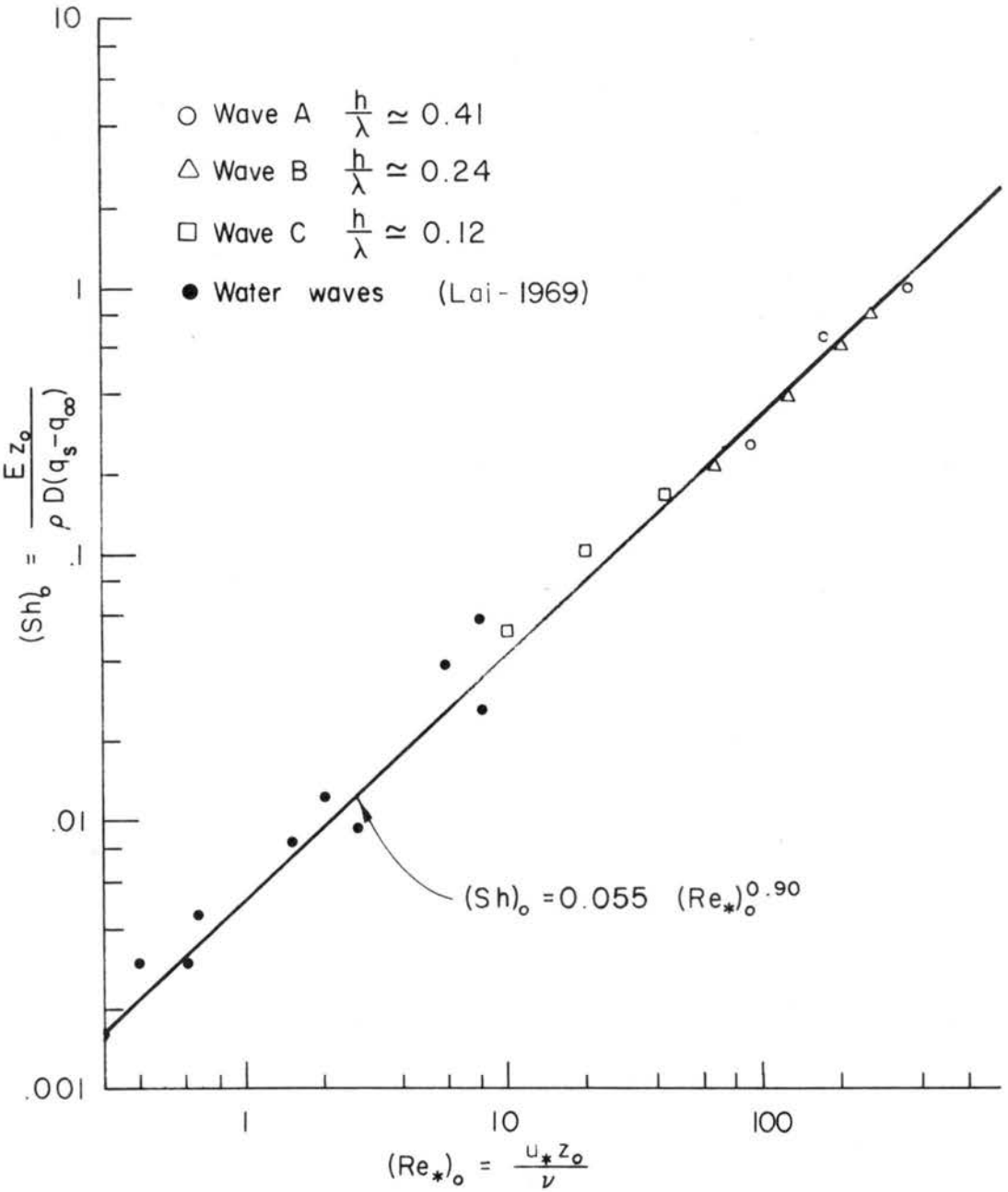

Fig. 74. Correlation of water waves data with the data of this study.

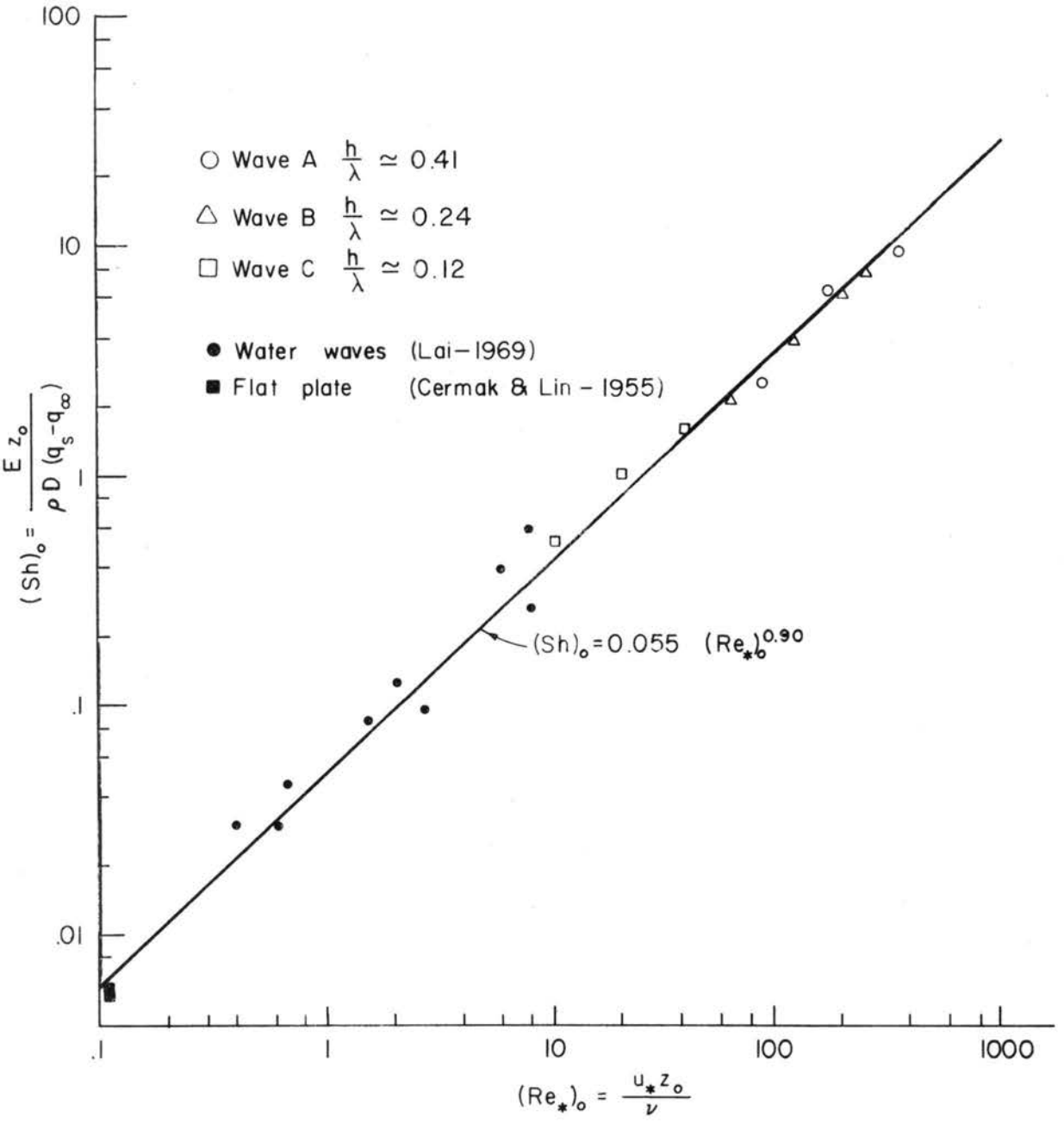

Fig. 75. Correlation of flat plate and water waves data with the data of this study.

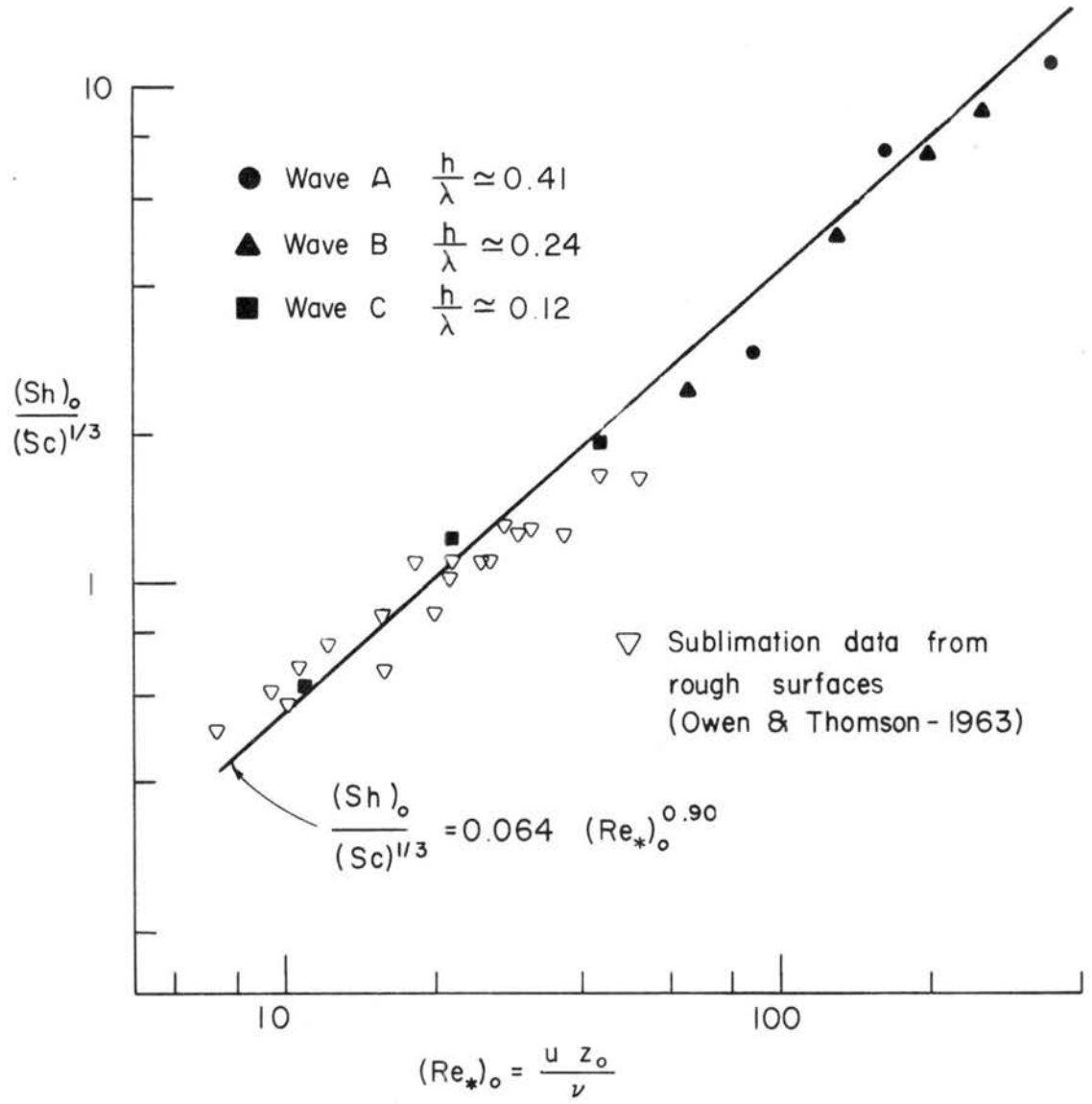

Fig. 76. Correlation of sublimation data from different kinds of rough surfaces (Owen and Thomson - 1963) with the evaporation data of this study.

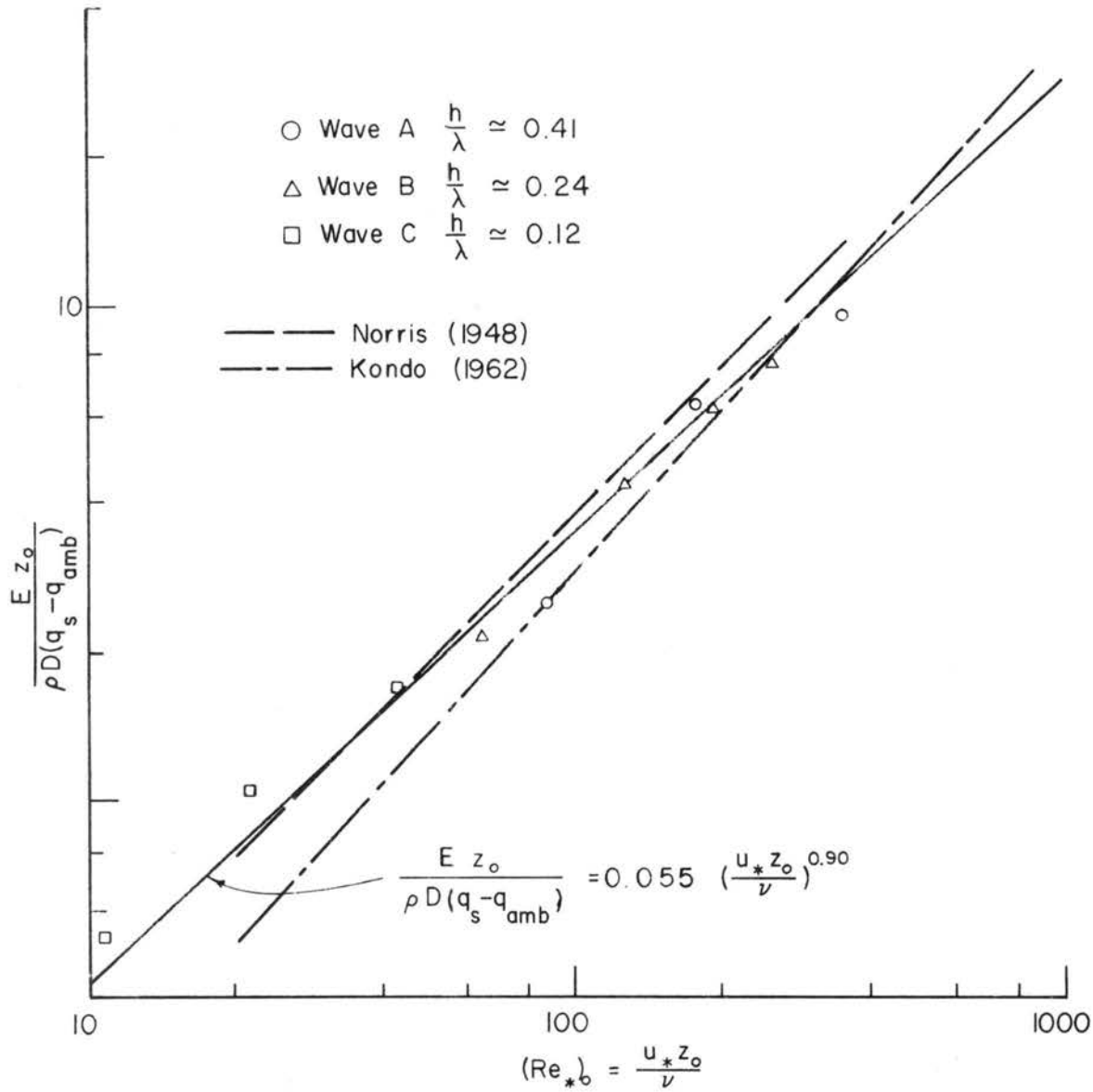

Fig. 77. Comparison with Norris' (1948) and Kondo's (1962) results.

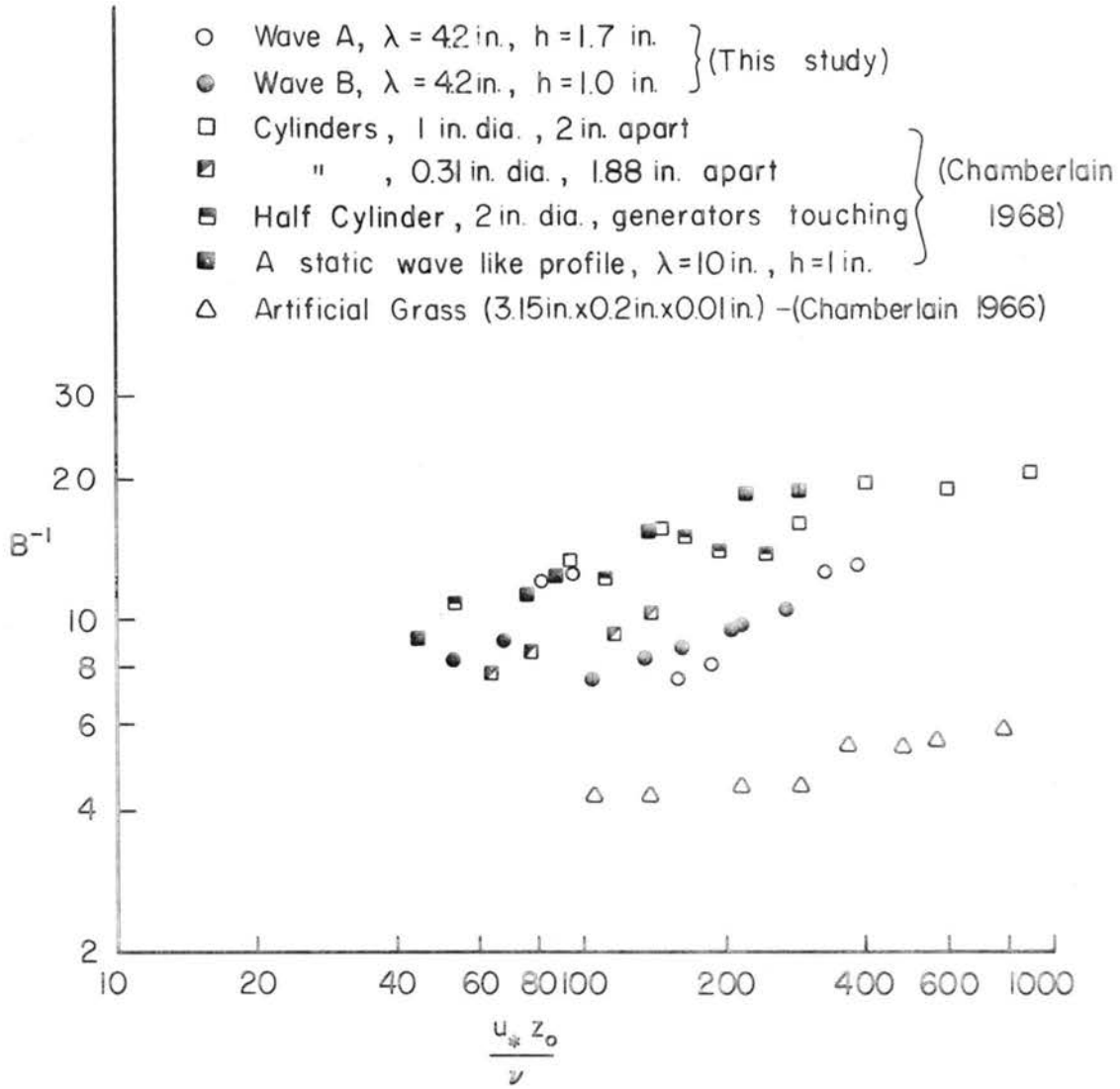

Fig. 78. Plot B^{-1} vs $\frac{u_* z_o}{\nu}$ for this study along with Chamberlain's (1966 and 1968) data.

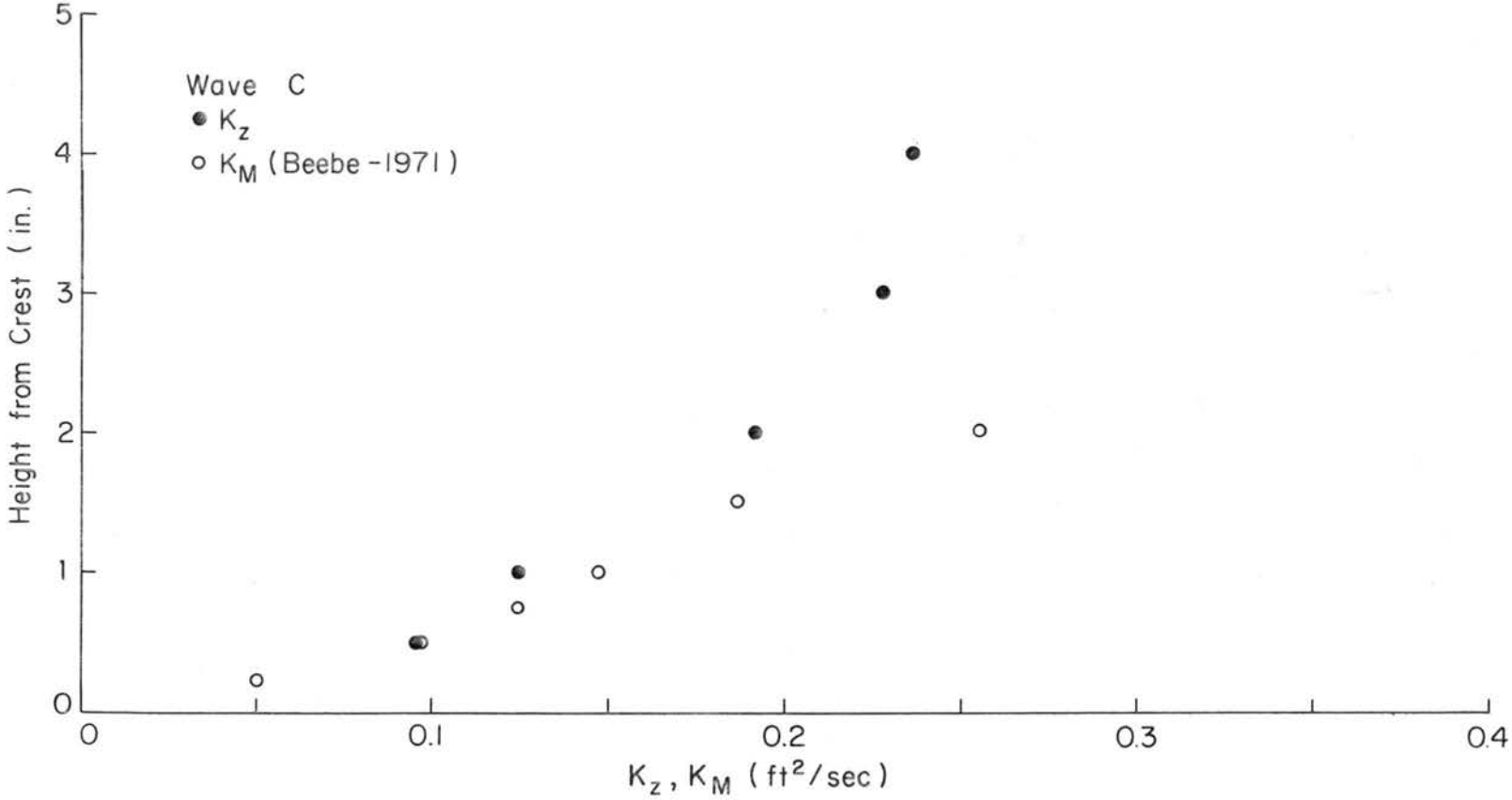

Fig. 79. Distribution of vertical exchange coefficient K_z and its comparison with the distribution of the corresponding exchange coefficient K_M for momentum transfer (Typical case).